Heinrich Heine
Universität
Düsseldorf

Exploiting protein self-interactions for inhibition of specific steps in amyloid formation

Inaugural-Dissertation

zur Erlangung des Doktorgrades der
Mathematisch-Naturwissenschaftlichen Fakultät der
Heinrich-Heine-Universität Düsseldorf

vorgelegt von

Celina Michelle Schulz

aus Euskirchen

Düsseldorf, 2024

aus dem Institut für Physikalische Biologie der Heinrich-Heine-Universität Düsseldorf

Gedruckt mit der Genehmigung der Mathematisch-Naturwissenschaftlichen Fakultät der Heinrich-Heine-Universität Düsseldorf

Berichterstatter:

1. Jun.-Prof. Dr. W. Hoyer
2. Prof. Dr. H. Gohlke

Tag der mündlichen Prüfung: 19. Juli 2024

Angefertigt im	Institut für Physikalische Biologie Heinrich-Heine-Universität Düsseldorf
Tag der Einreichung	20. März 2024
Erster Gutachter	Jun.-Prof. Dr. W. Hoyer
Zweiter Gutachter	Prof. Dr. H. Gohlke

Eidesstattliche Erklärung

Hiermit versichere ich an Eides statt, dass diese Dissertation von mir selbstständig und ohne unzulässige fremde Hilfe unter Beachtung der „Grundsätze zur Sicherung guter wissenschaftlicher Praxis an der Heinrich-Heine-Universität Düsseldorf“ erstellt worden ist. Die Arbeit wurde bisher keiner Prüfungsbehörde vorgelegt und auch noch nicht veröffentlicht. Ich habe bisher keinen erfolglosen Promotionsversuch unternommen.

Düsseldorf, den 21. August 2024

„Die Voraussetzung für Wissen ist die Neugier.“
∼Jacques-Yves Cousteau

Danksagung

Ich bin sehr dankbar für all die Unterstützung, die ich während meiner Promotion erhalten habe. Ohne diese wäre die Fertigstellung dieser Arbeit nicht möglich gewesen.

Ganz herzlich möchte ich mich bei meinem Erstgutachter Jun.-Prof Dr. Wolfgang Hoyer bedanken. Ich danke dir für die Bereitstellung eines so interessanten Themas. Es war immer sehr inspirierend mit dir zusammenzuarbeiten und von deiner langjährigen Erfahrung und deinem Wissensreichtum zu profitieren. Auch möchte ich mich bei dir für deine ständige Bereitschaft zu Diskussionen und Besprechungen über Probleme, alternative Vorschläge und Einschätzungen während all dieser Jahre bedanken. Ich schätze deine durchweg positive und gelassene Art. Ebenso möchte ich mich bei dir für die eigenständige Arbeitsatmosphäre bedanken, durch die ich meinen eigenen Ideen und Impulsen nachgehen konnte.

Als nächstes möchte ich mich bei Prof. Dr. Holger Gohlke für die Übernahme der Rolle als mein Mentor und Zweitgutachter bedanken. Ein weiteres Dankeschön geht an den Institutsleiter Prof. Dr. Dieter Willbold für die Bereitstellung aller Einrichtungen und einer geeigneten, interdisziplinären Umgebung.

Dankend möchte ich meine Kooperationspartner für die Zusammenarbeit und ihren wertvollen Input in den verschiedenen Projekten erwähnen: Prof. Dr. Erdem Tamgüney Gültekin, Miriam Alexander, Dr. Nima Abedpour, Dr. Matthias Stoldt und Prof. Dr. Henricke Heise. Ein großer Dank gilt auch meinen Kooperationspartnern aus Dresden. Stefan Bräuer und Prof. Dr. Björn Falkenburger, vielen Dank für eine schöne, entspannte und zielführende Zusammenarbeit. Durch diesen Austausch wurden mir vor allem Einblicke aus der medizinischen Sichtweise auf die Krankheiten, ihren Verlauf und den aktuellen Stand in der Diagnostik ermöglicht.

Des Weiteren möchte ich mich bei unseren Technischen Angestellten von Herzen bedanken, ohne die der funktionierende Laboralltag nicht möglich wäre. Vielen Dank an Robin Backer, Barbara Schulte, Linda Reinecke, Joanna Zeyer und Andrea Janosch. Ich schätze eure Leichtigkeit, mit denen ihr jeden Tag euch neuen, unerwarteten Aufgaben und Problemen stellt und trotzdem noch die Zeit findet, die Arbeitsatmosphäre in dem Institut durch eure positive und offene Art aufzulockern.

Von Herzen möchte ich mich bei Prof. Dr. Alexander Buell bedanken, durch den ich die Möglichkeit hatte, während meiner Promotion für ein Forschungsaufenthalt, Dänemark zu besuchen. Ich habe meine Zeit an der Technischen Universität in Kopenhagen sehr genossen, insbesondere durch die hervorragende Betreuung von Alex. Ich danke dir sehr für deinen Input, das Interesse an meiner Arbeit und deine freundliche Persönlichkeit. Es war enorm bereichernd für mich einen Einblick in deine Arbeitsweise und Arbeitsgruppe zu erhalten. Auch danke ich dir besonders für die weiteren Hilfsangebote nach meinem Aufenthalt bei euch. Zusätzlich möchte ich mich bei Dr. Soumik Ray für die Übernahme meiner Betreuung während dieser Zeit danken, ich konnte sehr viel von dir lernen. In dem Sinne möchte ich mich auch bei HERA

bedanken, die mir diesen Promotionsaufenthalt durch ein Stipendium ermöglicht haben.

Ein weiterer Dank gilt Dennis Hasenklever, der sich als Ansprechpartner um die neu angelegten FACS-Facility kümmert und bei Fragen und Problemen durchgängig zur Verfügung steht. Ebenso möchte ich mich bei Thorsten Wachmeister aus dem Genomik and Transkriptomik Labor der HHU für die NGS Durchführung und stetige Erreichbarkeit bedanken. Auch möchte ich mich bei Dr. Lothar Gremer für seine Hilfe und Ratschläge bedanken.

Ein herzlichster Dank gebührt Dr. Anne Pfitzer-Bilsing. Danke für die großartige Zusammenarbeit! Ich danke dir vor allem für die zielführende, leichte und immer lustige Zusammenarbeit. Ich schätze an dir deine offene und durchweg positive Art und dass du immer ein Grund zum Lachen findest, mit dem du andere anstecken kannst. Bedanken möchte ich mich auch für dein Engagement, leichte Absprachen und Diskussionsbereichschaft. Danke für alles und auch für die konstruktiven Korrekturen zu dieser Arbeit. Ich freue mich auf den nächsten Aperol mit dir.

Besonders zu erwähnen ist Dr. Emil Agerschou für die hervorragende Einarbeitung in die Thematik. Ich danke dir für dein ständiges Engagement als mein Betreuer, aber auch nach deiner Zeit an der HHU. Zusätzlich schätze ich sehr, dass du mir bei Fragen und Problemen immer zur Seite gestanden hast, für deine guten Ideen und deine Diskussionsbereitschaft.

Ein weiteres Dankeschön geht an Dr. Hamed Shaykhalishahia für die Zusammenarbeit, deine unterstützende Art, und deine ständige Disskusionsbereitschaft. Ich danke dir, dass ich mit dir in ein weiteres Themengebiet eintauchen konnte. Auch möchte ich mich bei dir für das Korrekturlesen des NGS Kapitels bedanken. Ebenso möchte ich mich bei Filip Hasecke und allen ehemaligen und derzeitigen Mitgliedern der Arbeitsgruppe, die sogenannte Wolf-Gang bedanken. Ohne den ständigen Austausch mit euch und eurer hohen Hilfsbereitschaft wäre die Fertigstellung der Arbeit nicht möglich gewesen. Danke! Zusätzlich möchte ich mich bei allen Studierenden bedanken, die mich in dem einen oder anderen Projekt unterstützt haben. Namentlich erwähnen möchte ich somit: Lara Rogazi, Max Burmeister, Fabian Russak, Joleene Kunk, Mattis Bollmann, Riecke Beuker, Martin Froning genannt Havixbeck und Sophia Werner.

Ausdrücklich zu erwähnen ist Nina Kirchgässler. Ich danke dir für deine selbstlose Art, deinen Humor, dein Engagement und deine Hilfsbereitschaft, die mir in den letzten Jahren als Sitznachbarin im Büro, aber auch schon während unseres gemeinsamen Studiums eine enorme Stütze war. Vor allem aber danke ich dir für die witzigen Mensa-Gänge, die mich immer den Alltagsstress vergessen haben lassen und die ich in Zukunft vermissen werde. Auch dankend zu erwähnen ist deine Diskussionsbereitschaft, mir auch bei einem für dich fremden Thema zu helfen und deine Rettungsversuche, wodurch ich bei der Anfertigung der Arbeit in Latex nicht komplett verloren gegangen bin. Danke für alles!

Im weiteren möchte ich mich auch bei Fatima Escobedo Gonzalez, Najoua Bolakhrif, Tatsiana Kupreichyk und Luis Gardon für eure ständige Erreichbarkeit, die vielen witzigen Momente und offenen Ohren bedanken. Ein weiterer Dank gebührt Dr. Nils-Alexander Lakomek für die lustigen Gespräche, aber auch für den konstruktiven Austausch. Auch danke ich dir, dass du mir die Möglichkeit gegeben hast mittels Zugang und Betreuung von NMR Messungen, meinen

eigenen Projektideen und Interessen nachzugehen. Zusätzlich danke ich allen ehemaligen und derzeitigen Mitarbeitern aus dem IPB für die schöne Arbeitsatmosphäre, große Hilfsbereitschaft und den konstruktiven Austausch.

Judith Geusen, Luisa Klein und Dr. Andrea Weiler danke ich für das Korrekturlesen meiner Arbeit und ihre Freundschaft, die mich alle die Zeit begleitet hat. Das größte Dankeschön gilt meiner Familie, meinen Eltern, Martina und Uwe, und meiner Schwester Laura auf deren Unterstützung ich immer bauen konnte. Zusätzlich möchte ich mich bei meinem Freund Fabian für seine Unterstützung bedanken. Danke, dass ihr immer ein offenes Ohr für meine Probleme und Bedenken habt und danke, dass ihr euch immer mit mir über meine Erfolge freut.

Vielen Dank!

CONTENTS

List of abbreviations . . . . . **v**

Abstract . . . . . **ix**

Zusammenfassung . . . . . **xi**

1. General introduction **1**
1.1. Amyloids 1
1.1.1. Occurence 2
1.1.2. Characteristics of amyloids 5
1.1.3. Mechanism of amyloid aggregation 7
1.2. Off-pathway oligomers as competitors of amyloid fibrils 10
1.2.1. Oligomers' role in amyloid disease 11
1.3. Synucleinopathies 12
1.3.1. Native properties of the protein α-synuclein 13
1.3.2. Aggregation properties of α-synuclein 15
1.3.3. Spreading of α-synuclein fibrils 16
1.3.4. Diagnostics 17
1.4. Inhibition of amyloid fibril formation 19
1.4.1. Molecular target sites 19
1.4.2. Strategies to improve the inhibitor specificity 21
1.5. Objective 22

2. Fibril core regions in engineered α-synuclein dimer are crucial for blocking of fibril elongation **25**
2.1. Publication information 25
2.2. Abstract 25
2.3. Introduction 26
2.4. Results 27
2.4.1. Fusion of α-syn WT and the disulfide mutant CC48 inhibits fibril elongation by blocking fibril ends 27
2.4.2. The WT part of WT-CC48 promotes inhibition of fibril elongation due to its HP and NAC regions 28
2.4.3. The HP and NAC regions of also the CC48 part of WT-CC48 are crucial for strong inhibition of fibril elongation 31
2.5. Discussion 32
2.6. Material and Methods 34
2.6.1. Transformation, expression and purification of α-syn and WT-CC48 variants 34
2.6.2. Elongation assay 34
2.6.3. Preparation and SDS-PAGE of soluble and insoluble fractions after elongation assay 35
2.6.4. Density Gradient Centrifugation (DGC) and SDS-PAGE 35

2.6.5. Atomic Force Microscopy (AFM) 35
2.7. Acknowledgments 36
2.8. Supplementary Information 37

3. Disordered regions of inhibitor-bound α-synuclein suppress the seed-induced fibril nucleation in cells 43
3.1. Publication information 43
3.2. Abstract 44
3.3. Introduction 45
3.4. Results 45
3.4.1. Fusion constructs exhibit intramolecular formation of the AS69:αS complexes 45
3.4.2. Validation of the secondary nucleation assay 47
3.4.3. The complex of AS69 and αS inhibits fibril nucleation at substoichiometric concentration by interacting with αS oligomers . . 48
3.4.4. αS IDRs of AS69-αS are required for nucleation inhibition 51
3.4.5. αS IDRs act in concert with the globular AS69:αS domain 52
3.4.6. The constructs' potency to inhibit seed-induced aggregation in cells correlates with their potency to inhibit fibril nucleation 52
3.5. Discussion 54
3.6. Materials and Methods 57
3.6.1. Generation of fusion constructs and αS 57
3.6.2. Expression and purification of fusion constructs and αS 57
3.6.3. SDS-PAGE 57
3.6.4. Nuclear Magnetic Resonance (NMR) 57
3.6.5. Circular Dichroism (CD) spectroscopy 57
3.6.6. Elongation assay 58
3.6.7. Lipid-induced primary nucleation assay 58
3.6.8. Secondary nucleation assay 58
3.6.9. Atomic Force Microscopy (AFM) 58
3.6.10. Density gradient ultracentrifugation (DGC) 58
3.6.11. Cell assay for αS aggregation 59
3.7. Acknowledgments 59
3.8. Supplementary Information 60

4. Nucleation processes drive α-synuclein fibril proliferation in shaking-induced seed amplification assay 71
4.1. Publication information 71
4.2. Abstract 72
4.3. Main Text 73
4.4. Material and Methods 77
4.4.1. Expression and purification of αS and his-αS 77
4.4.2. Expression and purification of AS69nuc 77
4.4.3. Elongation assay 78
4.4.4. Fragmentation-elongation assay 78
4.4.5. Secondary nucleation assay 78
4.4.6. Seed amplification assay of αS 78
4.4.7. Atomic Force Microscopy (AFM) 79
4.5. Acknowledgments 79

4.6. Supplementary Information 80

5. Deciphering upregulated mechanisms through expression profiling in SH-SY5Y cells when exposed to α-synuclein fibrils. 81
5.1. Chapter information 81
5.2. Abstract 81
5.3. Introduction 82
5.4. Results 83
5.4.1. Establishment of a fluorescence-assay to detect αS fibril uptake by differentiated SH-SY5Y cells. 83
5.4.2. Post-exposure upregulated proteins are not involved in fibril uptake. 86
5.4.3. Membrane-bound ICAM-1 does not drive the fibril uptake 88
5.5. Discussion 90
5.6. Material and Methods 92
5.6.1. Transformation, expression and purification of αS 92
5.6.2. Labeling of αS-C140 92
5.6.3. Fibril formation 92
5.6.4. Atomic Force Microscopy (AFM) 92
5.6.5. Density Gradient Centrifugation (DGC) 93
5.6.6. Cell culture 93
5.6.7. Flow cytometry 93
5.6.8. siRNA treatment 93
5.6.9. RNA Isolation and cDNA synthesis 94
5.6.10. Next Generation Sequencing (NGS) 94
5.6.11. Quantitative Polymerase Chain Reaction (qPCR) 94
5.6.12. Immunocytochemistry 95
5.6.13. SDS-PAGE and Western blot 96
5.7. Acknowledgments 97
5.8. Supplementary Information 98

6. An islet amyloid polypeptide oligomer model for the study of amyloid aggregation and oligomer induced pathophysiology 101
6.1. Publication information 101
6.2. Abstract 102
6.3. Introduction 103
6.4. Results 104
6.4.1. DimIAPP assembles into curvilinear oligomers 104
6.4.2. DimIAPP-O inhibit aggregation of IAPP 105
6.4.3. Exposure of RIN-m5f cells to dimIAPP-O and IAPP fibrils activate cellular stress response 107
6.5. Discussion 109
6.6. Material and Methods 111
6.6.1. Protein preparation 111
6.6.2. DimIAPP-O preparation 111
6.6.3. IAPP fibril preparation 112
6.6.4. Thioflavin T (ThT) fluorescence assay 112
6.6.5. Atomic Force Microscopy (AFM) 112
6.6.6. Reverse-Phase High-Performance Liquid Chromatography (RP-HPLC) 112
6.6.7. Cultivation of RIN-m5f cells 113

6.6.8. Cell viability assay 113
6.6.9. RNA isolation and cDNA synthesis 113
6.6.10. Quantitative Polymerase Chain Reaction (qPCR) 113
6.6.11. Immunocytochemistry 114
6.7. Acknowledgments 115
6.8. Supplementary Information 116

7. General discussion 121

8. Author Contributions 127

9. Literature 129

List of abbreviations

°C	degree Celsius
5-FAM	5-carboxyfluorescein
αS or α-syn	α-synuclein
βS	β-synuclein
γS	γ-synuclein
Å	Ångström
aa	amino acids
Aβ	amyloid-β
AC mode	intermittent contact mode
ACN	acetronitrile
AD	Alzheimer's disease
AFM	atomic force microscopy
ALS	amyotrophic lateral sclerosis
APLP1	amyloid beta precursor like protein 1
ALS	Amyotrophic lateral sclerosis
AS69nuc	fusion of AS69 with αS units
Atf4	activating transcription factor 4
Atf6	activating transcription factor 6
BDNF	brain-derived neurotrophic factor human
Cat	catalase
CD	circular dichroism
cDNA	complementary deoxyribonucleic acid
Chop	CCAAT-enhancer-binding protein homologous protein
COC	critical oligomer concentration
Cryo-EM	cryogenic-electron microscopy
CSF	cerebrospinal fluid
Da	dalton
DGC	density gradient centrifugation
dimAβ	dimeric construct of amyloid-β
dimIAPP	dimeric construct of modified IAPP (C2S, C7S)
dimIAPP-O	oligomers of dimeric construct of modified IAPP (C2S, C7S)
DLB	Lewy body dementia
DMEM	Dulbecco's modified eagle's medium
DMF	N,N-dimethylformamide
DMPS	1,2-dimyristoyl-sn-glycero-3-phospho-L-serine
DMSO	dimethyl sulfoxide
DNA	deoxyribonucleic acid
dNTPs	deoxynucleotide triphosphates
DTT	dithiothreitol
E. coli	*Escherichia coli*
eIF2α	eukaryotic translation initiation factor 2α
ER	endoplasmic reticulum
et al.	*et alia*
FDA	Food and Drug Administration

FPKM	fragments per kilobase of transcript per million
FSC	forward scatter
fwd	forward
G3BP	Ras-GTPase-activating protein (GAP)-binding proteins
$(G_4S)_4$	glycine-serine linker
h	hour
H_2O	water
H_2O_2	hydrogen peroxide
HFIP	1,1,1,3,3,3-hexfluoro-2-propanol
HPLC	high-performance liquid chromatography
HSPG	heparan sulfate proteoglycan
Hz	hertz
IAPP	islet amyloid polypeptide
IC50	inhibitor concentration at which the aggregation process is reduced by 50%
ICAM-1	intercellular adhesion molecule 1
IDR	intrinsically disordered regions
IEC	ion exchange chromatography
IMAC	immobilized metal affinity chromatography
IRE1	inositol-requiring protein 1
ISA	International society of amyloidosis
kg	kilogram
l	liter
LAG3	lymphocyte activation gene 3
LLPS	liquid-liquid phase separation
m	meter
min	minute
MES	2-(N-morpholino) ethanesulfonic acid
MQ	milli-Q
MSA	Multiple system atrophy
MWCO	molecular weight cut-off
NAC	non-amyloid-β component
NaCl	sodium chloride
NaN_3	sodium azide
NaOH	sodium hydroxide
NaPi	sodium phosphate buffer
NGS	next-generation sequencing
NMR	nuclear magnetic resonance
NPH	normal pressure hydrocephalus
OD	optical density
PAF	Pure autonomic failure
PBS	phosphate-buffered saline
PCR	polymerase chain reaction
PD	Parkinson's disease
PERK	pancreatic eukaryotic translation initiation factor 2α kinase
PMSF	phenylmethylsulfonyl fluoride
PrP^{C}	native cellular prion protein
PrP^{SC}	scrapy prion protein
pS129	phosporylated αS at position 129
PSP	Progressive supranuclear palsy

PTM	post-translational modification
qPCR	quantitative polymerase chain reaction
RBD	rapid eye movement sleep behavior disorder
rev	reverse
RNA	ribonucleic acid
ROS	reactive oxygen species
RP	reversed-phase
rpm	revolutions per minute
RT	room temperature
RT-QuIC	real-time quaking-induced conversions
s	second
SAA	seed amplification assays
SDS	sodium dodecyl sulfate
SDS-PAGE	sodium dodecyl sulfate – polyacrylamid gel electrophoresis
SEC	size exclusion chromatography
SG	stress granules
SI	supplementary information
siRNA	small-interfering ribonucleic acid
Sod2	superoxide dismutase 2
SSC	side scatter
ssNMR	solid-state nuclear magnetic resonance
T2DM	Type 2 *diabetes mellitus*
ThT	Thioflavin-T
TPM	transcript per million
Tris	Tris(hydroxymethyl)aminomethane
V	volt
WT	wildtype
WT-CC48	dimeric construct of αS comprising a hairpin motif in one of the two monomers fused
Xbp1	UPR transcription factors X-box binding protein 1

Abstract

Worldwide, a high number of patients are affected by protein misfolding diseases, caused by the formation of insoluble amyloid fibrils that accumulate as protein deposits. Amyloid fibrils represent highly ordered, insoluble protein aggregates with a characteristic cross-β conformation. Various sequences, despite their dissimilarity, can adopt this conformation and aggregate, a phenomenon frequently observed in amyloid diseases like Alzheimer's (AD) or Parkinson's diseases (PD). This thesis delves into two primary topics, examining the mechanistic role of the intrinsically disordered regions (IDRs) in amyloid formation and inhibition of α-synuclein (αS), as well as exploring the pathophysiological effects on cells induced by various aggregation species.

In the first part, the modes of action of amyloid inhibitors were under investigation. Inhibitors of amyloid formation can target different sites, such as the fibril ends to prevent elongation. Previously, the engineered protein WT-CC48, which is a fusion of wildtype (WT) αS with the disulfide-containing αS mutant CC48, exhibited high potential to inhibit fibril elongation. Here, we studied which regions of WT-CC48 are responsible for the strong inhibitory effect by characterizing a set of truncated versions of WT-CC48. We show that in both the WT and the CC48 part of the fusion construct the regions required for strong inhibition correspond to the segments forming the β-sheet core of αS fibrils. This suggests that coverage of the full β-sheet core interface exposed at the fibril end is beneficial for optimization of fibril elongation inhibitors.

Surprisingly, even an αS monomer binding protein can achieve substoichiometric inhibition of αS aggregation. The engineered binding protein β-wrapin AS69 sequesters monomeric αS in the region of amino acid 30-60, while the remaining sequence stays intrinsically disordered. We could show that this substoichiometric activity requires not only the globular part of the complex but also the IDRs of αS. This means that the ability of IDRs to interfere with amyloid formation can be exploited by inhibitors to inhibit specific mechanisms *in vitro* and in cellular aggregation assays. On this basis, an inhibitor called AS69nuc was developed that specifically inhibits the nucleation of αS fibrils, but not their elongation. The use of AS69nuc as an artificial tool gained valuable insights into aggregation proliferation in the diagnostic seeded amplification assay (SAA). Our findings reveal that under SAA conditions, secondary nucleation drives the proliferation initiated by PD patients' cerebrospinal fluid (CSF).

The second part of this thesis is centered around the understanding of cellular internalization and pathophysiological effects of fibrils and oligomeric species. Next generation sequencing (NGS) was performed to provide insights into cellular response systems against fibrils. This molecular snapshot allowed to identify the critical components of the cell response to fibrils, which may be further considered as potential biomarkers. In addition to looking at the impact of fibrils on cells, the study of oligomers remains an important issue, as these are often described as the toxic species. However, oligomers are difficult to study due to their transient nature, low population under standard conditions, and structural heterogeneity. Therefore, we developed an oligomer model, which enables the investigation of the effects of stable curvilinear oligomers.

The findings in this thesis highlight the significance of IDRs as facilitators of inhibition of amyloid formation. They can guide the design of inhibitors, enhancing their inhibitory potential, and offer a fresh perspective to exploit the aggregating protein's self-interaction for inhibition. Moreover, they contribute to the understanding of the individual steps of the amyloid formation reaction. Shedding light on the roles of various aggregation species, their pathophysiological effects, and the cellular response system is consistently intriguing, providing valuable insights to deepen our understanding of amyloid diseases.

Zusammenfassung

Weltweit sind zahlreiche Patienten von Proteinfehlfaltungskrankheiten betroffen, die durch die Bildung von unlöslichen Amyloidfibrillen verursacht werden, welche sich als Proteinablagerungen ansammeln können. Amyloidfibrillen stellen hoch geordnete, unlösliche Proteinaggregate mit einer charakteristischen *Cross*-β Konformation dar. Verschiedene Sequenzen können trotz ihrer Unterschiede diese Konformation annehmen und aggregieren, ein Phänomen, das häufig bei Amyloid-Krankheiten, wie Alzheimer oder Parkinson, beobachtet wird. Diese Arbeit befasst sich mit zwei Hauptthemen, der Untersuchung der mechanistischen Rolle der intrinsisch ungeordneten Regionen bei der Amyloidbildung von α-Synuclein (αS) und dessen Hemmung, sowie der Erforschung der pathophysiologischen Auswirkungen auf Zellen, die durch verschiedene Aggregationsarten hervorgerufen werden.

Im ersten Teil wurden die Wirkungsweisen von Amyloid Inhibitoren untersucht. Inhibitoren der Amyloidbildung können an verschiedenen Stellen ansetzen, z. B. an den Fibrillenenden, um das Fibrillenwachstum zu verhindern. Bisher zeigte das gentechnisch hergestellte Protein WT-CC48, eine Fusion von Wildtyp (WT) αS mit der disulfidhaltigen αS Mutante CC48, ein hohes Potenzial zur Hemmung des Fibrillenwachstums. Hier haben wir untersucht, welche Regionen von WT-CC48 für die stark hemmende Wirkung verantwortlich sind, indem wir eine Reihe von verkürzten Versionen von WT-CC48 charakterisiert haben. Wir zeigen, dass sowohl im WT- als auch im CC48-Teil des Fusionskonstrukts die Segmente, die den β-Faltblattkern der αS Fibrillen bilden, für die starke Hemmung erforderlich sind. Dies deutet darauf hin, dass die Abdeckung der gesamten Schnittstelle des β-Faltblattkerns, die am Fibrillenende exponiert ist, für die Optimierung von Fibrillenverlängerungsinhibitoren von Vorteil ist.

Überraschenderweise kann sogar ein αS-Monomer Bindungsprotein eine substöchiometrische Hemmung der αS-Aggregation erreichen. Das gentechnisch hergestellte Bindungsprotein β-wrapin AS69 komplexiert monomeres αS im Bereich der Aminosäuren 30-60, während die restliche Sequenz in der intrinsisch ungeordneten Struktur verbleibt. Wir konnten zeigen, dass diese substöchiometrische Aktivität nicht nur den globulären Teil des Komplexes, sondern auch die ungeordneten Proteinregionen von αS erfordern. Dies bedeutet, dass die Fähigkeit von ungeordneten Proteinregionen, die Amyloidbildung zu stören, von Hemmstoffen ausgenutzt werden kann, um spezifische Mechanismen *in vitro* und in zellulären Aggregationsexperimenten zu inhibieren. Auf dieser Grundlage wurde ein Inhibitor mit dem Namen AS69nuc entwickelt, der spezifisch die Nukleation von αS Fibrillen, nicht aber deren Wachstum hemmt. Durch die Verwendung von AS69nuc als künstliches Werkzeug konnten wertvolle Einblicke in die Aggregationsvermehrung im diagnostischen Amplifikationstest (SAA) gewonnen werden. Unsere Ergebnisse zeigen, dass unter SAA-Bedingungen die sekundäre Nukleation die Proliferation antreibt, die durch die Zerebrospinalflüssigkeit von Parkinson-Patienten initiiert wird.

Der zweite Teil konzentriert sich auf das Verständnis der Mechanismen der zellulären Internalisierung und der pathophysiologischen Auswirkungen von Fibrillen und oligomeren Formen. Die Sequenzierung der nächsten Generation (*Next Generation Sequencing*) wurde durchgeführt, um Einblicke in die zellulären Reaktionssysteme auf Fibrillen zu erhalten. Diese molekulare Momentaufnahme ermöglichte es, die entscheidenden Komponenten der Zellreaktion auf Fibrillen zu identifizieren, die als potenzielle Biomarker in Betracht gezogen werden können. Neben der Untersuchung der Auswirkungen von Fibrillen auf Zellen bleibt die Untersuchung von Oligomeren ein wichtiges Thema, da diese oft als die toxische Spezies beschrieben werden. Oligomere sind jedoch aufgrund ihrer instabilen Natur, ihres geringen Vorkommens unter Standardbedingungen und ihrer strukturellen Heterogenität schwer zu untersuchen. Daher haben wir ein Oligomermodell entwickelt, dass die Untersuchung der Oligomere eines bestimmten Phänotyps (genannt *curvilinear*) ermöglicht.

Die Ergebnisse dieser Arbeit unterstreichen die Bedeutung von intrinsisch ungeordneten Regionen als Vermittler der Hemmung der Amyloidbildung. Sie können die Entwicklung von Inhibitoren leiten und ihr hemmendes Potenzial verbessern. Außerdem bieten sie eine neue Perspektive, um die Selbstinteraktion des aggregierenden Proteins für die Hemmung zu nutzen. Darüber hinaus tragen sie zum Verständnis der einzelnen Schritte der Amyloidbildungsreaktion bei. Das Untersuchen der Rolle von verschiedenen Aggregationszuständen, ihre pathophysiologischen Auswirkungen und das zelluläre Reaktionssystem liefern wertvolle Erkenntnisse, um unser Verständnis dieser Fehlfaltungskrankheiten zu vertiefen.

1

GENERAL INTRODUCTION

1.1. Amyloids

The transformation of soluble proteins into insoluble and highly ordered amyloid deposits has focused the research attention of various scientific disciplines ranging from physics to chemistry, biology and medicine [1]. The first finding of amyloid structures dates back to 1639, which at that time led to the observation of a lard liver and white-stone spleen [2]. In 1854, Rudolph Virchow coint the term amyloid after discovering macroscopic tissue abnormalities, the so-called *corpora amylacea* within the brain [3]. Virchow initially concluded that these formations resembled cellulose or starch due to their characteristic staining pattern achieved by positive staining with iodine and a subsequent color change from pale blue to violet upon treatment with sulfuric acid. The term amyloid finds its origin in “amylum“ and “amylon,“ the Latin and Greek words for starch, respectively [4]. In 1859, however, Friedreich and Kekulé contradicted this misidentification based on a comprehensive study of the human spleen. They refuted the notion that amyloids consisted of carbohydrates and established that they are proteinogenic [5]. However, the term amyloid is still used today. In the following years, advances in light microscopy and the discovery that amyloid deposits exhibit a distinct red-green birefringence in the presence of the dye Congo red revealed the composition of amyloid as highly organized protein subunits [6]. In the 1970s, various proteins such as amyloid A [7], the light chain of antibodies [8] or transthyretin [9] were identified as protein building blocks of fibrils.

Meanwhile, the development of high-resolution structure-resolving techniques rapidly evolved. In 1968, the X-ray fiber differentiation of the egg stalk of the lacewing fly provided insight into the structure, revealing a repeating feature at approximately ~ 4.7 Å along the fibril axis, defining it as cross-β folding [10]. This cross-β folding has been attributed to amyloid fibrils as a clear and detailed characteristic, akin to a fingerprint [11]. In subsequent years, additional methods were refined to achieve higher resolution. Notably, solid-state Nuclear Magnetic Resonance (ssNMR) [12] and cryogenic-Electron Microscopy (cryo-EM) [13] gained prominence due to their near-atomic resolution and rapid implementation. The integration of these diverse methods enables a comprehensive understanding of amyloid structures at multiple scales [11].

To date, new high-resolution structures of amyloid fibrils are being reported daily [14]. This underscores the great diversity, variety and range of fibrils, hinging on two factors: *i.)* various proteins can give rise to amyloid fibrils, and/or *ii.)* during the aggregation process, the same protein can assemble into different conformations in the core of the fibrils, leading to distinct polymorphs [15]. Until now, there is no apparent correlation in sequence, structure, or function among numerous proteins capable of forming amyloid fibrils. For instance, aggregation-prone proteins, such as amyloid-β (Aβ) and lactoferrin exhibit

amino acid sequences ranging from 40-42 to 641, respectively [1].

Despite these differences, amyloid fibrils consisting of different protein building blocks have certain structural features in common, namely the formation of long, unbranched filaments with a cross-β structural motif. Due to this common architecture, amyloid-specific dyes become valuable tools for identifying the presence of amyloid structures in tissues and samples or monitoring the kinetic progression of amyloid formation [1, 16, 17]. Currently, Thioflavin-T (ThT), a synthetic aromatic heterocyclic compound, is widely used and the most well-known amyloid-specific dye. ThT selectively attaches to protein regions exhibiting a linear arrangement of β-sheets, such as those found in amyloid fibrils. Once bound to β-sheets, ThT adopts a stable planar conformation with a bathochromic shift in both excitation and emission wavelengths. Additionally, the fluorescence intensity multiplies [17].

The rapid pace of structural elucidations and mechanistic characterizations has revealed the correlation of amyloid fibrils with numerous neurodegenerative and systemic diseases, notably Alzheimer's disease (AD) [18], Parkinson's disease (PD) [19], and Type 2 *diabetes mellitus* (T2DM) [20]. Nonetheless, it has been shown that functional amyloids are also present in bacteria, fungi, and mammals [21]. To prevent ambiguity in the term "amyloid," the Nomenclature Committee of the International Society of Amyloidosis (ISA) has reached a consensus stipulating that the term "amyloid" should be reserved for all β-spanning fibrils [22]. However, it is strongly advised that the use of "amyloid" (without additional clarification) and "amyloidosis" be restricted to pathological deposits within the realms of human and veterinary medicine. Terms requiring additional explanations, such as amyloid fibrils or amyloid state, can be employed more broadly [23]. Given the continuously expanding knowledge about amyloid structures and their functional or disease-related roles, a final definition is still in progress and may undergo further refinement in the future [24].

1.1.1 Occurence

Transmissible Spongiform Encephalopathies, like Creutzfeldt-Jakob or Gerstmann-Sträussler-Scheinker diseases in humans result in the degeneration of brain cells. In 1982, Prusiner *et al.* identified a potential infectious agent: a protein termed prion. Contrary to expectations, this protein was also found in healthy cells. However, they demonstrated that prion monomers could undergo a conversion from their native cellular state (PrP^{C}) to a conformation characterized by a β-sheet dominated structure, the so-called scrapy PrP form (PrP^{SC}) [25, 26, 27]. This altered structure exhibited the ability to grow and replicate by recruiting monomeric cellular PrP^{C}. It is important to note that the prion protein in its monomeric conformation, PrP^{C}, is not infectious. However, when it undergoes conversion into PrP^{SC} fibrils, it transits into a infectious state and becomes a prion [28, 29]. This discovery clarified that proteins within their natural milieu can experience a template-like transformation into amyloid-like filaments, forming the foundation for these diseases. In recognition of this groundbreaking discovery, Prusiner was honored with the Nobel Prize in 1997 "for his discovery of prions — a new biological principle of infection" [30]. This revelation, indicating that proteins could exhibit infectious properties independently of genetic material like deoxyribonucleic acid (DNA) or ribonucleic acid (RNA), proved so astonishing that numerous scientific domains were re-evaluated using this innovative explanatory framework.

Amyloid diseases

Currently, over 50 disease-causing amyloidogenic proteins are identified, contributing to an even higher and diverse range of diseases based on the precursor sequence, formed polymorph, or the location of amyloid deposition [11, 31, 32, 33]. These diseases encompass neurodegenerative conditions like AD (Aβ [18] and/or tau aggregation [34]), PD and other synucleinopathies (α-synuclein (αS) aggregation [19]) or

Amyotrophic lateral sclerosis (ALS; superoxide dismutase aggregation [35]). Protein depositions can also be found in various tissues, including islets of Langerhans in T2DM (islet amyloid polypeptide (IAPP) aggregation [20]), kidney or heart in Amyloid light-chain amyloidosis (antibody light chain aggregation [36]), and osteoarticular tissues in Dialysis-related amyloidosis (β2-microglobulin aggregation [37]). This list, though not exhaustive, provides insight into the numerous and fundamentally different manifestations of amyloid-related diseases. However, they are all underlying the amyloid hypothesis describing a causal link between amyloid deposits (intra- or extracellular) and pathological symptoms (Figure 1.1, blue pathway) [38, 39].

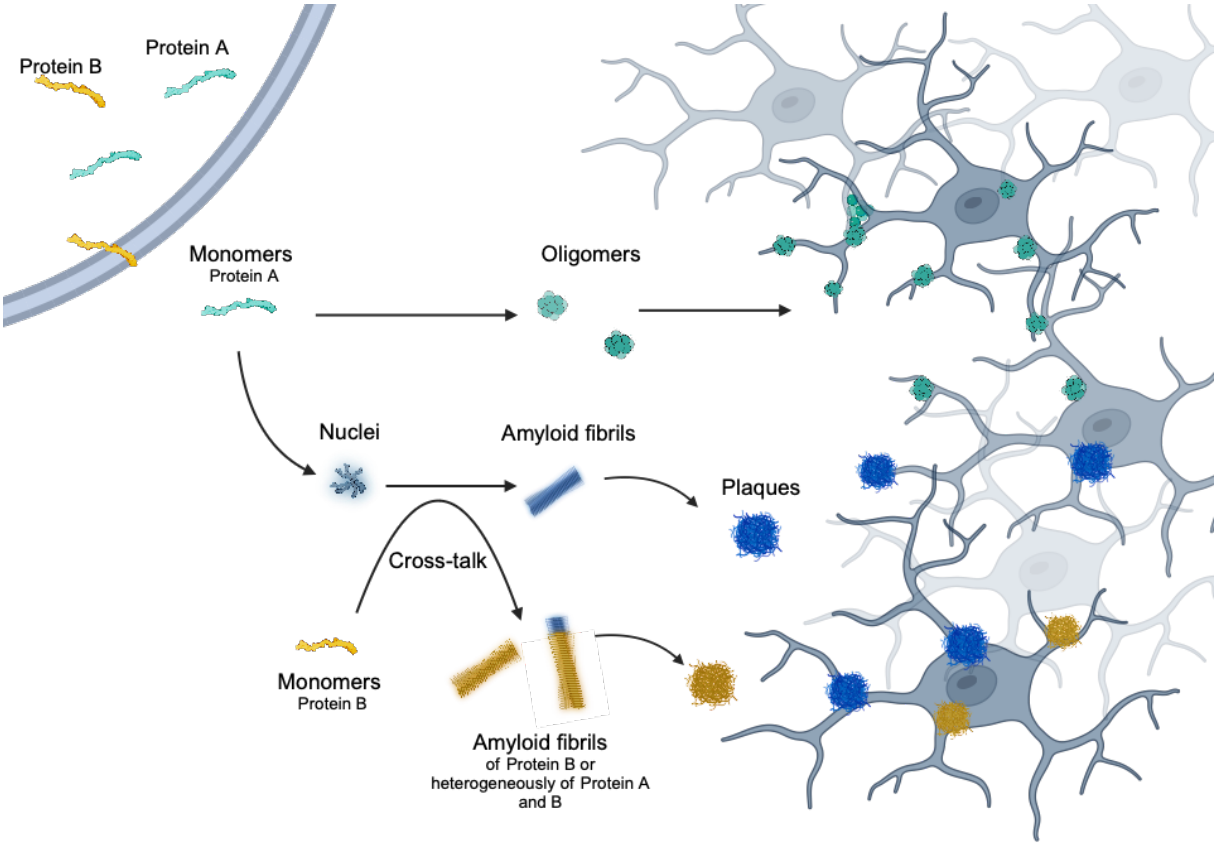

Figure 1.1: Overview of amyloid protein aggreagtion within cells. Endogenous proteins, here protein A and B, are in their native structure until they change their conformation and aggregate. Proteins can aggregate into oligomers that can enter cells (green pathway), leading to cytotoxicity. The protein can also form a nucleus that can grow into amyloid fibrils (blue pathway). These fibrils can cluster together to form plaques. The aggregation of one protein (protein A, blue) can trigger the aggregation of another protein (protein B, yellow pathway). These plaques and amyloidogenic species disturb the cellular functionality and exert cytotoxicity on cells.

In amyloid disease, the aggregation is attributed to the misfolding of a specific protein, however the diseases are not fully delineated. In patients suffering from cognitive impairment, 50% of these patients with Alzheimer's Aβ pathology also exhibit αS pathology [40]. The role of co-pathologies is currently under intensive investigation [41]. Moreover, an overlap of amyloid diseases through cross-talk between aggregation prone-proteins exists, indicating that the aggregation of a protein linked to one disease can trigger the aggregation of another protein, thereby contributing to the development of an additional disease (Figure 1.1, yellow pathway) [42, 43, 44, 45]. This phenomenon is evident, for instance, in the

aggregation of Aβ and IAPP. Because of their high structural similarities, these two proteins can seed the aggregation of each other [46, 47]. This is underscored by the increased risk to develop AD in patients with T2DM [48, 49].

Likewise, contemporary studies increasingly indicate that not just the structure and existence of amyloid fibrils are linked to the onset and advancement of diseases, but also various oligomeric forms (Figure 1.1, green pathway) [50, 51, 52]. According to the oligomer hypothesis [53], small amyloid oligomers play the prominent role in neurodegenerative diseases and T2DM, rather than the clearly visible deposits of fibrils [54, 55, 56]. This hypothesis is supported by the known lack of correlation between *postmortem* plaque load and neurological deficits in AD [57].

The trigger for the onset of amyloid diseases remains unclear. Many conditions, such as AD and PD, are linked to aging [58, 59]. With a growing elderly population, there are emerging social and economic challenges that necessitate effective control of these diseases [60]. Unfortunately, universal cures remain elusive until now. Furthermore, detecting these diseases in a timely manner poses a challenge, as they have traditionally been identified only with the emergence of severe clinical symptoms in the advanced stages. However, significant progress has been made in the recent years. The United States Food and Drug Administration (FDA) has approved antibodies for the treatment of AD [61, 62], and many other therapeutic approaches with promising clinical results are on their way [63, 64]. Also, the development in diagnostic tools is becoming more precise and refined [65].

Functional amyloids

A surprising discovery was the finding of functional amyloid as amyloids are typically linked to diseases. The term functional amyloid refers to amyloids with functional properties for their organism under physiological conditions [21]. Their functions encompass various roles such as structurally templating tasks for small chemical molecules (like Pmel17) [66] or participating in the formation of biofilm in bacteria (e.g. curli) [67]. Additionally, they serve as storage for peptides/proteins, providing protection from their surroundings or, *vice versa* (e.g. peptide hormones in mammalian secretory granules) [68]. Amyloids can function as information carriers, as seen in the fungal immune system (HET-s prion in *Podospora anserina* [69], yeast prions), or contribute to long-term memory (mnemons in yeast) [70]. They may also be involved in suppressing the native function of soluble proteins (Cdc19 in yeast stress granules) [71] or in signaling through the formation of oligomers (HET-s prion) [72].

Utilizing amyloids for these functions offers various advantages, including the transition from a soluble to an insoluble state, high stability, and a robust prion-like replication mechanism. Notably, it is remarkable that functional amyloids exhibit no toxicity, which implies that there must be differences in structure and their origin [21]. The aggregation mechanism in functional amyloids is meticulously controlled, involving regulation of the physico-chemical environment [68, 73, 74]. Additionally, functional amyloids undergo rapid and selective aggregation, preventing the accumulation of toxic oligomers or intermediates [75, 76]. Moreover, functional amyloids usually remain monomorphic and cannot fold into different polymorphic conformations [77], further emphasizing that this process is executed under strict control regimes.

The optimized evolutionary design of both the structure and sequence of functional amyloids, along with their finely tuned control mechanisms, highlights the possibility to redirect fibrils with their advantageous properties (and without being pathogenic) as a useful tool in nature. These findings also serve as a concept for replicating protein self-assembly in artificial approaches, enabling the creation of highly controllable, stable materials [78]. These artificial materials have broad applications, including slow-release depots for cancer therapeutics [79], components in active composites [80], sensors [81], and biomimetic functional

materials [82, 83, 84]. The compact packing of the amyloid structure, particularly advantageous for catalytic applications in modern enzyme design, results in high local protein concentration, offering notable pressure and temperature stability along with robust mechanical properties [85, 86].

This discovery underlines that understanding the mechanism and the aggregation phenomenon can be of fundamental importance in terms of functional and disease-related amyloids, which can be further exploited in artificial approaches. However, disease-related amyloids are of particular interest as they often lead to fatal diseases. So, the focus of this thesis was centered on the aggregation of disease-related amyloids.

1.1.2 Characteristics of amyloids

Amyloid fibrils are characterized by highly ordered and tightly packed, insoluble supra molecular assemblies, resulting from the stacking of proteins or peptide subunits within protofilaments, which intertwine in a 2-fold helical symmetry, leading to a distinctive kinetic stability. Once formed, such aggregates have the potential to persist over extended periods [29].

Amyloid fibrils represent an alternative state compared to the native conformation. Aggregation-prone proteins often possess an intrinsically disordered native conformation, as observed in proteins like αS and Aβ. Although there are examples of well-folded globular proteins, such as transthyretin, which are also aggregation-prone. Interestingly, the fact that proteins can transit from their native state to the amyloid state without the supply of additional energy implies that the latter must be thermodynamically more stable than the native state [87, 88]. This contradicts a fundamental hypothesis of Anfinsen's protein folding theory, which states that under physiological conditions the native state corresponds to the conformation with the lowest energy [89]. Thus, the native structure can only represent a local energy minimum [90] (Figure 1.2A). Modifications in the amino acid sequence or alterations in the chemical/biological environment, e.g. changes in ionic strength, pH values, temperature, and/or interactions with surfaces, facilitate self-aggregation into amyloid structures, ultimately reducing the free energy to a presumably global minimum [1, 91] (Figure 1.2A).

However, a substantial kinetic barrier needs to be surmounted, and this challenge is typically observed under highly non-physiological *in vitro* conditions, rarely occurring under physiological conditions [29]. Experimental studies reveal that the formation of fibrils necessitates reaching a critical concentration of monomers. Despite this, it seems that under the "right" conditions, a majority of polypeptide chains tend to form extended β-sheet containing structures [15, 93, 94, 95]. This observation leads to the hypothesis that the amyloid state can be adopted by any polypeptide chain and thus, represents a state with a universal global energy minimum [15, 90, 96].

Amyloid fibrils are elongated, unbranched fibrous structures with a diameter of 2 to 20 nm, which typically extend over several micrometers [1, 97, 98, 99] (Figure 1.2B). Fibrils from different building blocks share a uniform cross-β backbone in which the β-sheets are spaced $\sim$ 4.7-4.8 Å perpendicular to the long axis of the fibril (Figure 1.2C). This alignment corresponds to the hydrogen bond distances between paired carbonyl and amide groups in neighboring β-strands, forming a steric zipper [100]. Steric zippers are thus short peptide segments that form the structural basis for the hierarchical core of an amyloid fibril [1, 101, 102, 103]. These sheets can adopt either parallel or antiparallel orientations [103, 104]. In this manner, the cross-β core consists of stacks of steric zippers, while the remaining polypeptide chain adopts a random coil conformation at the periphery of the fibril surface [101, 105].

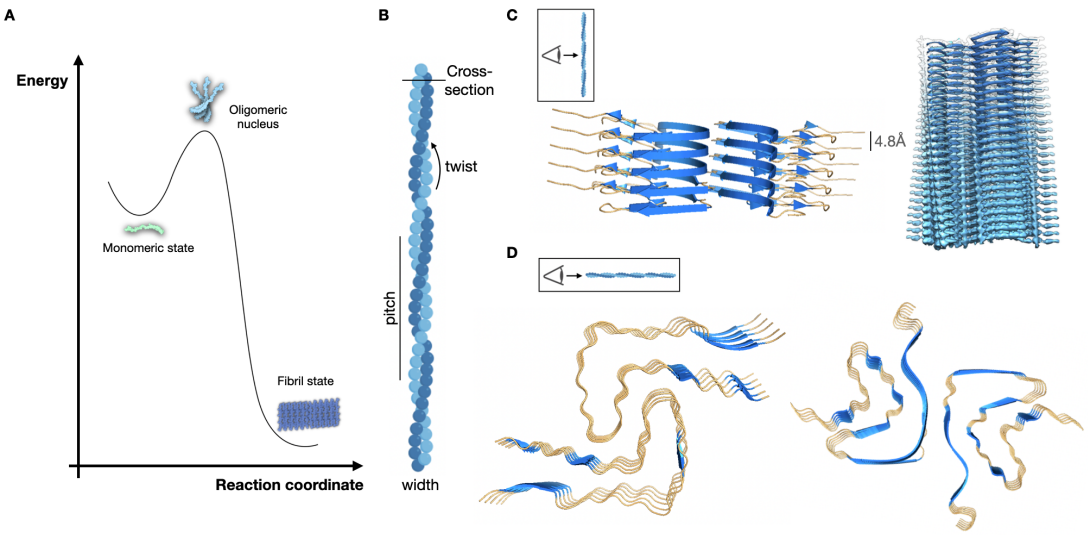

Figure 1.2: Characteristics of Amyloid fibrils. (A) Schematic energy diagram of the amyloid formation reaction. During amyloid formation, the native states (green) first undergo structrual changes to built up an oligomeric nucleus (light blue), which represents an energy maximum. Once that state is reached, the conversion into fibrils (blue) becomes thermodynamically favorable. (B) Macroscopic site view of a fibril model displaying width, pitch, twist and cross-section. (C) Close-up of a site view of a fibril protofilament showing the characterisitc distance between β-sheets of $\sim$ 4.8 Å. The polypeptide chain is shown in beige with the β-sheets in blue (left) and its calculated model form cryo-EM data (right, EMD-7618) of an αS fibril (PDB:6CU7). (D) Cross-section of a fibril. This shows the interface within the fibril core and signals the differences between the two conformations of rod (PDB: 6CU7) and twister (PDB: 6CU8) polymorphs in αS fibrils. The β-sheet forming segments within in core are marked in blue. The polymorphs shown here are taken from [92]. The perspective on the fibrils is indicated by the symbolic eye in the small black box.

Mature fibrils primarily consist of two protofilaments. The twisting of these protofilaments around each other results in a periodic arrangement, giving rise to a helical structure of the fibril [98, 106] (Figure 1.2B). However, examples of single filaments and triple filaments have also been detected [107, 108]. Despite the conserved basic structural arrangement of the fibrils, there are different ways in which protofilaments can be arranged into the pseudocrystalline nature, resulting in a range of amyloid fibril morphologies [109, 110, 111].

The folds ("morphs") of the fibril can vary in the assignment of the polypeptide chain forming β-strands or in the alignment of the β-strands in relation to each other, both leading to different protofilament conformations. This underlines that proteins with identical sequences can assume different conformation within the amyloid fibril core, leading to distinct protofilament interfaces [111, 112, 113, 114, 115]. For αS the most-known ones are the rod and twister polymorphs [116, 117, 118, 92] (Figure 1.2D). Amyloid fibril polymorphisms can be characterized by mesoscopic variations, including the frequency of fibril twisting, the number of protofilaments per fibril and the diameter or weight per length of the fibrils [119]. Environmental factors such as pH, ionic strength, mechanical movement, shear force or the presence of other co-solvents play a crucial role in the formation of polymorphs [1, 109, 120].

Recently, it has been shown that fibrils undergo transformations, adopting diverse structures during their lifetime and evolve, with new polymorphs emerging and others disappearing [121]. The observation of

transiently colonized fibril structures at certain time points during the fibrillation process has implications for understanding the mechanisms of amyloid build-up. It is quite a surprising result as it challenges the prior belief in the static nature of fibril aggregates. These results therefore also have the potential to provide fresh perspectives and explanations for the progression of amyloid formation in diseases.

1.1.3 Mechanism of amyloid aggregation

The formation of amyloid fibrils involves the conversion of soluble protein monomers into insoluble supramolecular aggregates. Aggregation is not driven by a single-step process; rather a combination of various mechanisms. One of the numerous models is the Finke-Watzky aggregation model, which proposes nucleation-elongation polymerization comprising two steps to describe aggregation: *i.)* nucleation and *ii.)* growth [122, 123].

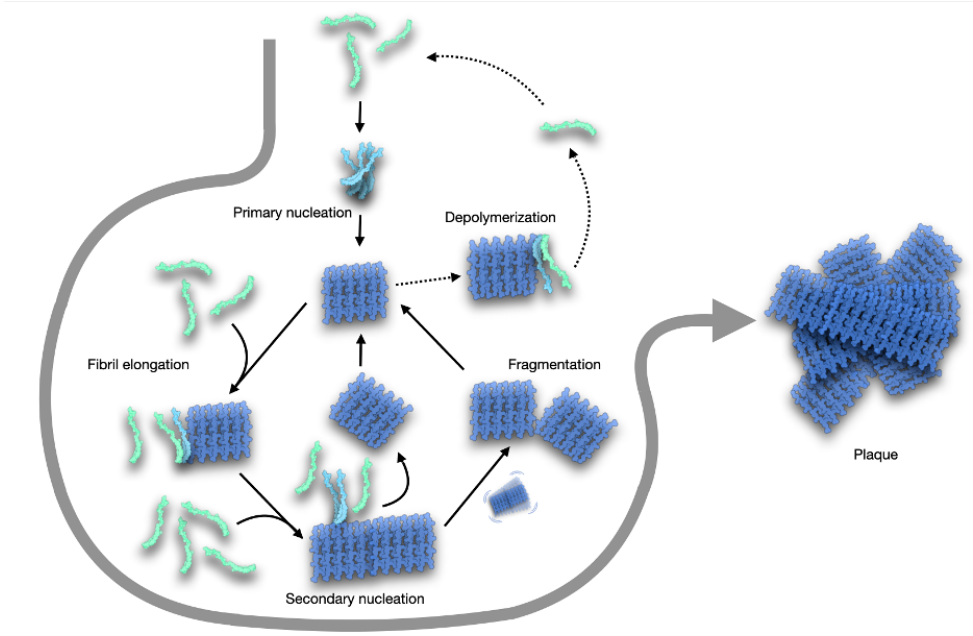

Figure 1.3: Schematic overview of aggregation mechanisms. Monomers (green) undergo a structural transformation to form a nucleus (light blue), which can proliferate into mature fibrils (blue). This process is termed primary nucleation. By attaching monomers at the fibril ends, fibrils can grow in length which is called elongation. During secondary nucleation, the fibril surfaces act as catalysts to convert monomers into new nuclei, which then proliferate into mature fibrils. In the process, which is termed fragmentation, fibrils break in smaller pieces by which the amount of fibril ends get doubled, serving as binding site for elongation. The process that counteracts the amyloid fibril formation is depolymerization, in which the monomers dissociate from the end of the fibrils. This dissociation process must be much slower (marked in dashed line) than the growth process to explain the rapid aggregation into large protein deposits and plaques.

The initial nucleation phase, also known as primary nucleation, corresponds to the assembly of transient, critical nuclei that act as intermediate stages of nucleation. Further monomeric subunits can attach to this stage, driving the assembly towards pre-formed fibrils [11, 124, 125]. This nucleation process is the rate-limiting step in fibril formation as it proceeds through this extremely unfavorable nucleation state. This nucleation phase can be shortened or eliminated by the addition of pre-formed fibrils, a process

known as seeding [1, 126, 127]. The elongation of the fibrils leads to a thermodynamically favorable state due to the continuous accumulation of monomers at the growing ends of the fibril [124, 125, 128]. This process is the main source for the generation of fibril mass and growth. Additionally, two other processes, namely *i.)* fragmentation [129, 130], the breaking of fibrils into smaller fragments, and *ii.)* surface-catalyzed secondary nucleation [131], contribute to the formation of small fibril species that exponentially increase amyloid formation, leading to new growing ends, which may have an increased seeding and cytotoxic potential [126, 131, 132]. However, fibril growth is reversible, suggesting that monomers can also dissociate from the fibril ends [133]. This dissociation process must be considerably slower than the growth process to explain the rapid aggregation into large protein deposits and inclusions. Collectively, these mechanisms underlie the rapid aggregation in a prion-like manner (Figure 1.3).

The aggregation kinetics of amyloid proteins strongly depend on the protein concentration, which varies greatly for different aggregation-prone proteins. The individual processes can occur simultaneously but are favored under certain conditions. In particular, *in vitro* experiments take advantage of the fact that the aggregation mechanisms depend on factors such as protein sequence, conformational states of the amyloidogenic monomer, and experimental conditions like temperature, pH, protein concentration, shaking parameters, and solvent effects [134, 135]. By selecting appropriate *in vitro* conditions, it is possible to study aggregation that is mainly driven by a specific mechanism. In the case of ThT kinetics (monitoring the aggregation in a timely manner via the fluorescence dye ThT), information about individual processes can be obtained via the lag time, the slope of the aggregation and the possibility to define the dominant or suppressed mechanism by mathematical fits/modeling [125, 136]. This offers the opportunity of gaining insights into the typically complicated aggregation process based on choosing the "right" *in vitro* conditions and enables the investigation of the dominant mechanism under these conditions.

Primary nucleation

The initial meeting of monomers to form a growth competent nucleus is termed primary nucleation. In this process, monomers undergo a transformation to form β-sheet containing nuclei regardless of their native structure. These nuclei exhibit a transient and structurally diverse nature. After passing through this extremely unfavorable and unstable oligomeric state, subsequent elongation progresses towards a thermodynamically favorable, amyloid state [11, 124]. In particular, the nucleation of amyloid fibrils is difficult to study due to their complexity, the short lifetime of the nuclei, the inherent heterogeneity reflected in the polymorphism of the reaction products and their poor separability from the subsequent reaction steps [126, 137, 138].

Recently, new insights to explain the process of nucleation have led to the field of liquid-liquid phase separation (LLPS) [139]. This phenomenon describes the initial conversion of monomers into amyloid aggregates using the model of phase transition from a soluble to a solid amyloid phase [140]. The formation of amyloids is characterized by nucleation, encompassing several distinct stages that may result in intermediate oligomeric states [141, 142, 143] or a dense liquid condensate phase [144, 145]. Driven by non-specific interactions within the biomolecular condensates, these heterogeneous oligomeric intermediates subsequently undergo conformational transformations to develop fibril cores capable of growing into mature fibrils [140]. These condensates are also observed *in vivo*, offering an explanation for achieving such high protein concentrations within cells [146, 147].

Fibril elongation

Elongation describes the binding of a monomer to the end of a fibril accompanied by the structural transformation of the newly attached molecule into the cross-β amyloid structure. Attachment of monomers to the growing ends of either the growth-capable nuclei or the mature fibrils ensures that fibrils

grow in length, whereby the fibril ends continuously recruit monomers [128, 148, 149]. Thus, elongation has been identified as a fundamental mechanism for generating fibril mass.

During the elongation process, the monomers and fibril ends interact weakly, followed by a conformational search to attain a stable thermodynamic state [150]. This mechanism is believed to act as induced-fit rather than conformational selection [151]. Thus, the fibril ends are considered to contribute to the correct folding by interacting with the monomers. This emphasizes that the fibril ends and monomers must be competent to elongate. Also, it has been shown that the fibril end sometimes remains in a state in which incoming monomers cannot be incorporated, resulting in a slowdown of the elongation rate [152]. However, the exact mechanism of how fibrils grow remains unclear. They may either grow individually or collectively as a unit, with monomer elongation occurring alternately along each strand. There is evidence for both ways, presumably depending on the system-specific nature of the process [153, 154].

Fibril fragmentation

Mature fibrils can break into smaller fragments that can serve as nuclei or generate multiple smaller fibrils, each with a double number of fibril ends that can recruit monomers. Fibril fragmentation is a key process as it leads to amyloid proliferation in an exponential manner. This enables the generation of small and active fibril seeds, which may be associated with an increased potential for toxicity and cell-to-cell spread [155]. The fragmentation stability depends on the polymorphs and the length of the fibrils [156].

Secondary nucleation

Monomer-dependent secondary nucleation is defined as a process in which the nucleation of monomers is catalyzed by the surface of existing aggregates [131]. So, the autocatalysis at the fibril surface generate new growth competent nuclei, thus, creating the basis for rapid proliferation of the aggregates. Recently, it has been shown that aggregate proliferation occurs much more rapidly at slightly acidic pH values, comparable to those in lysosomes and endosomes, than at neutral pH, mainly due to much more rapid secondary nucleation [135, 157].

This process is believed to involve at least three molecular events: the arrival of the peptide at the fibril surface, product formation, and release [158]. The precise sequence of these events remains unknown and is likely more complex than previously assumed. Given current knowledge, Törnquist *et al.* [158] considered four possible scenarios:

- The aggregate surface may act as an oligomer generator, leading to the final transformation/nucleation into an aggregate with the same structure and growth rate as the fibril after detachment.
- Monomers might bind to the surface before detaching and growing.
- Nucleated species may continue to grow along the aggregate surface before detaching.
- Clusters of monomers could be formed in the solution and nucleate upon contact with the fibril surface.

In addition, it is still unclear if secondary nucleation takes place at a specific location on the fibril surface or if it is a diffuse process. To answer this question and decipher this process is an important point to explain the catalysator's role of the surface of amyloid fibrils in the future.

1.2. Off-pathway oligomers as competitors of amyloid fibrils

Over the last two decades, increasing evidence has emerged that small amyloid oligomers play a prominent role in diseases, rather than the clearly visible deposits of fibrils [51, 54, 159, 160, 161, 162, 163]. Oligomers exhibit a variety of sizes, structures, stabilities and morphologies [164, 165].

There is no clear definition of the term oligomer. Broadly, oligomers are transient, stable entities. Their metastability means that they either accumulate in front of an energy barrier (nucleation) and/or are in a local minimum of free energy that differs from the global minimum of the fibrils [166, 167] (Figure 1.4A). These entities are compact, spherical protein aggregates or assemblies that can aggregate to form bulging curved fibrils, often referred to as protofibrils or curvilinear oligomers. Therefore, the morphologies and structures of oligomers differ from those of amyloid fibrils [168, 169]. Structural determinations have shown that oligomers represent a heterogeneous group of aggregates, including antiparallel β-folds [170, 171, 172, 173, 174, 175], α-helices [176, 177] as well as disordered and micellar structures [178, 179]. In order to classify the oligomers more precisely, they are commonly divided into on-pathway and off-pathway oligomers [167] (Figure 1.4A). On-pathway oligomers pertain to the oligomeric state that evolves directly towards the fibrillar state. In contrast, off-pathway oligomers do not undergo conversion into amyloid fibrils, constituting a group regarded as competitive to the fibrils.

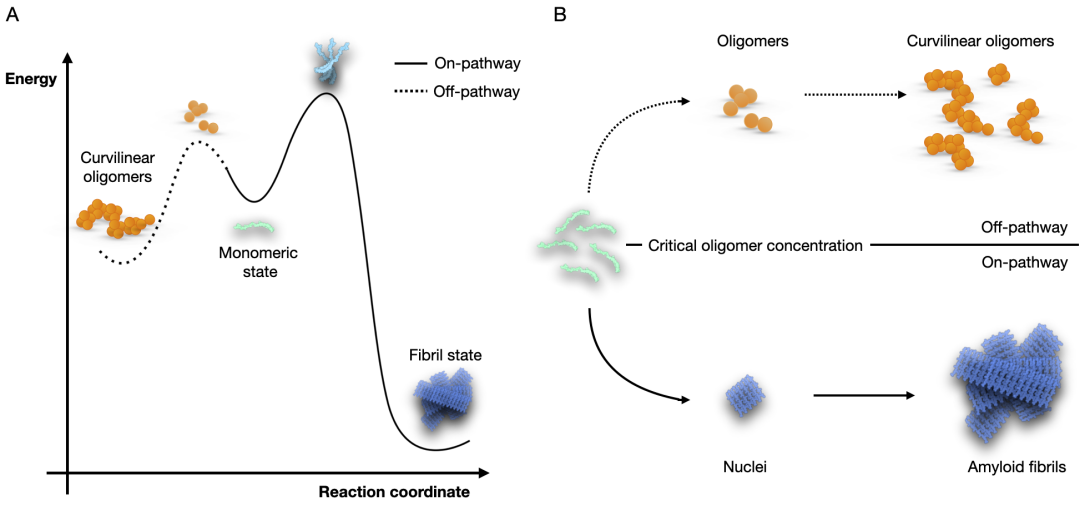

Figure 1.4: Formation of oligomers on and off the pathway towards amyloid fibrils. (A) Schematic energy diagram of the on (solid line) and off (dashed line) pathway toward amyloid formation. Amyloid formation is started from the native state (green). Native proteins first undergo structural changes to built up an oligomeric nucleus (light blue), which can aggregate further into fibrils (blue). This describes the pathway towards fibrils. On the other hand, the native state can also aggregate into off-pathway oligomers (light-orange), which can cluster together to curvilinear oligomers (orange). (B) Concentration-dependent formation of off-pathway or on-pathway oligomers. Off-pathway assemblies are formed to a significant extent above the critical oligomer concentration (COC), while the pathway towards fibrils is performed under the COC (Figure is adapted from Hasecke *et al.* [169]).

The conditions that allow the formation of fibrils and off-pathway oligomers vary. An increased local concentration promotes the highly concentration-dependent oligomer formation [169]. For biphasic formation of oligomers, there is a protein concentration, the so-called “critical oligomer concentration“ (COC), above which oligomer formation begins (Figure 1.4B). Below the COC, aggregation proceeds towards

fibril formation (Figure 1.4B). Furthermore, Gosal *et al.* [180] have developed a pH-dependent kinetic phase diagram for α2-microglobulin that depicts different aggregate morphologies in a three-dimensional matrix of pH, salt concentration and protein amount. The study showed that worm-like protofibrils, which were assigned to off-pathway oligomers, are formed under different *in vitro* conditions, than fibrils.

A further indication for off-pathway oligomers is that they are likely to inhibit fibril formation and growth in a concentration-dependent manner [88, 169, 180, 181, 182, 183, 184, 185]. Off-pathway oligomers compete with the fibril formation pathway for the pool of monomers and reduce it. When the available pool of free monomers for fibril growth is exhausted, fibrils can only continue to grow by separating monomers from existing off-pathway oligomers. However, owing to the metastability of oligomers, this process inherently proceeds slowly. Consequently, an increase in the oligomer population results in a delay in fibril formation rather than accelerate it [167]. Moreover, it has also been shown that off-pathway oligomers have the ability to bind to the fibril's surface and thereby suppress secondary nucleation [185].

1.2.1 Oligomers' role in amyloid disease

In neurodegenerative diseases, the oligomer hypothesis, which states that the toxic species are the oligomeric form, is still under intensive discussion. The FDA approval of the antibody drug lecanemab for AD, which specifically targets Aβ oligomers rather than monomers and fibrils, has given considerable impetus to this hypothesis [186, 187]. Nevertheless, the hypothesis remains controversial, partly due to the numerous conceptual and practical challenges associated with the study of amyloid oligomers [167, 188, 189].

It has been hypothesized that the oligomeric state has an inherent tendency to toxicity, either through the reactivity of the oligomers themselves or through the disruption of other cellular functions. An evident distinguishing characteristic is that monomers and oligomers are soluble in solution, whereas fibrils create insoluble, solid structures. Moreover, there is substantial evidence suggesting that mature aggregates are not solely harmful but, rather, constitute an end point species that intercepts oligomers by transforming them into their own species. In fact, these aggregates can even counteract certain types of toxicity, such as the generation of reactive oxygen species (ROS) and the modulation of cell membrane permeability [190, 191, 192, 193].

Numerous disease-associated oligomers have demonstrated direct, concentration-dependent cytotoxic effects on neurons. The size and pronounced surface hydrophobicity of oligomers appear to be a crucial factor influencing their cytotoxicity [194]. For small oligomers consisting of only a few monomeric units, an increase in oligomer size led to increased toxicity, as observed for Aβ and tau [195, 196, 197]. However, for larger oligomers (up to 2,000 kDa), toxicity decreases with growth until it is approximately similar to the toxicity level induced by amyloid fibrils [198].

Determining whether disease-associated amyloid oligomers are generated along the regular pathway of fibril formation or through an off-pathway route holds significant implications for therapeutic development. To investigate the role of oligomers, experimental set ups or models to generate stable oligomers are urgently needed. Overall, progress in these areas is essential to determine which aggregation species and especially types of oligomers are most relevant in different amyloid-related diseases.

1.3. Synucleinopathies

Synucleinopathies encompass a group of disorders characterized by the abnormal misfolding of the protein αS in both the peripheral and central nervous systems [199]. Clinically, synucleinopathies are classified into different entities, such as Pure autonomic failure (PAF), Multiple system atrophy (MSA), Lewy body dementia (DLB) and PD, which differ in the cellular localization and pattern of αS deposits [200, 201]. Dysfunction and neurodegeneration associated with abnormal αS aggregation are common features across synucleinopathies, with increasing evidence of a "prion-like" cell-to-cell spread of αS aggregates [202]. Another shared feature among synucleinopathies is the occurrence of rapid eye movement sleep behavior disorder (RBD), which may precede autonomic or motor symptoms [203, 204].

Despite overlapping symptoms, the various synucleinopathies exhibit differences in pattern and severity. PAF is distinguished by predominantly peripheral deposits of αS. In MSA, oligodendroglial cytoplasmic inclusions are prevalent in the central nervous system [205, 206]. While PD and DLB are characterized by central neuronal inclusions, particularly Lewy bodies and Lewy neurites [207]. It is essential to highlight that Lewy bodies are not solely composed of proteins; they also encompass organelles and lipid membranes, including damaged lysosomes, mitochondria, and various vesicles [208]. It has been shown that αS fibrils with different structures/polymorphs, characterized as fibril strains, have different properties, including the degree of toxicity, as well as *in vitro* and *in vivo* seeding properties [107]. A recent study showed that αS seeds isolated from oligodendrocytes of MSA patients had better seeding capacity than αS seeds isolated from Lewy bodies of PD patients [209]. The isolation of αS inclusions from tissues of different synucleinopathies, including MSA, PD and DLB, also suggests that there may be different strains of αS fibrils in the different synucleinopathies.

Among the synucleinopathies, PD has recently become the most common movement disorder and, after AD, the second most common neurodegenerative disease, affecting an average of 1-2% of the general population over the age of 65 [210]. In 1817, James Parkinson initially described it in his seminal work, "An Essay on the Shaking Palsy" [211]. Clinically, the disease manifests with symptoms such as resting tremor, muscle rigidity, and Bradykinesia [212]. In addition, mask-like facial expressions, festinating gait and cognitive impairments are often observed in a significant proportion of patients at advanced stages of the disease [213].

The first identification of a PD associated mutation, involving the substitution of threonine with alanine at position 53 was made through an investigation of an Italian family with an unusually high occurrence of early-onset PD at an age of 46 ± 13 years [214]. Various mutations in αS have been recognized as causative factors for PD through autosomal dominant inheritance, including A30P [215], E46K [216], G51D [217], and A53E [218]. Additionally, point mutations like A18T, A29S, and H50Q have been observed in individual patients [219, 220]. Duplications and triplications of the *SNCA* gene, encoding for the protein αS, also contribute to the onset of PD in a concentration-dependent manner [19, 221]. These observations highlight the central role of αS in the development of PD and indicate that even the wildtype form can lead to PD when present in higher concentrations.

In addition to fibrils, various oligomeric species of αS have been identified *in vivo* under pathophysiological conditions. Sodium dodecyl sulfate (SDS)-resistant dimers, as well as low and high molecular weight oligomers of αS, have been observed in the brains of individuals with diseases and in the brains of transgenic animal models of synucleinopathies [222, 223]. It is also not yet clear whether oligomers or fibrils are the toxic species driving the progression of these diseases. In its aggregated form, however, αS

can no longer fulfill its native functions, which could also lead to an imbalance in the cellular network.

1.3.1 Native properties of the protein α-synuclein

The synuclein family comprises closely related, abundant, and conserved presynaptic brain proteins, including αS, β-synuclein (βS), and γ-synuclein (γS). These proteins, ranging from amino acids (aa) 127 to 140, share a sequence identity between 55% and 62% within the family [224]. The αS gene (*SNCA*) and βS gene (*SNCB*) are located on the long arms of chromosomes 4 (region q21) and 5 (region q35), respectively. The γS gene (*SNCG*) is found on the long arm of chromosome 10 (region q21) [225, 226]. Immunohistochemical studies indicate that αS and βS are primarily concentrated in nerve endings, somata, dendrites, and in the immediate vicinity of synaptic vesicles [227]. The cellular localization of αS was initially determined using the electrical organ of the Pacific electric ray [228].

αS is a small protein with 140 aa, which has an intrinsically disordered structure in solution (Figure 1.5). A notable characteristic includes repeats of eleven residues with the consensus motif XKTKEGVXXXX. αS is commonly divided into three distinct regions [229] (Figure 1.5):

- **Amphipathic N-terminus (aa 1-60):** is highly conserved and has a capacity for lipid-binding, inducing a change in an α-helical conformation. In addition, the residues starting at aa 30 are located together with the NAC region in the fibril core and is mainly studied as important target sites for inhibitors [230, 231, 232].
- **Central hydrophobic region, so-called non-amyloid-β component (NAC) (aa 61-95):** has hydrophobic residues and presumably forms the core of the fibril during aggregation. When bound to lipids, the NAC region, together with the N-terminal region, adopts an α-helical conformation [233, 234].
- **Acidic C-terminus (aa 96-140):** is strongly enriched with acidic residues and prolines. This region is known as a binding site for metal ions (with the exception of copper). It is hypothesized that the intrinsically disordered form of the C-terminus acts as a shield for the NAC region, preventing aggregation [235, 236].

The native conformation of αS remains elusive. There is evidence indicating that αS may adopt a stable tetramer [237, 238], posited as the predominant species *in vivo*, but reproducing this state proves challenging [239]. On the other hand, it is well established that αS can form various oligomeric species, ranging from dimers to oligomers of several hundred kDa [240, 241]. Collectively, these studies suggest that αS predominantly exists as a monomer, though they do not rule out the possibility of it forming a stable multimer and/or adopting different structures under certain stress-induced conditions or in interaction with other proteins, specific ligands, lipids, and/or biological membranes [242].

Its biological function is not fully understood [243]. The protein's conformational flexibility enables it to assume various structures when interacting with diverse biological membranes, proteins, or protein complexes. This structural versatility appears to contribute to the multifunctional properties of αS. One of the generally recognized features is the binding to negatively charged lipids, both to micelle-forming lipids such as SDS [233] and to vesicle-forming lipids such as 1,2-dimyristoyl-sn-glycero-3-phospho-L-serine (DMPS) [244]. It is reported that αS increasingly adopt an α-helical conformation on membranes with acidic phospholipid headgroups and/or strong curvature [245]. However, most of what we know about the membrane interactions of αS is based on biochemical analysis of the recombinant protein *in vitro*.

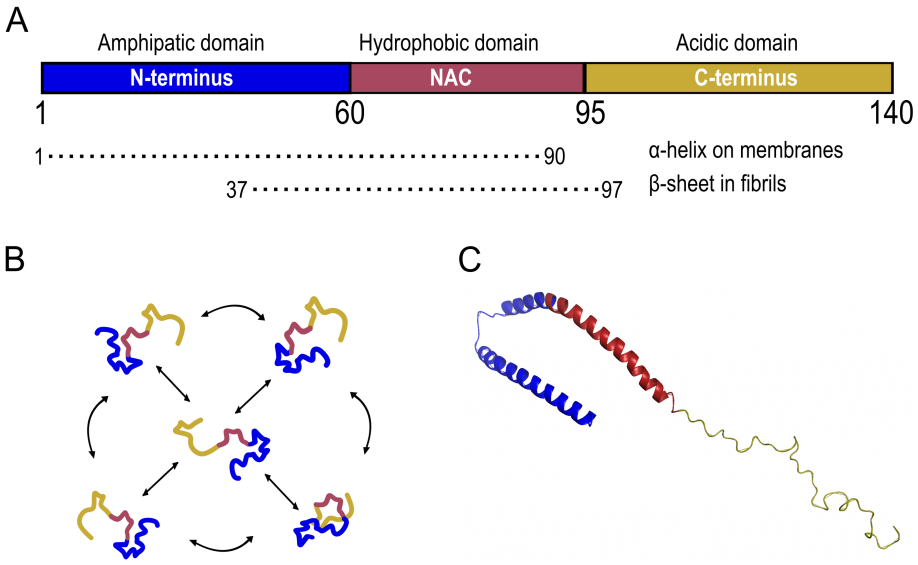

Figure 1.5: Dynamic structures of monomeric αS. (A) Monomeric αS is defined by three distinct regions: the N-terminus comprise the amphipathic domain from aa 1–60 (blue); the hydrophobic domain, so-called the non-amyloid-β component (NAC), comprises aa 60-95 (red); the region between aa 96–140 forms the acidic C-terminus (yellow). (B) Monomeric αS is highly dynamic and probes various conformations through transient intramolecular interactions. (C) By interacting with lipids, αS can change its structure into an α-helix in the N-terminal and NAC part, illustrating the remarkable structural dynamic. Figure is modified from Stephens *et al.* [229].

Research indicates that αS is implicated in membrane vesicle fusion by interacting with soluble N-ethylmaleimide-sensitive-factor attachment receptors, the so-called SNARE proteins [246]. Investigations reveal that αS facilitates the clustering of synaptic vesicles by engaging in transient interactions with the SNARE protein synaptobrevin-2, supporting the process of exocytosis [247]. Moreover, there is a hypothesis suggesting that both the membrane-bound state and/or the soluble monomer of αS may play a role in neurotransmitter release [248]. Experiments with *SNCA* knockout mice [249, 250] and deletion of αS using antisense oligonucleotides [251] have shown that synaptic responses in the hippocampus are impaired during prolonged high-frequency stimulation. This impairment leads to a reduction of both docked synaptic vesicles and their reserve pool. In addition, there is evidence that αS affects the replenishment, transport and release of synaptic vesicles by inhibiting the replenishment of docked vesicles from the reserve pool. Despite these findings, the viability of individual synuclein knockouts (αS, βS and γS) suggests that synucleins are not indispensable components of the neurotransmitter release machinery. Instead, they appear to contribute to the long-term regulation and maintenance of nerve terminal function [252]. Notably, *in vivo* experiments pose challenges in pinpointing the specific function of αS, as βS and γS can partially compensate for its function and are co-expressed in corresponding cellular locations.

Furthermore, it has been shown that the bird ortholog synelfin of αS is upregulated during song learning processes that require maximal neuronal plasticity [253]. Additionally, it has been shown that in developmental stages with increased formation of synapses, in this case comparing early *postnatal* rat brains to adult rats, mRNA expression of αS is upregulated [254]. This suggests that αS may play a role in the development, maintenance, and plasticity of synapses [255]. In addition, there are studies showing that a possible interaction between αS with tyrosine hydroxylase inhibits its activity, leading to reduced

formation of dopamine. This implies that αS could serve as an important control mechanism in dopamine biosynthesis. Due to the heterogeneous range of tasks that αS presumably performs, a loss of function triggered by the aggregation of the monomers leads to a major problem for the organism [256].

1.3.2 Aggregation properties of α-synuclein

Post-translational modifications (PTMs), truncations, and the local cellular environment, including factors like pH and ionic content, have the potential to impact the structure of monomeric αS. Alterations in the monomeric αS structure can influence the protein population, favoring conformations prone to aggregation and ultimately leading to the formation of amyloid fibrils. Surprisingly, αS exhibits a relatively hesitant tendency to aggregate. In *in vitro* experiments, external influences such as stirring with stir bars [257], shaking with or without beads [135, 258, 259], addition of various lipids [245, 258, 260, 261] increasing the temperature [262], increasing salt concentrations [263] and lowering the pH [135] need to be applied to accelerate aggregation.

The initial fibrillation process is believed to be driven by the stochastic misfolding of αS monomers. For formation of the primary nucleus, it is assumed that this takes place at an interface, such as an air-water interface under shaking conditions or lipid-water interface under quiescent conditions. This is in good agreement with several studies that have shown that aggregation can be induced by shaking or by the interaction between the N-terminus of αS and lipids. The hypothesis is, that the αS N-terminus tethers the protein to the membrane's phospholipid surface, leading to an increased local αS concentration that promotes aggregation [244, 260]. However, quite recently new results suggest that the presence of DMPS vesicles provide lipids for the growth and elongation of lipidic fibrils, which was underlined by solving the structure of lipidic fibrils using cryo-EM [264, 265]. Regarding this explanatory framework, lipids do not serve as nucleation sites of primary nucleation, which instead takes place at an air-water or plate interface [264]. Nevertheless, the experiments showed that the presence of DMPS vesicles can induce aggregation under conditions, in which αS cannot aggregate without the addition of lipids on its own.

Interactions between the highly negatively charged C-terminal region and the hydrophobic NAC regions were revealed using Nuclear Magnetic Resonance (NMR), suggesting that this shielding function of the C-terminal structure can inhibit αS aggregation [266]. By reducing the pH and/or covering it with salt, the C-terminus undergoes a structural change that can lead to the induction of aggregation. This notion is reinforced by the finding that C-terminally truncated forms are more susceptible to aggregation [267, 268].

During the aggregation of αS, the region between aa 30-60 is of particular importance. A mutant lacking residues 36-42 (called the master manipulator) and 45-57 cannot aggregate at physiological pH [269]. Furthermore, another study indicate that the preNAC segment (aa 47-56) is considered crucial for cell toxicity and fibril formation [92]. In addition, it has been shown that inhibitors, chaperones, peptides and foldamers targeting this very region can prevent αS aggregation [270, 271, 272]. The importance of this region is underscored by the presence of numerous disease-associated mutations localized in this region, including E46K, H50Q, G51D, A53E and A53T [273, 216, 220, 218].

Various structural studies have already revealed diverse polymorphs of αS fibrils. However, this variation has been primarily identified in the relatively stable region of the fibril core, specifically in the sequence between aa 35 and 95 [274, 275, 276, 277]. The NAC region consistently located in the fibril core, with residues up to aa 46 and in some cases even up to aa 14 observed in cryo-EM, contributing to the formation of a β-strand [278]. Notably, Gath *et al.* [107] demonstrated that the N-terminal regions

also form β-sheets between aa 16 and 20 in one polymorph of the studied fibrils. Another shared characteristic among the polymorphs is the absence of the C-terminus within the fibril core, which stays in a disordered conformation in a peripheral position to the core. Recent NMR experiments have shown that αS monomers bind to αS fibrils through interactions between the N-termini of the monomers and the exposed C-termini on the fibril surface [266, 279]. It is hypothesized that the resulting dynamic alignment of fully unfolded αS may trigger secondary nucleation.

1.3.3 Spreading of α-synuclein fibrils

The Braak model of PD states that Lewy bodies and Lewy neurites spread over time via neuronal connections in the peripheral and central nervous system [280]. *In vitro* studies show that fibrillar αS can be transported bidirectionally, anterograde and retrograde, along axons [281, 282, 283]. Transgenic mice with human αS develop aggregates at distant anatomical locations from the injection sites. Surprisingly, it has been shown in mice that intramuscular injection of pre-formed fibrils leads to the formation of amyloid aggregation in the brain, suggesting an impressive transport pathway [284]. Current research is considering that the αS pathology in PD may also originate in the gut and ascend to the brain [285]. Therefore, overcoming cell membrane barriers is necessary to enable the spread between cells (Figure 1.6).

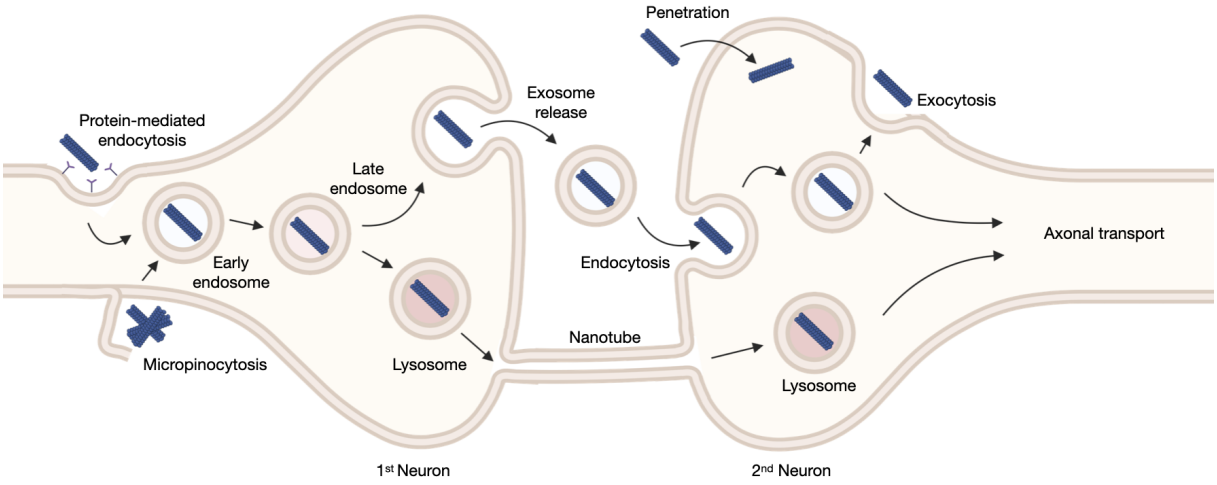

Figure 1.6: Internalization and spreading of αS fibrils between neurons. Fibrils (blue) are transported into the cell through micropinocytosis, membrane penetration or protein-mediated endocytosis. After internalization, the fibrils travel through the early and late endosomal compartment to the lysosome. During the development phase of the endosome, the pH value decreases to a slightly acidic pH, indicating by a color shift from white to red. The fibrils can also be released by exocytosis, but this can lead to immediate uptake by neighboring cells. Another mechanism of spreading is the formation of nanotubes between neighboring cells.

The mechanism of release and uptake of pathological aggregates between neurons are not yet fully understood. The challenge is to define the underlying molecular mechanisms in detail, with endocytosis being considered as one of the most important mechanisms [286]. It should be noted that the vesicles generated by endocytosis go through a development phase from early to late endosomes to lysosomes, whereby the pH value is reduced. In lysosomes, a slightly acidic pH value is present, which corresponds to that at which αS secondary nucleation or formation of oligomers are favored.

Endocytosis can occur via different pathways, including clathrin-mediated and receptor-mediated endocytosis. The interaction of αS with specific protein receptors, including heparan sulfate proteoglycans (HSPGs), leads to conformational changes of the protein and its entry into the plasma membrane [287, 288]. Studies also identify potential receptors such as neurexin 1, the amyloid beta precursor like protein 1 (APLP1) and the product of *lymphocyte activation gene 3* (LAG3), which is involved in the binding and endocytosis of αS pre-formed fibrils [289]. In addition, other cell surface proteins, in particular the Na^+/K^+-transporting ATPase subunit α3 (α3-NKA) and the membrane-bound PrP, were identified as binding partners of αS fibrils resulting in the clustering of αS fibrils and oligomers with these interaction partners at the membrane [290, 291].

Another mechanism, especially notable in oligodendrocytes and neurons, involves aggregate uptake through micropinocytosis, which include HSPG- and lipid raft-dependent processes, like Rac-1 mediated ones [292]. Moreover, fibrils may enter cells through membrane penetration, by inducing changes in membrane dynamics. Additionally, studies indicate that neurons can exchange fibrils via tunneling nanotubes, establishing a direct path from neuron to neuron [293] (Figure 1.6).

After spreading inside the cells, cellular processes get altered by these toxic species. Models of amyloid-associated cytotoxicity encompass various factors, including the inhibition of proteasomal degradation, impairment of autophagy, disruption of mitochondrial function, generation of ROS, binding of other proteins, inducing stress in mitochondria, endoplasmic reticulum (ER) and disruption of membranes, such as those of lysosomes and plasma membranes. All these factors can lead to cellular dysfunction and cell death [11]. However, clear identification of the important cytotoxic mechanism in a system as complex as a cell remains a difficult task.

1.3.4 Diagnostics

The diagnosis of PD and other synucleinopathies relies predominantly on clinical criteria, resulting in suboptimal diagnostic accuracy during the early stages of the disease [294, 295]. Furthermore, the course of PD is highly variable [296]. Given the similarities in symptoms among different neuronal disorders, achieving a definitive diagnosis often requires *postmortem* neuropathological analysis. Consequently, there is a growing emphasis on the development and validation of assays capable of identifying, quantifying, and validating various αS species as potential biomarkers for synucleinopathies [65].

These include the observation that the total αS concentration in the cerebrospinal fluid (CSF) of PD patients tends to show a decrease compared to control groups, but the reported concentrations vary considerably between studies [297, 298, 299, 300]. PTMs of αS are rare in biological fluids but occur abundantly in pathological aggregates in the brain and peripheral tissues [301]. Most studies focus on the detection and quantification of phosporylated αS at position 129 (pS129), which can be detected in blood components such as plasma or erythrocytes, but not in CSF [302, 303, 304]. The concentrations of oligomeric αS species appear to be elevated in various biological fluids in PD, but the sensitivity, specificity and reproducibility of assays for these forms are still unsatisfactory for the use in the diagnosis of individuals, but could also be promising approaches after further optimization [305, 306, 307].

Highly sensitive and specific seed amplification assays (SAA), such as real-time quaking-induced conversions (RT-QuIC), have been devised to identify aggregated αS not only in CSF but also in peripheral tissues [308, 309, 310, 311, 312, 313]. In these assays, the addition of a recombinant substrate to minute amounts of patient-derived aggregates leads to the exponential proliferation. Studies employing these assays demonstrate promising outcomes regarding reproducibility, sensitivity and specificity, both

in diagnosing PD and in distinguishing various synucleinopathies [314]. SAA exhibit a high level of accuracy in discerning patients with PD and DLB from healthy controls. Furthermore, these assays enable the diagnosis of synucleinopathies in the prodromal stage, such as PAF or idiopathic RBD [315]. In addition to the nervous system and CSF, αS aggregates have been detected in various body tissues and fluids such as skin, olfactory mucosa, saliva, tears, urine and blood of PD patients [316]. Recent studies show that αS aggregates have also been detected in the stool of patients with idiopathic RBD [317]. These discoveries open potential sources of easily accessible patient material to use in SAA and could enable innovative diagnostic tests that can support early diagnosis and patient recruitment in clinical trials.

Recently, however, there has been a growing recognition of co-pathologies in amyloid diseases, such as the presence of αS aggregates in AD [40]. The exclusive use of αS species as biomarkers may prove insufficient to distinguish between different diseases or to accurately monitor disease progression. Therefore, it is advisable in the future to try to broaden the range of biomarkers to include clinical markers, indicators of neuronal injury, axonal integrity and other relevant biological signaling pathways [318, 319, 320]. This broader spectrum could include markers for endoplasmic and oxidative stress, inflammation, energy failure and the extracellular matrix, thus enabling a more comprehensive approach to diagnosis and monitoring. If this early diagnosis can be reliably improved, inhibitors are urgently needed as therapeutic agents to stop these diseases and, in the best case, cure them completely.

1.4. Inhibition of amyloid fibril formation

Amyloid diseases are widespread, yet diverse strategies are under investigation for the development of potent pharmacological treatments. Numerous compounds have been suggested to interact with one or more species that are formed during the formation of amyloid fibrils, thereby disrupting and preventing aggregation. This includes peptides [321, 322], proteins [323], molecular chaperones [324], antibodies [325], small chemical compounds such as polyphenols [326, 327, 328], anti-inflammatory agents [329], metal chelators [330] and tetracycline [331], as well as inorganic and organic nanoparticles [332, 333].

1.4.1 Molecular target sites

An attractive therapeutic strategy against this class of diseases is the search for components that can interfere with aggregation processes, as reviewed by Galkin *et al.* [334]. Interestingly, there are diverse target sites to prevent specific mechanisms (Figure 1.7).

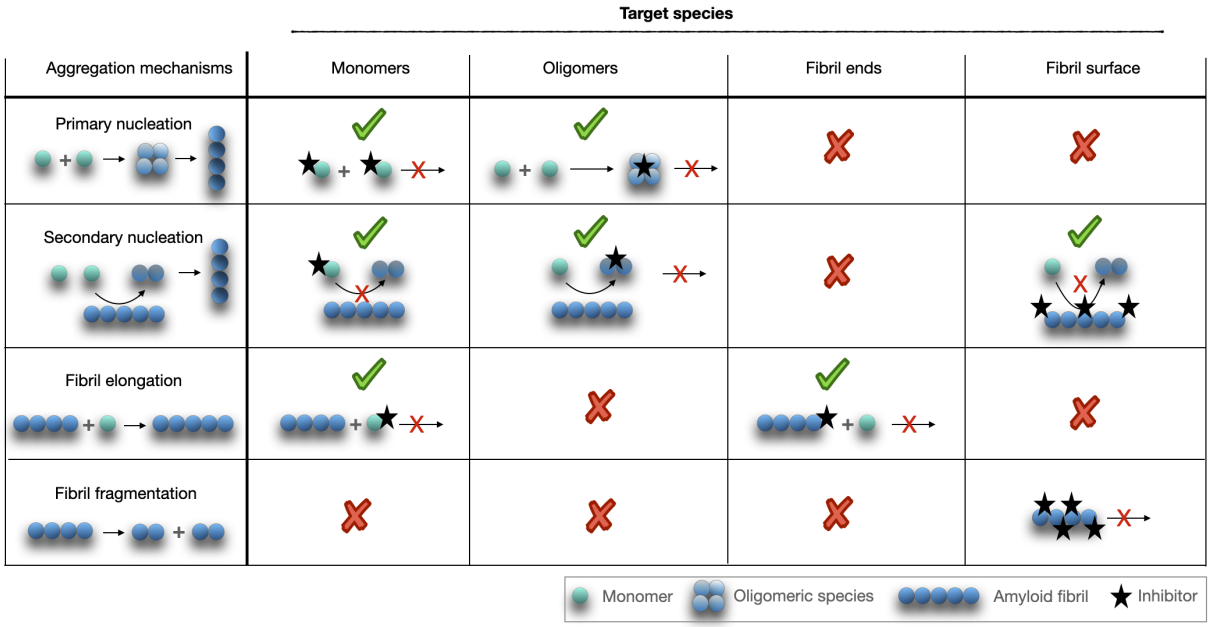

Figure 1.7: Target sites of aggregation inhibitors to selectively interfere within different mechanisms. Matrix to identify aggregation species corresponding to target point for inhibitors in each aggregation process. In aggregation mechanisms, namely primary and secondary nucleation, fibril elongation and fragmentation, different aggregation species get formed during the aggregation: monomers (green), oligomers (light blue), fibrils (dark blue). Inhibitors can selectivley target each mechanisms by interfereing with certain aggregation species. An overview of all possible inhibitory modes of action are shown for each mechanisms. If the interaction with this species does not result in an inhibition, it is crossed out in red. Figure is modified from Arosio *et al.* [335].

One option involves stabilizing the native monomeric form as the target species to prevent amyloid formation. The sequestration of monomers results in reduced rates of primary and secondary nucleation and elongation. However, achieving this requires an effective binding partner for the monomeric form. In the case of intrinsically disordered proteins, there is no opportunity for small molecules to be incorporate in hydrophobic pockets within the 3D structure. But, there are protein-based inhibitors achieved by protein

engineering, that completely sequester aggregation-prone peptide regions [336, 337, 338]. However, the utilization of monomer binders often alters the monomeric structure, for example through the insertion of β-hairpins after binding [339]. This alteration does not lead to the stabilization of the monomers in their native structure, potentially impairing the protein's native functions. It is important to note that monomer binders must be administered in a stoichiometric ratio to the monomer, which can be challenging to achieve at high protein concentrations, as seen for αS in presynaptic terminals with up to 20 µM concentration [340, 341]. This leads to the requirement of high drug doses which may be impractical for treatment approaches [334].

Another point of attack is targeting of oligomers, which can reduce the rate of primary and secondary nucleation. Antibodies targeting oligomers are proved to be clinically relevant therapeutic strategies [61]. However, oligomers do not have a clearly defined structure, which means that all forms of oligomers are targeted. Some of these oligomeric species, particularly αS tetramers, have been considered potentially natively relevant [238]. This makes it extremely difficult to develop inhibitors that target a specific oligomer type but do not recognize those with native function. Nevertheless, it is a prominent target point, as it is assumed that the oligomers are the most toxic species in the diseases [342].

In addition to address soluble components during aggregation, fibrils also present a potential target site. The inhibitor's binding to the ends of the fibrils by capturing the ends specifically slows down the rate of elongation. This is done by blocking the fibril ends and stopping the recruitment of monomers. The advantage lies in the fact that fibrils are pathogenic species absent in healthy cells and the well-known rigid conformation of the fibril facilitates the development of structure-based inhibitors [343]. Furthermore, as fibrils consist of several thousands of monomer units, the concentration of fibril ends is orders of magnitude lower than the total αS concentration. The inhibitor's mode of action lies in the competition of the inhibitor with monomeric αS for the fibril end, necessitating a stronger binding affinity for effectiveness [153, 344, 345]. Presently, inhibitors in this category exhibit the lowest IC50 values (inhibitor concentration at which the aggregation process is reduced by 50%) and are effective at nanomolar concentrations, maintaining a 1:1,000 ratio between inhibitor and αS [334].

However, in addition to elongation, there are other processes that are not inhibited by the capping of the fibril ends. Secondary nucleation and fragmentation contribute to the creation of fibril seeds characterized by high seeding potential and toxicity. To counteract this, directing inhibitors to the fibril surface is crucial, diminishing the rate of secondary nucleation. It is assumed that these inhibitors cause several fibrils to stick together to form clusters, making their surface less accessible for the formation of nucleation centers [334, 346]. However, it was also considered that the fibril surface is saturated by the inhibitor and therefore nucleation can no longer be catalyzed [185]. Additionally, the binding of inhibitors to the fibril surface might enhance its stability, impeding rapid fibril breakage and subsequently reducing the fragmentation rate [347].

Different types of aggregation species play a role in different aggregation mechanisms. To date, it is unclear which species is the most toxic and should be targeted by inhibitors for effective therapeutic intervention. It is crucial to understand exactly how inhibitors operate and which target structures they aim for. Only when these fundamental questions are clarified the development of optimal inhibitors can be achieved that are adapted to the external conditions and can selectively shut down the processes that prevail under these conditions.

1.4.2 Strategies to improve the inhibitor specificity

To develop drugs that target amyloid fibril formation, it is crucial for active compounds to demonstrate high inhibitory selectivity and specificity, ensuring effectiveness at low doses while minimizing severe adverse effects. Ideally, the inhibitor should recognize both the sequence of the monomer and its conformation [334].

Thus far, amyloid fibrils are the only species with a stable and well-defined structure and have been employed for rational inhibitor design. However, the existence of various structural polymorphs of fibrils further complicates the development of specific inhibitors. Compounds, such as small molecules with increased hydrophobicity, frequently display greater affinity for fibrils due to their interaction with hydrophobic β-sheet-rich regions. However, there is a likelihood that these compounds may also interact with other β-sheet-rich proteins abundant within cells, diminishing efficiency and potentially causing adverse effects [348, 349].

Protein-based inhibitors offer high selectivity, as these larger molecules can interact with multiple residues of the target protein, probing both its conformation and sequence. Engineered monomer-binders, such as affibodies (so-called β-wrapins), are particularly well-suited for such tasks due to their high affinity. They can form complexes with monomers by binding to aggregation-prone regions, while the remaining sequence stays intrinsically disordered (IDR) [336, 337, 339, 350, 351, 352]. Interestingly, the IDR of the monomers exposed to the complex was found to contribute to the inhibition, leading to a unique strategy for directing inhibitors towards aggregation processes [353].

The fusion of monomeric units is utilized in various protein-based inhibitors [334]. For instance, a fused WT monomer serves as a fibril end-binding domain, bringing the fused inhibitor domain into proximity to the second protofilament. The inhibitor acts as a steric bulk, preventing the incorporation of additional WT monomers [153, 344, 345]. Interestingly, in the case of αS dimers, the presence of a bulky group is not even necessary for inhibition. For instance, αS dimerization via a disulfide bond generates dimers that inhibit fibril elongation with an IC50 as low as 40 nM [344]. Similar inhibitory activity is observed for dopamine-crosslinked αS dimers, di-tyrosine dimers [240], and the dimeric construct of αS comprising a hairpin motif in one of the two monomers fused (WT-CC48) [354]. These compounds likely exhibit good specificity due to the presence of the αS moiety.

However, there are also peptide-based inhibitors that utilize the sequence and self-aggregation of the monomers as a template [334]. Eisenberg's research group, for instance, employed computer designs to create a series of small 45 aa proteins with a stabilized β-sheet scaffold, capable of binding to the end of the αS fibrils [355]. Also small fragments (9-11 kDa) were developed that mimic the monomeric sequence, effectively covering parts of the αS fibril with IC50 values as low as 6 nM, resulting in inhibition [356].

These strategies capitalize the incorporation of the native IDR of the monomers into the inhibitor. Inhibition is accomplished through self-interaction with the resultant aggregation species and inhibitor, which is a modified version thereof. The methodology provides a tool for pinpointing the specific IDRs pivotal for the inhibition of aggregation proliferation and, in turn, may hold the potential to optimize inhibitors to selectively target individual processes.

1.5. Objective

Amyloid diseases form a diverse group of illnesses. According to the amyloid hypothesis, the presence of amyloid aggregates serves as the hallmark for all of these diseases, suggesting a causal link between amyloid deposits and pathological symptoms. However, knowledge of the formation and their progression have been severely limited. There is a significant need for basic research to better understand the mechanism of how inhibitors can interfere with the aggregation processes. This study was divided into two parts. The first part revolves around exploring the mechanistic role of IDR interactions as an inhibitor's assistant to prevent amyloid fibril formation, aiming to elucidate how this may enhance inhibitory potential. The second part is focused on acquiring a deeper understanding of the induction of pathophysiological effects in cells by various aggregation species. Additionally, it explores the internal response mechanisms of neurons at a proteasomal level when exposed to aggregation species.

More specifically, the first objective was to understand the mechanism of the αS fibril elongation inhibitor WT-CC48. This consists of a fusion between a WT monomeric αS part and a β-hairpin forming cysteine mutant of αS, known as CC48. In previous studies, CC48 was identified as a highly potential inhibitor of fibril elongation in a nanomolar range. However, it was shown, that the fusion of the WT monomer to CC48 further increased the inhibitory effect, speaking for a contribution of this component to the inhibitor's mode of action. The exact mechanism, however, remained unclear. Here, a detailed investigation was performed to elucidate which IDRs of both subunits of the inhibitor contribute to the enhanced inhibitory potential. The data that sheds light on this question is presented in Chapter 2.

The second objective was to investigate the role of IDRs of αS on nucleation inhibition. The engineered binding protein β-wrapin AS69 binds to monomeric αS. In this complex, AS69 induces local folding of the region, comprising residues 37-54, into a β-hairpin conformation within the otherwise intrinsically disordered protein. Surprisingly, AS69 can achieve substoichiometric inhibition of αS nucleation, meaning the substoichiometric activity was not attributed to the binding protein *per se* but rather to its 1:1 complex with αS. The IDRs unaffected by binding must play a pivotal role, as examined in detail in Chapter 3. The identification of the role of IDRs led to the development of inhibitors that can inhibit one specific aggregation mechanism and identify their role in cells.

The third objective was to identify the aggregation mechanism driving proliferation in the diagnostic shaking-induced SAA. Exponential increase in αS aggregation may occur through secondary nucleation or fragmentation/ elongation. So, the question arose whether a nucleation-specific inhibitor can gain further insight to the underlying mechanism. For that, we applied the in Chapter 3 identified nucleation-specific inhibitor, here called AS69nuc, as an artificial tool to gain insight into the aggregation proliferation. The data is presented in Chapter 4.

The next objective is focused on the understanding of the cellular answering machinery when exposed to amyloid fibrils. Deciphering the proteasomal landscape allows us to gain insight in processes involved in fibril internalization, defense, and self-protection. The resulting data is summarized in Chapter 5.

The last objective is centered on elucidating which aggregation species exhibit toxic effects. Given the challenges in studying oligomers, a stable oligomer model is urgently needed. In this study we developed an oligomer model for IAPP. This choice for using IAPP as the aggregation-prone protein was influenced by the well-characterized oligomer model for Aβ (dimAβ) and the high structural similarity between Aβ and IAPP. The introduction of this model enables the investigation of the effects of curvilinear oligomers, on overall IAPP aggregation and their pathophysiolgical impact on cells in comparison to IAPP fibrils.

The findings are documented in Chapter 6.

Overall, the objectives one to five all contribute to the better understanding of amyloid formation and inhibition as well as the role of oligomers and the identification of cellular effects induced by aggregation species – each one to their individual degree.

2

FIBRIL CORE REGIONS IN ENGINEERED α-SYNUCLEIN DIMER ARE CRUCIAL FOR BLOCKING OF FIBRIL ELONGATION

This Chapter reflects content on the following publication.

2.1. Publication information

Author: Celina M. Schulz[*a], Anne Pfitzer[*a] and Wolfgang Hoyer[ab]
a: Institut für Physikalische Biologie, Heinrich Heine University Düsseldorf, Düsseldorf, Germany
b: Institute of Biological Information Processing (IBI-7: Structural Biochemistry) and JuStruct: Jülich Center for Structural Biology, Forschungszentrum Jülich, Jülich, Germany
*: These authors contributed equally: Celina M. Schulz, Anne Pfitzer

Published in: BBA Advances (17 November 2023)

2.2. Abstract

Synucleinopathies like Parkinson's disease (PD) are neurodegenerative diseases which are associated with the deposition of fibrillar aggregates of the endogenous protein α-synuclein (α-syn). The inhibition of the elongation of α-syn fibrils is of great scientific interest and an option in the design of therapeutic strategies. Previously, we developed a disulfide-containing mutant of α-syn, called CC48, which inhibits fibril elongation by blocking of fibril ends. Surprisingly, wildtype (WT) α-syn molecules supported the blocked state, and a fusion of CC48 with WT α-syn, denoted WT-CC48, exhibited increased inhibitory potential. Here, we studied which regions of WT-CC48 are responsible for the strong inhibitory effect. To this end, we investigated a set of truncated versions of WT-CC48 by kinetic elongation assays, density gradient centrifugation, and atomic force microscopy. We show that in both the WT and the CC48 part of the fusion construct the hairpin region (residue 32-60) and NAC region (61-95), but not N- and C-terminal regions, are required for strong inhibition of fibril elongation. The required regions correspond to the segments forming the β-sheet core of α-syn fibrils. As α-syn fibrils typically consist of two protofilaments, the dimeric construct WT-CC48 provides the critical regions sufficient to cover the full β-sheet core interface exposed at the fibril end, which can explain its high inhibitory efficiency. We suggest a mechanistic model of CC48-mediated inhibition of fibril elongation in which CC48 and WT α-syn cooperatively form an oligomer-like cap at the amyloid fibril end.

2.3. Introduction

A large number of proteins and peptides have been shown to undergo aggregation processes resulting in the loss of function and the build-up of toxic debris [357, 358, 359, 360]. The aggregates often consist of fibrils with a highly ordered β-sheet core, the so-called cross-β amyloid structure [31, 361]. Amyloid fibril formation is associated with many diseases, including Alzheimer's disease and PD [33, 362]. Synucleinopathies, like PD, are believed to be triggered by amyloid fibril formation of the 140 amino acid long presynaptic protein α-syn. In PD patients, it is found in Lewy bodies as insoluble inclusions [273, 363].

α-syn can assemble into several distinct fibril structures, referred to as polymorphs, which were termed, e.g., ribbons, rod, and twister [116, 117, 118, 92]. Almost all α-syn fibril polymorphs resolved structurally up to this day consist of two protofilaments. In all polymorphs, the central region of α-syn comprising amino acids 30-100 contributes the largest part of the cross-β fibril core. The precise fold of the α-syn units within the fibril core, however, can be quite variable among polymorphs, including diverse protofilament interfaces.

Amyloid formation can be described as a mechanism of nucleated polymerization and is a multistep process, comprising primary nucleation, secondary nucleation and elongation [11, 124, 158]. In the process of primary nucleation, monomers undergo a structural transformation to form growth-competent nuclei [364]. In secondary nucleation, oligomer formation and conversion to a fibril seed is catalyzed on the surface of a pre-existing fibril [158, 365]. Elongation describes the binding of a monomer to a fibril end and the structural conversion of the newly attached molecule into the cross-β amyloid structure [149, 365]. As elongation is a fundamental reaction step of fibril growth, fibril mass cannot be generated under conditions that prohibit elongation. Therefore, the fibril end is an interesting target site to achieve inhibition of elongation and fibril formation in general. Moreover, the number of fibril ends is low compared to that of aggregated protein units, which may support inhibitory activities at low inhibitor concentrations [335]. Different types of molecules have thus been designed and/or selected to occupy the fibril ends and block elongation, such as antibodies [366], peptides [367], or protein constructs [344, 345, 355].

Previously, our group introduced an α-syn double cysteine insertion mutant which specifically inhibits the elongation of WT α-syn fibrils [354, 368]. The mutant, here called CC48, comprises the mutations of G41C and V48C allowing the formation of an intramolecular disulfide bond. The position of the disulfide bond was chosen to promote formation of a hairpin in the region comprising α-syn residues 32 to 60 (labeled here HP region, Figure 2.1) that was observed upon binding to the engineered protein AS69. Several studies showed that this region is of critical importance for α-syn aggregation: AS69 [350] and chaperones, peptides, and foldamers targeting this region [270, 271, 272] inhibit α-syn aggregation; a mutant lacking from residues 36-42 (called "master manipulator" [269]) and 45-57 was shown not to aggregate under physiological pH [269, 217]; the so-called preNAC segment (residues 47-56) [92] is critical for cell toxicity and fibril formation. The great significance of this region is emphasized by the fact that many disease-associated mutations are localized here, for instance E46K, H50Q, G51D, A53E and A53T [207, 216, 218, 220, 273].

CC48 is an intrinsically disordered protein just like WT α-syn, but in contrast to WT α-syn does not aggregate as long as the disulfide bond is closed [368]. It inhibits elongation of WT α-syn fibril elongation, which could be analyzed with the framework of enzyme inhibition, with the fibril end acting as the enzyme and α-syn monomers corresponding to the substrate [354]. CC48 acted as a competitive inhibitor.

Interestingly, monomeric WT α-syn promoted inhibition presumably by stabilizing the blocked state at the fibril end. In line with this, a fusion construct of WT α-syn and CC48 was shown to drastically enhance the inhibitory effect (Figure 2.2A). In order to gain further mechanistic insight into α-syn fibril elongation and its inhibition, we here tested which regions of WT-CC48 are responsible for the strong inhibitory effect. For this purpose, we exploited the dimeric nature of the WT-CC48 fusion to generate fusion constructs with deletions of specific regions (Figure 2.1) either in the WT or the CC48 part. For this set of truncated versions of WT-CC48 we compared their potential to inhibit fibril elongation. The data demonstrates that the central regions of α-syn, which constitute the fibril core, are also most critical for inhibition of fibril elongation.

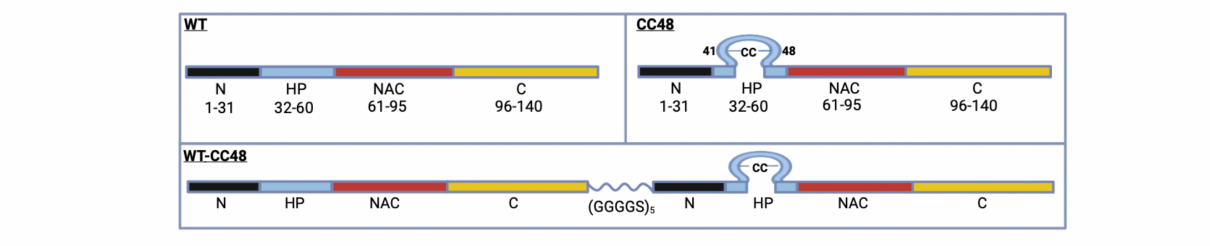

Figure 2.1: WT α-synuclein illustrated by its characteristic regions: N-terminus (N) from residue 1-31 (black), hairpin (HP) from residue 32-60 (blue), non-amyloid-β component (NAC) from residue 61-95 (pink) and C-terminus (C) from residue 96-140 (yellow). The double cysteine mutant CC48 (G41C, V48C) only differs in the HP region (32-60). The WT-CC48 construct is composed of the wildtype sequence linked via a $(G_4S)_5$-linker to CC48. A linker length of 25 amino acids was chosen to ensure sufficient conformational flexibility and length to bridge binding sites at the fibril end.

2.4. Results

2.4.1 Fusion of α-syn WT and the disulfide mutant CC48 inhibits fibril elongation by blocking fibril ends

To test the effect of inhibitors on fibril elongation, we applied a well-established assay in which 2.5 μM pre-formed fibrils (concentration in monomer units) are added to 25 μM α-syn monomers at neutral pH, followed by monitoring of fibril growth under quiescent conditions to suppress nucleation of new fibrils [135, 354]. The amount of amyloid is detected using the amyloid specific fluorescent dye, Thioflavin-T (ThT), which changes intensity dramatically upon binding to amyloids (Figure 2.2B). Inhibition of fibril elongation can be displayed by calculating the ratio of the initial rates of increase in ThT fluorescence with inhibitor (R) vs. without inhibitor (R_0) (Figure 2.2C). The dependence of R/R_0 on inhibitor concentration can be explained by a competition of inhibitor and WT substrate for the binding sites at the fibril end (competitive inhibition model, more specifically the FI model, devised in [354]). In presence of WT-CC48, a complete inhibition of fibril elongation could be detected at nanomolar concentrations (Figure 2.2B,C). At the end of the kinetic assay, elongation of the pre-formed fibril seeds was confirmed by atomic force microscopy (AFM), with higher fibril length in the absence of inhibitor (Figure 2.2D,E).

In our previous study, we hypothesized that binding of CC48-based inhibitors to the fibril end would lead to a templating-incompetent, i.e., blocked, state [354]. To obtain further evidence for this mechanism, we tested if fibrils lose the ability to elongate upon pre-incubation with WT-CC48 followed by fibril

isolation. The pre-formed fibrils were incubated with 25 µM WT-CC48 and as a control with α-syn WT monomers overnight at 37 °C under quiescent conditions. Subsequently, the fibrils were separated by centrifugation and used as pre-formed fibrils in the ThT assay. The sample containing pre-formed fibrils pre-incubated with WT-CC48 did not show any increase in ThT signal, in contrast to the control sample (Figure 2.2F). Two conclusions can be drawn from this experiment: *i.)* WT-CC48 binds α-syn fibrils with high kinetic stability of the bound state, *ii.)* WT-CC48 inhibits fibril elongation. This is in line with WT-CC48 inhibiting fibril elongation by capping of fibril ends.

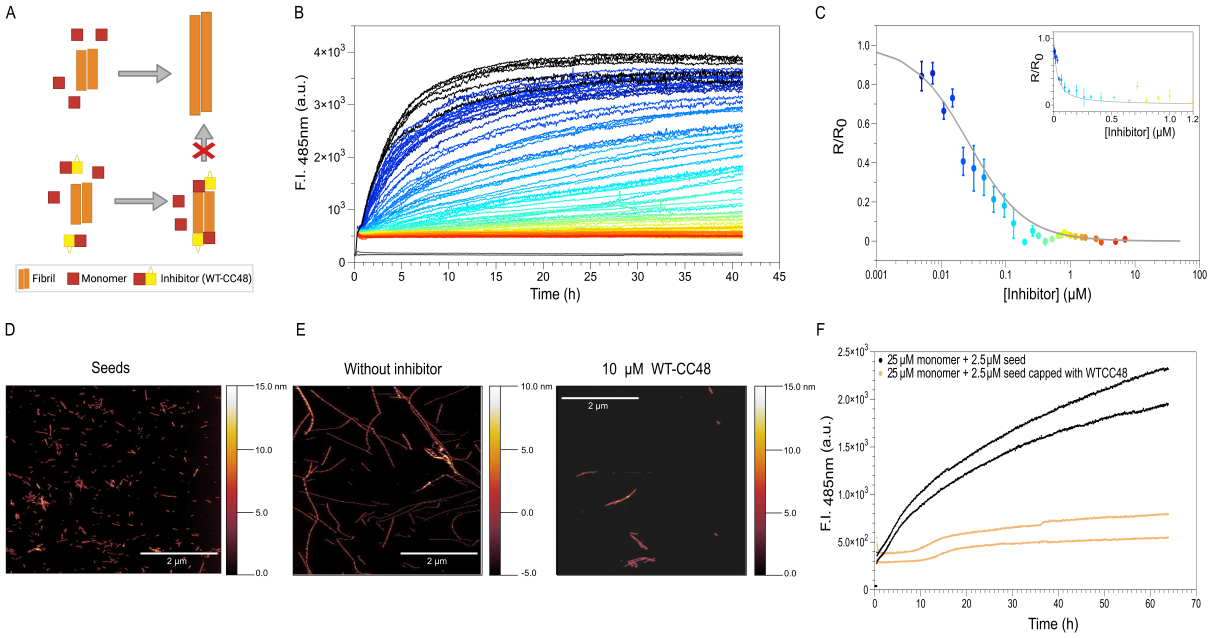

Figure 2.2: WT-CC48 inhibits fibril elongation at low substoichiometric ratios. (A) Schematic overview of the suggested mode of action of WT-CC48 [354]. Monomeric α-syn WT is shown as a red square, while the CC48 part is shown as a yellow square with a disulfide-bound. In the presence of pre-formed fibrils, monomeric WT can bind to the fibril end and the fibril grows in length. However, in the presence of WT-CC48, WT-CC48 can get incorporated in the fibril structure and stops fibril growth. (B) ThT assay performed at pH 7.4 with 25 µM α-syn WT monomers, 2.5 µM seeds and different inhibitor concentrations between 5 nM and 10 µM, shown in a color gradient from blue to red, under quiescent conditions. The measurement was performed in triplicates. Negative controls are shown in grey shades and positive control (NoWT-CC48) in black. (C) Relative rates of fibril elongation were plotted against the inhibitor concentration (µM) with logarithmic scale or linear scale (inset). The solid line is a fit to a model of competitive inhibition (FI model). (D,E) AFM of (D) fibril seeds and (E) fibrils generated in the ThT assays of α-syn WT without inhibitor and with 10 µM WT-CC48. (F) ThT assay using seeds that were pre-incubated with a 1to1 ratio of WT-CC48 or α-syn WT. Pre-incubation was done overnight and seeds were isolated by centrifugation at 100,000 xg for 1 h. The measurement was performed in duplicates.

2.4.2 The WT part of WT-CC48 promotes inhibition of fibril elongation due to its HP and NAC regions

To identify the regions of the WT part of WT-CC48 that interact with the fibril end, different truncations of the WT part were generated. Structurally, α-syn is commonly divided into three distinct regions: the amphipathic N-terminus (aa 1-60), the central hydrophobic region termed NAC (aa 61-95), and the acidic

C-terminus (aa 96-140) (Figure 2.1). In this study, we further subdivided the N-terminus into two parts: the very N-terminus (aa 1-31) and the HP region (aa 32-60). Our experimental goal was to investigate the relevance of these regions in the inhibitory mechanism of WT-CC48 on fibril elongation. To this purpose, eight fusion constructs were designed in which the N, HP, NAC or C region, or combinations thereof, were removed from the WT part of WT-CC48 (Figure 2.3).

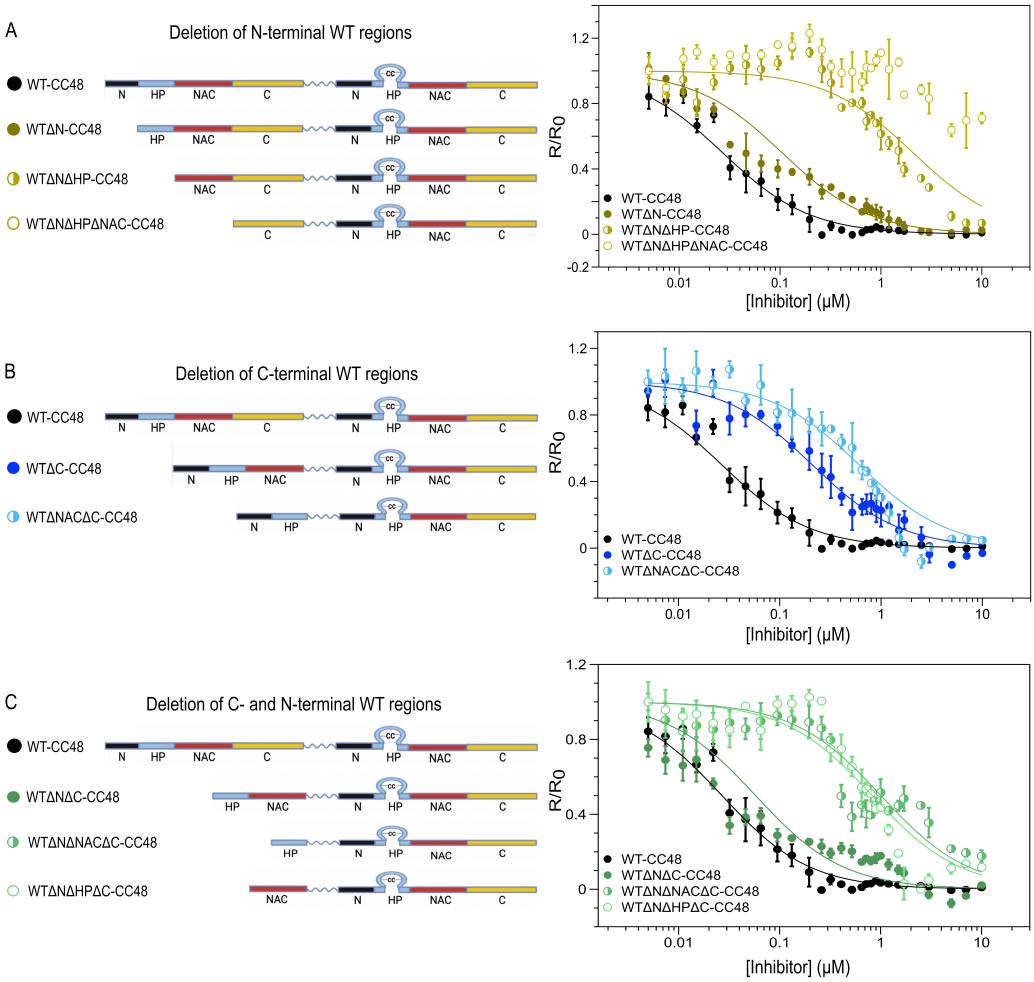

Figure 2.3: Truncations of α-syn WT regions in WT-CC48 affect inhibition of fibril elongation. Left, Schematic representation of the constructs visualizes the truncation of the N-terminal WT regions (A), the deletion of the C-terminal WT regions (B) and the deletion of both C- and N-terminal WT regions (C). The individual α-syn regions are displayed in different colors: N-terminus (residues 1-31) in black, hairpin region (residues 32-60) in blue, NAC region (residues 61-95) in pink and the C-terminus (residues 96-140) in yellow. The HP region of the CC48 part is shown as a loop. Right, relative rates of fibril elongation obtained from elongation assays (SI Figures 2.8-2.10) were plotted against the inhibitor concentration (μM). For the constructs WTΔNΔHPΔNAC-CC48, WTΔNΔHP-CC48, WTΔNACΔC-CC48, WTΔNΔNACΔC-CC48, and WTΔNΔHPΔC-CC48 the R/R_0 values were normalized to 1.0 for the lowest inhibitor concentration, as the R/R_0 values at low inhibitor concentrations were stable at a value above 1.0 for these constructs (see SI Figures 2.8-2.10 for the non-normalized data). Solid lines are fits to a model of competitive inhibition (FI model).

Truncation of the N-terminus (WTΔN-CC48) did not change the inhibitory strength compared to the full-length construct (Figure 2.3A, SI Figure 2.8A). However, further removal of the HP region (WTΔNΔHP-CC48) led to a strong reduction of the capability of the inhibitor (Figure 2.3A, SI Figure 2.8B). Additional reduction of inhibitory strength is caused by the deletion of the NAC region (WTΔNΔHPΔNAC-CC48) (Figure 2.3A, SI Figure 2.8C). Truncation of the C-terminus only (WTΔC-CC48) showed a moderate decrease in inhibition strength, whereas additional deletion of the NAC region (WTΔNACΔC-CC48) strongly decreased inhibition potency (Figure 2.3B, SI Figure 2.9). From these results we infer that the removal of the NAC and HP regions lead to strong reductions in inhibition of fibril elongation. However, the removal of the N- or C-termini has only minor effects, which was confirmed by a fusion construct which lacks both termini (WTΔNΔC-CC48) (Figure 2.3C, SI Figure 2.10A). This construct shows the same inhibitory efficiency as full-length WT-CC48. Interestingly, removal of either the HP or NAC region reduced the inhibitory effect of the fusion construct dramatically, indicating that both regions are required for potent inhibition (Figure 2.3C, SI Figure 2.10B,C).

The inhibitory effects observed in the kinetic assay were confirmed by sucrose density gradient centrifugation (DGC) and AFM. Size distribution analysis by DGC showed that α-syn in the absence of inhibitor formed high molecular weight (HMW) assemblies which sedimented in the bottom fractions (Figure 2.4A). AFM confirmed that these aggregates were amyloid fibrils (Figure 2.4A). 10 µM WTΔC-CC48, with only the C-terminus removed, ensured that α-syn remained predominantly in monomeric form (Figure 2.4B). The less effective inhibitor WTΔNΔNACΔC-CC48, which lacks the important NAC region, retained α-syn only partially in monomeric form (Figure 2.4C).

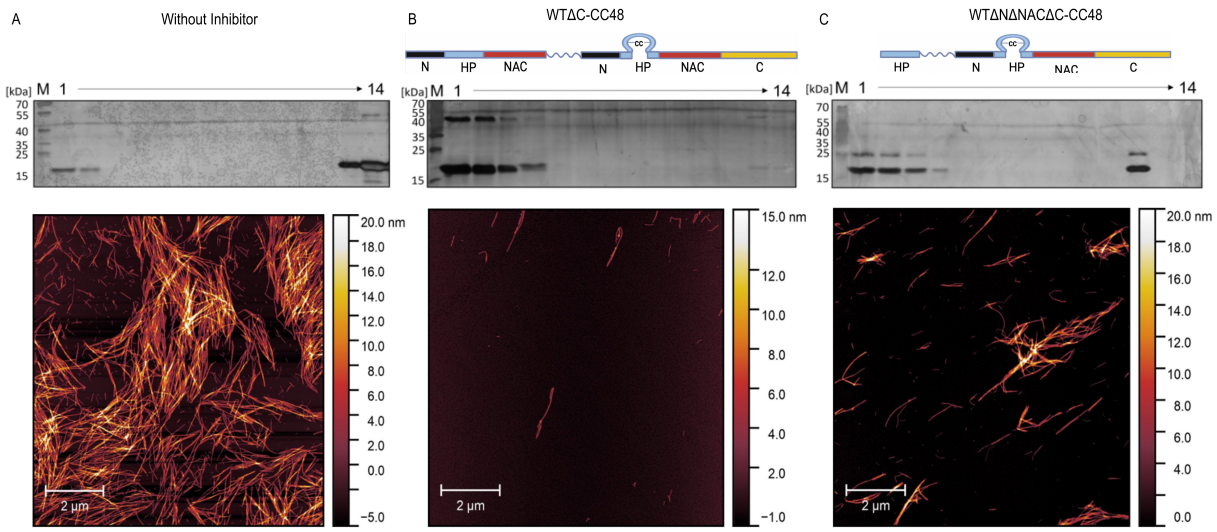

Figure 2.4: Different efficiency of inhibition of fibril elongation of truncated WT-CC48 constructs. Sucrose DGC and AFM imaging of samples at the end of the kinetic aggregation for α-syn WT without inhibitor (A), with 10 µM WTΔC-CC48 (B), or with 10 µM WTΔNΔNACΔC-CC48 (C). DGC fractions, analyzed by SDS-PAGE (15% tris-glycine gel), are numbered from 1 to 14, with low-density fractions given lower numbers and higher density fractions higher numbers. M, marker. α-syn monomers are obtained in low-density fractions 1-4, whereas α-syn aggregates are found in high-density fractions 12-14 [369]. In SDS-PAGE, α-syn runs at an apparent MW of 17 kDa. WTΔC-CC48 and WTΔNΔNACΔC-CC48 co-migrate with α-syn in DGC and run in SDS-PAGE at apparent MWs of 45 and 25 kDa, respectively.

2.4.3 The HP and NAC regions of also the CC48 part of WT-CC48 are crucial for strong inhibition of fibril elongation

The inhibitor CC48 differs from WT monomer only by the introduction of two cysteines at position 41 and 48 and retains the intrinsically disordered nature of WT α-syn [368]. The fusion of the inhibitor CC48 and its co-inhibitor, WT, increases the inhibition strength [354]. Assuming that WT promotes inhibition by binding to fibril ends, the question arises whether the binding of the structurally similar CC48 to fibril ends occurs by the same mechanism. We wondered whether removal of the different regions in the CC48 part had the same effect on inhibition as truncations of the corresponding regions in the WT part. In one of the constructs, the C-terminal and N-terminal region of the CC48 part were removed (WT-CC48ΔNΔC). For this construct, the inhibition is in the same nanomolar range as for the full-length construct (Figure 2.5, SI Figure 2.11A). In contrast, additional removal of the NAC (WT-CC48ΔNΔNACΔC) region decreased the inhibitory effect (Figure 2.5, SI Figure 2.11B). We finally compared the effects of truncations of corresponding regions in the two parts of the fusion construct, WT or CC48. Deletion of N- and C-terminus in either the WT or the CC48 part did not have a clear effect on the inhibitory potential (SI Figure 2.12A). However, the NAC region is required in both parts to maintain their high inhibitory potency (SI Figure 2.12B). Thus, we suggest that both, the WT part and the CC48 part, require the NAC and HP regions for optimal interaction with the protofilaments' cross-β core interfaces at the fibril end.

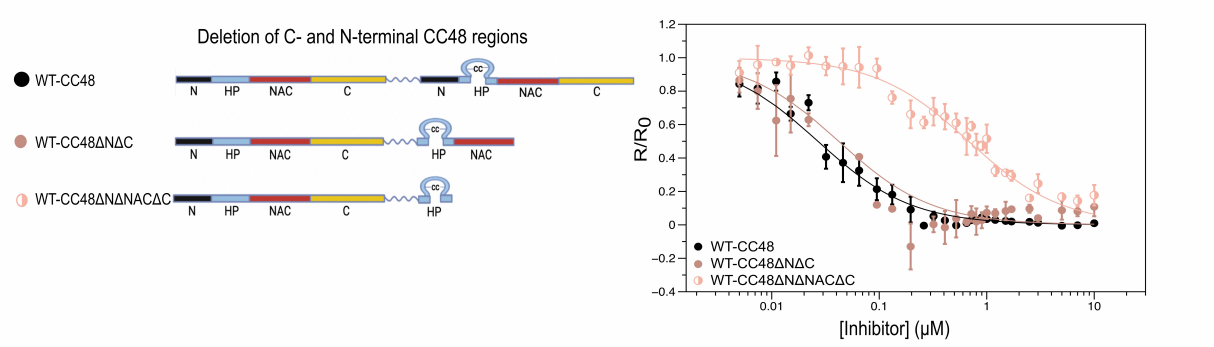

Figure 2.5: Truncations of CC48 regions of WT-CC48 affect inhibition of fibril elongation. Left, schematic representation of the constructs visualizes the deletion of C- and N-terminal regions. The different regions of α-syn are displayed in different colors: N-terminus (residues 1-31) in black, hairpin region (residues 32-60) in blue, NAC region (residues 61-95) in pink and the C-terminus (residues 96-140) in yellow. The HP region of the CC48 part is shown as a loop. Right, relative rates of fibril elongation obtained from elongation assays (SI Figure 2.11) were plotted against the inhibitor concentration (μM). Solid lines are fits to a model of competitive inhibition (FI model)

As a control experiment, we investigated two concentrations of all constructs on the same microtiter plate using the same seed preparation in a ThT experiment (SI Figure 2.13A-E) to ensure that any observed differences in inhibitory activity were not due to or compromised by differences between seed preparations. In addition, the insoluble vs. soluble fractions *post* aggregation were analyzed by ultracentrifugation followed by SDS-PAGE (SI Figure 2.13F-I). The data confirmed the previous observations regarding the relative inhibitory activity of the different fusion constructs.

2.5. Discussion

In this study we could confirm that WT-CC48 is a potent inhibitor of fibril elongation of α-syn. Comparing the IC50 values of all investigated constructs, we find that all constructs containing the HP and the NAC region in both WT and CC48 part show strong inhibition similar to that of full-length WT-CC48 (Figure 2.6A). This indicates that both, the HP and the NAC region (together residues 32-95), of both, the WT and CC48 part of the fusion construct, are necessary for the nanomolar inhibitory strength. In contrast, the N- and C-termini do not play an important role in CC48-mediatied inhibition of fibril elongation (Figure 2.6A). Regardless of the fibril polymorph, the region between residues 32-95 lies in the fibril core [92, 276, 278, 370, 371, 372, 373, 374]. At the fibril ends, this region exposes the open cross-β structure as an interface for monomer attachment and as a template for their conversion into the fibril conformation. Since almost all α-syn fibril polymorphs reported to date consist of two protofilaments, this open cross-β structure interface extends over two HP and NAC regions (Figure 2.6B). The observation that two HP and two NAC regions are required to maximize inhibition suggests that the full cross-β interface can be recruited for interaction with the inhibitor WT-CC48.

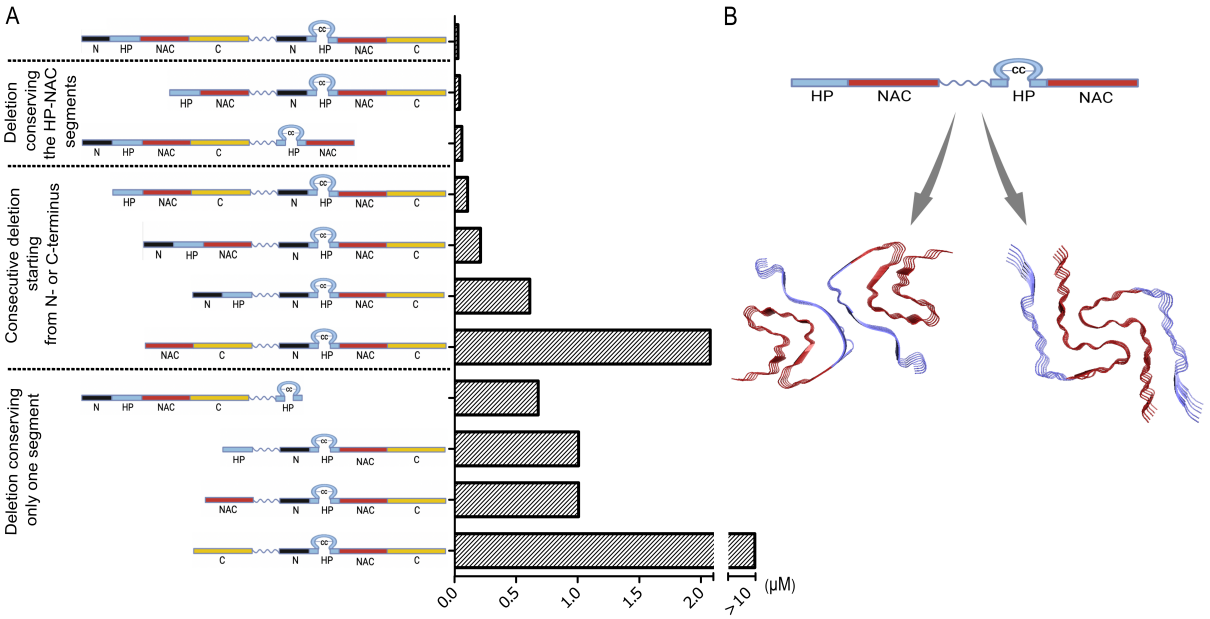

Figure 2.6: Overview of important regions in WT-CC48 for inhibition of fibril elongation. (A) IC50 values of the investigated constructs derived from the fits to the competitive inhibition model. (B) From the data, it can be concluded that in both parts of the constructs, WT and CC48, the HP and the NAC region are of great importance for the inhibition of the α-syn fibril elongation. Both parts, HP and NAC region, build the fibrillar core of α-syn fibrils, suggesting that elongation is driven by self-interactions between HP and NAC regions at the fibril end and in the inhibitor. The polymorphs shown here are taken from [92], PDB codes 6CU7 (rod polymorph) and 6CU8 (twister polymorph).

The data obtained here for the WT-CC48 fusion constructs allows to refine a model describing how CC48 achieves inhibition of fibril elongation, and how WT molecules support this activity. The model is illustrated in Figure 2.7, in which the CC48 corresponds to the inhibitor (yellow), whereas the supportive WT molecules are displayed in red. Note that the WT-CC48 fusion would in this scheme correspond to the linkage of the yellow CC48 inhibitor with a red WT molecule. The fact that the same regions are required for fibril inhibition as for fibril elongation supports a model in which CC48 establishes

similar interactions with the fibril end as WT monomers but prohibits conformational conversion into the templating-competent structure of the seed fibril (Figure 2.7). CC48 may bind to one protofilament, engaging in largely the same interactions as a WT monomer would (Figure 2.7, point 2). A WT monomer can bind to the second protofilament and stabilize the CC48-bound state. However, due to the presence of CC48, it does not adopt precisely the same conformation as the other WT units in the seed fibrils, resulting in a fibril end that is not anymore templating-competent (Figure 2.7, point 3). Kinetic analysis previously suggested that even more than one WT unit supports fibril end blocking [354]. This can be explained by formation of an oligomer-like cap, consisting of a few α-syn molecules, on the fibril end (Figure 2.7, point 4). By the direct linkage of CC48 with WT in the fusion constructs, their cooperative action is exploited to achieve blocking of fibril ends at two orders of magnitude lower inhibitor concentration than CC48 alone [354].

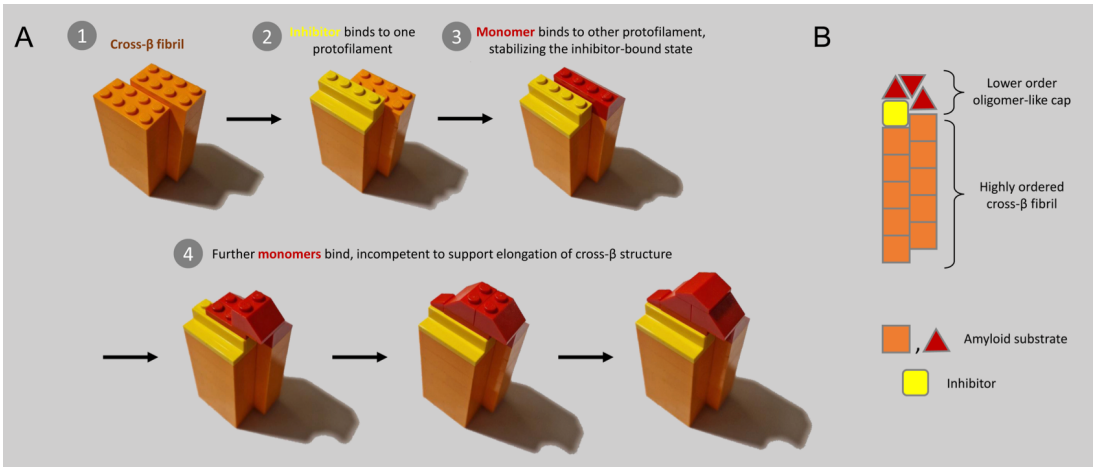

Figure 2.7: Model of CC48-mediated inhibition of fibril elongation. In this scheme, CC48 corresponds to the inhibitor (yellow), whereas the supportive WT molecules are displayed in red. Note that the WT-CC48 fusion would in this scheme correspond to the linkage of the yellow CC48 inhibitor with a red WT molecule. (1) α-syn fibril polymorphs typically consist of two protofilaments, each exposing at the fibril end an open cross-β interface (pins on the click brick) consisting of HP and NAC region. (2) CC48 (yellow) may bind to one protofilament, engaging in largely the same interactions as a WT monomer (orange) would. (3) WT monomer (red) can bind to the second protofilament, stabilizing the CC48-bound state that is incompetent to template further elongation of the ordered fibril structure. (4) Further WT monomers can add to the fibril end, creating an oligomer-like cap.

The strategy applied here to interfere with fibril formation is based on recruitment of self-interactions between an amyloidogenic protein and an inhibitor that is a modified version thereof. The results indicate that for this type of inhibitor rather large protein segments are required to achieve sufficient inhibition activity. In the case of α-syn, we find that the HP and NAC regions are important to maximize the inhibitory efficiency. The particular need for HP and NAC once again highlights the role of self-interactions in amyloid assembly and inhibition. Fusion of the HP and NAC regions of WT α-syn might be a useful strategy to improve the activity of fibril elongation inhibitors.

2.6. Material and Methods

2.6.1 Transformation, expression and purification of α-syn and WT-CC48 variants

α-syn was encoded in the expression vector pT7-7 and expressed in *Escherichia coli* (*E. coli*) strain BL21(DE3). The WT-CC48 variants were encoded in the expression vector pET11-a purchased from GenScript Biotech and expressed in *E.coli* BL21(DE3). For transformation, the cells were thawed on ice for 10 min. Then, 10 ng of the plasmid was added to the cells and incubated on ice for another 10 min. After that, heat shock was performed by heating the cells to 42 °C for 60 s. The cells were immediately placed on ice again for 2 min. Preheated (37 °C) LB medium was added to the cells, and they were incubated at 37 °C, 800 rpm for 1 h. The cells were plated on LB-agar plates supplemented with 100 µg/ml ampicillin and incubated at 37 °C overnight. The next day, a pre-culture of 50 ml 2YT supplemented with 100 µg/ml ampicillin was prepared and incubated at 37 °C and 160 rpm overnight. The next day, the main culture (500 ml in a 2 l Erlenmeyer flask) was inoculated with 5 ml of the pre-culture. It was incubated at 37 °C and 110 rpm until an OD_{600} of 0.6 was reached and induced with a final concentration of 1 mM IPTG. The culture was incubated for growth for 4 h at 37 °C and 110 rpm. The cells were harvested at 5,000 xg, 4 °C for 20 min. The supernatant was discarded. The pellet was resuspended in 10 ml distilled water. Protease inhibitor was added. The cells were frozen at -20 °C. α-syn and fusion constructs were purified as described previously [135, 263, 354].

2.6.2 Elongation assay

For seed preparation 25 µM of α-syn, 20 µM ThT, 0.04% NaN_3 and 20 mM MOPS pH 7.4, 50 mM NaCl were incubated in a volume of 1 ml with an added glass bead at 37 °C at 800 rpm for 72 h. Before addition to the 96-well plate, the seeds were pipetted to a 2 ml Eppendorf tube and sonicated at 70% for 30 s twice using UP200St Ultrasonic Processor from Hielscher.

In the elongation assay 25 µM α-syn monomers supplemented with 20 µM ThT, 0.04% NaN_3 in 20 mM MOPS pH 7.4, 50 mM NaCl were incubated with different concentration of the WT-CC48 constructs. Seeds were added to a final concentration of 2.5 µM. As controls, the seeded monomer without any WT-CC48 construct, the unseeded monomer without any WT-CC48 construct, the WT-CC48 constructs only, and the seeds only were used. All components except for the seeds were added to a 96-well half-area, non-binding surface, black with clear bottom, polystyrene plate (3881, Corning) and incubated at 37 °C for 10 min. Then, the sonicated seeds were added to start the elongation kinetics. The ThT fluorescence was observed over 40 h. The ThT signal was measured at 482 nm after excitation at 448 nm in a BMG FLUOstar Omega platereader. Measurements were done every 100 s in cycle 1 to 110 and every 300 s in the following cycles. The fluorescence measurement was set in a ring with 12 points with a diameter of 3 mm.

For the evaluation of the elongation kinetics, the slope in the initial stages of the experiment (i.e., in the time window between 1 and 3 hours after addition of seeds to monomers) was calculated, yielding the rate R. For comparing inhibitory activity between fibril elongation samples containing different seed preparation, we found it imperative to normalize the elongation rate to that of an uninhibited control (R_0), yielding R/R_0 [354]. Some of the constructs exhibited R/R_0 values consistently above 1.0 at low inhibitor concentrations. We normalized these R/R_0 data sets to a value of 1.0 for the lowest inhibitor concentration investigated. The non-normalized R/R_0 data is shown in the SI (SI Figure 2.8-2.11).

The R/R_0 data was fitted to a model of competitive inhibition (FI model), assuming that the inhibitor competes with WT molecules for the fibril end [354]:

$$\frac{R}{R_0} = \frac{K_\mathrm{m} + [\mathrm{M}]}{[\mathrm{M}] + K_\mathrm{m}(1 + \frac{[\mathrm{I}]}{K_\mathrm{i}})}$$

K_m and K_i are the dissociation constants of WT monomer or inhibitor, respectively, binding to the fibril end, and [M] and [I] are the concentrations of WT monomer and inhibitor, respectively. IC50 values were obtained from the fits to the FI model.

In the elongation assay with WT-CC48 capped seeds, 25 µM WT-CC48 were incubated with 25 µM (monomer concentration) pre-formed fibrils overnight at 37 °C, 800 rpm. The seeds were spun down for 1 h at 100,000 xg. The supernatant was discarded, and the pellet resuspended in 20 mM MOPS pH 7.4, 50 mM NaCl supplemented with 20 µM ThT and 0.04% NaN_3. The elongation assay was prepared as described above.

2.6.3 Preparation and SDS-PAGE of soluble and insoluble fractions after elongation assay

After the elongation assay serving as a further control (inhibitor concentrations: 0.5 µM and 5 µM), the soluble and the insoluble fractions were separated by ultracentrifugation at 100,000 xg for 1 h. The supernatant was transferred to a new reaction tube and the pellet resolved in 20 mM MOPS pH 7.4, 50 mM NaCl in a volume equivalent to the volume of the supernatant. The samples were diluted 1:4 with SDS-loading buffer (200 mM Tris-HCl pH 6.8, 400 mM DTT, 8% SDS, 0.4% bromophenol blue, 40% glycerol) followed by 15% tris-glycine SDS-PAGE. PageRuler™ Protein Ladder was used. Gel electrophoresis was performed at 120 V.

2.6.4 Density Gradient Centrifugation (DGC) and SDS-PAGE

The samples from the 96-well plates after the ThT measurements were taken and loaded on a discontinuous sucrose gradient and centrifuged for 3 h at 259,000 xg at 4 °C in a TLS-55 rotor (Beckmann). The sucrose gradient (as described in [375]) contained the following volumes and concentrations (w/w, from bottom to top): 300 µl of 60%, 200 µl of 50%, 200 µl of 25%, 400 µl of 20%, 400 µl of 15%, 150 µl of 10% and 400 µl of 5%. The gradient was layered stepwise in a 11 x 34 mm polyallomer centrifuge tube (Beckmann). After fractionating the gradient, each fraction was diluted 1:6 with SDS-loading buffer (50 mM Tris-HCl pH 7.4, 12% glycerol, 4% SDS, 2% β-mercaptoethanol) and analyzed by 15% tris-glycine SDS-PAGE. PageRuler™ Protein Ladder was used as a marker and the gel electrophoresis was performed at 120 V.

2.6.5 Atomic Force Microscopy (AFM)

AFM images were taken with a Bruker Multimode 8 microscope with ScanAsyst-Air cantilevers using the ScanAsyst PeakForce Tapping Mode in air. 10 µl of the protein solution was applied to a freshly cleaved mica and incubated for 10 min at RT under humified conditions. The sample was washed with 100 µl distilled water five times. Then, the sample was dried using gaseous N_2. The software Gwyddion was used for processing the AFM images.

2.7. Acknowledgments

This project has received funding from the European Research Council under the European Union's Horizon 2020 research and innovation program, grant agreement No. 726368. AP thanks the Jürgen Manchot Foundation for funding. Figures were partially created with BioRender.com.

2.8. Supplementary Information

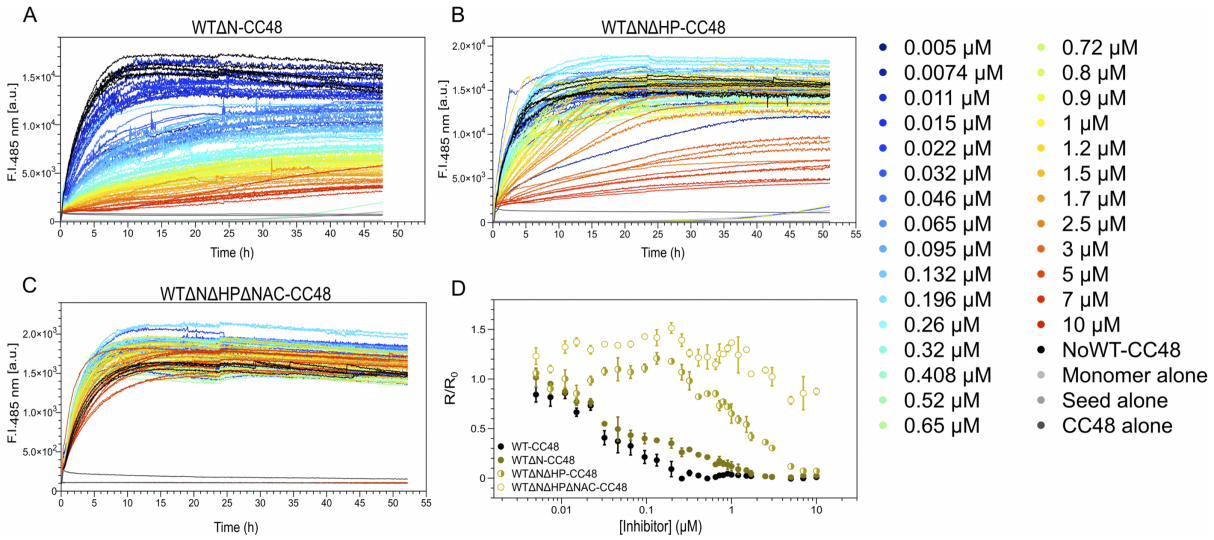

Figure 2.8: Elongation of α-syn in the presence of different WT-CC48 fusion constructs with deleted N-terminal WT regions. Detection of the change in ThT fluorescence with 25 μM of monomeric α-syn incubated in the presence of 2.5 μM pre-formed fibrils under quiescent conditions at pH 7.4. Inhibitors: WTΔN-CC48 (A), WTΔNΔHP-CC48 (B), and WTΔNΔHPΔNAC-CC48 (C). The assay was performed with different inhibitor concentrations from 5 nM to 10 μM shown in a color gradient from blue to red. The negative controls are shown in grey shades and the positive control (NoWT-CC48) in black. (D) Relative rates of fibril elongation (R/R_0) obtained from elongation assays in panels A-C plotted against the inhibitor concentration.

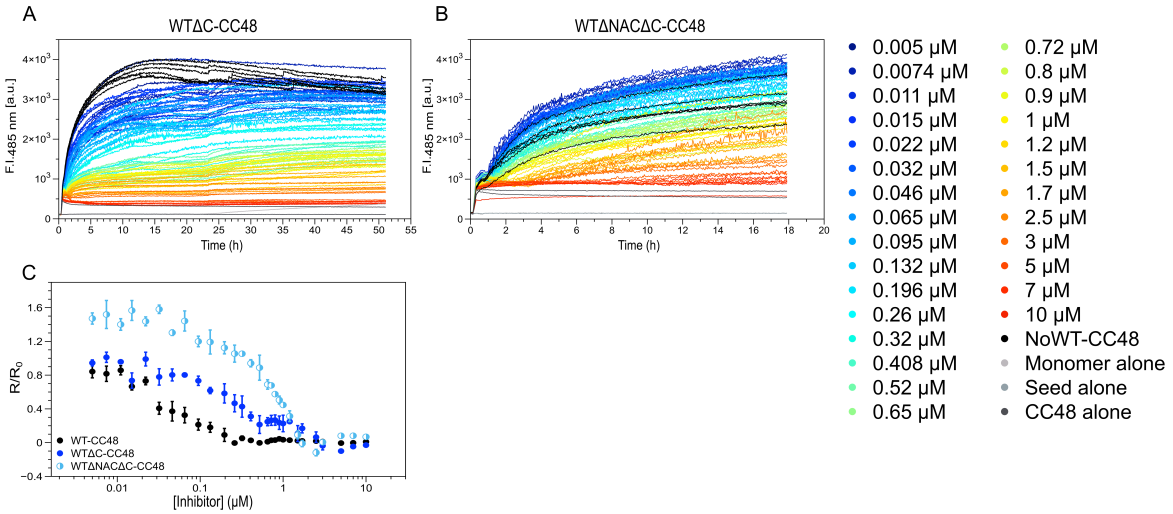

Figure 2.9: Elongation of α-syn in the presence of different WT-CC48 fusion constructs with deleted C-terminal WT regions. Detection of the change in ThT fluorescence with 25 μM of monomeric α-syn incubated in the presence of 2.5 μM pre-formed fibrils under quiescent conditions at pH 7.4. Inhibitors: WTΔC-CC48 (A) and WTΔNACΔC-CC48 (B). The assay was performed with different inhibitor concentration from 5 nM to 10 μM shown in a color gradient from blue to red. The negative controls are shown in grey shades and the positive control (NoWT-CC48) in black. (C) Relative rates of fibril elongation (R/R_0) obtained from elongation assays in panels A and B were plotted against the inhibitor concentration.

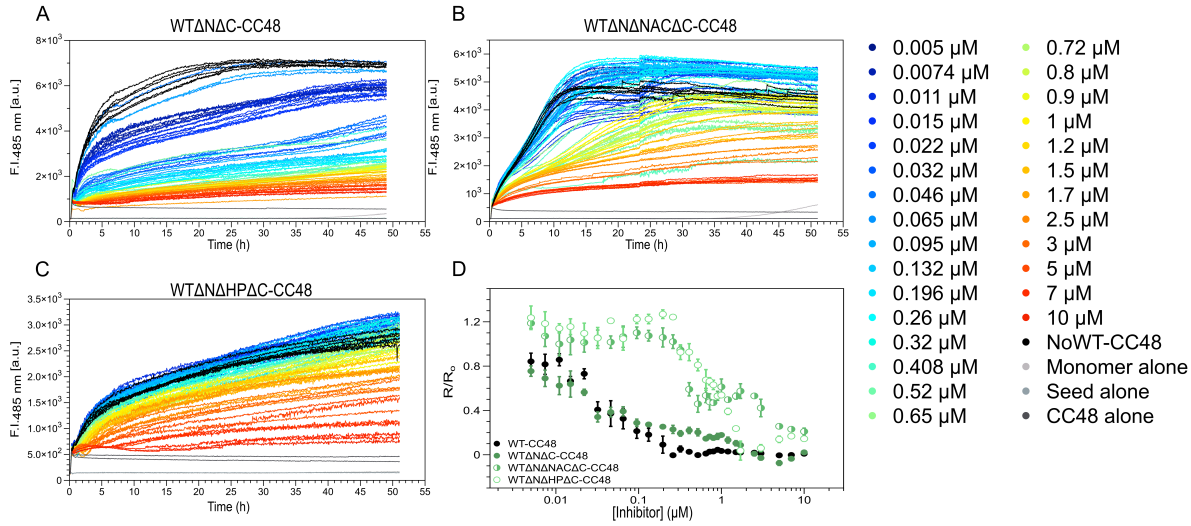

Figure 2.10: Elongation of α-syn in the presence of different WT-CC48 fusion constructs with deleted N-terminal and C-terminal WT regions. Detection of the change in ThT fluorescence with 25 μM of monomeric α-syn incubated in the presence of 2.5 μM pre-formed fibrils under quiescent conditions at pH 7.4. Inhibitors: WTΔNΔC-CC48 (A), WTΔNΔNACΔC-CC48 (B), and WTΔNΔHPΔC-CC48 (C). The assay was performed with different inhibitor concentration from 5 nM to 10 μM shown in a color gradient from blue to red. The negative controls are shown in grey shades and the positive control (NoWT-CC48) in black. (D) Relative rates of fibril elongation (R/R_0) obtained from elongation assays in panels A-C were plotted against the inhibitor concentration.

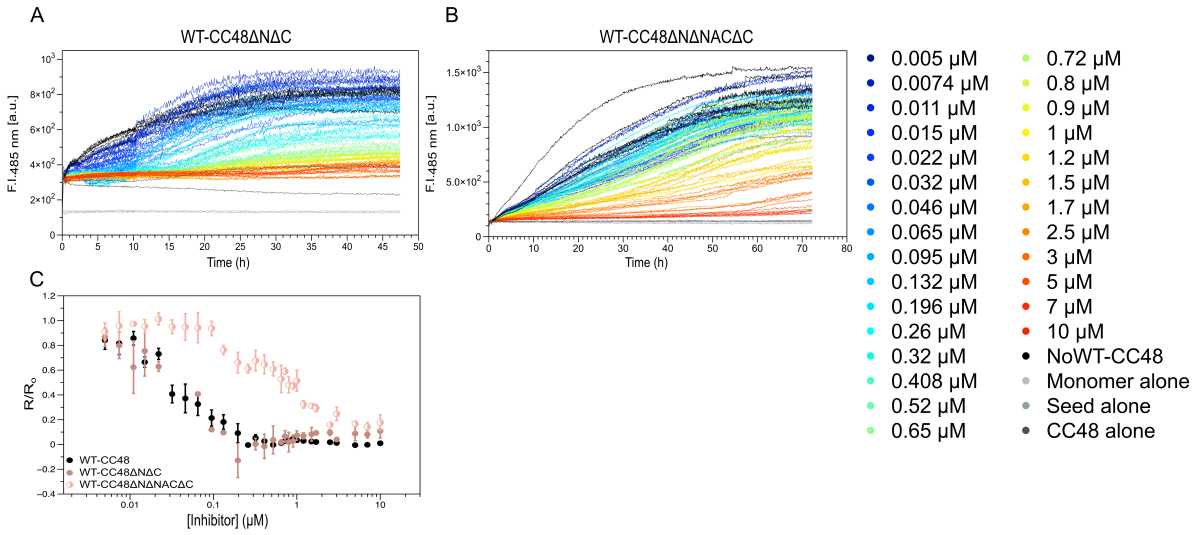

Figure 2.11: Elongation of α-syn in the presence of different WT-CC48 fusion constructs with deleted N-terminal and C-terminal CC48 regions. Detection of the change in ThT fluorescence with 25 μM of monomeric α-syn incubated in the presence of 2.5 μM pre-formed fibrils under quiescent conditions at pH 7.4. Inhibitors: WT-CC48ΔNΔC (A) and WT-CC48ΔNΔNACΔC (B). The assay was performed with different inhibitor concentration from 5 nM to 10 μM shown in a color gradient from blue to red. The negative controls are shown in grey shades and the positive control (NoWT-CC48) in black. (C) Relative rates of fibril elongation (R/R_0) obtained from elongation assays (SI Figures 2.11A-B) were plotted against the inhibitor concentration.

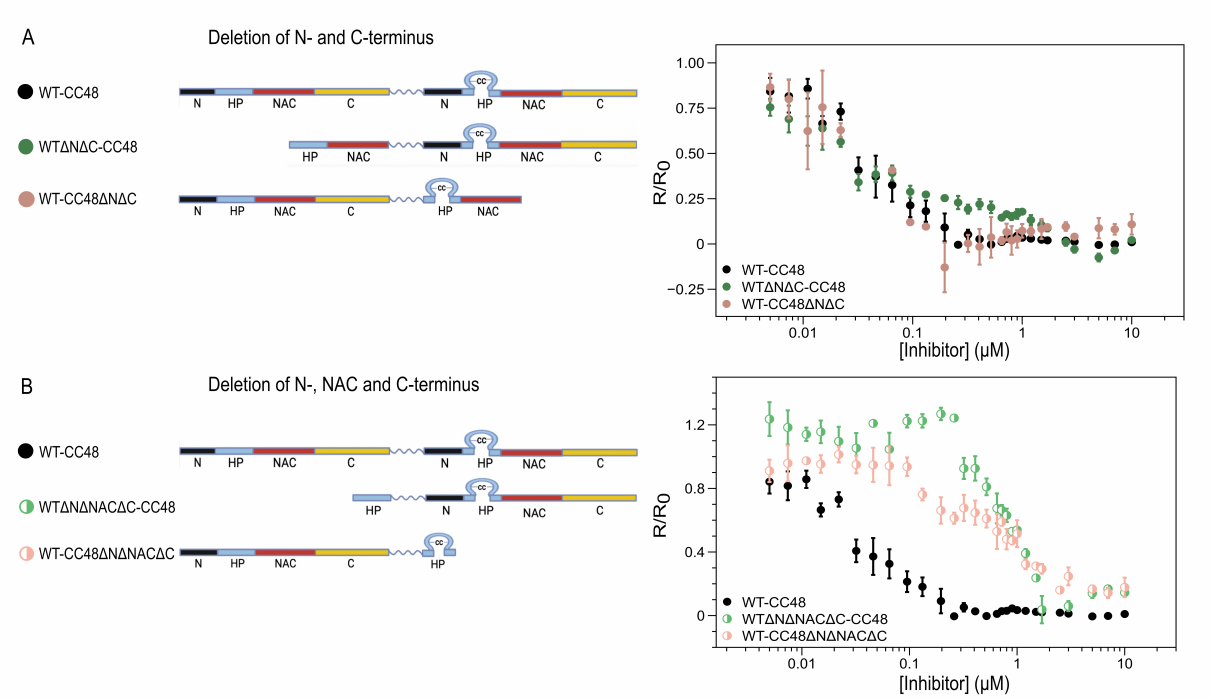

Figure 2.12: Truncation of corresponding regions of α-syn WT and CC48 results in similar inhibition efficiency. Left, Schematic representation of the constructs visualizing the truncation of the N- and C-terminus in either the WT part or the CC48 part (A), as well as the deletion of N-, NAC and C-terminal region in either the WT part or the CC48 part of the fusion construct (B). The different regions of α-syn are displayed in different colors: N-terminus (residues 1-31) in black, hairpin region (residues 32-60) in blue, NAC region (residues 61-95) in pink and the C-terminus (residues 96-140) in yellow. The HP region of the CC48 part is shown as a loop. Right, relative rates of fibril elongation obtained from elongation assays were plotted against the inhibitor concentration.

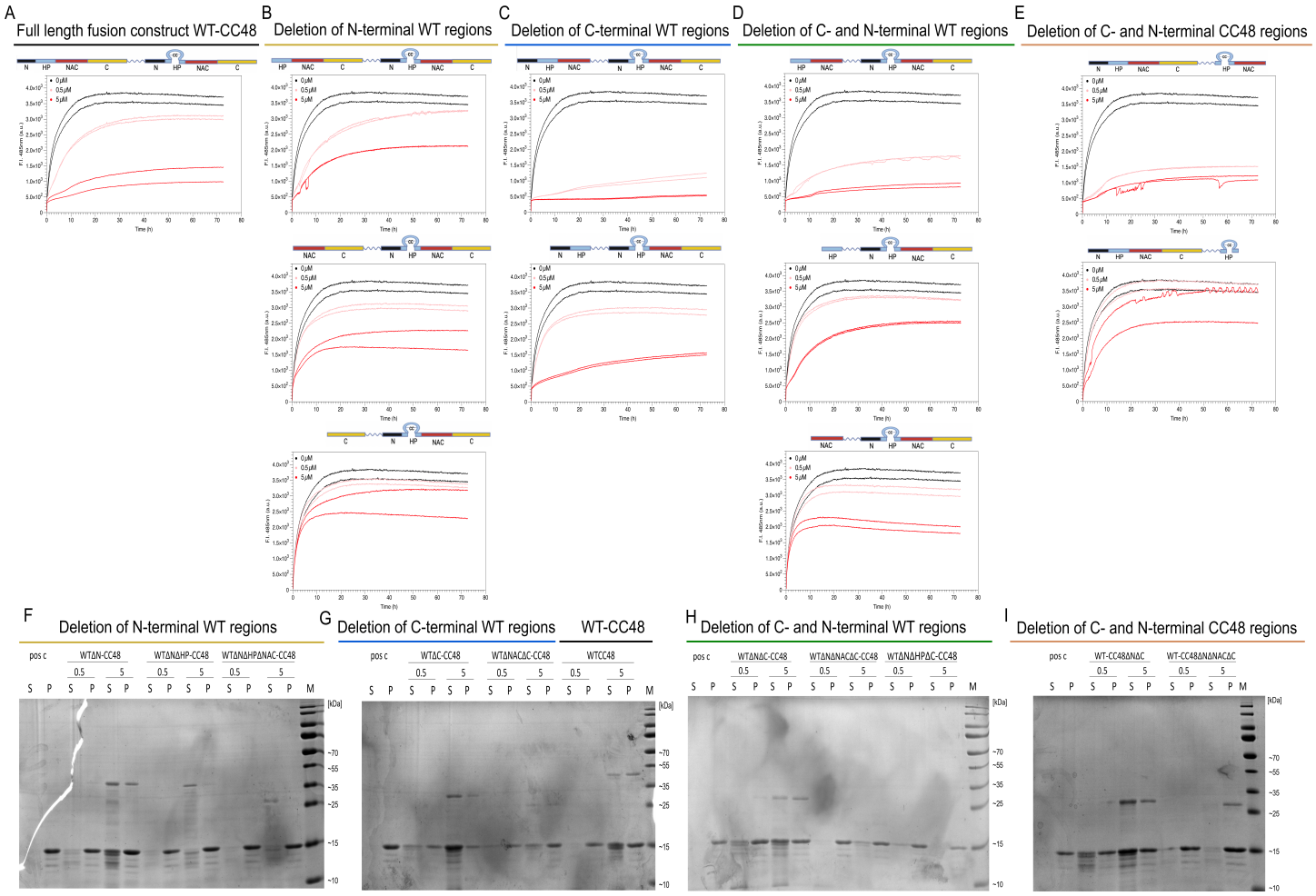

Figure 2.13: Validation of inhibitory potentials of all constructs using the same seed preparation. (A-E) Two concentrations (0.5 µM (light redrosa) and 5 µM (red)) of all constructs were investigated on the same microtiter plate using the same seed preparation in a ThT experiment. Detection of the change in ThT fluorescence using 25 µM of monomeric α-syn incubated in the presence of 2.5 µM pre-formed fibrils under quiescent conditions at pH 7.4 in absence (black) and presence of inhibitors (red shades). The inhibitors are classified in full length WT-CC48 (A), deletion of N-terminal WT regions (B), deletion of C-terminal WT regions (C), deletion of C- and N-terminal WT regions (D) and deletion of C- and N-terminal CC48 regions (E). (F-I) Insoluble vs. soluble fractions *post* aggregation, analyzed by SDS-PAGE (15% tris-glycine gel), denoted S for soluble (supernatant) fractions and P for insoluble (pellet) fractions. M, marker. The inhibitors are classified in deletion of N-terminal WT-regions (F), deletion of C-terminal WT-regions and the full length WT-CC48 (G), deletion of C- and N-terminal WT regions (H) and deletion of C- and N-terminal CC48 regions (I). Alongside all inhibitor samples a positive control (pos c, without inhibitor) is applied on each gel.

3

DISORDERED REGIONS OF INHIBITOR-BOUND α-SYNUCLEIN SUPPRESS THE SEED-INDUCED FIBRIL NUCLEATION IN CELLS

This Chapter reflects content on the following publication.

3.1. Publication information

Author: Celina M. Schulz[a], Emil D. Agerschou[a], Luis Gardon[ab], Miriam Alexander[b], Matthias Stoldt[b], Henrike Heise[ab], Gültekin Tamgüney[ab] and Wolfgang Hoyer[ab]

a: Institut für Physikalische Biologie, Heinrich Heine University Düsseldorf, Düsseldorf, Germany
b: Institute of Biological Information Processing (IBI-7: Structural Biochemistry) and JuStruct: Jülich Center for Structural Biology, Forschungszentrum Jülich, Jülich, Germany

Pre-accepted in: Cell Reports Physical Science (05 August 2024)

3.2. Abstract

In order to inhibit amyloid fibril formation at low compound concentration, higher-ordered protein assemblies such as fibril ends are the usual targets. However, the engineered binding protein β-wrapin AS69 binds monomers of Parkinson's disease-associated α-synuclein (αS), yet achieves inhibition at substoichiometric concentration. The substoichiometric activity was not attributed to the binding protein *per se*, but to its 1:1 complex with αS, in which AS69 sequesters αS residues 30-60 into a globular protein fold whereas other αS parts remain intrinsically disordered regions (IDRs). Here, we investigate AS69-αS fusion constructs which form the AS69:αS complex by intramolecular folding and expose different IDRs. We find that not only the globular part of the complex, but also αS IDRs, are critical for substoichiometric inhibition, which is achieved by interference with primary and secondary fibril nucleation. The effects *in vitro* are reproduced in cellular seeding assays, indicating that secondary nucleation drives seeding in aggregate biosensing.

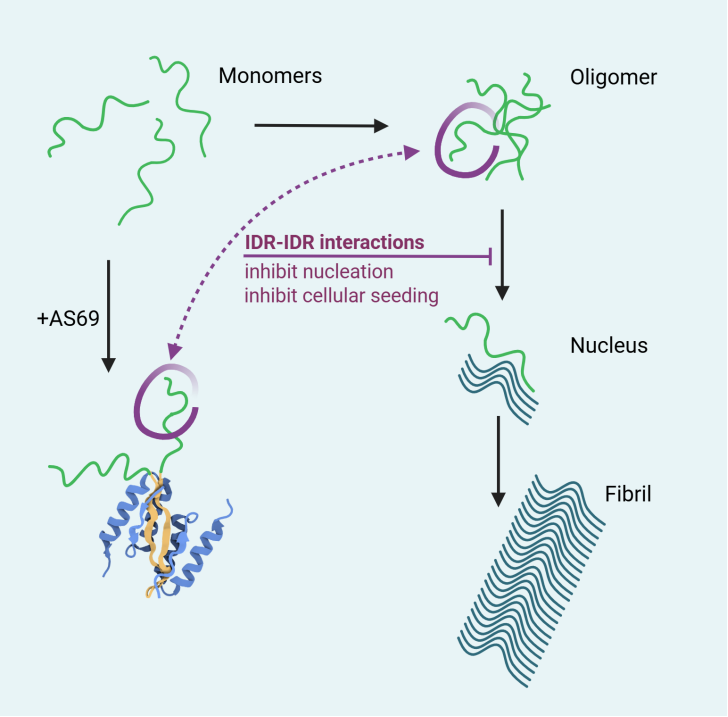

Figure 3.1: Mode of action of AS69:αS. The inhibitor AS69 sequesters monomeric αS into an 1to1 complex. αS IDRs exposed to the complex interact with oligomers on the aggregation pathway towards amyloid fibrils and stabilize the oligomeric form leading to an inhibition of nucleation and cellular seeding.

3.3. Introduction

The formation of amyloid fibrils of the protein αS is involved in Parkinson's diseases (PD), Lewy body dementia, Multiple system atrophy and further synucleinopathies [363, 376]. Amyloid formation is a multistep reaction that in its initial stages passes through a highly unfavorable nucleus state, followed by the energetically favorable addition of monomers to the fibril ends during fibril elongation [11, 124, 125]. In particular the nucleation of amyloid fibrils is difficult to study, owing to its complexity, the short lifetimes of the nuclei, the inherent heterogeneity that is reflected in the polymorphism of the reaction products, and its poor separability from the subsequent reaction steps [126, 137, 138]. Nevertheless, factors that strongly promote amyloid fibril nucleation could be identified which are thought to contribute to amyloid formation and propagation *in vivo*. For example, lipid membranes of specific composition can enhance αS fibril nucleation, depending on the lipid composition and αS concentration at the membrane surface [244, 260]. Furthermore, pre-existing fibrils can catalyze the formation of new fibril nuclei in a process that is termed secondary nucleation, to distinguish it from the primary nucleation which does not involve pre-existing fibrils [131].

Molecules with the capacity to modulate amyloid formation are of great interest as they help to define the mechanism of protein aggregation and inform the development of therapeutic agents [377]. We recently showed that the β-wrapin AS69, an engineered protein binding the αS monomer, acts as a highly potent inhibitor of primary and secondary nucleation and elongation of αS [353]. AS69 is a dimer of two identical subunits covalently linked by a disulfide bond between the Cys-28 residues of both subunits. For inhibition, AS69 induces local folding of the αS region containing residues 37-54 into a β-hairpin conformation in the otherwise intrinsically disordered protein [350] (Figure 3.2(A)). Binding of this αS region can thus inhibit αS aggregation, which has been confirmed by other agents targeting the same αS region, including chaperones [270, 271, 272]. For AS69, inhibition of fibril elongation could be explained by sequestration of αS monomers, which lose the competence to elongate fibrils when incorporated in the AS69 complex [353]. While this inhibitory activity required stoichiometric amounts of AS69, substoichiometric amounts sufficed for inhibition of primary and secondary nucleation, which is remarkable for a monomer binding agent [353]. A fusion construct of AS69 and αS, in which the αS-binding site of AS69 is occupied by the fused αS, showed similar inhibition potency on secondary nucleation as AS69 alone. This indicated that the complex between AS69 and αS is the inhibitory species in secondary nucleation [353]. Here, we determined the αS regions within the AS69:αS complex that assist in substoichiometric inhibition, with the aim to *i.)* better understand how a monomer binder accomplishes inhibition of amyloid fibril nucleation and to *ii.)* gain further insights into the elusive primary and secondary nucleation mechanisms. We generated a set of AS69-αS fusion constructs which form the AS69:αS complex by intramolecular folding and expose different IDRs of αS. Testing the fusion constructs' effects on lipid-induced primary nucleation, secondary nucleation, and fibril elongation *in vitro*, and on seed-induced fibril formation in cells, allowed to *i)* delineate the αS IDRs involved in inhibition of the different reaction steps, and *ii)* identify the critical contribution of nucleation processes to aggregate biosensing.

3.4. Results

3.4.1 Fusion constructs exhibit intramolecular formation of the AS69:αS complexes

We generated a set of six AS69-αS fusion constructs in which two AS69 subunits were fused to one full-length or truncated αS unit (Figure 3.2A, SI Figure 3.10). The three polypeptide (sub)units were

separated by glycine-serine linkers to ensure sufficient conformational flexibility for intramolecular formation of the AS69:αS complex. The construct containing the full-length αS sequence is termed here either AS69-αS or AS69-αS(N-B-NAC-C), as it contains all αS segments, the N-terminus (residues 1-30), the AS69-Binding region (residues 30-60), the NAC region (residues 60-95), and the C-terminus (residues 95-140). The other five constructs lack one or more of these αS segments and are named according to the segments they contain (Figure 3.2A).

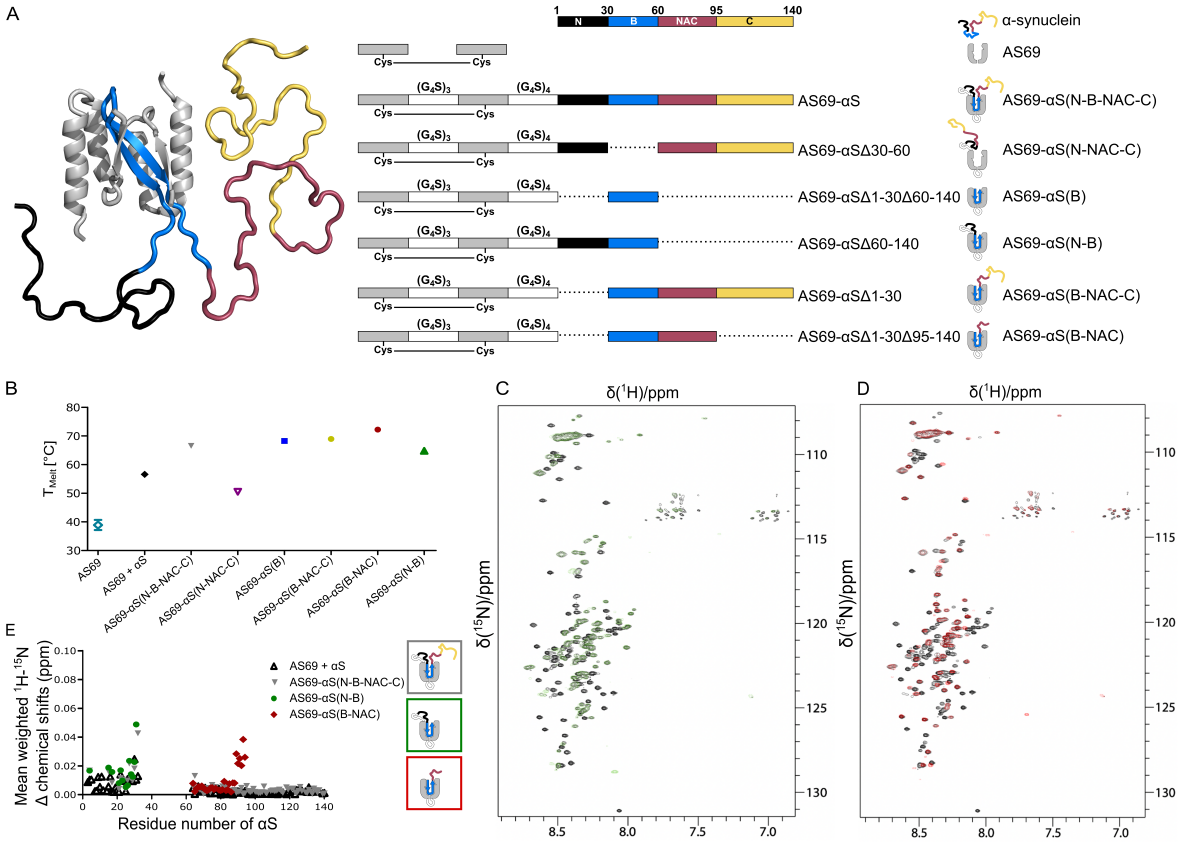

Figure 3.2: AS69-αS fusion constructs to study the role of αS IDRs in inhibition of amyloid formation. (A) Structural model of the AS69:αS complex based on NMR (pdb entry 4BXL [350]). AS69 (grey) is a homodimer linked through a disulfide bridge. αS locally adopts β-hairpin conformation in the AS69-binding region (B, blue), while the other αS regions (N-terminus, black; NAC region, red; C-terminus, yellow) remain intrinsically disordered. Scheme of the primary structure of αS, AS69, and the six AS69-αS fusion constructs investigated, schematic illustration of the conformations of the polypeptide segments in the different constructs and the constructs' nomenclature are given in (A). (B) Melting temperatures of free AS69, the intermolecular AS69:αS complex, and the AS69-αS fusion constructs determined by CD spectroscopy at 222 nm, pH 5.0. Melting curves are shown in SI Figure 3.11. (C,D) ^{1}H-^{15}N HSQC NMR spectra of AS69-αS(N-B) (green, C) and AS69-αS(B-NAC) (red, D) overlaid with the one of full-length AS69-αS(N-B-NAC-C) (black). The spectra were recorded at 10 °C where only the IDR segments but not the complex core are visible. (E) Mean weighted ^{1}H-^{15}N chemical shift changes of αS backbone amides in the intermolecular AS69:αS complex and within AS69-αS fusion constructs compared to the chemical shifts of free αS.

CD and NMR spectroscopy were performed to test if the fusion constructs form the AS69:αS complex. In CD spectroscopy, addition of αS to AS69 results in increased thermostability of AS69 due to coupled

folding-binding [353, 378] (Figure 3.2B, SI Figure 3.11). The melting temperature (T_{Melt}) of the AS69-αS fusion is another 10-15 °C higher than that of the mixture of AS69 and αS, indicating that intramolecular complex formation within the fusion construct is facilitated compared to intermolecular complex formation [353]. Almost all fusion constructs with truncations in the αS segment have thermostabilities similar to that of full-length AS69-αS, with melting temperatures in in the range of 65-72 °C (Figure 3.2B, SI Figure 3.11). The one exception is AS69-αS(N-NAC-C) with a melting temperature of 51 °C. This construct lacks the AS69-binding region of αS and is therefore unable to form the AS69:αS complex. The CD data demonstrates that the intramolecular AS69:αS complex is established in all fusion constructs that contain the AS69-binding region of αS.

In ^{1}H-^{15}N HSQC NMR spectroscopy performed at 10 °C, the globular core of the AS69:αS complex is invisible due to intermediate exchange, leaving only IDRs of αS visible [350]. This observation is recovered for the fusion constructs (Figure 3.2C and D, SI Figures 3.12 and 3.13). The N, NAC, and C segments of the αS units within the fusion constructs did not show any significant shift changes compared to free αS (Figure 3.2C-E, SI Figures 3.12 and 3.13), indicating that intramolecular complex formation does not have a great impact on the flexible conformation of the αS segments that remain intrinsically disordered. By increasing the temperature to 30 °C, the globular core of the AS69:αS complex becomes visible in ^{1}H-^{15}N HSQC NMR spectroscopy as a set of well-dispersed resonances [350]. The resonances of the intermolecular AS69:αS complex are reproduced by all fusion constructs that contain the AS69-binding region of αS (SI Figure 3.12B). Collectively, the CD and NMR data demonstrate that these fusion constructs form the globular core of the AS69:αS complex in an intramolecular fashion and present the N, NAC and/or C segments of αS as IDRs attached to this core. The conformations of the segments in the different constructs are schematically illustrated in Figure 3.2A.

3.4.2 Validation of the secondary nucleation assay

We tested the effects of the fusion constructs on three individual steps of the aggregation reaction: lipid-induced primary nucleation, secondary nucleation and fibril elongation. To investigate primary nucleation of αS, an assay employing 1,2-dimyristoyl-sn-glycero-3-phospho-L-serine (DMPS) small unilamellar vesicles (SUVs) as a nucleation trigger has been established as a model of lipid-induced αS aggregation, which might represent the main source of primary αS fibril nuclei *in vivo* [244]. For fibril elongation, highly-seeded assays were performed at neutral pH, resulting in fibrils with lengths in the µm range [135].

With regard to secondary nucleation, *in vitro* studies have shown that this process is dominant in αS aggregation at slightly acidic pH values and under low-seeded conditions, resulting in rather short fibrils [135, 379]. However, limited reproducibility of secondary nucleation assays can pose a challenge. To avoid fragmentation and primary nucleation, the acidic pH should be coupled to quiescent conditions and low concentrations of pre-formed fibrils [155, 380]. We recently devised a secondary nucleation protocol to study how AS69 inhibits secondary nucleation of αS [353]. This method gave very consistent kinetic traces within a single seed preparation, and consistently resulted in the characteristic steep and asymmetric sigmoidal growth curve as measured by *in situ* fluorescence of the amyloid specific dye Thioflavin T (ThT) [381, 382]. Furthermore, we observed the same characteristic inhibition effects using different seed preparations [353]. However, this required normalization as the absolute rates varied considerably between different seed preparations. The normalization was done by dividing the maximal observed growth rate of a sample, r_{max}, by the maximal observed growth rate of uninhibited controls, $r_{max,0}$, which were run alongside the samples. In the present study, we wanted to further improve the assay to yield more consistent absolute rates. As we observed previously, the secondary nucleation kinetics data was very variable when different seed preparations (prepared under the same conditions) were used (SI

Figure 3.14). We therefore prepared several seed samples in parallel (from the same initial solution of monomers) and tested them in a pre-run of the secondary nucleation assay (SI Figure 3.14). For the final secondary nucleation assays, seed preparations showing homogenous sigmoidal shapes in the pre-runs were chosen. This yielded increased reproducibility of absolute rates in the secondary nucleation kinetics data (SI Figure 3.14).

In order to validate that the assay is indeed reporting on secondary nucleation, an experiment with varying monomer concentration was performed (Figure 3.3). At monomer concentrations below 50 µM no exponential increase in fluorescence was observed, indicating no secondary nucleation-triggered formation of amyloid fibrils, probably due to the limited amount of monomers to form precursors on the fibril surface during secondary nucleation. At the same time, an excess of monomers, above about 80 µM, did not increase the aggregation rate, suggesting that at this concentration the fibril surface of the added 0.3 µM fibril seeds (concentration in monomer units) is saturated. Only in the monomer concentration range from 50 to 80 µM a pronounced monomer-dependent sigmoidal curve was detected. These data are in strong agreement with theoretical simulations of the process [131]. For the subsequent secondary nucleation assays, concentrations of 0.3 µM fibril seeds and 70 µM monomer were applied.

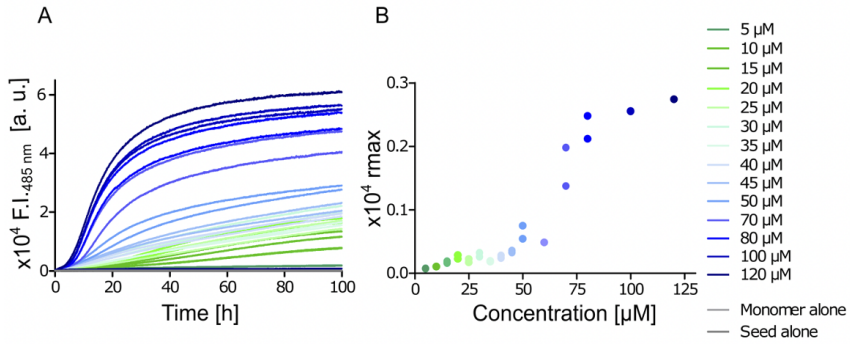

Figure 3.3: Validation of secondary nucleation assay at pH 5.0. (A) Detection of the change in ThT fluorescence when different concentrations of monomeric αS were incubated in the presence of 0.3 µM pre-formed fibrils under quiescent conditions. (B) Relative rates of secondary nucleation (r_{max}) plotted against monomer concentration.

3.4.3 The complex of AS69 and αS inhibits fibril nucleation at substoichiometric concentration by interacting with αS oligomers

The inhibitory potential of AS69-αS on elongation, lipid-induced primary nucleation, and secondary nucleation was compared to that of AS69 (Figure 3.4). For inhibition of fibril elongation, stoichiometric amounts of AS69 were required, as previously reported [353] (Figure 3.4A). This can be explained by sequestration of αS, which cannot be incorporated into the fibril end when bound to AS69. In contrast, AS69-αS does not inhibit fibril elongation, in line with pre-occupation of the AS69 binding site with the fused αS (Figure 3.4A). This interpretation is supported by the restoration of inhibition only for the one fusion construct that lacks the part of αS that binds to AS69 (AS69-αS(N-NAC-C)), which renders the AS69 part of this construct capable of sequestering free αS as confirmed by T_{Melt} measurements (SI Figures 3.15-3.17).

In DMPS SUV-induced primary nucleation at pH 6.5, αS fibril nuclei are formed on the lipid surface and grow exclusively by elongation into long fibrils [244] (Figure 3.4B). To reduce the rate of lipid-induced primary nucleation to 50% (i.e., $r_{max}/r_{max,0} = 0.5$), a 1:10 ratio of inhibitor to αS monomer was required for both AS69 and AS69-αS (Figure 3.4B, SI Figure 3.18). αS fibril amplification by secondary nucleation at low pH results in short fibrils (Figure 3.4C, SI Figure 3.19). As for primary nucleation, AS69 and AS69-αS showed similar effects, in this case with a 1:50 ratio of inhibitor to αS monomer required for 50% inhibition (Figure 3.4C, SI FIgure 3.19). The activity of AS69-αS, with its pre-occupied αS binding site in the AS69 part, in the primary and secondary nucleation assays indicates that the free binding site of AS69 is not involved in inhibition of nucleation processes. Instead, it is the 1:1 complex of AS69 and αS that exerts the inhibitory activity.

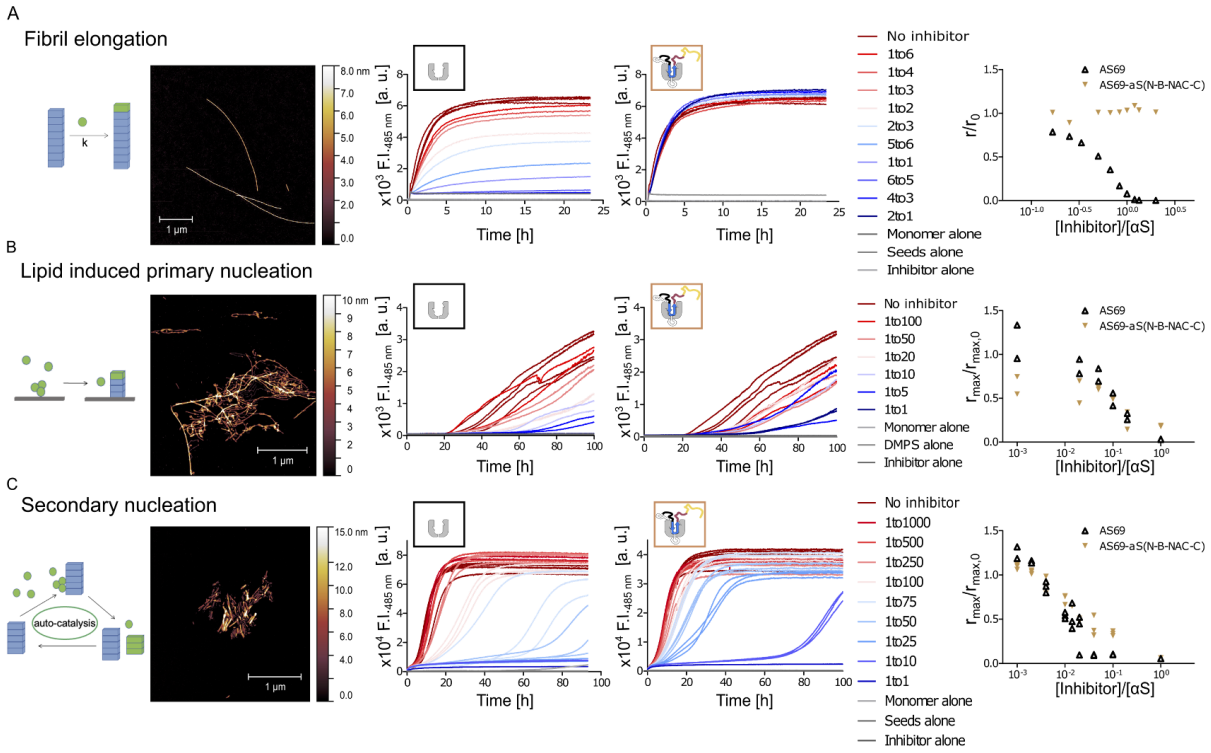

Figure 3.4: Fusion of αS to AS69 has different consequences for inhibition of fibril elongation (A), lipid-induced primary nucleation (B) and secondary nucleation (C). From left to right: (*i*) Schematic overview of the individual reaction step investigated; (*ii*) AFM of fibrils generated in the different aggregation assays; (*iii*) and (*iv*) ThT fluorescence time traces of the aggregation assays in presence of different concentrations of AS69 (*iii*) or AS69-αS(N-B-NAC-C) (*iv*), including indicated controls; (*v*) relative aggregation rates compared to uninhibited control. Conditions: (A) fibril elongation, 25 µM monomeric αS was incubated in the presence of 2.5 µM pre-formed fibrils under quiescent conditions, pH 7.4; (B) lipid-induced primary nucleation, 70 µM monomeric αS was incubated in the presence of 70 µM DMPS SUV under quiescent conditions, pH 6.5; (C) secondary nucleation, 70 µM monomeric αS was incubated in the presence of 0.3 µM pre-formed fibrils under quiescent conditions, pH 5.0. The different inhibitor-to-monomer ratios used in each assay are shown in a color gradient from red to blue. Negative controls are shown in grey shades and the positive control (NoAS69) in dark red.

The substoichiometric activity requires an interaction of AS69-αS with higher order αS assemblies. For example, AS69-αS might bind to pre-nucleus oligomers and prohibit their conversion to amyloid fibrils. We applied sucrose density gradient centrifugation (DGC) to analyze the size distribution of

αS species at the end of aggregation assays in absence and presence of AS69-αS (Figure 3.5A). DGC allows to separate αS monomers, oligomers, and larger species such as fibrils or condensates (Figure 3.5B) [291]. αS monomers were localized in the upper DGC fractions 1-4 (Figure 3.5C). At the end of the secondary nucleation assay in absence of AS69-αS, the majority of αS was found in the lower DGC fractions 12-14, reflecting the formation of amyloid fibrils (Figure 3.5D). In addition, monomers were still detectable in fractions 1-4, but no oligomeric species between fractions 4 and 12. When the secondary nucleation assay was carried out in presence of increasing concentrations of AS69-αS, the formation of large aggregates localizing to the low DGC fractions was essentially abrogated (Figure 3.5E-G), in agreement with the low ThT fluorescence intensity (Figure 3.5A). Instead, increasing αS amounts were found in the intermediate fractions 5-8, reflecting the population of oligomeric states. According to the band intensity in SDS-PAGE, the amount of αS within these oligomers was much lower than the amount of αS monomers (Figure 3.5E-G) and also much smaller than the amount of fibrillar αS in the assay performed in the absence of AS69-αS (Figure 3.5D). AS69-αS colocalized with αS in the oligomer fractions 5-8. These findings suggest that AS69-αS inhibits fibril nucleation by interacting with αS oligomers, which leads to stabilization of low amounts of oligomers. The SDS band intensities for the sample at a 1:5 inhibitor:substrate ratio allowed to compare the partitioning of αS and AS69-αS into monomer and oligomer states (Figure 3.5G). αS and AS69-αS exhibited similar monomer:oligomer distributions, indicating similar propensities to integrate into oligomers.

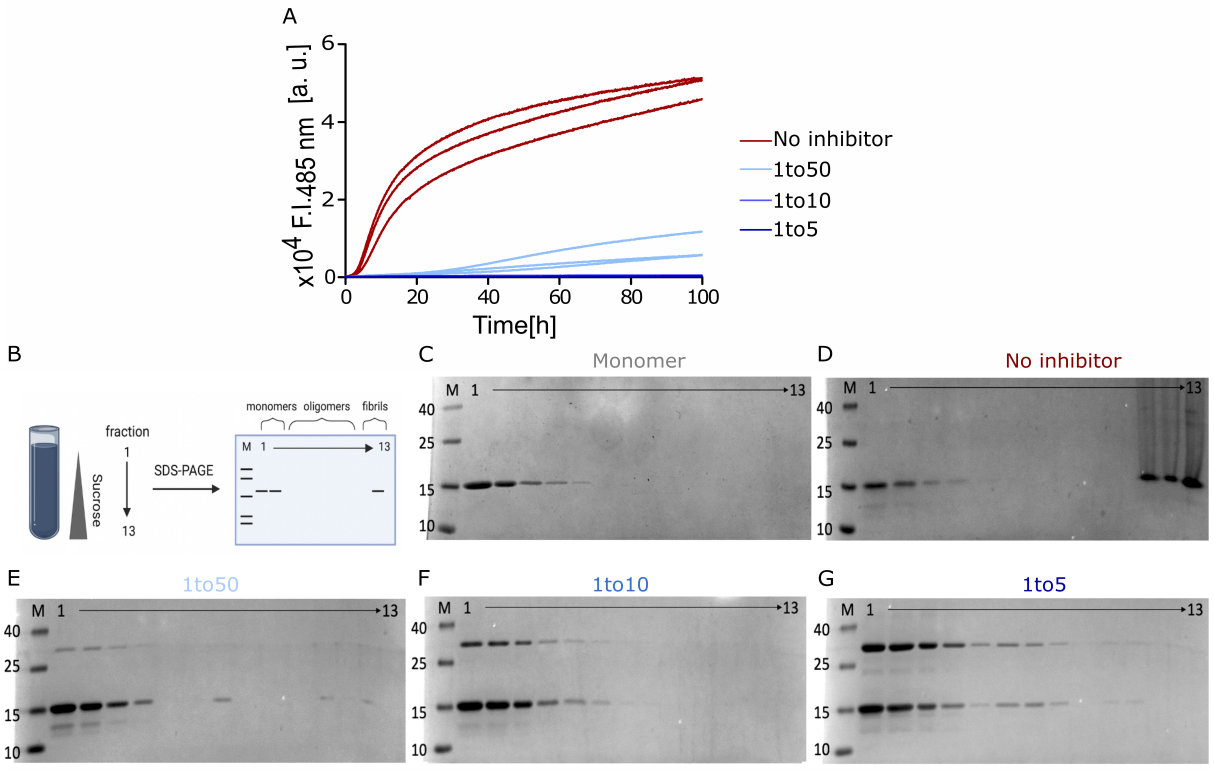

Figure 3.5: AS69-αS inhibits fibril nucleation by interacting with αS oligomers. (A) ThT fluorescence time traces of secondary nucleation assays in presence of different concentrations of AS69-αS(N-B-NAC-C). (B) Schematic of the DGC assay. (C) Tris/Tricine SDS-PAGE gels show the distributions of αS and AS69-αS(N-B-NAC-C) within the DGC gradients from left to right corresponding to the fractions from top to bottom of each gradient. Monomeric proteins are found in the top (left) fractions, oligomers in the middle fractions, and fibrils in the bottom (right) fractions.

3.4.4 αS IDRs of AS69-αS are required for nucleation inhibition

To gain insight into how the 1:1 complex of AS69 and αS inhibits nucleation processes, we next tested the inhibitory potential of the set of AS69-αS fusion constructs on lipid-induced primary nucleation and secondary nucleation. In the fusion constructs, the AS69:αS complex is pre-formed (with the exception of AS69-αS(N-NAC-C) lacking the binding region) and different (or no) IDRs of αS are exposed on the exterior of the globular part of the complex.

The construct AS69-αS(B), in which all αS IDRs are deleted, does not exhibit substoichiometric inhibition of nucleation. This demonstrates that αS IDRs, although not directly taking part in binding to AS69, are involved in substoichiometric inhibition of nucleation processes (Figure 3.6A, SI Figures 3.18 and 3.19). The fusion construct where the N-terminus of αS had been removed (AS69-αS(B-NAC-C)) was inhibiting both lipid-induced primary nucleation and secondary nucleation as strongly as AS69 (Figure 3.6B, SI Figures 3.18 and 3.19), showing that the N-terminal IDR is not required for inhibition of nucleation. Additional truncation of the C-terminus (AS69-αS(B-NAC)) did also not reduce the inhibitory activity (Figure 3.6B). Thus, the presence of the NAC IDR exposed on the globular part of the AS69:αS is sufficient for substoichiometric inhibition of fibril nucleation. Interestingly, the construct AS69-αS(N-B), lacking the NAC IDR, showed substoichiometric inhibition of secondary nucleation but not lipid-induced primary nucleation (Figure 3.6C, SI Figures 3.18 and 3.19). This demonstrates that the two nucleation processes have different susceptibilities with the regard to the presence of αS IDRs. For inhibition of secondary nucleation, the presence of either the NAC IDR or the N-terminal IDR is sufficient. In contrast, inhibition of lipid-induced primary nucleation strictly requires the presence of the NAC IDR.

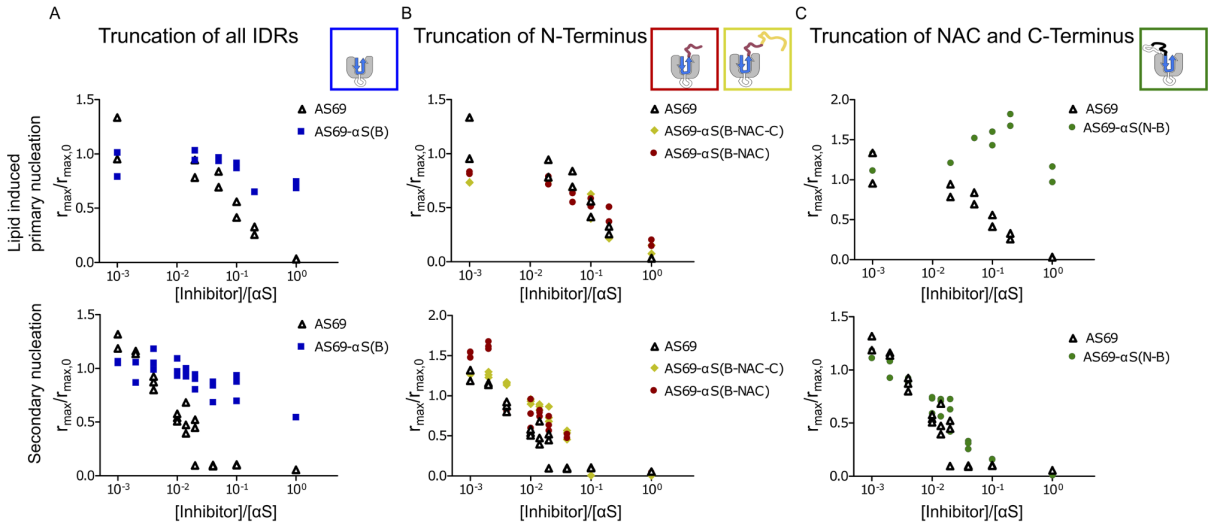

Figure 3.6: Truncated versions of the AS69-αS fusion inhibit primary and secondary nucleation. Relative rates of lipid-induced primary nucleation (upper row) and secondary nucleation (lower row) with increasing concentration of truncated versions of AS69-αS(N-B-NAC-C) fusion constructs (inhibitor) in dependence on the inhibitor-to-monomer ratios. Data is shown for truncation of all IDRs (A), of N-terminal IDR (B), and of NAC and C-terminal IDRs (C). The time traces used to derive the relative rates are shown in SI Figures 3.18 and 3.19.

3.4.5 αS IDRs act in concert with the globular AS69:αS domain

It is noteworthy that inhibition requires the parts of αS that are not interacting with AS69 to accomplish inhibition of primary and secondary nucleation. It was therefore of interest to investigate if these IDRs could have inhibitory effects on their own without AS69 altogether. For this reason, we investigated whether αS fragments would be able to accomplish inhibition of primary and secondary nucleation on their own or fused to the linker employed in the fusion constructs. The fragments *i.)* N-terminus without AS69 binding site (αS(1-37), or in domain notation αS(N-$B_{aa31-37}$)) and *ii.)* N-terminus without AS69 binding site containing $(G_4S)_4$-linker ($(G_4S)_4$-αS(N-$B_{aa31-37}$)), *iii.)* αS(NAC-C), and *iv.)* αS(N-NAC-C) were investigated as peptides without fusion to AS69 (Figure 3.7).

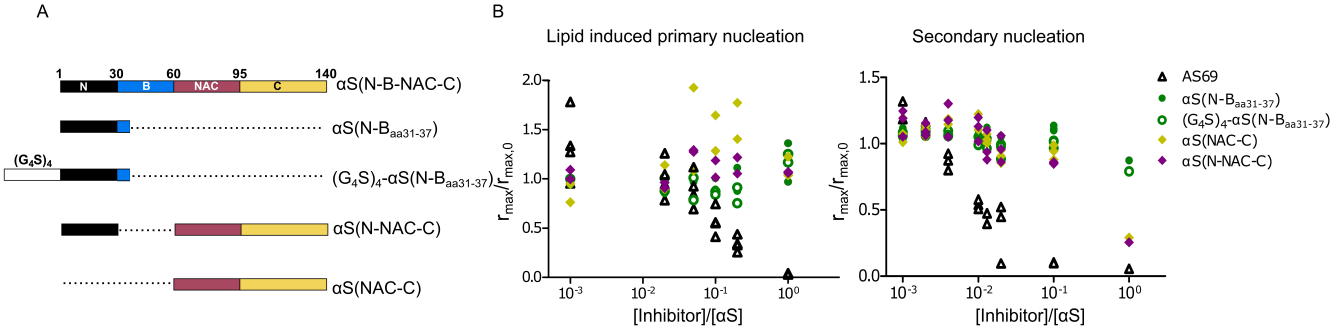

Figure 3.7: Effects of truncated versions of αS on nucleation of full-length αS. (A) Schematic overview of the sequence of αS and the four truncated versions investigated. (B) Relative aggregation rates of lipid-induced primary nucleation and secondary nucleation with increasing concentration of truncated versions of αS monomers (inhibitor) are plotted against the inhibitor-to-monomer ratios. The time traces used to derive the relative rates are shown in SI Figures 3.20 and 3.21.

Hardly any inhibition of primary or secondary nucleation was observed for the N-terminal peptides with and without the linker (Figure 3.7, SI Figures 3.20 and 3.21). Hence, the N-terminal IDR on its own is not sufficient to accomplish inhibition but needs to be in complex with AS69 for inhibitory activity. For the fragments including the NAC and C regions, no inhibition of primary nucleation but some inhibition of secondary nucleation was observed (Figure 3.7). Inhibition of secondary nucleation occurred at stoichiometric inhibitor concentrations and was therefore weaker than that of the corresponding AS69 fusions. In conclusion, the substoichiometric inhibition of the AS69-αS fusions was not observed for the corresponding isolated αS IDR fragments, which shows that αS IDRs act in concert with the globular part of the AS69:αS complex in inhibition of fibril nucleation.

3.4.6 The constructs' potency to inhibit seed-induced aggregation in cells correlates with their potency to inhibit fibril nucleation

The transmission of protein aggregates to cells that express fluorescent monomeric proteins is a method to determine the seeding activity of aggregates. The emergence of fluorescent puncta indicates that aggregates converted the monomeric substrates to an aggregated state. Such biosensor cell assay can for example be applied to test the ability of compounds to interfere with aggregate spreading. Here, we tested the ability of the AS69-αS fusion constructs to interfere with seeding in HEK cells expressing YFP-labeled αS containing the A53T mutation (Figure 3.8A). αSA53T occurs in familial PD and is more

aggregation-prone than wildtype αS.

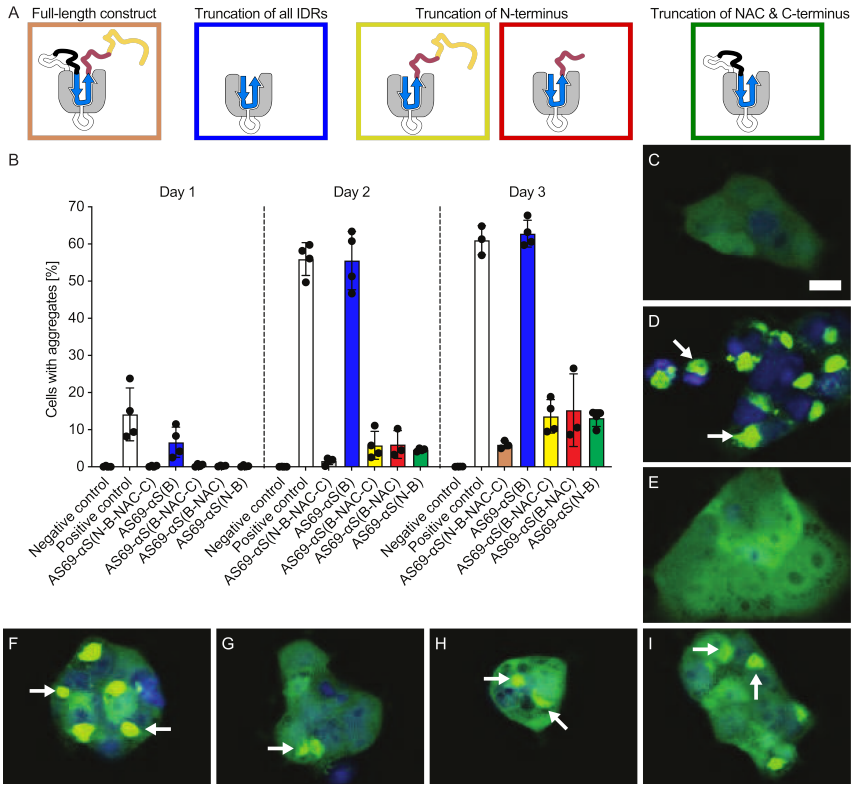

Figure 3.8: N- or C-terminal IDRs of αS confer AS69-mediated inhibition of seeding. The ability of AS69-bound wildtype and deletion mutants of αS (A) were tested to inhibit seeded aggregation of αS in αSA53T-YFP cells (B), which stably express human αS with the familial A53T mutation fused to YFP in HEK293T cells and allow fluorescence-based detection of αS aggregates, which appear as highly fluorescent intracellular puncta after seeding. Bars indicate standard deviation. In contrast to unseeded cells (negative control), which showed only a diffuse fluorescence signal (C) three days after seeding, cells seeded with αS fibrils (positive control) accumulated intensely fluorescent αS aggregates, as indicated by white arrows (D). Full-length αS bound to AS69 (AS69-αS(N-B-NAC-C), orange) completely inhibited cellular αS aggregation (E), whereas αS lacking all IDRs bound to AS69 (AS69-αS(B), blue) failed to inhibit αS aggregation (F). Deletion mutants of αS that still retained some IDRs, including those that retained the NAC and/or C-terminus, AS69-αS(B-NAC-C) (yellow, G), NAC AS69-αS(N-B-NAC-C) (red, H), or only the N-terminus AS69-αS(N-B) (green, I), were still able to inhibit αS aggregation. Nuclei were stained blue with Hoechst 33342. The scale bar in (C) is 20 µm and applies to all cell images.

When αS fibril seeds prepared *in vitro* were added to the cells, >50% of the cells showed emergence of fluorescent puncta over the course of three days, which were absent when no seeds were added (Figure 3.8B-D, positive vs. negative control). Addition of AS69-αS(N-B-NAC-C) strongly inhibited seeded aggregation (Figure 3.8B,E), in line with its effects on fibril nucleation *in vitro*. AS69-αS(B-NAC-C), AS69-αS(B-NAC) and AS69-αS(N-B), the three other constructs that inhibited secondary nucleation *in vitro*, were also effective at inhibition of cellular seeding (Figure 3.8B,G-I). In contrast, AS69-αS(B), which did not inhibit fibril nucleation *in vitro*, did also not inhibit cellular seeding (Figure 3.8B,F). The correlation of the inhibitory effects on nucleation *in vitro* and on cellular seeding suggest that aggregate proliferation in biosensor cells is not just a consequence of fibril seed elongation, but involves secondary

nucleation of amyloid fibrils on the surface of the added seeds.

As recombinant proteins transfected into cells, AS69-αS and its variants are expected to be degraded relatively quickly. However, they inhibit seeded aggregation over the course of three days. We did not analyze the time-dependent concentrations of intact proteins. Due the substoichiometric activity low concentrations of the inhibitors may suffice to inhibit seeded aggregation. Furthermore, in the cell assay compounds were co-transfected with fibril seeds and might have been stabilized by attaching to the seeds, possibly at the critical sites of secondary nucleation, already before entering the cellular milieu.

3.5. Discussion

Due to the complexity of protein aggregation mechanisms, inhibitors can act in various ways [335, 383]. β-wrapin AS69 is an engineered binding protein that sequesters the αS region containing amino acids 30-60 by inducing a local β-hairpin conformation while the other regions of αS remain intrinsically disordered [350]. The mechanisms of inhibition of αS aggregation and the involved αS regions identified in this work are schematized in Figure 3.9. Sequestration of αS monomers into the AS69:αS complex leads to stoichiometric inhibition of fibril elongation. Upon formation of the 1:1 AS69:αS complex, substoichiometric inhibitory activity is gained that specifically targets fibril nucleation processes. For this inhibitory activity, two components are required: First, the globular part of the AS69:αS complex, including the region αS(30-60), is essential. This is demonstrated by the loss of inhibitory activity in αS fragments that are not fused to AS69. Second, the presence of αS IDRs is essential for substoichiometric inhibition. Interestingly, lipid-induced primary nucleation and secondary nucleation exhibit a difference in the required IDRs. While inhibition of secondary nucleation can be enabled by either the N-terminus or the NAC region, inhibition of lipid-induced primary nucleation strictly necessitates the NAC region. The minimized active fusion constructs identified here are therefore AS69-αS(B-NAC) for primary nucleation and AS69-αS(B-NAC) or AS69-αS(N-B) for secondary nucleation, respectively (Figure 3.9).

The mechanism of inhibition of fibril elongation by monomer sequestration is easy to comprehend, considering that the αS-B region, which is an essential part of the αS fibril core [92, 276, 278, 384], is not available anymore for incorporation into the fibril structure upon binding to AS69. In line with this, AS69-αS, with pre-occupied αS binding site, does not inhibit fibril elongation (Figure 3.4).

In contrast, the substoichiometric activity of the AS69:αS complex on fibril nucleation is more challenging to elucidate. DGC of secondary nucleation assay samples detects low levels of oligomers from both αS and AS69-αS when fibril formation is abrogated (Figure 3.5E-G). αS and AS69-αS exhibit similar propensities to integrate into oligomers (Figure 3.5G), suggesting a scenario in which AS69-αS co-integrates with αS into pre-nucleus oligomers, whose further conversion into fibril nuclei is then hampered due to the presence of the AS69-bound αS-B region. This scenario is in line with the observation that the NAC IDR can enable inhibition of both lipid-induced primary and secondary nucleation. The NAC region is the most hydrophobic segment of αS and critical for αS self-assembly [234, 385]. The NAC IDR exposed on the AS69:αS complex might therefore drive the co-integration into αS pre-nucleus oligomers. But how does AS69-αS co-integrated into pre-nucleus oligomers prohibit their conversion into fibril nuclei? The AS69-bound αS-B region is critical for the substoichiometric inhibitory activity, as αS fragments without this region do not exhibit this activity (Figure 3.7). The AS69-bound αS-B region might act in different ways: *i.)* as in the case of elongation, it is not available anymore for incorporation into the fibril structure, which will prohibit formation of a seeding-competent fibril nucleus; *ii.)* the globular complex of AS69 and αS-B represents a steric bulk that might interfere with well-ordered assembly of other αS chains; *iii.)* the globular complex of AS69 and αS-B might also,

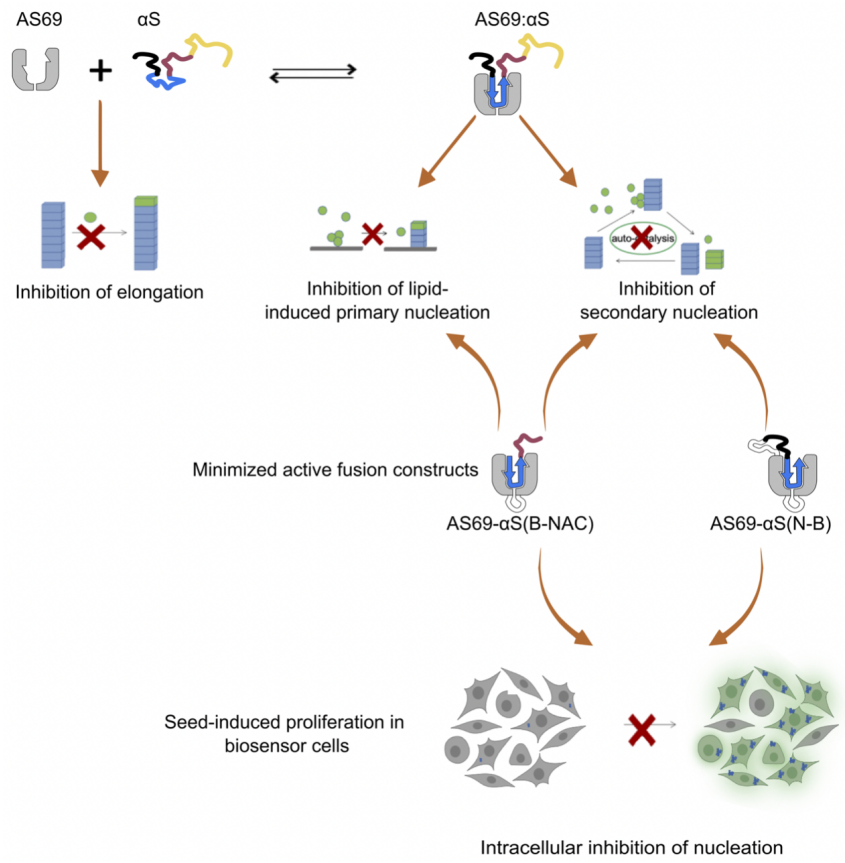

Figure 3.9: Schematic overview of the inhibitory effect of the complex between AS69 and αS on amyloid formation. AS69 binds free αS monomer and inhibits elongation, whereas the complex between AS69 and αS inhibits nucleation processes. Shown are the minimal fusion constructs that achieve substoichiometric inhibition of αS fibril nucleation and of aggregate seeding in biosensor cells.

more actively, engage in a direct interaction with other parts of pre-nucleus oligomers; *iv.)* AS69 binding to αS-B might alter the conformational ensembles of αS IDRs in subtle ways, i.e., with only minute resonance changes in ^{1}H-^{15}N HSQC NMR spectroscopy (Figure 3.2C-E), such as the modulation of transient long-range interactions [386, 387]. Together, the AS69-bound αS-B region and the αS-N and/or NAC IDRs achieve a remarkable substoichiometric activity, with one AS69-αS molecule sufficient to achieve 50% suppression of secondary nucleation at a 50-fold excess of αS monomers (Figure 3.4C). This is striking when considering that the nucleus size will likely be much smaller than 50 αS units. A potential explanation would be a particularly high propensity of AS69 αS to partition into pre-nucleus oligomers, i.e., an enrichment of AS69 αS in pre-nucleus oligomers in comparison to αS. However, this is not supported by the DGC data, which indicates similar propensities of AS69 αS and αS for integration into oligomers. We therefore propose an alternative explanation: Oligomers containing AS69 αS might not just be unable to convert into fibril nuclei themselves, but they might also gain an inherent activity to inhibit fibril nucleation. This activity, resulting in substoichiometric inhibition of secondary nucleation, has been observed before for off-pathway oligomers in other amyloid systems and has been attributed to the blocking of secondary nucleation sites on the fibril surface by the oligomers [185]. Together, the inability of AS69-αS-containing oligomers to convert to fibril nuclei and an active role of these oligomers in inhibition of secondary nucleation may explain the high efficiency of AS69-αS particularly in inhibiting secondary nucleation.

For inhibition of secondary nucleation, the NAC IDR is not required but can be replaced by the N-terminal IDR (Figure 3.6C). This suggests that in secondary nucleation the αS N-terminus can drive the incorporation into pre-nucleus oligomers. This is exactly the conclusion of recent NMR experiments that have found that αS monomers bind to αS fibrils via interactions of the monomers' N-termini with C-termini exposed on the fibril surface [266, 279]. The resulting dynamical alignment of N-termini of fully unfolded αS molecules can trigger secondary nucleation [266, 279]. The αS N-terminus also plays a role in lipid-induced primary nucleation, where it tethers the protein to the phospholipid membrane surface, leading to an increased local αS concentration that promotes aggregation [244, 260]. However, the inhibitory effect of AS69-αS(N-B) on secondary nucleation but not on lipid-induced primary nucleation suggests that the αS N-terminus is more deeply involved in secondary nucleation, where it interacts with the unfolded αS C-termini.

Importantly, the activities of the different fusion constructs on amyloid formation *in vitro* correlate very well with their effects in cellular seeding assays. Thus, the αS IDRs that are important in the *in vitro* assays are also critical for inhibition of seeding in the biosensor cells (Figure 3.9). The precise mechanism of aggregate proliferation in biosensor cells has not been determined before. Here, we observed that cellular seeding is inhibited by all constructs that inhibit secondary nucleation *in vitro*. This strongly suggests that secondary nucleation drives aggregate seeding in αS biosensor cells. Thus, the monomers in seed-receiving cells do not only convert to the fibrillar state by addition to the fibril end template during fibril elongation, but they also form new fibril nuclei in secondary nucleation on the surface of added seeds.

The present study highlights the importance of IDR-IDR interactions in amyloid formation and its inhibition. Monomer binding agents are usually thought to affect protein assembly only at stoichiometric concentrations. Here, we observe that the complex of aggregation-prone monomer with monomer-binding agent can gain new inhibitory activity. In the case of AS69-αS, this activity depends on the presence of αS IDRs that remain unfolded in the AS69-bound state. As for the mechanistic basis, we find evidence that the IDRs can recruit the complex of inhibitor and amyloid protein monomer into oligomers formed by the latter, which blocks the conversion of oligomers into fibril nuclei. Furthermore, the inhibitor-containing oligomers might actively interfere with further nucleation processes. The processes underlying this inhibitory mechanism (complex formation, IDR presentation, oligomer formation, nucleation, inhibition of nucleation by incompatible oligomers) are generally applicable to amyloid proteins. Therefore, monomer-binding agents other than AS69, targeting αS, αS mutants, or other amyloid proteins, may act by the same mechanisms as AS69. For drug design, this strategy requires *i.*) targeting a binding site whose recruitment interferes with fibril nucleation (e.g., a segment indispensable for formation of the cross-β fibril core), *ii.*) retaining sufficient IDRs in the amyloidogenic target upon drug-target complex formation to afford incorporation into oligomers. The particular capacity of IDRs to engage in variable interactions, which provides the basis for αS amyloid formation, can thus also be exploited to inhibit amyloid formation.

3.6. Materials and Methods

3.6.1 Generation of fusion constructs and αS

The full-length fusion construct was previously described [353]. The truncated fusion constructs were ordered from GenScript already inserted into the same vector (pET302/NT-His) as the full-length. The αS fragment αS(N-NAC-C) was ordered from GenScript and inserted in the plasmid pET11a, while the fragment αS(NAC-C) was inserted in the plasmid pt7-7. Transformation was done into chemically competent *Escherichia coli* (*E. coli*) JM109 (DE3) cells in the same way as previously described [353]. αS(N-$B_{aa31-37}$)) and $(G_4S)_4$-αS(N-$B_{aa31-37}$) were synthesized by CASLO with a purity >96% by high-performance liquid chromatography (HPLC) according to the manufacturer.

3.6.2 Expression and purification of fusion constructs and αS

The expression and purification of αS was performed as described [263, 388] and the expression and purification of truncated AS69-αS fusion constructs were performed as previously described [350, 353]. For NMR samples, ^{15}N- and ^{13}C-labeled fusion constructs were prepared from *E. coli* cultures grown in M9 minimal medium supplemented with $^{15}NH_4Cl$ and ^{13}C-D-glucose from Cambridge Isotope Laboratories [389].

3.6.3 SDS-PAGE

The samples were diluted 1:4 with SDS-loading buffer (200 mM Tris-HCl pH 6.8, 400 mM DTT, 8% SDS, 0.4% bromophenol blue, 40% glycerol) followed by 15% tris-glycine SDS-PAGE. Spectra^{TM} Multicolor Low Range Protein Ladder was used as marker. Gel electrophoresis was performed at 120 V.

3.6.4 Nuclear Magnetic Resonance (NMR)

NMR spectra were acquired on a 900 MHz VNMRS spectrometer (Varian) equipped with a cryogenically cooled z-axis pulse-field-gradient triple resonance probe. NMR samples contained 300 µl of isotope-labeled protein solution with a concentration above 200 µM, 30 µl D_2O and 0.03% NaN_3. The buffer used was 20 mM sodium phosphate, 50 mM NaCl, pH 7.4. NMR data were processed using NMRPipe [390] and analyzed with CCPNmr [391]. Formula (1) was used to quantify the changes of the backbone amide chemical shifts in the αS part of the fusion constructs in comparison to the chemical shifts in free αS.

$$Mean\ weighted\ chemical\ shifts = \sqrt{(\Delta^1\mathrm{H})^2 + (\frac{\Delta^{15}\mathrm{N}}{5})^2} \qquad (1)$$

3.6.5 Circular Dichroism (CD) spectroscopy

CD data was recorded on a JASCO J-815 spectropolarimeter. Data acquisition and determination of melting temperatures was performed as described [353, 378, 392].

3.6.6 Elongation assay

Fibril elongation was monitored following established protocols [135, 354]. Briefly, fibril seeds were produced in 20 mM MOPS (pH 7.4), 50 mM NaCl, in a 1.5 ml tube containing a glass bead at 37 °C and 800 rpm for 75 h. Seeds were sonicated using a Hielscher UP200St ultrasonic processor for 30 s at 70% maximal amplitude. 100 µl samples of 25 µM αS monomers in 20 mM MOPS (pH 7.4), 50 mM NaCl, 20 µM ThT, 0.04% NaN_3, were prepared in black 96-well half area polystyrene plates with non-binding surface and clear bottom (REF 3881, Corning), before adding sonicated seeds to a concentration of 2.5 µM. Plates were sealed with clear sealing tape and placed into a FLUOstar Omega plate reader (BMG Labtech, Ortenberg, Germany) for incubation at 37 °C for 40 h. ThT was excited with a wavelength of 448 nm and the emission was measured at 482 nm. Measurements were done every 100 s in cycle 1 to 110 and every 300 s in further 490 cycles.

3.6.7 Lipid-induced primary nucleation assay

Primary nucleation assays were performed in 50 mM NaPi (pH 6.5) in the presence of DMPS SUVs as previously described [244, 353]. Briefly, DMPS lipid powder was dissolved in 20 mM sodium phosphate, (pH 6.5), 0.01% NaN_3 and stirred at 45 °C for 2 h. The solutions were then frozen in dry ice and thawed at 45 °C five times. Lipid vesicles were prepared by sonication using Bandelin, Sonopuls MS-72, 3 × 5 min, 50% cycle, 10% maximum power, and centrifuged at 15,000 rpm for 30 min at 25 °C. 70 µM αS monomers were prepared in 20 mM NaPi (pH 6.5), 50 mM NaCl, 20 µM ThT, 0.04% NaN_3, before adding 100 µM DMPS SUVs. Measurements were performed as described for the elongation assay for 100 h with measurements every 360 seconds for 1000 cycles.

3.6.8 Secondary nucleation assay

Secondary nucleation assays were conducted as described [135, 353] with modifications outlined in SI Figure 3.14. Briefly, seed fibrils were produced in 20 mM acetate buffer (pH 5.0), 50 mM NaCl, in a 96 well plate along with a glass bead at 37 °C and 500 rpm for at least 75 h. After formation of seeds, they were sonicated using a Bandelin Sonopuls HD 2070 sonicator with MS-72 probe for 1 s at 10% maximal amplitude. 70 µM αS monomers were prepared in 20 mM sodium acetate buffer (pH 5.0), 50 mM NaCl, 20 µM ThT, 0.04% NaN_3, before adding 0.3 µM sonicated seeds. Measurements were performed as described for the elongation assay for 100 h with measurements every 360 s for 1000 cycles.

3.6.9 Atomic Force Microscopy (AFM)

Sample preparation for AFM was performed as described [353]. AFM was performed on a Bruker Multimode 8 microscope using ScanAsyst-Air cantilevers in the ScanAsyst PeakForce tapping mode in air. The software Gwyddions was used for image processing.

3.6.10 Density gradient ultracentrifugation (DGC)

DGC was performed as previously described [353, 375]. In short, 100 µl samples were applied onto a discontinuous 30 mM Tris-HCl, pH 7.4 buffered sucrose gradient layered in an 11 mm x 34 mm centrifuge tube. The gradients were centrifuged for 3 h at 259,000 xg and 4 °C in an Optima MAX-XP ultracentrifuge (Beckman Coulter) using a TLS-55 swing-out rotor (Beckman Coulter) and manually fractionated into 13 142 µl fractions. Afterwards the fractions were analyzed using SDS-PAGE.

3.6.11 Cell assay for αS aggregation

The pMK-RQ vector was used to carry a synthetic construct that encodes full-length A53T-mutated human αS fused with YFP at the C-terminus (GeneArt; Thermo Fisher Scientific, USA). The αSA53T–YFP construct was inserted into the pIRESpuro3 vector (Clontech; Takara Bio, JPN) via NheI (5 ') and NotI (3 ') restriction sites. HEK293T cells (American Type Culture Collection) were cultured in high glucose Dulbecco's Modified Eagle's Medium (DMEM; Sigma-Aldrich, USA) supplemented with 10% fetal calf serum (Sigma-Aldrich, USA), and 50 units/ml penicillin, and 50 µg/ml streptomycin (Sigma-Aldrich, USA). The cells were cultured at 37 °C in a humidified atmosphere containing 5% CO_2. Lipofectamine 2000 (Invitrogen; Thermo Fisher Scientific, USA) was used to transfect the cells plated in DMEM. Stable cells were selected in DMEM containing 1 µg/ml puromycin (EMD Millipore, USA). Monoclonal lines were generated by fluorescence-activated cell sorting of a polyclonal cell population in 96 well plates using a MoFlo XDP cell sorter (Beckman Coulter, USA). Finally, the clonal cell line B5, referred to as αSA53T–YFP cells, was selected from among 24 clonal cell lines. The αSA53T–YFP cells were plated in a 384-well plate with poly-D-lysine coating (Greiner, AT) at a density of 800 cells per well with 0.1 µg/ml Hoechst 33342 (Thermo Fisher Scientific, USA). To induce cellular aggregation of αS in αSA53T–YFP cells and to test its inhibition, fibrillar αS seeds (50 nM final concentration per well) were incubated with 1.5% Lipofectamine 2000 in Opti-MEM (Thermo Fisher Scientific, USA), in the presence or absence of AS69-αS fusion constructs (15 µM final concentration per well), for 2 h at room temperature. The resulting mixture was added to each well 4 h after the cells had been plated. The plate was incubated in a humidified atmosphere containing 5% CO_2 at 37 °C. The cells were imaged using the blue and green fluorescence channels with an IN Cell Analyzer 6500HS System (Cytiva, SE). The images were analyzed using IN Carta Image Analysis Software (Cytiva, SE). To ensure objectivity, an automated algorithm was used to identify intracellular aggregates in living cells.

3.7. Acknowledgments

This project has received funding from the European Research Council under the European Union's Horizon 2020 research and innovation program, grant agreement No. 726368. We acknowledge Nina Kirchgässler for support with CD spectroscopy. We acknowledge access to the Jülich-Düsseldorf Biomolecular NMR Center.

3.8. Supplementary Information

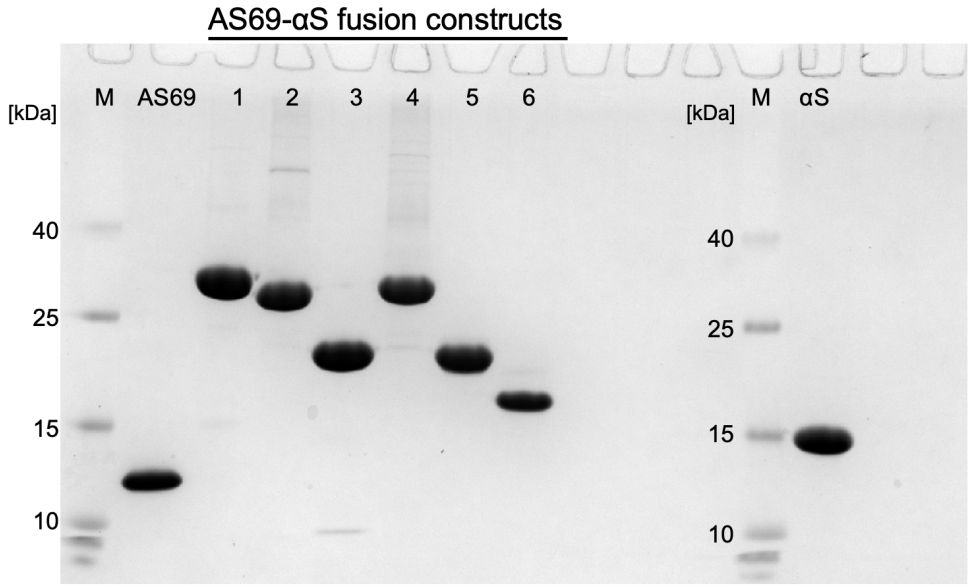

Figure 3.10: SDS-PAGE of the AS69 constructs and αS after purification. AS69, AS69-αS fusion constructs (1-6) and αS was applied to the SDS gel with a concentration of 25 µM each. The order of the fusion constructs is shown as follows: AS69-αS(N-B-NAC-C) (1), AS69-αS(B-NAC-C) (2), AS69-αS(N-B) (3), AS69-αS(N NAC C) (4), AS69-αS(B-NAC) (5) and AS69-αS(B) (6). M, marker.

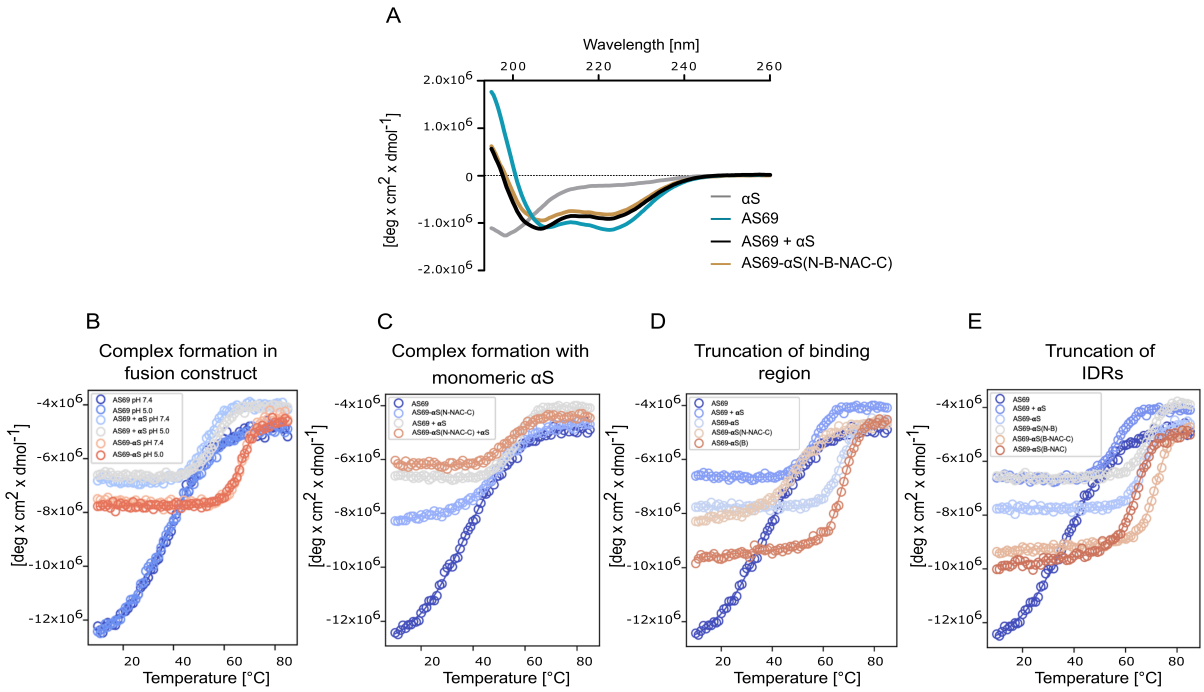

Figure 3.11: CD spectroscopy of AS69 and fusion constructs to investigate complex formation. (A) Mean residue ellipticity against wavelength in the range of 190 to 260 nm of 12 µM AS69, 12 µM AS69-αS, 12 µM αS, and 12 µM AS69 with 12 µM free αS in 20 mM NaPi (pH 7.4), 50 mM NaCl. The α-helical structure of AS69 dominates the spectra of the samples where AS69 is present. In contrast, αS is intrinsically disordered, which leads to a random coil CD spectrum. (B)-(E) Melting curves were determined by CD spectroscopy at 222 nm using 25 µM protein concentration and plotted as mean residue ellipticity. Melting points (T_{Melt}) determined from the data are given in Figure 3.2B. Melting curves of AS69 in presence and absence of αS show that complex formation is associated with an increase in T_{Melt}. Fusion of AS69 with αS leads to an additional increase in T_{Melt} of 10-15 °C, demonstrating that intramolecular folding stabilizes the AS69:αS complex in the fusion construct. The data obtained is similar for the two pH values applied in the kinetic assays. (C) Increases in T_{Melt} upon addition of αS indicate that both AS69 and the fusion construct AS69-αS(N-NAC-C), which lacks the AS69-binding region of αS, are able to bind monomeric αS. (D,E) Apart from the fusion construct AS69-αS(N-NAC-C) lacking the AS69-binding region of αS, all fusion constructs with truncations in the αS segment have a thermostability similar to that of full-length AS69-αS (T_{Melt} in the range of 65-72 °C for the fusion constructs with IDR truncations; T_{Melt} of 67.6±0.4 °C for full-length AS69-αS). This demonstrates that the intramolecular AS69:αS complex is established in all fusion constructs with IDR truncations.

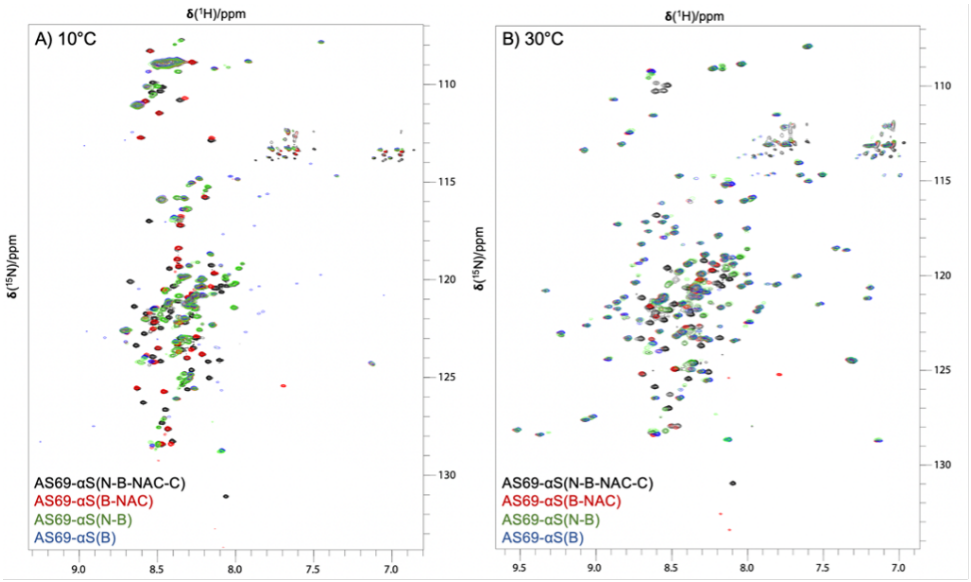

Figure 3.12: ^{1}H-^{15}N HSQC NMR spectra of the fusion constructs at 10 °C (A) and 30 °C (B) in 50 mM NaPi (pH 7.4), 50 mM NaCl. Overlay of backbone amide region of the ^{1}H-^{15}N HSQC spectra of AS69-αS(N-B) (green), AS69-αS(B-NAC) (red), AS69-αS(B) (blue) and AS69-αS(N-B-NAC-C) (black). At 10 °C, the globular core of the AS69:αS complex is invisible due to intermediate exchange, only the regions that remain intrinsically disordered are visible (Mirecka, *et al.* [350]). Upon increasing the temperature to 30 °C, the globular core of the AS69:αS complex becomes visible in ^{1}H-^{15}N HSQC NMR spectroscopy as a set of well-dispersed resonances.

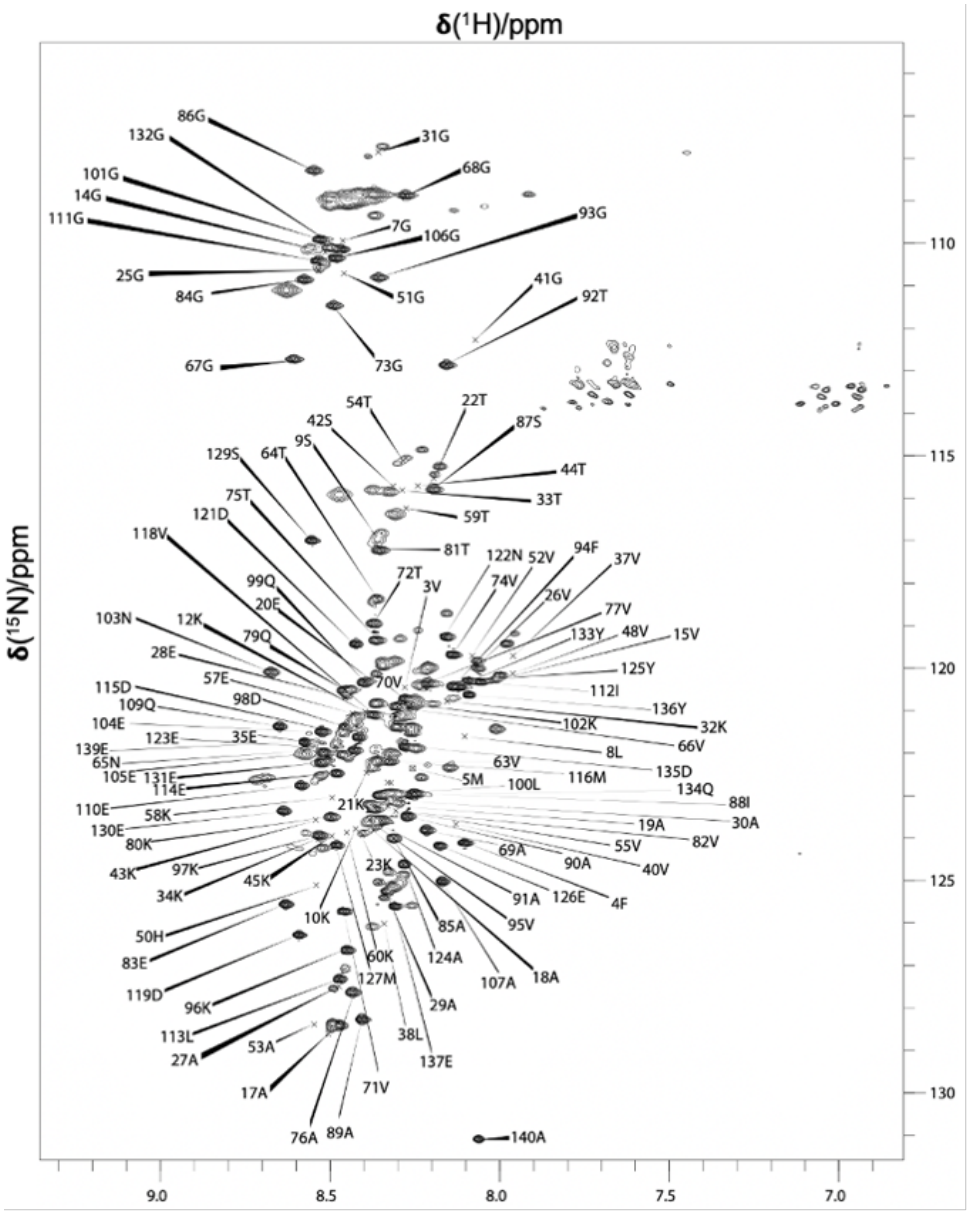

Figure 3.13: ^{1}H-^{15}N HSQC NMR spectrum of full length AS69 αS(N-B-NAC-C) at 10 °C in 50 mM NaPi (pH 7.4), 50 mM NaCl. Peaks of the spectrum are overlaid with the assignment of free αS obtained under the same conditions in Mirecka, *et al.* [350]. The majority of the peaks of free αS are recovered in AS69-αS(N-B-NAC-C) at the same positions. However, the peaks of residues 34-62, i.e., of the AS69-binding region, were absent due to intermediate exchange, as observed before for the intermolecular AS69:αS complex [350].

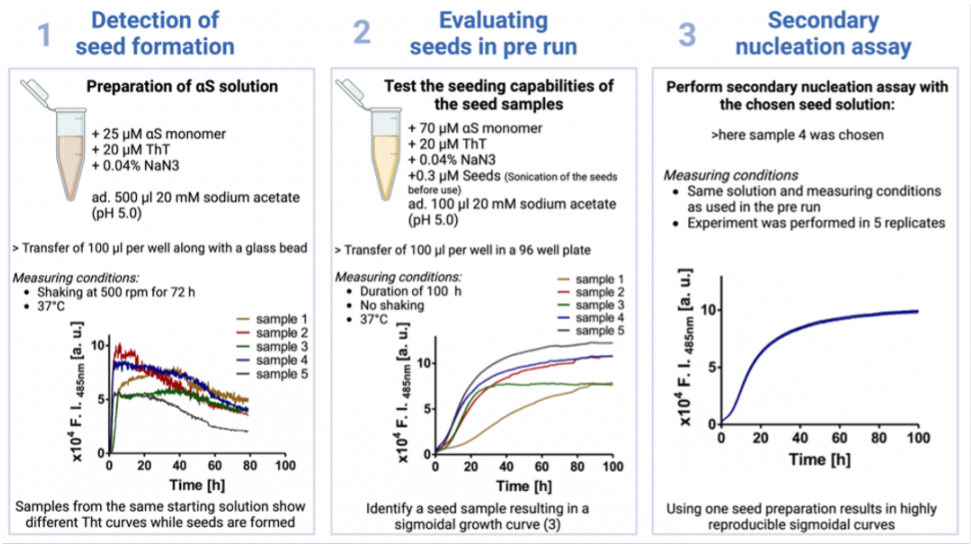

Figure 3.14: Improvement of the workflow of the secondary nucleation assay at pH 5.0. (1) Production of seeds was performed: 25 µM solution of monomeric αS was incubated under shaking conditions with a glass bead in a 96 well plate at 37 °C for 72 h. Seed formation is shown for five samples and the ThT signal is plotted against the time (h). (2) To test the functionality of the seeds, a pre-run of the assay was performed. 70 µM solution of monomeric αS was incubated with 0.3 µM seeds under quiescent conditions in a 96 well plate at 37 °C. The five seed samples were tested, and the fluorescence signal was measured over 100 h. Despite the same starting stock for seed preparation, there are differences in the seeded ThT curves. Seed preparations showing a pronounced sigmoidal curve in the pre-run were taken for the secondary nucleation assay. (3) In this case, seed sample 4 was chosen. The secondary nucleation assay was performed in five replicates under the same conditions as described for the pre-run resulting in reproducible curves.

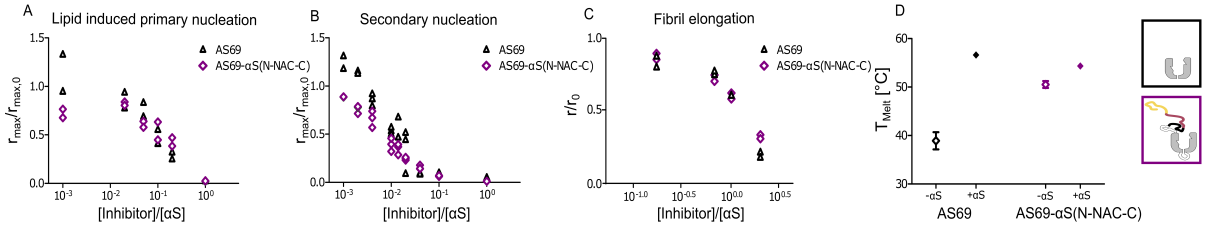

Figure 3.15: AS69-αS(N-NAC-C) exhibits similar behavior as AS69 since it also binds monomeric αS. Relative rates of lipid-induced primary nucleation (A), secondary nucleation (B) and fibril elongation (C) were plotted against the inhibitor-to-monomer ratios in the presence of AS69 (black) or AS69-αS(N-NAC-C) (purple). (D) Complex formation between αS and AS69 (black) or AS69(N-NAC-C) (purple) was confirmed by increases in T_{Melt} values obtained from the CD melting curves shown in SI Figure 3.11C.

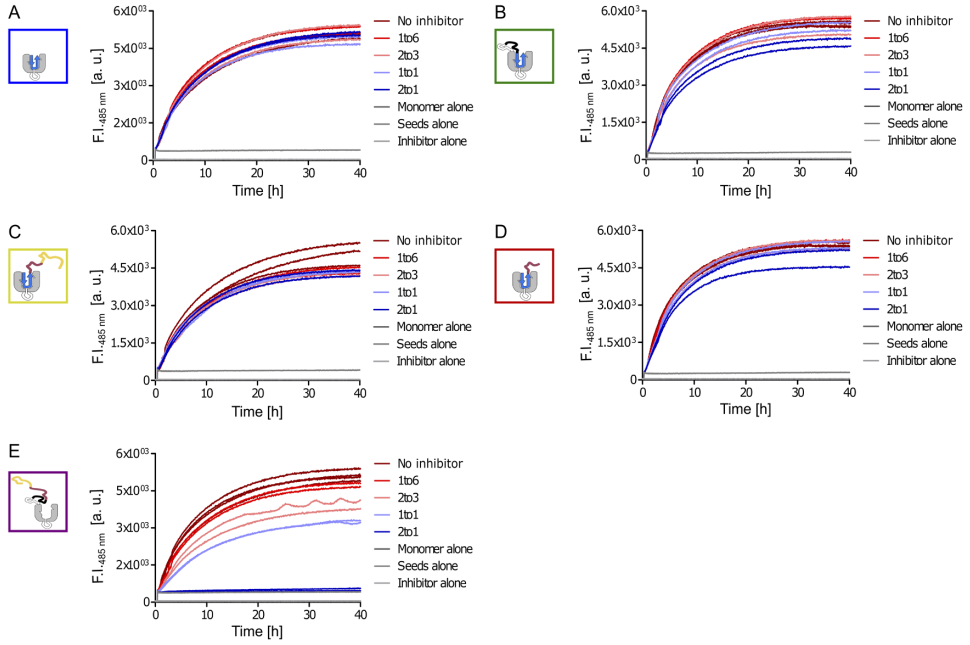

Figure 3.16: Elongation of αS fibrils in the presence of different AS69-αS fusion constructs at pH 7.4. Time course of ThT fluorescence when a 25 µM solution of monomeric αS was incubated in the presence of 5 µM pre-formed fibrils under quiescent conditions in the presence of different inhibitors at pH 7.4. Inhibitors were AS69-αS(B) (A), AS69-αS(N-B) (B), AS69-αS(B-NAC-C) (C), AS69-αS(B-NAC) (D) and AS69-αS(N-NAC-C) (E). The assay was performed with different inhibitor-to-monomer ratios between 1to6 and 2to1 shown in a color gradient from red to blue. The negative controls are shown in grey shades and the positive control (NoAS69) in dark red. No AS69-αS fusion construct is able to inhibit fibril elongation to any larger extent, with the exception of AS69-αS(N-NAC-C) (E).

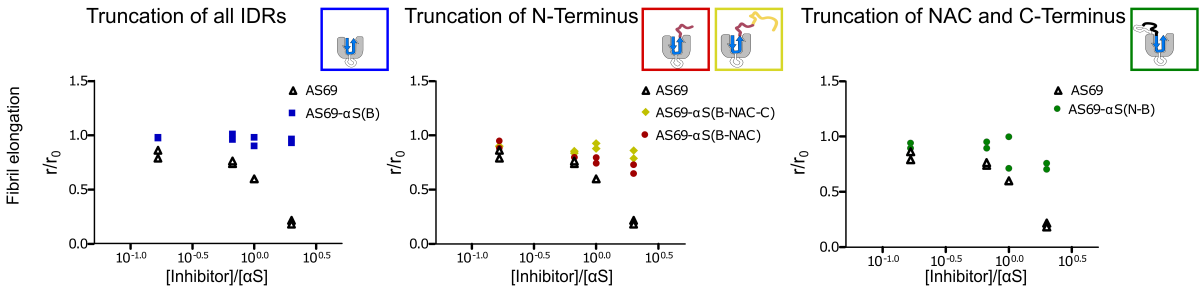

Figure 3.17: Truncation of αS IDRs in the AS69-αS fusion does not recover inhibition of fibril elongation. Relative rates of elongation with increasing concentration of truncated versions of AS69-αS were derived from the data shown in SI Figure 3.16 and plotted against the inhibitor-to-monomer ratios. The fusion constructs with αS IDR truncations do not recapitulate the inhibition of fibril elongation exhibited by AS69 (black).

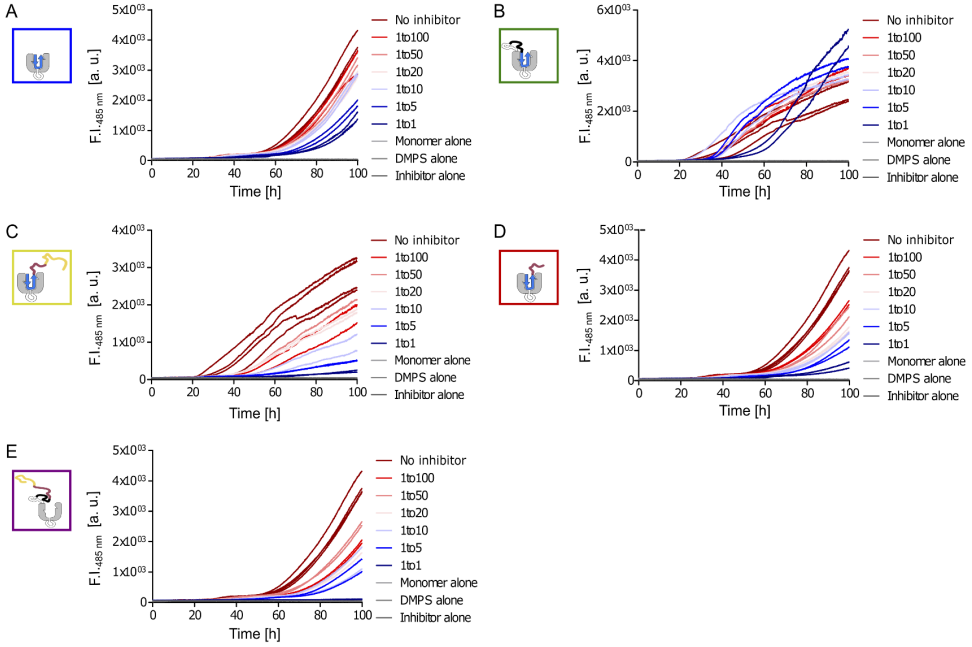

Figure 3.18: Lipid-induced primary nucleation of αS in the presence of different AS69-αS fusion constructs at pH 6.5. Time course of ThT fluorescence when a 70 µM solution of monomeric αS was incubated in the presence of 70 µM DMPS SUV under quiescent conditions in the presence of different inhibitors at pH 6.5. Inhibitors were AS69-αS(B) (A), AS69-αS(N-B) (B), AS69-αS(B-NAC-C) (C), AS69-αS(B-NAC) (D) and AS69-αS(N-NAC-C) (E). The assay was performed with different inhibitor-to-monomer ratios between 1to100 and 1to1 shown in a color gradient from red to blue. The negative controls are shown in grey shades and the positive control (NoAS69) in dark red.

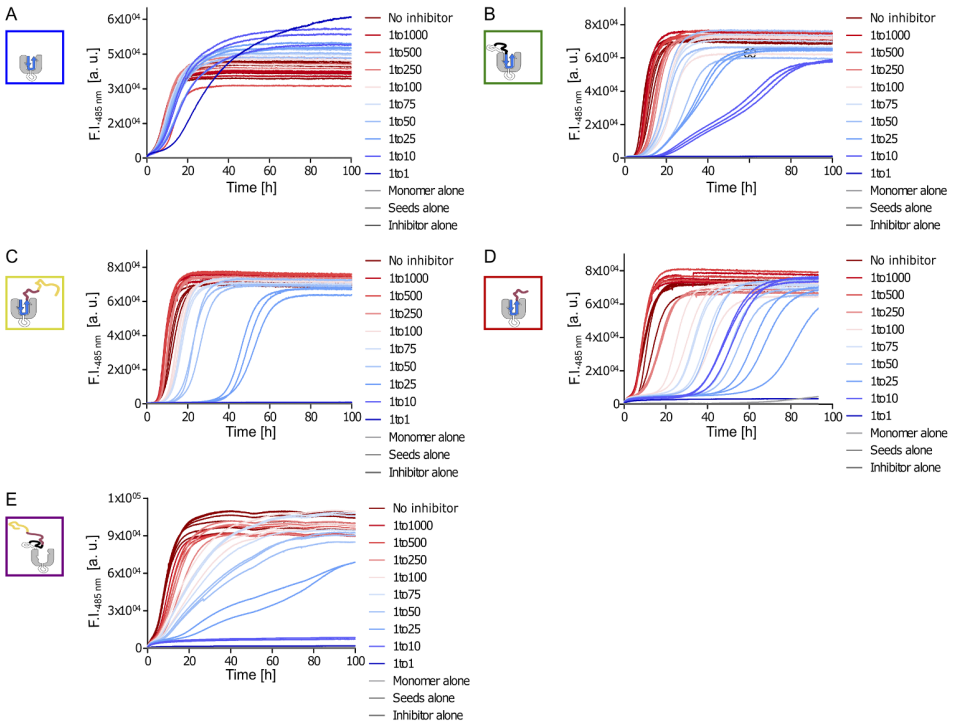

Figure 3.19: Secondary nucleation of αS in the presence of different AS69-αS fusion constructs at pH 5.0. Time course of ThT fluorescence when a 70 µM solution of monomeric αS was incubated in the presence of 0.3 µM pre-formed fibrils under quiescent conditions in the presence of different inhibitors at pH 5.0. Inhibitors were AS69-αS(B) (A), AS69-αS(N-B) (B), AS69-αS(B-NAC-C) (C), AS69-αS(B-NAC) (D) and AS69-αS(N-NAC-C) (E). The assay was performed with different inhibitor-to-monomer ratios between 1to1000 and 1to1 shown in a color gradient from red to blue (D). The negative controls are shown in grey shades and the positive control (NoAS69) in dark red.

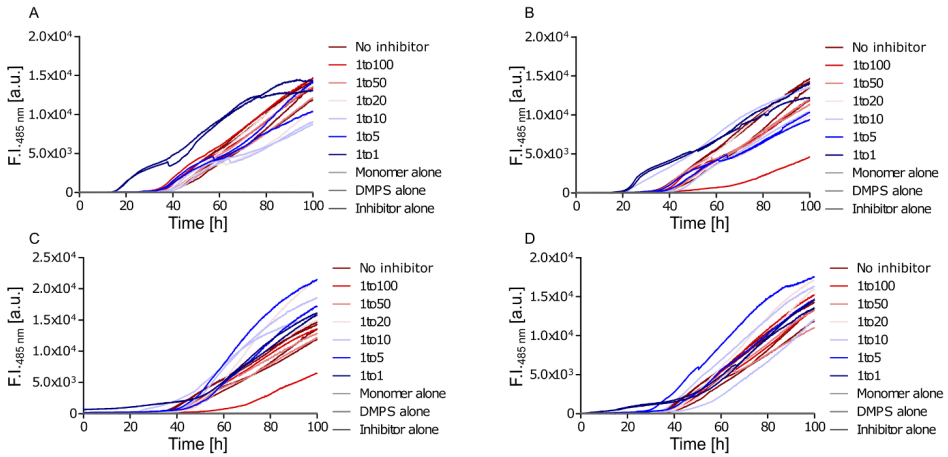

Figure 3.20: Lipid-induced primary nucleation of αS in the presence of truncated αS monomers. Time course of ThT fluorescence when a 70 µM solution of monomeric αS was incubated in the presence of 70 µM DMPS SUV under quiescent conditions in the presence of different inhibitors at pH 6.5. Truncated αS monomers were αS($N_{aaB31-37}$) (A), $(G_4S)_4$-αS($N_{aaB31-37}$) (B), αS(N-NAC-C) (C) and αS(NAC-C) (D). The assay was performed with different inhibitor-to-monomer ratios between 1to100 and 1to1 shown in a color gradient from red to blue. The negative controls are shown in grey shades and the positive control (NoAS69) in dark red.

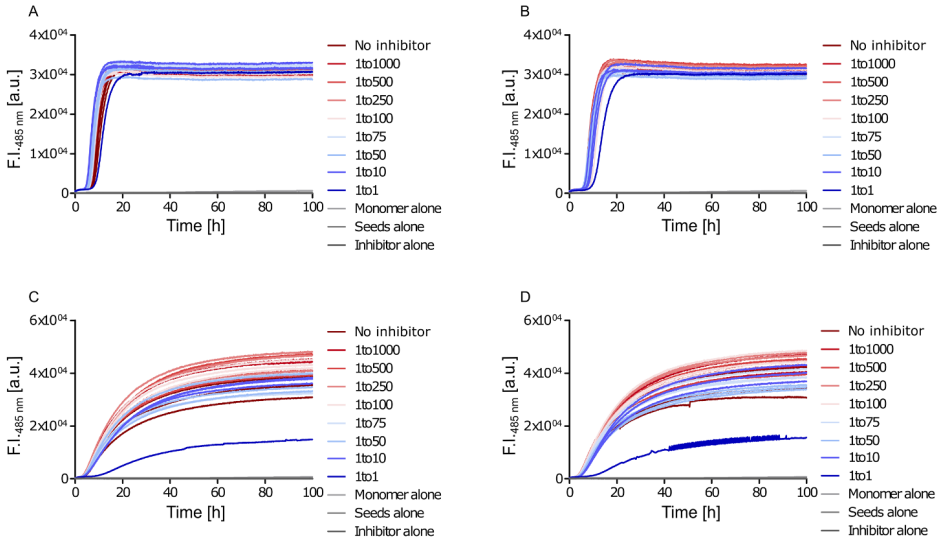

Figure 3.21: Secondary nucleation of αS in the presence of truncated αS monomers. Time course of ThT fluorescence when a 70 µM solution of monomeric αS was incubated in the presence of 0.3 µM pre-formed fibrils under quiescent conditions in the presence of different inhibitors at pH 5.0. Truncated αS monomers were αS($N_{aaB31-37}$) (A), $(G_4S)_4$- αS($N_{aaB31-37}$) (B), αS(N-NAC-C) (C) and αS(NAC-C) (D). The assay was performed with different inhibitor-to-monomer ratios between 1to100 and 1to1 shown in a color gradient from red to blue. The negative controls are shown in grey shades and the positive control (NoAS69) in dark red.

4

NUCLEATION PROCESSES DRIVE α-SYNUCLEIN FIBRIL PROLIFERATION IN SHAKING-INDUCED SEED AMPLIFICATION ASSAY

This Chapter reflects content on the following publication.

4.1. Publication information

Author: Celina M. Schulz[*a], Stefan Bräuer[*bc], Björn Falkenburger[bc] and Wolfgang Hoyer[ad]

a: Institut für Physikalische Biologie, Heinrich Heine University Düsseldorf, Düsseldorf, Germany
b: Institut für Zelluläre Neurobiologie, Klinik für Poliklinik für Neurologie, Universitätsklinikum Carl Gustav Carus, Dresden, Germany
c: German Center for Neurodegenerative Diseases (DZNE), Dresden, Germany
d: Institute of Biological Information Processing (IBI-7: Structural Biochemistry) and JuStruct: Jülich Center for Structural Biology, Forschungszentrum Jülich, Jülich, Germany
*: These authors contributed equally: Celina M. Schulz, Stefan Bräuer

in preparation

4.2. Abstract

Parkinson's disease (PD) and other synucleinopathies are neurodegenerative disorders characterized by the deposition of fibrillar aggregates of the endogenous protein α-synuclein (αS). Diagnostic tools at early disease stages are urgently needed. Recently, the ability of αS fibrils to self-amplify was exploited in seed amplification assays (SAA) such as real-time quaking-induced conversion (RT-QuIC), achieving high specificities and sensitivities. Yet, the underlying mechanisms of aggregate proliferation remain unclear. Here, we applied an engineered artificial αS-binding protein, AS69nuc, to specifically inhibit nucleation of αS fibrils, but not their elongation. Addition of AS69nuc to SAA thus allows detection whether nucleation processes contribute to aggregate proliferation. We find that, depending on seed and substrate, seeded αS aggregation *in vitro* can occur exclusively by fragmentation and elongation of fibrils. SAA employing patient cerebrospinal fluid (CSF) is dramatically inhibited by AS69nuc, indicating that secondary nucleation, i.e., the formation of new fibril nuclei on the surface of pre-existing fibrils, plays a dominant role in the proliferation of patient-derived aggregates by seeded amplification. The gained mechanistic insights may support the development of improved diagnostic assays.

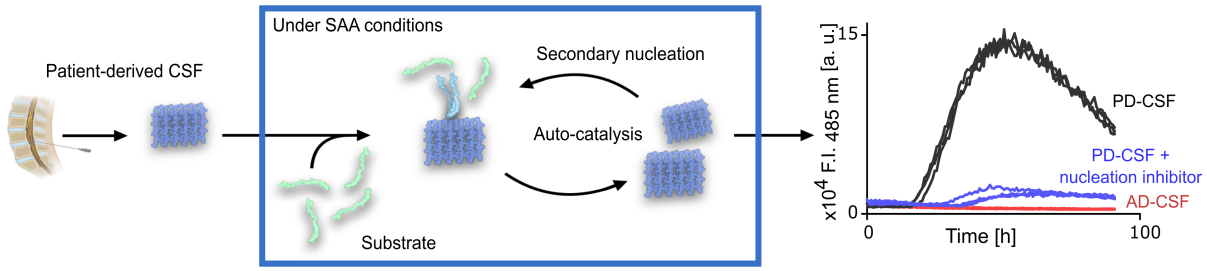

Figure 4.1: Auto-catalytic amplification of amyloid fibrils for the diagnosis of Parkinson's disease. Amplification of αS aggregate seeds in patient-derived materials is a promising approach for diagnosis of synucleinopathies such as Parkinson's disease (PD). An inhibitor that specifically targets fibril nucleation processes reveals that secondary nucleation plays a pivotal role in seed amplification.

4.3. Main Text

In many neurodegenerative diseases, neuronal dysfunction is associated with the aggregation of endogenous proteins into amyloid fibrils that accumulate in the brain. These deposits are composed of misfolded proteins such as prion protein, αS, amyloid-β or tau, and often occur in combination as co-pathologies [11, 357, 393]. Major challenges for diagnosis lie in the detection of abnormal proteins during the early disease stages, often preceding the onset of severe clinical symptoms by years or even decades, and in the identification and differentiation of co-pathologies [40].

In recent years, considerable efforts have been dedicated to enhancing the sensitivity and reliability of diagnostic tests for prion-like diseases from biomaterial of living patients [309, 394, 395, 396, 397]. Presently, a promising diagnostic tool that can be used with biomaterial obtained from living individuals are shaking-induced SAA [394] such as RT-QuIC [396]. In these assays, minute amounts of aggregates present in CSF or brain material are added to recombinant substrate, resulting in exponential proliferation initiated by seeding of patient-derived material, which is meticulously detected in real-time by the amyloid-specific fluorescent dye Thioflavin-T (ThT). An increase fluorescence signal in the SAA signifies the presence of disease-related aggregates (Figure 4.2A).

For synucleinopathies, characterized by the aggregation of the protein αS, these assays have undergone protocol optimization since the pioneering work of Fairfoul *et al.* [309]. They first introduced the RT-QuIC assay using seeds isolated from the brains and CSF of patients with Parkinson's disease (PD) or Lewy body dementia (DLB). Numerous studies have reported sensitivities exceeding 90% when analyzing CSF samples from PD and DLB patients [310, 398, 399, 400]. These results underscore the relatively well-established and reliable nature of SAA. However, significant heterogeneity exists among patient-isolated samples, suggesting a strong dependence on the seed strain and its seeding potential [401].

These assays capitalize on the property of misfolded proteins to self-amplify through seeding. However, the molecular mechanism of self-amplification by SAA has not been revealed to date. Two alternative mechanism may drive the proliferation of minute amounts of aggregates (Figure 4.2A): *i.)* Fragmentation: Promoted by shaking, fibrils can break into smaller fragments, which increases the number of fibril ends and hence the sites of fibril elongation [129, 138, 155, 156]. *ii.)* Secondary nucleation: The surfaces of existing fibrils can auto-catalyze the formation of new growth competent nuclei [131, 135, 158]. It is widely believed that fragmentation is the source of exponential aggregate proliferation in SAA since most SAA occur under mechanical force involving shaking-rest cycles that favor fragmentation [402, 403, 404]. Furthermore, it has been reported that the sensitivity and specificity of SAA depend on the shaking parameters, supporting the significance of fragmentation [405]. However, recent hypotheses also consider a contribution of secondary nucleation in SAA [40, 406]. To allow optimization of SAA in terms of sensitivity and specificity, elucidation of the mechanistic basis is required.

In order to test whether secondary nucleation contributes to aggregate proliferation in SAA, we applied here an engineered αS-binding protein that inhibits the nucleation processes but not fragmentation-elongation (Figure 4.2B). To obtain this type of inhibitor, our starting point was AS69, a β-wrapin with affinity for monomeric αS (SI Figure 4.5A), that inhibits αS fibril formation in two ways [350, 353]. First, AS69 inhibits fibril elongation by sequestration of αS monomers, which lose the competence to elongate fibrils when incorporated in the AS69 complex [353] (SI Figure 4.5B, orange box). Second, the AS69:αS complex formed in this binding reaction proved to be a potent inhibitor of both primary and secondary nucleation (SI Figure 4.5B, blue box). To obtain a compound that inhibits nucleation but not

fragmentation-elongation, we deprived AS69 of its elongation inhibition function by fusing an αS moiety to its C-terminus, resulting in a construct that we term here AS69nuc (SI Figure 4.5B, blue box). The fused αS moiety in AS69nuc occupies the binding site in the AS69 moiety [353].

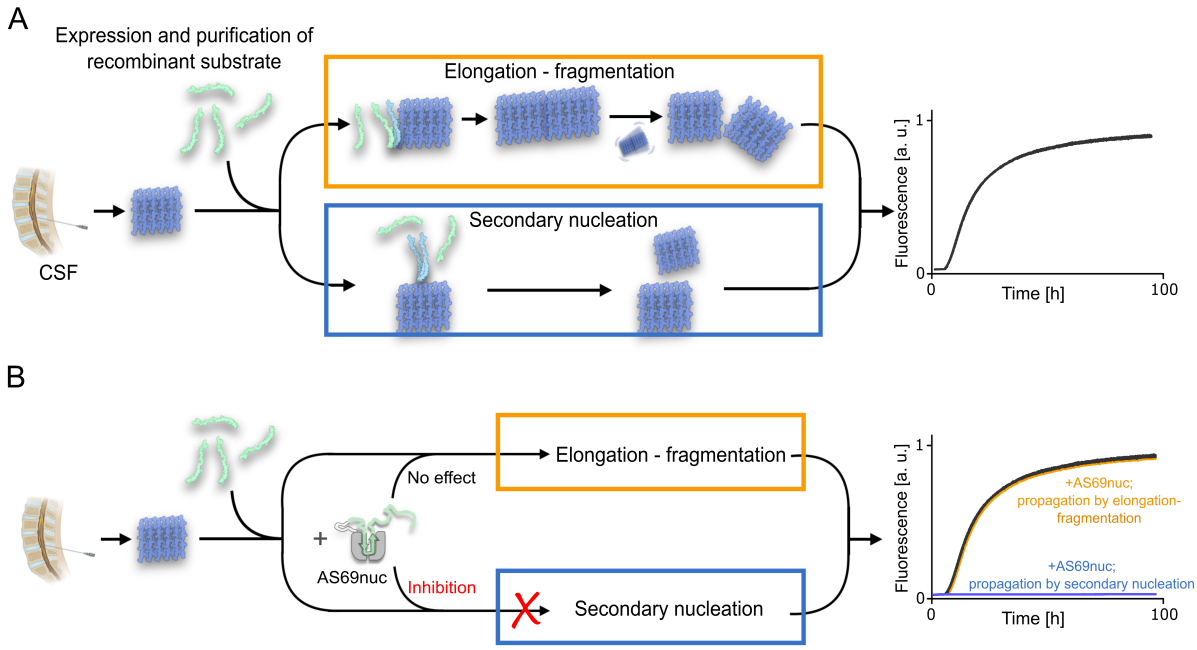

Figure 4.2: Alternative mechanisms for aggregate proliferation in SAA and engineering of nucleation inhibitor. (A) Schematic overview of proliferation of αS fibrils during SAA. CSF of synucleinopathy-afflicted patients, containing small amounts of aggregated αS species, is incubated with purified recombinant substrate to amplify the amount of fibrillar aggregates, which are detected by ThT fluorescence. Two pathways may account for fibril amplification in SAA: elongation-fragmentation (orange box), where fragmentation generates new fibril ends, or secondary nucleation (blue box), where new fibril nuclei are created auto-catalytically on existing fibril surfaces. (B) The secondary nucleation inhibitor AS69nuc can identify the mechanism of proliferation. If fibril proliferation is dominated by fragmentation-elongation, AS69 does not affect aggregation kinetics (orange). However, if secondary nucleation drives fibril proliferation, aggregation is inhibited (blue).

In ThT-detected aggregation kinetics that specifically monitor fibril elongation (quiescent, high number of fibril ends), we find that AS69nuc has lost the ability to inhibit αS fibril elongation (Figure 4.3A), in agreement with its inability to bind free αS monomers. This finding was confirmed by atomic force microscopy (AFM). Similarly, in a seeded assay under conditions where aggregation kinetics are dominated by fragmentation-elongation (shaking, low initial number of fibril ends), AS69nuc does not show a major effect on the time course (Figure 4.3B). AFM images show that the fibrils at the end of the assay are small and fragmented both in absence and presence of AS69nuc (Figure 4.3B). Taken together, these observations confirm that AS69nuc affects neither elongation nor fragmentation of αS fibrils. In contrast, AS69nuc inhibits αS aggregation under conditions where aggregation kinetics are dominated by secondary nucleation [135] (quiescent, low initial number of fibril ends, pH 5.0) at substoichiometric concentration (Figure 4.3C).

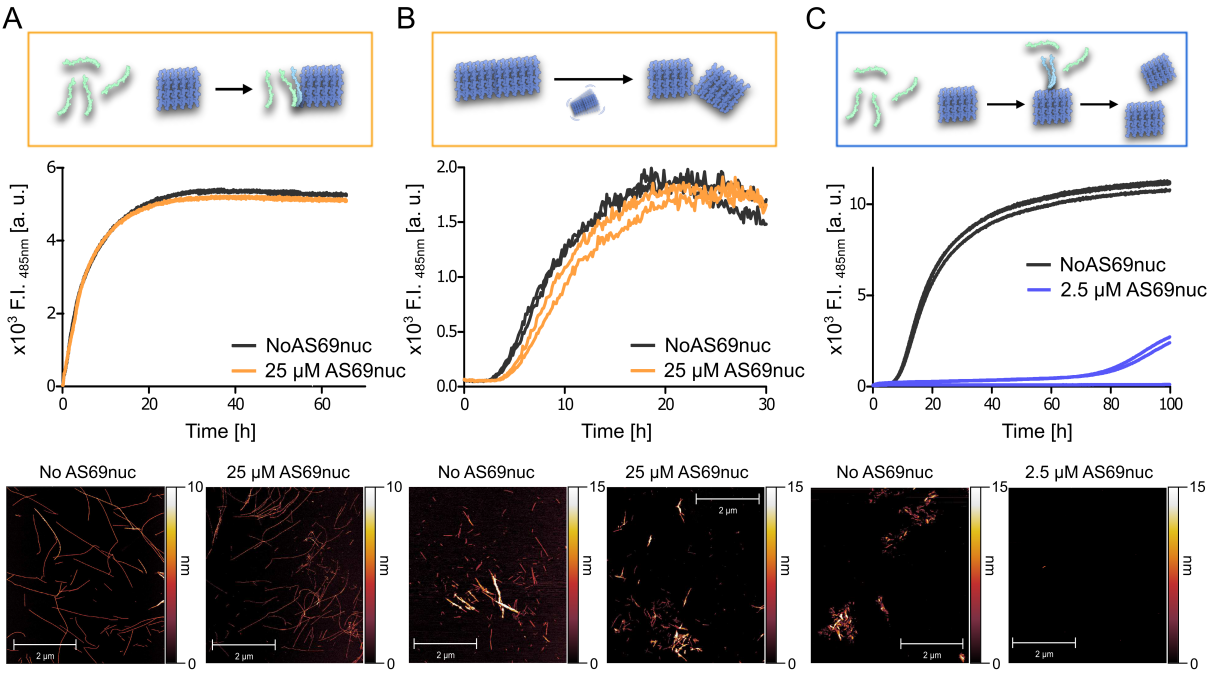

Figure 4.3: Distinctive effects of AS69nuc on fibril elongation (A), elongation-fragmentation (B) and secondary nucleation (C). (Top row) Schematic representation of the individual reaction step investigated; (Middle row) ThT fluorescence time traces of the aggregation assay in absence (NoAS69nuc, black) and presence of AS69nuc (colored); (Bottom row) AFM of fibrils generated in the different aggregation assays in the absence (left) and presence (right) of AS69nuc. Conditions of the kinetic assays, (A) fibril elongation: 25 µM monomeric αS was incubated with 2.5 µM pre-formed fibrils under quiescent conditions at pH 7.4, (B) fragmentation-dominated proliferation: 25 µM monomeric αS was incubated with 0.1 µM pre-formed fibrils under shaking conditions (500 rpm in a 60 s shaking-rest cycle) at pH 8.0, (C) secondary nucleation: 70 µM monomeric αS was incubated with 0.3 µM pre-formed fibrils under quiescent conditions at pH 5.0. All preformed seeds were generated in the buffer in which they were used subsequently.

After characterizing AS69nuc as a nucleation-specific inhibitor, its efficiency was tested under buffer conditions frequently applied in SAA (40 mM NaPi (pH 8.0), 170 mM NaCl, 0.0015% sodium dodecyl sulfate (SDS)) [397, 399, 407]. When AS69nuc was tested under SAA buffer conditions in presence of pre-formed fibrils, referred to as seeds, generated *in vitro* under SAA buffer conditions, no inhibitory effect was observed (Figure 4.4A), indicating that aggregate proliferation occurred by fragmentation-elongation. However, addition of seeds generated under the low pH conditions of the secondary nucleation assay (see Figure 4.3C) to the SAA led to a substantial delay in aggregation (Figure 4.4B), suggesting that secondary nucleation strongly contributes to fibril amplification in this case. This demonstrates that AS69nuc is capable to identify divergent seed characteristics in SAA. While seeds generated under SAA conditions proliferated by fragmentation-elongation, secondary nucleation accelerated the amplification of seeds generated at low pH.

SAAs frequently employ N-terminally his-tagged αS (his-αS) monomers as substrate since the his-tag facilitates purification of αS under mild conditions and improves the data reproducibility [397, 399, 407]. Using *in vitro* αS wildtype (WT) seeds and his-αS substrate under SAA conditions, addition of AS69nuc led to a substantial increase in the lag-time (Figure 4.4C), indicating a prominent role of fibril amplification

through secondary nucleation. Comparing the data for WT αS substrate (Figure 4.4A) with that for his-αS substrate (Figure 4.4C) under the same conditions shows that a relatively minor modification of the substrate can lead to a significant shift in the mode of aggregate proliferation from a process dominated by fragmentation-elongation to a process dominated by secondary nucleation.

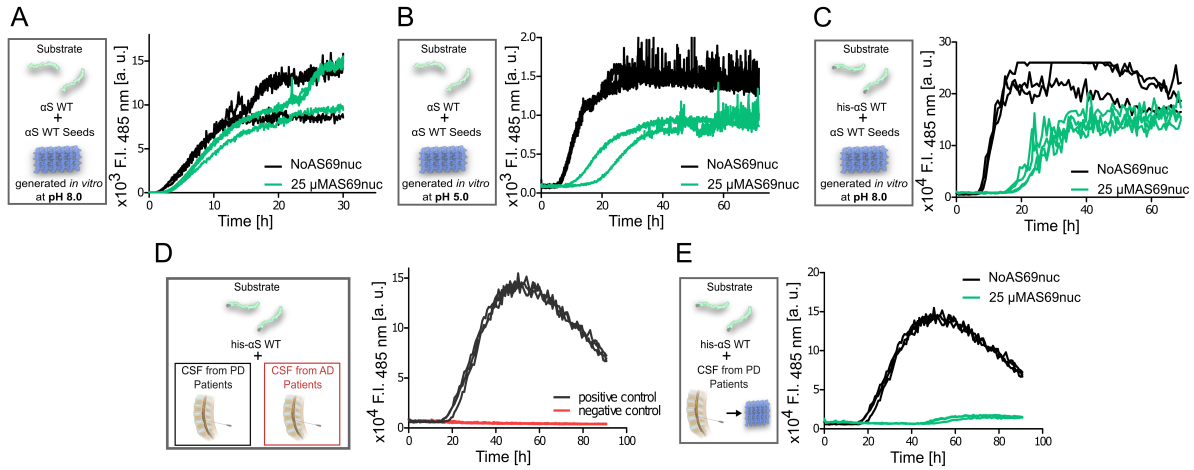

Figure 4.4: AS69nuc efficacy depends on the different prepration of αS substrate and seeds. The contribution of secondary nucleation to aggregate proliferation in SAA depends on both seed and substrate and is strong in SAA of PD-derived CSF. (A-E) Time courses of aggregation under SAA buffer conditions (40 mM NaPi (pH 8.0), 170 mM NaCl, 0.0015% SDS) using the indicated combinations of substrate and seeds.

To test for a contribution of secondary nucleation to SAA of patient-derived seeds, we used CSF from two patients diagnosed with PD and, as negative controls, of two patients with multifactorial gait disorder, one patient with Alzheimer's diseases (AD), and one patient each with Progressive Supranuclear Palsy (PSP) and normal pressure hydrocephalus (NPH). While the PD-derived CSF led to an increase in ThT fluorescence, the negative controls did not, confirming sensitivity and specificity of the SAA (Figure 4.4D and SI Figure 4.6). Addition of AS69nuc to SAA using the PD patient-derived seeds dramatically inhibited aggregation (Figure 4.4E). This indicates that secondary nucleation does strongly contribute to SAA of patient-derived material.

The results demonstrate that patient-derived seeds are not efficiently proliferated by elongation and subsequent fragmentation under SAA conditions. Instead, secondary nucleation is remarkably effective at driving seed amplification. Importantly, this activity is highly protein-specific, as no amplification from CSF of patients with neurodegenerative diseases other than synucleinopathies can be detected. Secondary nucleation of amyloid involves interactions of disordered monomers with the lateral fibril surface, with subsequent oligomerization and conformational conversions leading to new fibril nuclei [131, 157, 408]. It is remarkable that these interactions are highly protein-specific, leading to efficient amplification of homotypic seeds from CSF.

To sum up, the engineering and application of an inhibitor that specifically targets fibril nucleation processes revealed that secondary nucleation plays a pivotal role in amplification of αS in SAA. This finding offers valuable mechanistic insights for optimization and refining the assay for diagnostic applications.

4.4. Material and Methods

4.4.1 Expression and purification of αS and his-αS

The expression and purification of αS wildtype was performed as previously described in Hoyer *et al.* [263] and Wördehoff *et al.* [388]. *Escherichia coli* (*E. coli*) BL21 (DE3) pT7-7 cells were grown at 37 °C and 110 rpm. After induction of the gene expression using IPTG the cells were incubated for 4 h under the same conditions. After centrifugation at 5,000 rpm for 15 min the cells were lysed using the MS-72 sonication probe (Bandelin) set at an amplitude of 35% with a pulse of 3 s and a pause of 5 s in between for 5 min. The lysate was heated to 100 °C for 10 min and briefly vortexed every 2 min. 4 M $(NH_4)_2SO_4$ was added to a final concentration of 1.75 M, then stirred for an additional 3 min before incubation on ice for 10 min. After centrifugation at 11,000 rpm for 30 min at 4 °C, ion exchange chromatography (IEC) was performed using a 5 ml Q HP Hi-trap column (Cytiva) on a NGC chromatography system (BioRad) equilibrated in 25 mM TrisHCl (pH 8.0). The protein solution was eluted with a linear gradient from 0 mM to 500 mM NaCl over 40 min. Afterwards, αS was, again, precipitated in 2 M $(NH_4)_2SO_4$ using a saturated solution of 4 M $(NH_4)_2SO_4$. For buffer exchange, size exclusion chromatography (SEC) was performed with a Superdex 75 Increase 10/300 GL column (Cytiva) using the respective buffer and was stored at −80 °C until further use.

The expression and purification of recombinant his-tagged wildtype human αS were conducted as previously described in Bräuer *et al.* [407]. In brief, *E. coli* BL21 (DE3) (Thermo Fischer Scientific) were transformed with the vector plasmid pET-28a(+) (Merck) containing wildtype human αS. The gene expression was induced via the Overnight Express Autoinduction System (Merck). After 18 h, the cells were harvested by centrifugation at 3,200 rcf for 10 min. Afterwards, the pellet was lysed via osmotic shock (400 g/l sucrose, 30 mM TrisHCl pH 7.2, 2 mM EDTA) and centrifuged at 9,000 rcf for 20 min. The pellet was resolved in water. After centrifugation at 9,000 rcf for 30 min, the supernatant's pH was reduced to 3.5. The solution was, again, centrifuged at 9,000 rcf for 30 min and the supernatant's pH was increased to 7.5. Next, immobilized metal ion affinity chromatography (IMAC) using an NGC chromatography system (BioRad) was performed. The protein solution was loaded on a 5 ml HisTrap FF-column (Cytiva) and was washed with 20 mM TrisHCl, pH 7.5 and subsequently with 50 mM imidazole, 20 mM TrisHCl, pH 7.5. The protein was eluted with a linear gradient up to 500 mM imidazole, 20 mM TrisHCl, pH 7.5. Then, the protein solution was loaded on a 5 ml HiTrap Q-HP anion exchange-column (Cytiva). The column was washed with 20 mM TrisHCl, pH 7.5 and subsequently with 200 mM NaCl, 20 mM TrisHCl, pH 7.5 and then, the his-tagged protein was eluted with a linear gradient up to 500 mM NaCl, 20 mM TrisHCl, pH 7.5. After dialyzing the protein against water, using a 3.5 kDa MWCO dialysis membrane (Thermo Fisher Scientific) overnight at 4 °C, the samples were lyophilized and stored at −80 °C until further use.

4.4.2 Expression and purification of AS69nuc

Expression and purification of the AS69nuc construct with N-terminal his-tag was performed as described previously in Mirecka *et al.* [350] with all modifications described in Agerschou *et al.* [353]. Briefly, *E. coli* JM109 (DE3) cells containing plasmid pET302_NTHis_AS69nuc were grown at 37 °C and 110 rpm. After induction of gene expression, the cells were incubated another 4 h under the same conditions. The cell suspension was sonicated for 10 min using an MS-72 sonification probe (Bandelin) set at 35% maximum power with cycles of 3 s pulse followed by 5 s pause. After centrifugation at 13,500 rcf for 20 min, IMAC was performed with the lysate using a 5 ml Ni-NTA Histrap FF column (Cytiva) equilibrated in loading buffer containing 50 mM TrisHCl (pH 8.0), 500 mM NaCl and 20 mM imidazole. The protein was eluted in 250 mM imidazole. After dialyzing the protein solution against 1.4 l of a

25 mM TrisHCl (pH 8.0) overnight at 4 °C, the buffer exchange was performed using a SEC (Superdex 75 Increase 16/600 column (Cytiva)) in the respective buffer.

4.4.3 Elongation assay

As previously described by Buell *et al.* [135] and Agerschou *et al.* [354], the kinetics of the elongation process were investigated in 20 mM MOPS (pH 7.4), 50 mM NaCl buffer. Briefly, for seed generation, 25 µM αS monomers were incubated in 20 mM MOPS (pH 7.4), 50 mM NaCl along with a glass bead at 37 °C and shaking at 800 rpm for 75 h. To promote fibril elongation, the number of fibril ends was increased by fibril fragmentation achieved by sonication using a UP200St ultrasonic processor (Hielscher) for 30 s at 70% maximal amplitude. Then 100 µl aliquots of 25 µM αS monomers in 20 mM MOPS (pH 7.4), 50 mM NaCl containing 20 µM ThT and 0.04% NaN_3 were transferred to the wells of a 96-well half area, non-binding surface, black with clear bottom, polystyrene plate (REF 3881, Corning) before adding 2.5 µM sonicated seeds. The plate sealed by a clear sealing tape was then placed into a FLUOstar Omega plate reader (BMG Labtech) for incubation under quiescent conditions at 37 °C for 40 h. ThT was excited with a wavelength of 448 nm and the emission was measured at 482 nm.

4.4.4 Fragmentation-elongation assay

Kinetics were performed in 40 mM NaPi (pH 8.0), 170 mM NaCl. Briefly, for seed generation, 25 µM αS monomers were incubated in 40 mM NaPi (pH 8.0), 170 mM NaCl along with a glass bead at 37 °C and shaking at 800 rpm for 75 h. Then, samples of 25 µM αS monomer were prepared in 40 mM NaPi (pH 8.0), 170 mM NaCl containing 20 µM ThT, 0.04% NaN_3, and added to the wells of a 96-well half area, non-binding surface, black with clear bottom, polystyrene plate (REF 3881, Corning), followed by addition of 0.1 µM non-sonicated seeds. The plate was sealed by a clear sealing tape and placed into a FLUOstar Omega plate reader (BMG Labtech) for incubation at 37 °C for 60 h with cycles of 1 min double orbital shaking at 400 rpm and 1 min rest. ThT was excited at a wavelength of 448 nm and the emission was measured at 482 nm.

4.4.5 Secondary nucleation assay

Secondary nucleation assays were conducted similarly as to what was described previously by Buell *et al.* [135] and Agerschou *et al.* [353]. Briefly, seed fibrils were produced in 20 mM acetate buffer (pH 5.0), 50 mM NaCl in a 96 well plate along with a glass bead at 37 °C and 500 rpm for at least 75 h. The seeds were subsequently sonicated using a probe sonicator (Bandelin Sonopuls HD 2070 with MS-72 probe) for 1 s at 10% maximal amplitude. Then, 70 µM αS monomers were prepared in 20 mM sodium acetate buffer (pH 5.0) containing 20 µM ThT and 0.04% NaN_3 before adding 0.3 µM sonicated seeds. Measurements was performed as it is described for elongation assay for 100 h.

4.4.6 Seed amplification assay of αS

SAA kinetics of αS wildtype were performed in 40 mM NaPi (pH 8.0), 170 mM NaCl, 0.0015% SDS. Briefly, seeds were preformed *i.)* under SAA conditions: by incubation of 25 µM αS monomers in 40 mM NaPi (pH 8.0), 170 mM NaCl, 0.0015% SDS or *ii.)* under slightly acidic pH in 20 mM acetate buffer (pH 5.0), 50 mM NaCl. In both cases, temperature was set to 37 °C and seeds were formed under shaking at 800 rpm with six 0.8 mm silica beads (OPS Diagnostics) per well. Then, 25 µM αS monomer substrate was prepared in 40 mM NaPi (pH 8.0), 170 mM NaCl, 0.0015% SDS containing 20 µM ThT and 0.04% NaN_3 before adding 0.1 µM seeds. Measurements were performed as described for

the fragmentation-elongation assay for 100 h in presence of six 0.8 mm silica beads (OPS Diagnostics) per well.

The αS-SAA with CSF was performed as previously described in Bräuer *et al.* [407]. In brief, the measurements were performed using a black 96-well plate (Thermo Fischer Scientific) and each well contained six 0.8 mm silica beads (OPS Diagnostics). In each well, 15 µl of CSF were added to 85 µl of reaction buffer, which resulted in the final concentrations of 40 mM phosphate buffer pH 8.0, 0.0015% SDS, 10 µM ThT, 7.2 µM recombinant his-tagged αS and 170 mM NaCl. The plate was incubated in a BMG FLUOstar Omega plate reader at 42 °C with cycles of 1 min double orbital shaking at 400 rpm and 1 min rest. Fluorescence measurements were performed every 45 min.

For the distinction between positive and negative CSF samples, each sample was measured as four technical replicates on the same plate. Each plate included at least two negative control and two positive controls, each with four replicates. For every time point, relative fluorescence units were expressed as a percentage of the maximum intensity reached on that plate. We considered a replicate positive if fluorescence crossed a threshold within a 40 h time window. The fluorescence threshold was defined as the average intensity of previously measured negative controls during the first 10 h of recording, plus 40 standard deviations. We considered a sample positive if at least two replicates were positive and negative if no replicate was positive. A sample was run again if only one replicate was positive, which was not the case in this study.

In the experiments testing the influence of AS69nuc, it was added to the reaction buffer in the respective concentrations. The final concentrations of the reaction buffer and the amount of CSF were unchanged.

4.4.7 Atomic Force Microscopy (AFM)

At the end of the aggregation kinetics assay, 10 µl (for assays at neutral pH) or 5 µl (for assays at slightly acidic pH) sample was directly applied in the middle of the freshly cleaved mica followed by incubation at RT for 15 min in humified conditions. Subsequently, the drop was dried in a circular pattern with a gentle stream of N_2. After five washing steps by gently pipetting 100 µl ddH_2O to remove residual buffer salt, the sample was dried with a gentle stream of N_2. AFM was performed on a Bruker Multimode 8 (Billerica, Massachusetts, USA) using ScanAsyst-Air cantilevers (Camarillo, California, USA) in the ScanAsyst PeakForce tapping mode in air. Afterwards, the software Gwyddions was used for processing the AFM images.

4.5. Acknowledgments

This project has received funding from the European Research Council under the European Union's Horizon 2020 research and innovation program, grant agreement No. 726368.

4.6. Supplementary Information

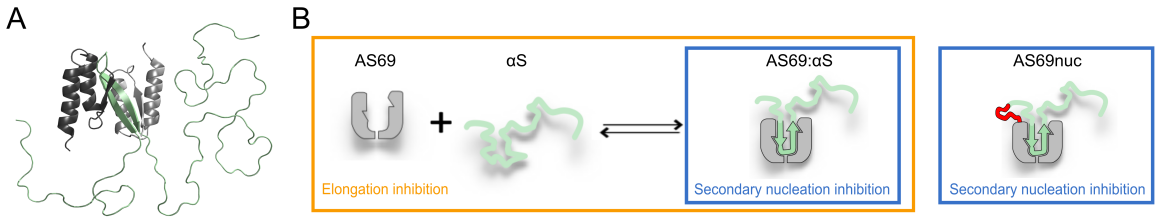

Figure 4.5: Mode of action of the monomer binder AS69. (A) Structural model of the AS69:αS complex based on NMR (pdb entry 4BXL [350]). AS69 (grey) is a homodimer linked through a disulfide bridge. αS (green) locally adopts β-hairpin conformation in the AS69-binding region, while the other αS regions remain intrinsically disordered. (B) AS69 binds free αS monomer resulting in inhibition of fibril elongation (orange box), while the complex between AS69 and αS (AS69:αS) inhibits nucleation processes (blue box within orange box). Fusion of αS to AS69 via a flexible linker (shown in red, AS69nuc) enhances the stability of the complex and impedes fibril nucleation but not elongation (right blue box).

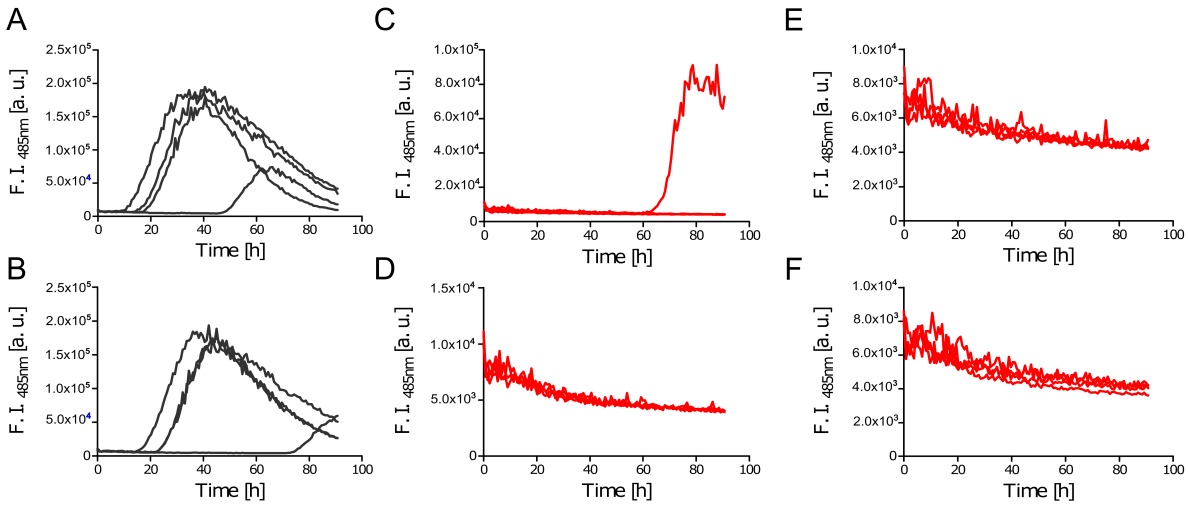

Figure 4.6: SAA seeded by CSF from patients suffering from different diseases. Time courses of aggregation under SAA buffer conditions (40 mM NaPi (pH 8.0), 170 mM NaCl, 0.0015% SDS) using the PD Patient's CSF (A, B), and as controls the CSF of Patients with PSP (C), NPH (D) or multifactorial gait disorder (E, F) in four replicates.

5

DECIPHERING UPREGULATED MECHANISMS THROUGH EXPRESSION PROFILING IN SH-SY5Y CELLS WHEN EXPOSED TO α-SYNUCLEIN FIBRILS.

5.1. Chapter information

Author: Celina M. Schulz[a], Hamed Shaykhalishahia[a], Nima Abedpour[b] and Wolfgang Hoyer[ac]

a: Institut für Physikalische Biologie, Heinrich Heine University Düsseldorf, Düsseldorf, Germany
b: Department of Translational Genetic, University Köln, Köln, Germany
c: Institute of Biological Information Processing (IBI-7: Structural Biochemistry) and JuStruct: Jülich Center for Structural Biology, Forschungszentrum Jülich, Jülich, Germany

5.2. Abstract

Synucleinopathies are characterized by neuronal dysfunction linked to the aggregation of α-synuclein (αS) into amyloid fibrils. Once fibril formation begins, these aggregates propagate, disrupting cellular functionality. Recent studies are focused on understanding the cellular processes of internalization and self-defense mechanisms against fibrils, aiming to enrich our understanding of the associated diseases. Cellular uptake mechanisms encompass endocytosis pathways, membrane penetration, and cell-to-cell transmission through tunneling nanotubes. Defense mechanisms against fibril exposure include chaperone-mediated protein folding, proteasomal degradation, autophagy, and activation of neuroinflammatory pathways. This variety of responses underlines the complexity of cellular reaction when exposed to fibrils. Next-generation sequencing (NGS) offers insights into the cellular responses to fibrils, shedding light on molecular mechanisms involved in fibril internalization, defense, and self-protection. This molecular snapshot allows us to identify upregulated proteins, and thus recognize the critical components of the cellular response to fibrils. This proteomic analysis indicates similarities between the cellular response to fibrils and that of a viral infection. Understanding these complex mechanisms is crucial for the development of effective therapeutics as well as the advancement of biomarker diagnostics, enhancing our understanding of synucleinopathies and neuroinflammatory responses.

5.3. Introduction

In synucleinopathies, such as Parkinson's disease or Multiple system atrophy, neuronal dysfunction is associated with the aggregation of αS, a protein consisting of 140 amino acids [11, 213, 363]. In its soluble state, αS plays a crucial role in maintaining the homeostasis of the synaptic vesicle pool at presynaptic terminals [246, 251, 255, 409]. Upon aggregation, monomers undergo a structural transition into a cross-β fold, incorporating themselves into highly ordered, and insoluble supra-molecular assemblies known as amyloid fibrils. These fibrils accumulate within neurons as protein inclusions [410, 411, 412, 413].

The initial fibrillation process of αS is believed to be driven by the stochastic misfolding of αS monomers [128]. This phenomenon may be more likely to occur in specific vulnerable neuronal compartments characterized by slightly acidic pH, like lysosomes [131, 135], or in areas with elevated local concentrations of the protein. For example, individuals with duplications or triplications of the *SNCA* gene which encodes for αS, are at a higher risk for this process [221, 414, 415]. Furthermore, aggregation can be accelerated by missense mutations, such as the best-known A53T, A30P and E46K [379], or by environmental changes related to smaller molecules like metal ions [416]. However, the initial reason for aggregation remains unclear.

Once the formation of amyloid fibril commences in a specific region, these aggregates spread throughout the brain, disturbing the cellular functionality [417, 418]. Several studies have documented the uptake of αS fibrils within neuronal networks, which subsequently stimulates the misfolding of endogenous αS [419, 420]. In recent years, there has been an increasing emphysis on exploring the mechanisms underlying cellular internalization of fibrils and self-defense of cells against this process, with the objective of developing therapeutic strategies and enhancing our overall understanding of the invasion process. Intriguingly, the identification of multiple uptake, defense and self-protection pathways has underlined the complicated nature of the cellular answer when exposed to fibrils.

In cellular uptake, endocytosis encompasses multiple pathways [281, 286, 421]. These pathways include clathrin-mediated endocytosis [292, 422], micropinocytosis [292, 423], and receptor-mediated endocytosis [286, 290, 424, 425]. In receptor-mediated endocytosis, specific cell surface receptors, such as scavenger receptors or glycosaminoglycan receptors, facilitate the uptake of αS fibrils by binding to them and triggering their internalization [288, 289]. Additionally, another mechanism of uptake involves membrane penetration, where fibrils interact directly with the cell membrane and gain entry by disrupting the lipid bilayer [426, 427, 428]. Recent research has also demonstrated that neurons can transfer fibrils between each other through tunneling nanotubes from neuron to neuron [429].

Furthermore, defense mechanisms become amplified in cells when they are infiltrated by amyloid fibrils. Cells employ diverse strategies to combat these aggregates and prevent the misfolding of endogenous proteins. They may activate chaperone-mediated protein folding [430, 431, 432], to counteract against misfolding or engage in proteasomal degradation [433]. Alternatively, cells initiate autophagy for degradation of damaged components [434, 435]. Moreover, cells start the activation of neuroinflammatory pathways [436, 437], as self-protection mechanism to enable a response of immune cells, cytokines, and other molecules. Understanding autophagy and neuroinflammatory processes is equally intriguing, as it opens the possibility of identifying promising indicator-proteins or markers that could be utilizied for developing biomarker diagnostics. This exploration could lead to significant advancements in the early detection and monitoring of neurodegenerative conditions.

To gain a molecular overview in the internal answering machinery of neurons when exposed to fibrils, NGS provides comprehensive insights into all these potential processes that occur concurrently within the cell. Consequently, it raises the question of whether certain mechanisms are preferentially activated in cells, as evidenced by visible upregulation of proteins involved in *i.)* fibril internalization, *ii.)* degradation of fibrils via defense mechanisms, or *iii.)* self-protection by activating inflammatory responses. This approach allows for the identification of specific pathways and mechanisms that neurons utilize to combat the presence of fibrils. This chapter is centered on investigating whether the upregulated proteins are involved in the cellular uptake of fibrils.

5.4. Results

5.4.1 Establishment of a fluorescence-assay to detect αS fibril uptake by differentiated SH-SY5Y cells.

In our study, we developed a fluorescence-based assay to detect fibril uptake in neuronal cells. This assay provides several key advantages, including its ease of use, speed, and the capacity to analyze the entire population of cells treated with fibrils.

To evaluate the effect of fibrils on a model system that closely resembles functional neurons, we induced the differentiation of SH-SY5Y cells by treating them with retinoic acid and brain-derived neurotrophic factor (BDNF) (Figure 5.1A). By comparing the morphology of the cells in the undifferentiated and differentiated states, the successful differentiation from a heterogeneous population of adherent and suspended cells to functional neurons can be confirmed (Figure 5.1B). The differentiated cells exhibit significantly enhanced dendrite-like extensions, making them resemble neurons more closely. Additionally, we observed a remarkable upregulation in the expression levels of *trk339* and *trk350* genes in the differentiated sample, with increases of 1000-fold and 3000-fold, respectively (Figure 5.1C). This further affirms the successful differentiation, as these genes are critical markers for the differentiation process and exhibit upregulation exclusively in the differentiated state [438].

After successful differentiation, SH-SY5Y cells were treated with 1 µM pHrodo-labeled αS fibrils and then incubated overnight at 37 °C and under 5% humidified conditions (Figure 5.1A). The pHrodo-labeled fibrils were generated by incubating C-terminally pHrodo-labeled αS monomers with αS monomers in a 1:10 ratio with shaking over 7 days at 37 °C (Figure 5.1D). The selection of pHrodo dye for this process was due to its sensitivity to changes in pH, making it an ideal choice for tracking the internalization of fibrils within the cellular environment. It is hypothesized that once inside cells, fibrils are either transported within vesicles or are targeted for degradation within lysosomes, both of environments characterized by a slightly acidic pH. However, pHrodo remains fluorescent at neutral pH, such as in the cytosol. Subsequently, the fibrils were pelleted through centrifugation at 100,000 xg for 1 h, and fibril formation was confirmed using atomic force microscopy (AFM) (Figure 5.1E). Upon incubation with cells, these fibrils can be internalized through various cellular uptake mechanisms. Flow cytometry was employed to detect and analyze this uptake of fibrils along the whole cell population (Figure 5.1A). To achieve this, the cells were treated with trypsin, which serves to cleave off all components that bind extracellularly to the membrane receptors. The results show that the entire SH-SY5Y population takes up fibrils as evidenced by the shift along the x-axis (red), in contrast to untreated cells (gray) (Figure 5.1F). This highlights that this assay is useful for detecting the fibril uptake of the whole cell population. Additionally, insights into the behavior of single cells of a whole population can be gained.

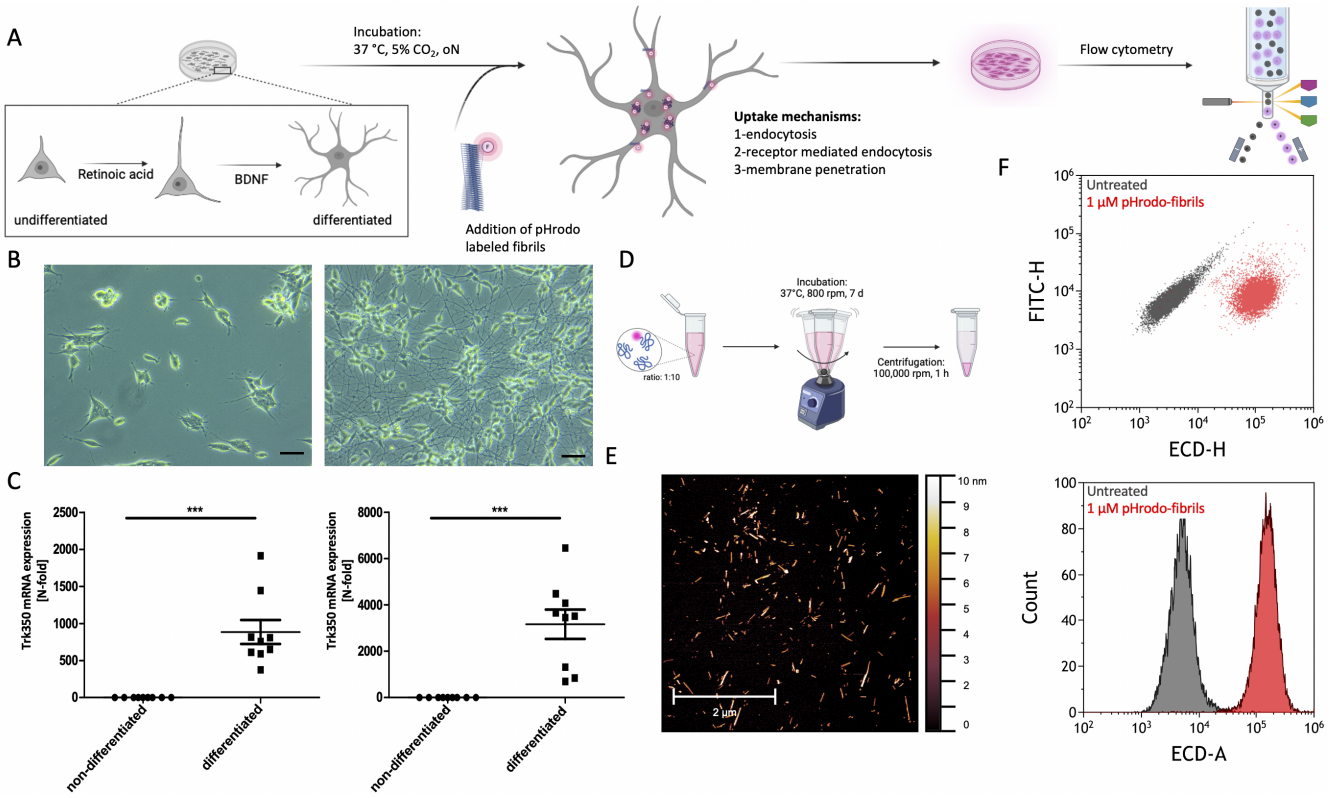

Figure 5.1: Overview of the fluorescence assay to detect fibril uptake by differentiated SH-SY5Y. (A) Schematic illustration of the workflow of the fluorescence assay. (B) Microscopy imaging of undifferentiated (left) and differentiated (right) SH-SY5Y cells. Scale bar (black) represents 50 µm. (C) Differentiation of SH-SY5Y was confirmed by the increased transcription level of the marker genes *trk339* and *trk350*. Statistical analysis was applied using an unpaired student's t-test (*** = $p < 0.001$). (D) Schematic overview of the generation of pHrodo-labeled fibrils. (E) Atomic force microscopy of the labeled fibrils. (F) Analysis of flow cytometry as dot plot (upper), showing the FITC laser intensity against the intensity of the EDC laser and histogram (lower), plotting frequency against the intensity of the EDC laser. Shifting along the x-axis represents the uptake of pHrodo fibrils in the 1 µM fibril treated sample (red) compared to the untreated sample (gray).

To confirm the intracellular localization of fibrils and to exclude the possibility of interaction only with the extracellular lipid membrane, fluorescence microscopy using z-stack imaging was employed, allowing for a 3-dimensional visualization within the cells (Figure 5.2A-D). The fibrils, labeled with Atto-488 (green), were found within the actin signal (red) and in close spatial proximity to the nucleus (DAPI, blue). This fluorescence imaging unequivocally demonstrated that the fibrils had indeed penetrated the interior of the cell, indicating their interaction occurred intracellularly, not solely at the extracellular surface.

To further validate the uptake in SH-SY5Y, SDS-PAGE and western blot was performed (Figure 5.2E, F). The cells treated with fibrils exhibited a band at 15 kDa, corresponding to the size of the monomeric form of αS. Detection was done using the fluorescent dye pHrodo. No band was detected in untreated samples (Figure 5.2F). The western blot signal for actin across different samples validates that an equal number of cells was applied to all samples (Figure 5.2E). In a supplementary control sample, which excluded cells and was designed specifically to examine if fibrils adhered solely to the plate or Eppendorf tubes because of their sticky nature, no pHrodo-labeled αS monomers were detected. This control highlights

the essential role of cells in the transfer of fibrils, showing that a brief 5-min centrifugation at 3,000 rpm is inadequate for pelleting the fibrils. Ultimately, a second method validated the incorporation of fibrils into the cells, evidenced by the detection of labeled αS within the treated cells.

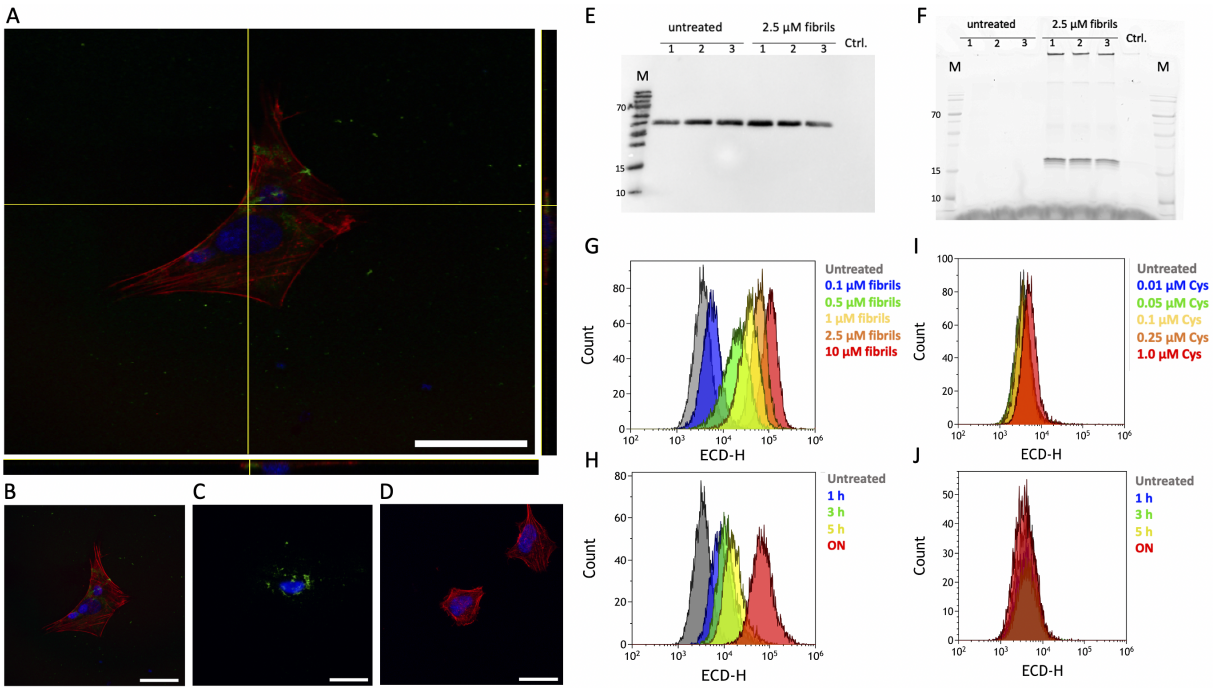

Figure 5.2: Validating of the fluorescence assay by control experiments. (A) 3-dimensional fluorescence microscopy images of differentiated SH-SY5Y cells treated with 1 µM Atto-488 labeled fibrils (green) as a z-stack. Actin signal is shown in red and the Nucleus in blue. Due to the z-stack it is confirmed that the fibrils are indeed intracellular. (B,C) Fluorescence images of differentiated SH-SY5Y cells treated with 1 µM Atto-488 labeled fibrils (green), showing the spatial proximity to the nucleus (blue). (D) Fluorescence images of untreated, differentiated SH-SY5Y cells. Scale bar of each microscopy images represents 35 µm. (E) Western blot of the actin signal of the cell lysate of untreated and pHrodo-labeled fibril SH-SY5Y cells in triplicates as well as a control without cells. This shows that the same amount of the cells was applied to the gel. (F) SDS-PAGE of cell lysate of untreated and pHrodo-labeled fibril SH-SY5Y cells in triplicates as well as a control without cells to detect the fibrils within the cells. Detection was performed by measuring the fluorescence of the pHrodo dye. (G-J) Analysis of flow cytometry as histogram, plotting frequency against the intensity of the EDC laser. In the experiment the concentration of fibril treatment (ranging from 0.1 to 2.5 µM) (G) and the duration of exposure (from 1 hour to overnight (oN)) (H) was varied. Shifting along x-axis represent the uptake of pHrodo fibrils in treated samples compared to the untreated sample (gray). As a control, the equivalent amount of pHrodo-Cys was used under the same conditions with different concentrations (I) and duration of exposure (J), to validate that the dye alone cannot be uptaken by cells.

The uptake process was characterized as being dependent on both the concentration of fibril treatment (ranging from 0.1 to 2.5 µM) and the duration of exposure (from 1 hour to overnight), indicating that both time and concentration significantly influence the process. The trend is further highlighted by the shift along the x-axis in the histogram, which indicates variations in the measured parameter under different conditions, underscoring the dependency on both factors (Figure 5.2G,H). However, to ascertain that the observed effect was indeed attributed to the fibrils rather than being an artifact of the fluorescent dye, a control was introduced by attaching pHrodo to a cysteine (pHrodo-Cys). The control samples treated

with the equivalent amount of pHrodo-Cys showed no shift in the population treated compared to the untreated sample (Figure 5.2I,J). This observation highlights that the fluorescence signal exclusively corresponds to the uptake of the fibrils and not merely the dye itself. Notably, when the samples treated with pHrodo-labeled fibrils were mixed with those treated in a similar manner with pHrodo-Cys, two distinct populations emerged (SI Figure 5.6). Two possible conclusions can be drawn form this: *i.)* The uniformity in cell response regarding fibril uptake is evident, as only a single population is observed in our data via flow cytometry. This suggests that all cells internalize fibrils in a similar manner, without the presence of distinct subpopulations that would indicate variable uptake capabilities among cells. *ii.)* The crucial role of the highly structured amyloid fibrils in facilitating the uptake of the fluorescence dye is highlighted. This points to a significant interaction between the fibrils and the internalization process, which may involve membrane proteins or direct penetration of the membrane bilayer, underlining the intricate relationship between the fibrils' structure and their cellular uptake mechanism.

5.4.2 Post-exposure upregulated proteins are not involved in fibril uptake.

Validation of the fluorescence assay revealed a uniform shifted towards pHrodo positive cells, indicating a consistent uptake of fibrils across all cells. To gain a snapshot of the proteins upregulated in the cellular answer when infiltrated by fibrils, NGS was performed (Figure 5.3).

Therefore, NGS analysis was performed on the entire cell population to further investigate this response. Three experimental groups, each with four replicates were investigated: *i.)* cells exposed to 2.5 µM unlabeled fibrils, *ii.)* cells treated with 2.5 µM pHrodo-labeled fibrils, and *iii.)* an untreated control group. The selection of these groups was based on the hypothesis that the pHrodo-labeled fibrils might exert a milder impact on cells compared to the unlabeled fibrils, due to the increased hydrophobic characteristics caused by the labeled dye. After preprocessing of the raw NGS data, the differentially expressed genes were identified between treated and untreated groups (Figure 5.3).

In contrast to the untreated sample, there were sets of RNA sequences that were either upregulated or downregulated (Figure 5.3A). Within this chapter, our focus is solely on the upregulated genes. Upon closer examination, we identified 11 upregulated genes (Figure 5.3B), with the majority playing a role in the activation of immune cells or initiating cascades of internal defense mechanisms. The only membrane-bound protein identified is ICAM-1, making it a particularly interesting candidate interacting with fibrils on the membrane surface. The upregulation of these genes was notably more pronounced in the group treated with unlabeled fibrils, though cells treated with pHrodo-labeled fibrils exhibited a similar trend. Our qPCR analysis confirmed that 7 out of the 11 genes were upregulated upon exposure to fibrils (Figure 5.3C,D). Intriguingly, 3 of the examined genes were found to be downregulated according to qPCR results, which contradicted their upregulated pattern observed in the NGS data (Figure 5.3C). Consequently, these genes were excluded from further analysis.

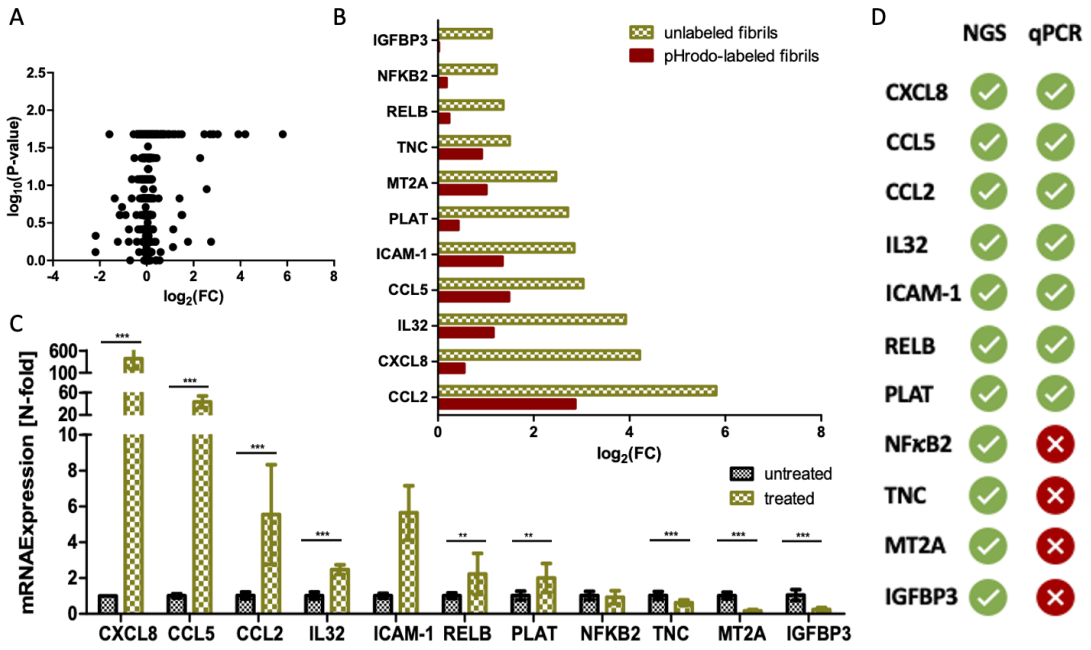

Figure 5.3: Validating of the NGS data. (A) Volcano plot based on the transcriptome data of cells treated with 2.5 µM fibrils, generated by NGS. The log of the fold change is plotted against its p-value. The fold change was related to an untreated control group. Each dot represents an mRNA and indicates whether it is upregulated or downregulated in the sample relative to the negative control. (B) 11 upregulated genes were identified from the NGS data. In this bar graph, cells treated with 2.5 µM unlabeled fibrils (yellow) or with pHrodo-labeled fibrils (red) were plotted. A similar tendency of upregulation can be recognized for all proteins. However, the samples treated with unlabeled fibrils show a stronger upregulation. (C) Identified upregulated genes were validated by qPCR in 3 technical replicates and 3 biological replicates. The transcription levels of upregulated genes in SH-SY5Y treated with 2 µM fibrils (yellow) were compared with untreated cells (black). Statistical analysis was applied using an unpaired student's t-test. *=p<0.05, **=p<0.01, ***=p<0.001. (D) Overview of transcriptional upregulation detected by NGS and qPCR. Upregulated gene transcription was marked with a green arrow indicating which method confirmed this result.

In the initial data analysis, we explored the impact of upregulated proteins on fibril uptake. To this end, cells underwent siRNA treatment to suppress protein expression (Figure 5.4A). To confirm the successful delivery of siRNA into the cells, fluorescently labeled siRNA was utilized (Figure 5.4B). The observed shift of the population along the y-axis confirmed the entry of siRNA into the cells via electroporation. Suppressing the expression of individual genes through siRNA did not reveal any difference in fibril uptake when compared to the positive control (cells treated with fibrils) after overnight treatment (Figure 5.4C). Consequently, it was demonstrated that none of the upregulated proteins play a role in fibril uptake under these experimental conditions.

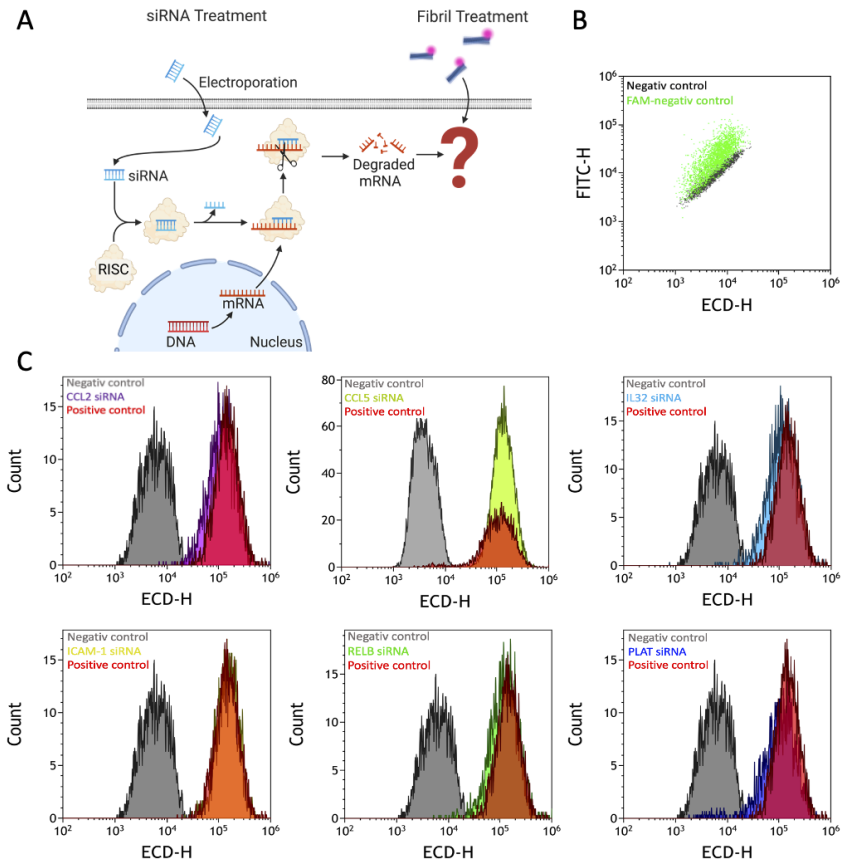

Figure 5.4: The upregulated proteins are not involved in the uptake of fibrils. (A) Schematic overview of how siRNA prevents transcription. The siRNA was introduced into the cell via electroporation. Intracellular, it can interact with the mRNA in a single-stranded manner and initiate its degradation. The question of this experiment remains whether the uptake of the fibrils is influenced by the suppression of the expression of the identified upregulated genes. (B) A control experiment in which siRNA labeled with the fluorophore FAM was used to verify that the cells take up the siRNA. Compared to the negative control (gray), the population treated with FAM-siRNA shifts along the y-axis (green), indicating uptake of the siRNA. (C) The expression of the individual upregulated genes are suppressed with siRNA and then the uptake of the fibrils is validated. In the negative and positive control, the proteins were treated with a non-targeting siRNAs control (negative control-siRNA from Thermo Fischer). Subsequently, the negative control was not treated and the positive control was treated with 1 µM fibrils, which explains the shift of the population along the x-axis. All samples treated with siRNA targeting one upregulated gene behave similarly to the positive control.

5.4.3 Membrane-bound ICAM-1 does not drive the fibril uptake

Considering that ICAM-1 primarily functions in cell adhesion and immune responses and is linked to actin through a signaling cascade, it roses the question of whether ICAM-1 is involved in the uptake of fibrils via micropinocytosis or opening of junctions (Figure 5.5A). Micropinocytosis is a cellular process through which small particles are engulfed by forming vesicles called micropinosomes. Intriguingly, some indications emerged, as a micropinocytosis inhibitor appeared to affect fibril uptake [292]. While ICAM-1 and micropinocytosis have not shown a direct connection so far, there are potential indirect interactions within the broader context of cellular responses to infections or other stimuli.

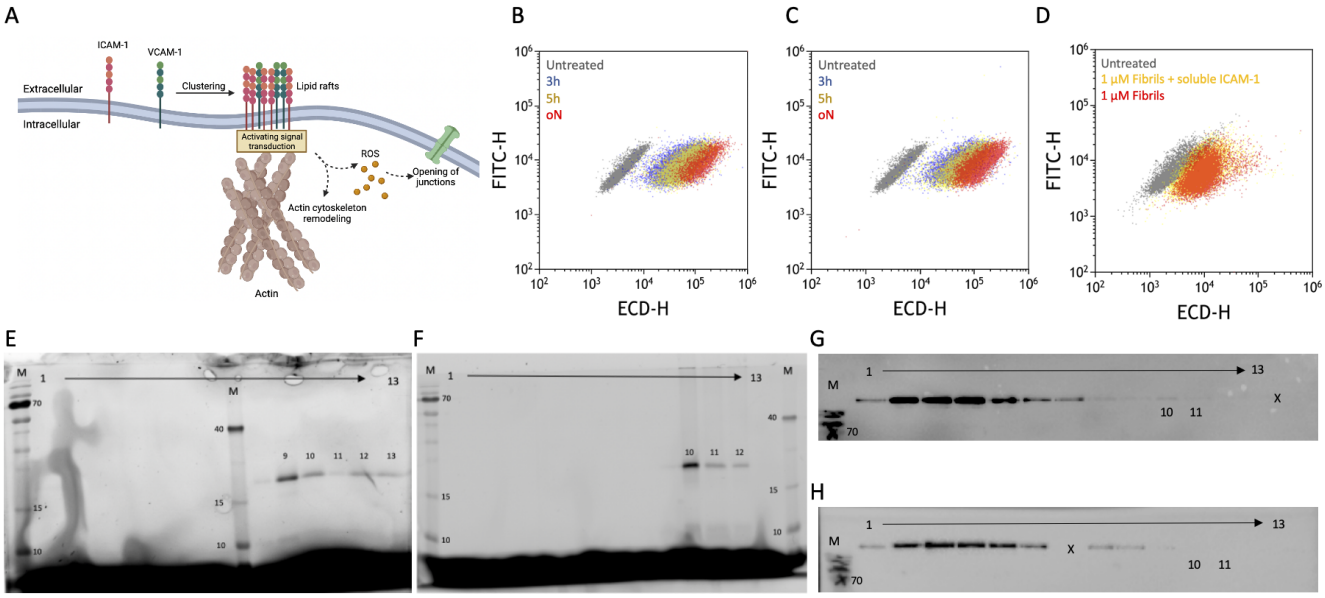

Figure 5.5: ICAM-1 interacts with fibrils but is not involved in fibrillar uptake. (A) Schematic illustration of the functionality of ICAM-1. Together with VCAM-1, ICAM-1 clusters into lipid drafts, which can induced a cascade to remodel the actin cytoskeleton and opening the junctions in the membrane. (B, C) Analysis of flow cytometry as histogram, plotting frequency against the intensity of the EDC laser. In the experiment, (B) ICAM-1 was downregulated by siRNA and (C) a control treated with non-target siRNA were used. By varying the duration of exposure (from 3 hour to overnight (oN)) no impact of the absence of ICAM-1(B) on fibril uptake was detected in comparison to the control (C). (D) By adding the soluble part of ICAM-1 extracellular to the cells as competitive interaction partner, no difference in terms of the uptake behavior of fibrils was detected. (E-H) DGC fractions, analyzed by SDS-PAGE or western blot, are numbered from 1 to 14, with low-density fractions given lower numbers and higher density fractions given higher numbers, x marks the spot on which no sample was applied. Two different protein markers were used: PageRuler^{TM} pre-stained protein ladder, in which the size of the bands in kDa was written to the right of the marker band, and Spectra^{TM} Low Range protein ladder, in which the size of the bands in kDa was written to the left of the bands. αS fibrils are obtained in higher-density fractions 9-13. SDS-PAGE was performed to analyze samples containing (E) pHrodo-labeled fibrils and (F) pHrodo-labeled fibrils pre-incubated with ICAM-1. ICAM-1 do not change the fibrillar structure, since in both samples the αS is detected most dominantly in fraction 9-11. Western blot was performed to anaylze samples containing (G) pHrodo-labeled fibrils pre-incubated with ICAM-1 and (H) ICAM-1 alone. ICAM-1 is found predominantly in fraction 1-8. Interestingly, in the sample pre-incubated with fibrils a subtle band is found in fraction 10 and 11, in which also the fibrils occur predominantly.

Therefore, we thoroughly investigated the influence of ICAM-1. However, when the protein was downregulated using siRNA, it had no impact on internalization, even when varying the incubation duration (Figure 5.5B,C). Additionally, adding the soluble domain of ICAM-1 as a competitive interaction partner extracellularly did not alter the uptake, either (Figure 5.5D). The rationale behind this approach was that by binding the soluble ICAM-1 component, the binding sites on the fibrils might already be occupied, preventing membrane-bound proteins from binding and potentially hindering uptake. Here it must be noted, that the uptake in general was not as efficient as it has been in previous experiments. Only a slight shift along the x-axis was detected in the fibril treated sample. However, the sample treated with fibrils and soluble ICAM-1 showed the same shift, meaning that the cellular uptake was similar to the positive control (red). Our experiments did not reveal any differences in either the competitive

environment or the downregulated variant, ultimately suggesting that ICAM-1 does not influence the uptake of fibrils into the cells.

Considering the lack of a significant role for ICAM-1 in the fibril uptake mechanism, the question emerged regarding the potential interaction of ICAM-1 with firbils. To explore this further, sucrose density gradient centrifugation (DGC) experiments were performed. The analysis of size distribution via DGC revealed that αS fibrils are high molecular weight assemblies predominantly sedimented in the higher-density fractions (Figure 5.5E).

In the sample where ICAM-1 was incubated with αS fibrils, αS was also present in high molecular weight assemblies, primarily within fraction 10 and 11 (Figure 5.5F). However, an exceptionally subtle ICAM-1 band was observed in fraction 10 and 11 (Figure 5.5G), which is not detected in the ICAM-1 alone sample (Figure 5.5H). This subtle presence hints at the possibility of a minimal interaction between ICAM-1 and fibrils. While this interaction does not affect fibril internalization, it implies that ICAM-1 might play a role in activating the immune system.

5.5. Discussion

In this study, we established an assay that enables the validation and quantification of fibril uptake. As a result, the uptake of fibrils by cells is dependent of both time and concentration. This process is specific to fibrils, requiring the presence of fibril components, as cells do not take up a Cys-pHrodo control. Moreover, it was characterized that the entire cell population is capable of taking up fibrils. This observation is significant because it suggests that cells can uniformly uptake fibrils without exhibiting specific and rapid responses to environmental influences, which could otherwise lead to variations within the population. Thus, it highlights that all cells are equally susceptible to fibrils. An interesting next step is to investigate whether uptake is caused by penetration into the cells [439]. To this end, we suggest to use mimicking systems of cell membranes, such as unilamellar vesicles. Studying fibril uptake in these artificial membrane systems could further confirm that the process occurs independently of the involvement of intra- or extracellular proteins, or initiators of protein cascades.

NGS analysis enabled the identification of crucial proteins during fibril infiltration, with 7 out of the 11 upregulated proteins being validated through qPCR. Although some studies have indicated an upregulation of the NFκB2 pathway in response to fibril treatment, suggesting a significant involvement [440], our study could not replicate this finding. While our NGS analysis indicated a minor upregulation of NFκB2, subsequent validation with qPCR failed to corroborate this finding. Consequently, our data did not conclusively identify the upregulation of any particular process or pathway. Nevertheless, it is notable that many of the identified upregulated proteins are implicated in defense mechanisms against invasions, such as viral infections [441]. Through our experiments, we demonstrated that certain proteins, including ICAM-1 as a membrane protein, do not influence fibril intake. DGC results suggest a potential interaction between ICAM-1 and fibrils, which would require confirmation through other methods. In viral infections, ICAM-1 can be upregulated on the surface of infected cells and can trigger an increase in viral infectivity via interactions [442, 443, 444]. The role of ICAM-1 in the infiltration of fibrils could not be clarified in this study. However, it has no influence on the uptake of fibrils but might have a possible role in fibril-related immune responses.

The question of which process the proteins are involved in — *i.)* fibril internalization, *ii.)* degradation of fibrils via defense mechanisms, or *iii.)* self-protection by activating inflammatory responses — should be

investigated in this project. From these preliminary data, it appears that while these upregulated proteins may not directly influence fibril uptake, they are likely to be involved in *ii.)* and *iii.)*. Further investigation is necessary to explore these functions in depth. Additionally, it is crucial to establish the relevance of the identified proteins in disease-contexts, for instance, by analyzing their concentrations in the cerebrospinal fluid (CSF) of patients with synucleinopathies compared to a control group. Confirmation of their significance in diseases could render these proteins promising candidates as potential biomarkers in diagnostic tools.

5.6. Material and Methods

5.6.1 Transformation, expression and purification of αS

The protein αS was encoded in the expression vector pt7-7 or the C140 mutation of αS (αS-C140) in pt7-7-αS140C, and expressed in *Escherichia coli* (*E. coli*) strain BL21(DE3). For the transformation step, 10 ng of the plasmid was introduced to the cells, followed by a 10 min incubation. Subsequently, the cells underwent a heat shock at 42 °C for 6 s, then were cooled on ice for 2 min. After incubating at 37 °C, with shaking at 800 rpm for 1 h, the cells were plated on LB-agar plates supplemented with 100 µg/ml ampicillin and incubated at 37 °C overnight. The liquid pre-culture was prepared containing 2YT medium with 100 µg/ml ampicillin, was inoculated with *E. coli* BL21(DE3) pt7-7 and incubated at 37 °C and 110 rpm overnight. The main culture (500 ml LB medium containing 100 µg/ml ampicillin, were inoculated with the cells from the liquid pre-culture. After reaching an OD_{600} of 0.6, the cells were induced with a final concentration of 1 mM IPTG. The culture was incubated for growth for 4 h at 37 °C and 110 rpm. The cells were harvested at 5,000 xg, 4 °C for 20 min. For purification, the cells were heated up to 95 °C for 10 min, before they were lysed by sonification. The purification of αS was conducted following the methodology outlined in Mirecka *et al.* [350], incorporating all modifications detailed in Agerschou *et al.* [353]. Subsequent to purification, the protein solutions were aliquoted, flash-frozen in liquid nitrogen (N_2), and stored at -80 °C until needed.

5.6.2 Labeling of αS-C140

αS was site-specifically labeled at a single position by introduction of a cysteine at residue 140. For labeling reactions, freshly purified αS (typically 200–300 µl of approximately 200 µM protein) was incubated with 5 mM TCEP for 30 min at room temperature (RT) to reduce the cysteines. The protein solution was passed over high-perfomance liquid chromatographie (HPLC) to remove TCEP and subsequently lyophilized. The protein was dissolved in 50 mM HEPES (pH 7.6) to a final concentration of 1 mg/ml. The dye pHrodo-maleimide (pHrodo^{TM} Red C2-maleimide from life technologies) was freshly solved in DMF. The protein was incubated with the dye in a (protein:dye) ratio of 1:0.1 at 25 °C, 450 rpm for 2 to 4 h. Afterwards, a HPLC was performed to remove of unreacted dye. HPLC was performed on an Agilent 1260 Infinity system using an Agilent Zorbax SB300 C8, 5 µm, 4.6x250 mm column at 50 °C column temperature. A flow rate of 4.0 ml/min was applied. The gradient from 40% to 64% acetonitrile (ACN) was used. After the gradient, the column was washed for 4 min with 64% ACN with 0.1% TFA. Re-equilibration was performed for 6 min using 40% ACN.

5.6.3 Fibril formation

Purified pHrodo-labeled αS was mixed with WT αS at a ratio of 1:10 to achieve a final concentration of 25 µM in sterile 1x PBS. The αS monomer solution was then incubated along with a glass bead under constant shaking at 800 rpm for 5 days at 37 °C. Following the incubation, the pre-formed fibrils were centrifugated at 100,000 xg for 1 h. Subsequently, the supernatant was removed and the fibril-containing pellet was resuspended in sterile PBS. The concentration was calculated on monomer units, with the assumption that 80% of the monomers underwent conversion to fibrils [420].

5.6.4 Atomic Force Microscopy (AFM)

AFM images were captured using a Bruker Multimode 8 microscope equipped with ScanAsyst-Air cantilevers, employing the ScanAsyst PeakForce Tapping Mode in air. A 10 µl aliquot of the protein

solution was applied to a freshly cleaved mica and incubated for 10 min at RT under humidified conditions. The sample was then washed five times with 100 µl distilled water and subsequently dried using gaseous N_2. The software Gwyddion was used for processing the AFM images.

5.6.5 Density Gradient Centrifugation (DGC)

The samples were added on a discontinuous sucrose gradient and centrifuged for 3 h at 259,000 xg at 4 °C in a TLS-55 rotor (Beckmann). The sucrose gradient (as described in [375]) was composed of the varying volumes and concentrations (w/w, from bottom to top): 300 µl of 60%, 200 µl of 50%, 200 µl of 25%, 400 µl of 20%, 400 µl of 15%, 150 µl of 10% and 400 µl of 5%. The gradient was carefully layered stepwise in an 11 x 34 mm polyallomer centrifuge tube (Beckmann). The sucrose gradient was separated stepwise in 142 µl fractions resulting in 13 fractions which the lower number containing a smaller amount of sucrose.

5.6.6 Cell culture

SH-SY5Y cells were cultured in Dulbecco's modified eagle's medium (DMEM from Gibco) supplemented with 10% fetal calf serum (Sigma, F9665) and 1% penicillin/streptomycin (ThermoFisher, 15140122) in T75 tissue culture flasks (Sarstedt, 83.3911.002) in a humidified incubator with 5% CO_2 at 37 °C. Depending on their confluence, cells were passaged every three to five days.

For the differentiation, cells were seeded in well plates (Sarstedt, Cell+ treated). Upon reaching 60-70% confluence, the cells were treated with 1 mM retinoic acid for 5 days, with the medium being replaced every 2 days, and incubated in 5% CO_2 at 37 °C. Subsequently, 40 ng brain-derived neurotrophic factor (BDNF) form Sigma-Aldrich were added to the DMEM, containing only 1% penicillin/streptomycin for 3 days with daily medium exchanges. The treatment was concluded on day 9 [438].

5.6.7 Flow cytometry

For the treatment, the medium was removed from the cells and a fresh medium containing the supplements, such as fibrils or pHrodo-Cys, was added. After an incubation time, the supernatant was discarded and the cells trypsinized for 5 min at 37 °C. Afterwards, the cells were pelleted by centrifugating at 3,000 xg for 5 min, washed with PBS and centrifuged again. Then, the cells were resuspended in PBS and analyzed by Flow Cytometry CytoFLEX S from Beckman Coulter. The data was analyzed by the Kaluza software of Beckman Coulter. An example of the evaluation is shown in SI Figure 5.7. The side scatter (SSC) is plotted against the forward scatter (FCS) to identify cells of interest based on size and granularity. The events form two populations (SI FIgure 5.7A): depris and cells. The population of cells is selected and plotted in the second graph: FSC-h against FSC width (SI FIgure 5.7B). This allows the cells to be divided into single and doublet cells. The single cells are then plotted against the EDC laser (λ_{ex}: 561 nm and λ_{em}: 610 nm), which can detect the pHrodo-dye (SI FIgure 5.7C). A shift in the direction of the x-axis shows a higher intensity of the dye, which corresponds to pHrodo-positive cells.

5.6.8 siRNA treatment

The medium of the differentiated SH-SY5Y cells were discarded and trypsin was added and incubated for 10 min at 37 °C. Afterwards the cells were centrifuged at 3,000 rpm for 5 min and washed with PBS. After a second centrifugation step at 3,000 rpm for 5 min, the cells were resuspended in 300 µl PBS and incubated on ice. After an incubation time of 10 min, 1 µl siRNA (from Ambion by life technologies)

were added to the cells and incubated again for 5 min on ice. The cell suspension was added in a cuvette and placed it into the device Gene Pulser Xcell from BioRad. The methods for mammalian cells Cos7 was used for cell electroporation. Immediately, 1 ml pre-heated medium was added and the cells were plated out in a 24 well plates with a final volume of 2.5 ml. The cells were incubated over night with 5% CO_2 at 37 °C before treated with fibrils.

5.6.9 RNA Isolation and cDNA synthesis

For RNA isolation, after treatment with fibrils, cells were incubated with trypsin for 10 min at 37 °C and, then, harvested by centrifugation at 5,000 rpm for 5 min. After counting the cells using Neubauer chamber, the cells were dissolved in TRIzol^{TM} (Thermofisher, 15596026) normalized to the same number of cells per ml. Each cell pellet was dissolved in 1 ml of TRIzol, and the RNA-containing aqueous phase was isolated. This was followed by digestion with DNase I and further purification using the Direct-zol RNA Miniprep kit (Zymo Research, R2050), following the procedures outlined in the kit's manual.

5.6.10 Next Generation Sequencing (NGS)

DNase digested total RNA samples used for transcriptome analysis were quantified (Qubit RNA HS Assay, Thermo Fisher Scientific, MA, USA) and quality measured by capillary electrophoresis using the FragmentAnalyzer and the 'Total RNA Standard Sensitivity Assay' (Agilent Technologies, Inc. Santa Clara, USA). All samples in this study showed high RNA Quality Numbers (RQN; mean = 10.0). The library preparation was performed according to the manufacturer's protocol using the VAHTS stranded mRNA Universal V6 Library Prep v9.1. Briefly, 250 ng total RNA were used as input for mRNA capture, fragmentation, synthesis of cDNA, adapter ligation and library amplification. Bead purified libraries were normalized and finally sequenced on the NextSeq2000 system (Illumina Inc. San Diego, CA, USA) with a read setup of 1x101 bp. For analysis the bcl convert tool was used to convert the bcl files to fastq files as well as for adapter trimming and demultiplexing. Sequencing reads were aligned to the GRCh38.95 reference genome utilizing the STAR aligner (version 2.7.0e) and gene annotations were based on GRCh38.p12. Gene expression metrics at both transcript and gene levels were generated using the software package RSEM (version 1.3.1). Samtools (version 1.3) was employed for the handling of BAM files. RSEM calculated read counts, transcript per million (TPM), and fragments per kilobase of transcript per million (FPKM) were used for further downstream analysis. The Wilcoxon rank-sum test were used to calculate the p-values for the differentially expressed genes within each two groups.

5.6.11 Quantitative Polymerase Chain Reaction (qPCR)

qPCR was performed using Luna Universal qPCR Master Mix from New England Biolabs. The 2x master mix was mixed with 0.25 µM forward and reverse primer (primer sequences are shown in table 5.1) and measured at qTOWER3 by Analytik Jena.

Table 5.1: Primers used for qPCR. Shown are the name of the primers with the addition forward (fwd) and reverse (rev) as well as the primer segeunce for the 5' to 3' direction.

Name of primer	Sequence of primer (5'>3')
CCL2 fwd	CTTCAAGACCATTGTGGCCA
CCL2 rev	AGTCTTCGGAGTTTGGGTTTG
CCL5 fwd	TCATTGCTACTGCCCTCTGC
CCL5 rev	TACTCCTTGATGTGGGCACG
CXCL8 fwd	TTGCCAAGGAGTGCTAAAGA
CXCL8 rev	ATTTCTGTGTTGGCGCAGTG
ICAM-1 fwd	AAGGAGCTGAAACGGGAG
ICAM-1 rev	GTGCGGCACGAGAAATTG
IFGBP3 fwd	ATCTACACCGAGCGCTGT
IFGBP3 rev	TGACGGCACTAGCGTTGA
IL32 fwd	GATGTTGAGGATCCCGCAAC
IL32 rev	TTCTCCTTCACCCAGGCCAGAA
M2TA fwd	TGCACCTCCTGCAAGAAA
M2TA rev	CAGCAGCTGCACTTGTCC
NFκB2 fwd	ATCGAGGTGGACCTGGTAAC
NFκB2 rev	TCCTTGGGCCCCACAGAAAC
RELB fwd	ATCAGTGGTGTTCAGCAGGG
RELB rev	CGTCTTGAACACAATGGCAA
TNC fwd	GAAGGTGGGGTCCTCAAGAA
TNC rev	ACGTGGTTAAACACCACTGG
PLAT fwd	CTACGAGGACCAGGGCATCA
PLAT rev	TGTAGGGCTTCTGGGCCAAC
GAPDH fwd	GGAAACTGTGGCGTGATGG
GAPDH rev	TGAGCTTCCCGTTCAGCT
Trk339 fwd	CTGCAAATGCAGTGCCTCTC
Trk339 rev	TTGCCCACCAGGATCAGTTC
Trk350 fwd	TCGGGAACATCTCTCGGTCT
Trk350 rev	TGTCTGGCTTGAGCTGACTG

For this study, we chose to report the results in terms of N-fold expression changes, rather than employing the ΔΔCt-method, due to our inability to identify suitable, expression-stable housekeeping genes (SI Figure 5.8 and Chapter 6; SI Figure 6.11).

5.6.12 Immunocytochemistry

For confocal imaging, the cells were seeded on coverslips. Four coverslips were transferred into one well of a 6-well plate (Sarstedt, 83.3920.300) and incubated under the UV-lamp for 30 min. Each well containing the coverslips was washed five times with 500 µl of PBS, before adding 500 µl of Poly-D-lysin. The coverslips were incubated for 1 h at 37 °C. After the incubation, Poly-D-lysin was discarded and the coverslips were washed five times with 500 µl PBS. Then the cells were seeded on the coverslips.

Table 5.2: Solutions for the preparation of immunocytochemically stained RIN-m5f cells. Shown are the name of solutions with each chemical compounds.

Solutions	Chemicals
Solution 1	40 ml PBS + 100 µl TritonX-100
Solution 2	20 ml solution 1 + 20 ml PBS
Solution 3	10 ml solution 2 + 0.25 g BSA
Solution 4	5 ml solution 3 + 5 ml PBS

After the treatment, the medium was discarded, and the wells were washed six times with 1 ml of PBS. 350 µl of 4% PFA was added, followed by an incubation of 20 min at RT. Afterwards the wells were washed eight times with 1 ml of PBS and then filled with 1.5 ml of PBS and stored at 4 °C until immunocytochemistry was performed.

The coverslips containing the cells were removed from the wells. To permeabilize the membrane, solution 1 (referenced in table 5.2) was added to the cells for 2 min at RT. The cells were blocked with solution 3 (table 5.2) and incubated at RT for 1 h. This was followed by a further incubation step with the antibodies Alexa FluorTM Plus 555 Phalloidin (ThermoFisher, A30106) for 1 h in the dark. The antibody was diluted 1:500 in solution 4 (table 5.2). Afterwards, the cells were washed six times with solution 2 (table 5.2) and the cells were incubated with 300 µM DAPI for 5 min at RT. The cells were washed four times with solution 2 (table 5.2) and then twice with PBS. The coverslips were then shortly dipped in ddH_2O and glued onto microscopic slides using Immu-Mount from Epredia. Confocal microscopy was performed on a Leica AF6000LX inverted microscope equipped with a Hamamatsu C9100-02-LNK00 EM CCD camera. Afterwards, the images were processed with the software Fiji to add a scale bar.

5.6.13 SDS-PAGE and Western blot

A 15% polyacrylamide bis-tris glycine gel was prepared for SDS-PAGE. The protein samples were mixed in a ratio of 1:5 with a 4x SDS-PAGE loading buffer (200 mM Tris-HCl pH 6.8, 400 mM DTT, 8% SDS, 0.4% bromophenol blue, 40% glycerol) before incubating for 15 min at RT. 3 µl Spectra Multicolor Low Range Protein Ladder from Thermo Fischer Scientific were utilized as size standard and 10 µl of the samples containing SDS-PAGE loading buffer were applied to the gel. An electric field with a constant voltage of 120 V was applied for 75 min. To detect fluorescent labeled proteins, an image was taken using the camera of the gel documentation system from BioRad. For SDS-PAGE, the gel was subsequently stained in staining solution containing 10% acetic acid, 25% EtOH and 250 mg Coomassie Brilliant Blue. This was done by briefly heating the gel in the microwave followed by an incubation period of 5 min while shaking at RT. Afterwards, the gel was distained in 10% acetic acid and 25% EtOH solution at RT under shaking. Finally, the stained proteins were recorded with the camera of the gel documentation system from BioRad. For the western blot, a PVDF membrane (Amersham Hybond from cytiva) was activated in EtOH and shortly incubated in tris/gycine-buffer from BioRad together with 6 Whatman papers. 3 Whatman papers are placed in a Trans blot Turbo chamber from BioRad followed by the membrane, the SDS-Gel and the remaining Whatman papers. An electric field with a constant voltage of 25 V was applied for 30 min. To determine the quality of the transfer, the membrane can be stained with Ponceau S. Afterwards, the membrane must be carefully destained by washing steps with MQ water and TBST. For the staining, the membrane was blocked in 5 ml 5% milk, which was dissolved in TBST, for 1 h at RT. This was followed by a further incubation step with the primary antibodies anti-hActin or anti-hICAM-1 (from R&D Systems) for 1 h at RT or overnight at 4 °C. The antibody was diluted 1:2,500 in 5% milk. The membrane was washed five times for 5 min with TBST. After that, the membrane was

incubated with the secondary antibody HRP-tagged goat anti-mouse antibody, diluted 1:5,000 in 5% TBST, for 1 h at RT. After that incubation time, the membrane was washed five times for 5 min with TBST. The membrane was incubated in Super Signal West Pico Plus from Thermo Scientific for a few minutes and the signal was detected with the documentation system from BioRad.

5.7. Acknowledgments

This project has received funding from the European Research Council under the European Union's Horizon 2020 research and innovation program, grant agreement No. 726368. We acknowledge Dennis Hasenklever for support with flow cytometry and Lothar Gremer for his help on labeling αS. We also would like to thank Thorsten Wachmeister and the Genomics and Transcriptomics Labor of the HHU for the performance of NGS. Figures were partially created with BioRender.com.

5.8. Supplementary Information

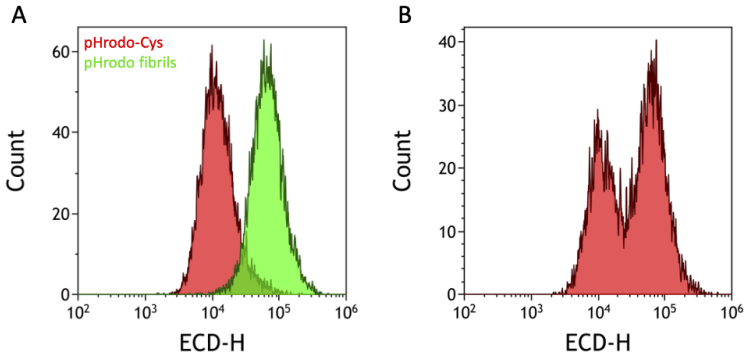

Figure 5.6: Pre-mixing experiment of samples treated with pHrodo-labeled fibrils and pHrodo-Cys. (A) Analysis of flow cytometry as histogram to compare samples treated with pHrodo-Cys (red) and pHrodo-labled fibrils (green). Shifting along x-axis represents the uptake of pHrodo fibrils in treated samples compared to the pHrodo-Cys treated cells which did not intake the dye. (B) To illustrate that flow cytometer can distinguished between cells that take up the dye and those that do not, the pHrodo-Cys and pHrodo-fibrils treated samples were mixed in a 1to1 ratio, before analyzing again with Flow cytometer. The results are shown as a histogram. This underlines that if the cells would behave differently in terms of uptake fibrils, two populations would be detected during flow cytometer analysis.

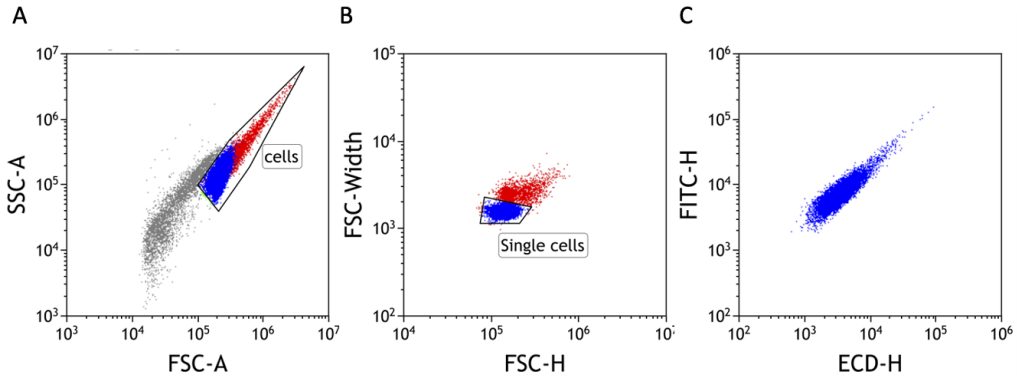

Figure 5.7: Evaluation of flow cytometry. (A) The side scatter (SSC) is plotted against the forward scatter (FCS) to identify cells of interest based on size and granularity. The events form two populations: depris and cells (marked). (B) The population of cells is selected and plotted in the second graph: FSC-H against FSC-Width. This allows the cells to be divided into single and duplicate cells. (C) The single cells are marked in blue and are then plotted in the next diagram. The FITC laser is plotted against the EDC laser (λ_{ex}: 561 nm and λ_{em}: 610 nm). The EDC channel can detect the pHrodo-dye. A shift in the direction of the x-axis shows a higher fluorescence intensity of the dye, which corresponds to pHrodo positive cells.

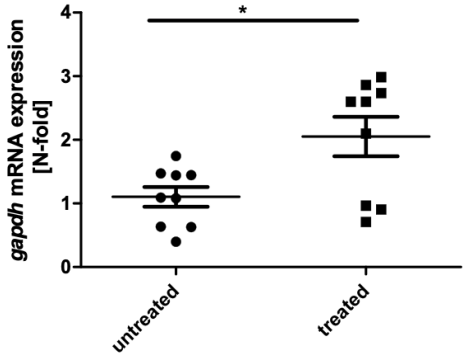

Figure 5.8: GAPDH is no reliable housekeeper for fibril treated samples. The mRNA level of *gapdh* in SH-SY5Y treated with 2 µM fibrils were compared with that of untreated cells in 3 technical replicates and 3 biological replicates. The samples show an significant increase of the transcription level of *gapdh* in the treated sample. Statistical analysis was applied using an unpaired student's t-test. *=$p<0.05$. Therefore, the ΔΔCt-method was not used for evaluation.

6

AN ISLET AMYLOID POLYPEPTIDE OLIGOMER MODEL FOR THE STUDY OF AMYLOID AGGREGATION AND OLIGOMER INDUCED PATHOPHYSIOLOGY

This Chapter reflects content on the following publication.

6.1. Publication information

Author: Anne Pfitzer[*a], Celina M. Schulz[*a], Robin Backer[a], Filip Haseck[a] and Wolfgang Hoyer[ab]

a: Institut für Physikalische Biologie, Heinrich Heine University Düsseldorf, Düsseldorf, Germany
b: Institute of Biological Information Processing (IBI-7: Structural Biochemistry) and JuStruct: Jülich Center for Structural Biology, Forschungszentrum Jülich, Jülich, Germany
*: These authors contributed equally: Anne Pfitzer, Celina M. Schulz

in preparation

6.2. Abstract

Type 2 *diabetes mellitus* (T2DM) is a multifactorial metabolic and widespread disease. In patients' pancreas islet amyloid polypeptide (IAPP) is found as aggregates. The aggregation process and toxicity of different aggregate species of IAPP are under intense investigation. As for other disease-related amyloidogenic proteins, oligomeric species of IAPP have been suggested to exhibit cytotoxic activity. Here, we developed an IAPP model, denoted dimIAPP, which assembles into curvilinear oligomers (dimIAPP-O) and remains stable in this conformation. DimIAPP is an engineered dimer of an IAPP cysteine mutant (C2S, C7S) connecting two monomers via a flexible $(G_4S)_4$-linker. We investigated the effect of this stable oligomer model, first, on the amyloid aggregation of IAPP and second, on stress gene transcription in pancreatic rat cells RIN-m5f. The aggregation of IAPP is partially inhibited by dimIAPP-O, indicating that it is not being incorporated into IAPP fibrils in the same manner as IAPP monomers but instead prevents amyloid assembly. DimIAPP-O as well as IAPP fibrils trigger stress responses in RIN-m5f cells, albeit IAPP fibrils upregulate more stress genes than dimIAPP-O do. We conclude the model to be a useful tool to gain further insights into the aggregation of IAPP and the characterization of the effect of stable, curvilinear oligomers on cells.

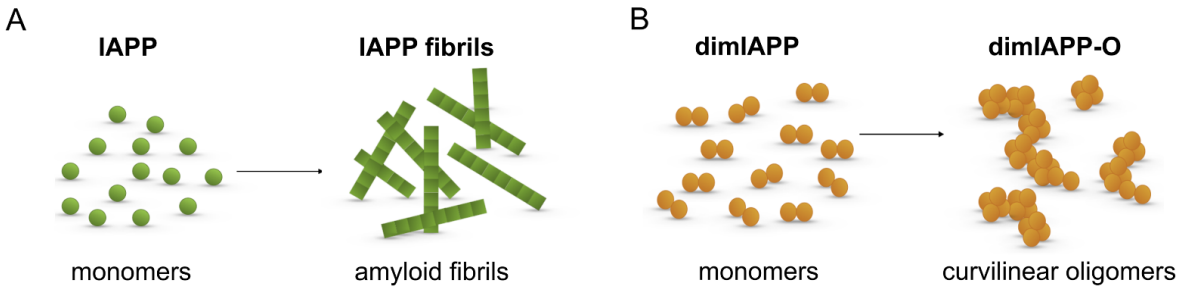

Figure 6.1: Schematic overview of the generation of oligomers using the model system dimIAPP or IAPP fibrils, respectively. (A) IAPP monomers form amyloid fibrils (green). (B) DimIAPP corresponds to two linked monomeric units of an IAPP cysteine mutant and forms stable curvilinear oligomers (orange).

6.3. Introduction

Loss of β-cell function in T2DM is caused by a multitude of insults. Islet amyloid was found in the pancreatic parenchyma of more than 90% of T2DM patients and is believed to inflict cytotoxicity [56, 445, 446, 447, 448, 449, 450, 451]. The main constituent of islet amyloid is IAPP, a 37-residue long peptide hormone co-secreted with insulin [452]. It plays a role in gastric emptying [453], glucose homeostasis [454], regulating satiety [455] and suppression of glucagon release [456]. Amyloid deposits are found in a plethora of diseases, including T2DM, Alzheimer's disease and Parkinson's disease. The unifying feature of these peptides is the characteristic cross-β structure adopted by their amyloid aggregates [457, 458]. In T2DM, prominent hyaline lesions were first described in 1901, more than 120 years ago [459, 460], in the pancreas of a young patient suffering from hyperglycemia and was later identified as amyloid depositions of IAPP in 1986 [461, 462].

Oligomeric IAPP species have gained increased attention as they might be important players in the pathogenic processes [20, 50, 56, 161, 449, 450, 451, 463, 464, 465, 466, 467]. In support of this, a poor correlation of IAPP amyloid load with β-cell death was observed [468]. Different natural and synthetic IAPP oligomer preparations were characterized and found to exhibit variable levels of toxicity, e.g., to induce apoptosis [469] or disrupt the cell membrane [192]. The exact linkage between IAPP oligomer formation and toxicity is unknown. It has been suggested that IAPP oligomers are related to the formation of a membrane channel inducing an upregulated Ca^{2+} influx or membrane disruption causing stress of the endoplasmic reticulum (ER) [192, 193]. However, oligomers are difficult to study, due to their transient nature [470], low population under standard conditions, and structural heterogeneity [165]. This complicates the identification of the most critical species in amyloid diseases [53, 471]. It also leads to an uncertainty regarding the position of different types of oligomers on or off the pathway towards amyloid fibrils [141, 165, 167, 472]. Therefore, it is crucial to invent reliable models for studying oligomers.

Studies on oligomers are not only of great interest in T2DM, but also in over 50 other diseases [11] associated with the assembly of amyloids, such as AD [473, 474, 475]. For Alzheimer's amyloid-β (Aβ), it was shown that low-molecular weight species are more toxic than monomers and fibrils [195]. Previously, our group invented a model for oligomer-forming Aβ40, called dimAβ [163, 169, 185]. DimAβ is a polypeptide containing two units of Aβ40 connected by a flexible glycine-serine linker. The linkage of two Aβ units does not affect Aβ conformation, but results in an increased local concentration which promotes the highly concentration-dependent oligomer formation. DimAβ assemble into stable curvilinear oligomers that faithfully reflect the properties of off-pathway Aβ oligomers previously observed in many labs, including the binding to dendritic spines and induction of tau missorting, a key factor in tauopathies [163, 476]. DimAβ oligomers provided insight into the properties of off-pathway Aβ oligomers and their relationship to amyloid fibrils [163, 169, 185]. For example, metastable dimAβ oligomers bind to the surface of Aβ fibrils and inhibit secondary nucleation [185]. Furthermore, studies employing dimAβ allowed to identify the importance of low pH, as present in endosomal/lysosomal compartments, for rapid Aβ oligomer formation [163].

Beside other amyloid peptides, generation of IAPP oligomer models are of great importance to improve our understanding of this type of aggregate species. As stable IAPP oligomers cannot be obtained directly from monomeric human IAPP for the reasons stated above, we tested here if oligomers can be obtained using an IAPP construct analogous to dimAβ. This approach is motivated by the sequence similarity of IAPP and Aβ [47, 477]. Moreover, certain Aβ and IAPP oligomers may be structurally and functionally related, as suggested by the cross-reactivity of oligomer-specific antibodies [50]. We introduce an engineered dimer of an IAPP mutant, called dimIAPP (Figure 6.2A), in which both subunits are connected via a flexible linker in a head-to-tail fashion. With the help of this model, we obtained

insights into the effect of oligomers on IAPP aggregation and pathophysiology.

6.4. Results

6.4.1 DimIAPP assembles into curvilinear oligomers

We developed an artificial dimer of an IAPP mutant called dimIAPP (Figure 6.1A), in analogy to the design of the artificial Aβ dimer dimAβ. In dimIAPP, two IAPP units are connected by a $(G_4S)_4$-linker. The linker is supposed to provide sufficient flexibility to the IAPP units, such that they are not restricted in adopting all assembly types accessible to natural IAPP. In order to avoid formation of aberrant disulfide bonds, the cysteines at positions 2 and 7 of both IAPP units were exchanged to serines (Figure 6.2A). This modification leads to loss of the disulfide loop connecting IAPP residues 2 and 7 under oxidizing conditions. In fibrils, amino acids (aa) 1-12 are not part of the core but located at the periphery [458, 478, 479], indicating that the Cys-to-Ser exchanges are not essential for IAPP aggregation. This is confirmed by kinetics studies [480], which show that loss of the disulfide loop actually promotes IAPP amyloid fibril formation. Furthermore, we note that dimIAPP is not C-terminally amidated.

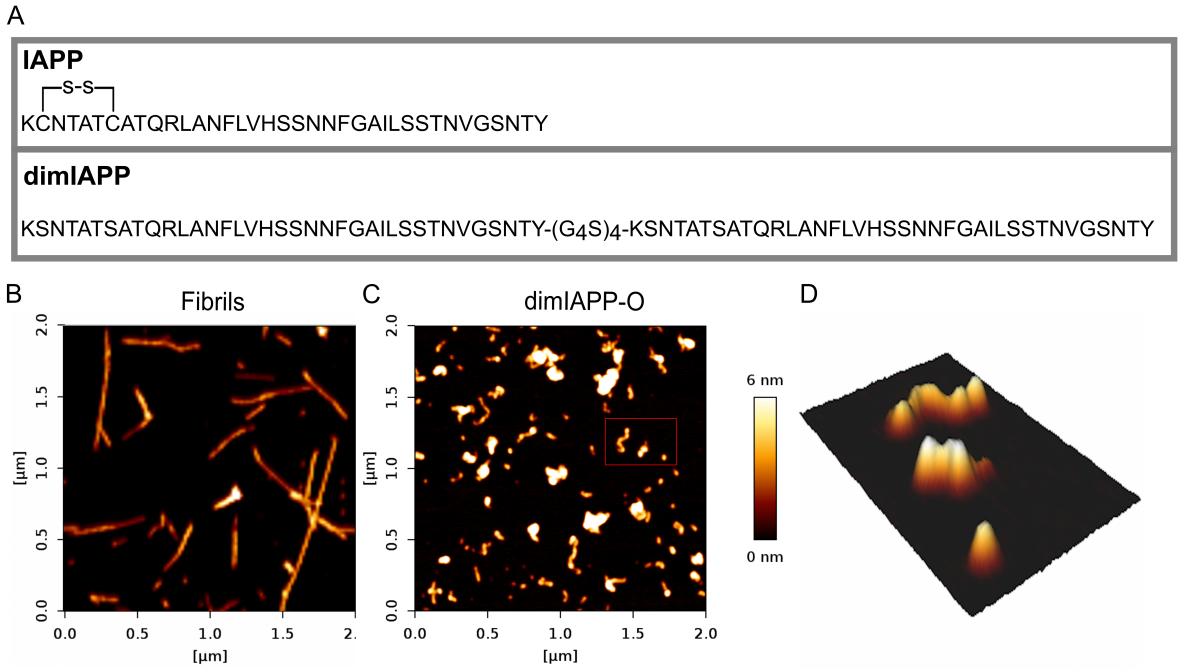

Figure 6.2: Model system for IAPP oligomers utilizing a tandem IAPP construct called dimIAPP. (A) Amino acid sequences of IAPP and dimIAPP. DimIAPP is an engineered dimer of an IAPP cysteine mutant. The subunits are connected via a flexible $(G_4S)_4$-linker to provide conformational freedom. (B,C) Morphologies of IAPP fibrils (B) and dimIAPP-O (C) after 16 h of quiescent incubation at 37 °C in 50 mM MES pH 6.5, 50 mM NaCl, imaged using atomic force microscopy (AFM). Color scale: height in nm. (D) 3 dimensional view of curvilinear oligomeric dimIAPP-O in a zoomed-in area of C (marked in a red box).

While IAPP formed amyloid fibrils upon incubation in 50 mM MES pH 6.5, 50 mM NaCl, dimIAPP assembled into spherical and curvilinear oligomers, as imaged by atomic force microscopy (AFM) (Figure

6.2B-D, SI Figure 6.7). These oligomers, which we named dimIAPP-O, are reminiscent of the metastable off-pathway oligomers formed by dimAβ [169, 163, 185]. DimIAPP-O exhibit a tendency to assemble into clusters (Figure 6.2B, SI Figure 6.7), which has also been observed for dimAβ oligomers at this slightly acidic pH [163].

To monitor the formation of dimIAPP-O and IAPP fibrils, we performed aggregation kinetics with the amyloid-specific dye Thioflavin-T (ThT). Initially monomeric IAPP exhibits an increase in ThT fluorescence attributed to the formation of cross-β containing amyloid fibrils (Figure 6.3A,B). In contrast, the preparation of dimIAPP-O showed no ThT fluorescence over 25 h (Figure 6.3A). At 0 h, almost double amount of the monomers remained in monomeric form, as it was detected in the supernatant fraction after centrifugation (Figure 6.3C, SI Figure 6.8). However, larger amorphous aggregates were also detected under the AFM at 0 h incubation (Figure 6.3D). During incubation, the oligomers get formed and adopt their stable and curvilinear oligomeric state (Figure 6.3D, see 16 h). Once it is formed into these curvilinear form, the structure of dimIAPP-O does not change, namely no increase in ThT signal could be detected for an incubation time of 20 h (SI Figure 6.9A). The ThT-negativity is a feature that distinguishes dimIAPP-O from dimAβ oligomers but does not provide insights into the structural organization of these oligomers, as the molecular basis of ThT binding to oligomers lacking cross-β structure is not well understood.

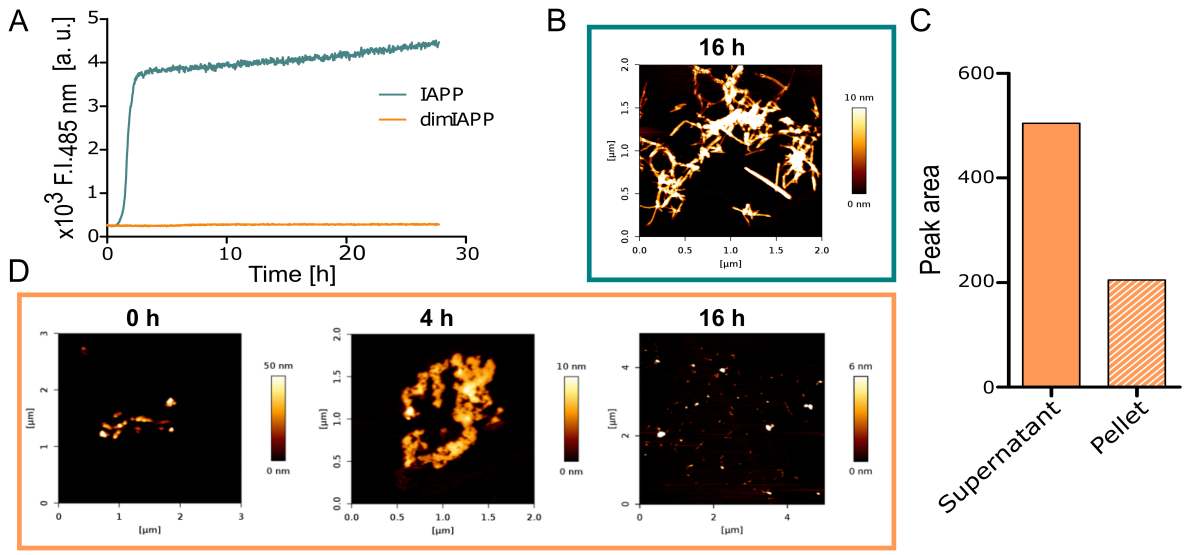

Figure 6.3: Monitoring the dimIAPP-O formation. (A) Aggregation kinetics of 2 µM IAPP (green) and 2 µM dimIAPP-O (orange) monitored by ThT. DimIAPP-O are ThT negative and do not show any change over a period of 25 h. (B) AFM image of 2 µM IAPP after aggregation kinetics. Color scale: height in nm. (C) Peak areas of a pellet and supernatant fraction of monomeric dimIAPP sample at 0 h analyzed via RP-HPLC. Before applying on HPLC, the sample was centrifuged at 11,000 rpm for 5 min (SI Figure 6.8). (D)Monitoring the dimIAPP kinetics from panel A via AFM. AFM images were taken at 0, 4 and 16 h. Color scale: height in nm.

6.4.2 DimIAPP-O inhibit aggregation of IAPP

We next investigated the effect of dimIAPP-O on IAPP amyloid fibril formation. The addition of dimIAPP-O to 3 µM monomeric IAPP (colored) inhibits the aggregation of IAPP when comparing it to

the equivalent monomer concentrations of IAPP (Figure 6.4, colored and black). Notably, 2 molecules of IAPP (in monomer units) equilibrate 1 molecule of dimIAPP (dimeric construct). This indicates that dimIAPP-O act differently from IAPP monomers in terms of their aggregation properties.

Adding substoichiometric concentrations of dimIAPP-O to 3 µM monomeric IAPP decelerates or completely inhibits the aggregation of IAPP (Figure 6.4A, colored and grey). At the end of this kinetic, small protein aggregates corresponding to the structure of stable dimIAPP-O could be detected under AFM (SI Figure 6.9B). This suggests small concentrations of dimIAPP-O to actively stop the nucleation or growth of the substrate IAPP.

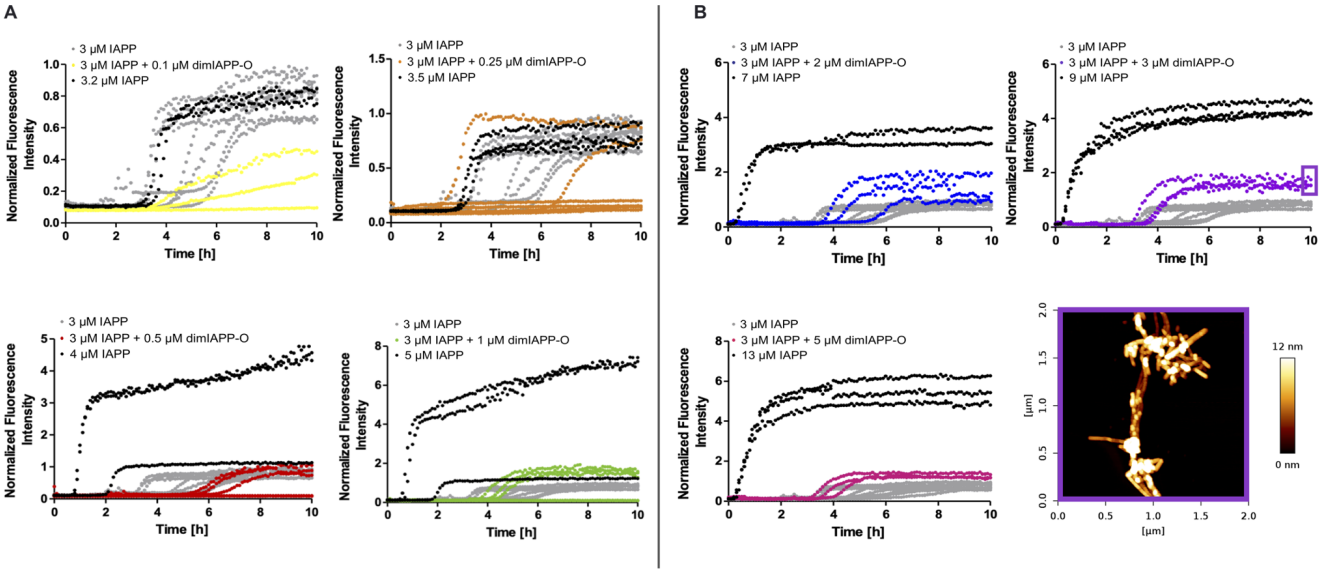

Figure 6.4: Influence of dimIAPP-O in low and high concentrations on IAPP aggregation kinetics. (A) Kinetics of 3 µM IAPP (grey) were incubated in presence of substochiometric concentration of dimIAPP. Kinetics of 3 µM IAPP with 0.1 µM dimIAPP-O (yellow), 0.25 µM dimIAPP-O (orange), 0.5 µM dimIAPP-O (red), 1 µM dimIAPP-O (green) was performed. For all approaches, 3 µM IAPP (grey) was used as control as well as the IAPP concentration representing the summed up concentration between dimIAPP units and monomeric IAPP (black). (B) Kinetics of 3 µM IAPP (grey) were incubated in presence of higher than stochiometric concentration of dimIAPP-O. Kinetics of 3 µM IAPP with 2 µM dimIAPP-O (blue), 3 µM dimIAPP-O (purple), 5 µM dimIAPP-O (pink) were performed. For all approaches, 3 µM IAPP (grey) was used as control as well as the IAPP concentration representing the summat concentration between dimIAPP units and monomeric IAPP (black). (C) AFM images were taken of 3 µM IAPP + 3 µM dimIAPP-O after aggregation kinetics (purple box). Color scale: height in nm. Size of image: 2x2 µm.

When adding dimIAPP-O in higher ratios than 1:1 to 3 µM IAPP, we observe no difference in the lag time in comparison to the 3 µM IAPP control (Figure 6.4B, colored and grey). This indicates that in high concentrations dimIAPP-O do not interfere with IAPP. Considering the higher plateau and the observation that dimIAPP-O act differently as monomers suggests that dimIAPP molecules might get triggered by IAPP monomers or aggregation species to leave their off-pathway state and built ThT-positive cross-β structures. In line, the formation of dimIAPP fibrils was observed by AFM when dimIAPP monomers were incubated at a concentration of 10 µM (SI Figure 6.9C). After kinetic measurements, fibril structures were detected by AFM, whereas dimIAPP-O could not be distinguished from IAPP fibrils in form of

curvilinear oligomers and exhibited the same appearance as the 3 μM IAPP control (Figure 6.4C).

However, in substochiometric ratios, dimIAPP-O are capable of inhibiting amyloid aggregation of IAPP and behaves differently regarding aggregation in comparison of IAPP monomers, which identify them as stable oligomers off the pathways towards amyloid fibrils.

6.4.3 Exposure of RIN-m5f cells to dimIAPP-O and IAPP fibrils activate cellular stress response

Next, to gain more insights on how the presence of the different aggregation species, IAPP fibrils or curvilinear dimIAPP-O, affects the induction of stress phenotypes in pancreatic RIN-m5f cells. Therefore, the upregulation of transcripts of stress markers associated with the ER and mitochondrial oxidative stress was investigated. We were interested exclusively in the effect of externally added IAPP fibrils and dimIAPP-O on stress genes. Therefore, the RIN-m5f cell line, derived from *Rattus norwegicus* was selected as the model cell line because rodent IAPP is aggregation incompetent due to six mutations primarily localized between aa 20 and 29. Contrary, human pancreatic cell lines express aggregation competent IAPP innately. The origin of the observed effect would not have been clearly assigned by the external addition of the species to human pancreatic cells.

Oxidative stress is believed to play a pivotal role in the pathogenesis of T2DM [481, 482]. In other diseases connected to the amyloid aggregation of peptides, such as AD, a higher production of ROS is observed [483]. Key oxidative stress markers are superoxide dismutase 2 (Sod2) and catalase (Cat) (Figure 6.5A). Sod2 converts two superoxide anion molecules into H_2O_2 while Cat reduces H_2O_2 to water (Figure 6.5A). After exposure to dimIAPP-O, *sod2* expression was significantly upregulated (20-fold) while treatment with IAPP fibrils did not alter the expression level compared to untreated cells (Figure 6.5B). Contrary to that a distinct effect was seen for *cat* expression. Exposure of RIN-m5f to dimIAPP-O resulted in a significant downregulation while exposure to IAPP fibrils resulted in almost 5-fold increased *cat* expression (Figure 6.5C).

When stressed, the cell activates different pathways to rescue itself before apoptosis is initiated. Here, we investigated the influence of dimIAPP-O and IAPP fibrils to four main players involved in the ER stress response (Figure 6.5A). Three of them are involved in rescuing mechanisms: Activating transcription factor 6 (Atf6), Pancreatic eukaryotic translation initiation factor 2α kinase (PERK) and Inositol-requiring protein 1 (IRE1) [484]. When those transducers are activated, they induce unfolded protein response (UPR) transcription factors X-box binding protein 1 (Xbp1) and activating transcription factor 4 (Atf4) [484]. One of the downstream targets of Atf4 is CCAAT-enhancer-binding protein homologous protein (Chop) [485]. Chop is a key player in apoptosis [486]. Here, all tested stress markers for ER stress, namely *atf6* (10-fold), *xbp1* (4-fold), *aftf4* (6-fold) and *chop* (5-fold) were significantly upregulated after the treatment with IAPP fibrils while only *chop* was upregulated approximately 3-fold after the treatment with dimIAPP-O (Figure 6.5D-G).

Another mechanism to react to stress situations is the formation of stress granules (SG) [153] whose formation is triggered by the phosphorylation of the downstream target of PERK and upstream regulator of Atf4: eukaryotic translation initiation factor 2α (eIF2α) [487]. Stress granules are condensates composed of untranslated RNA and proteins forming by liquid-liquid phase separation (LLPS) [488, 489, 490]. The protein class of Ras-GTPase-activating protein (GAP)-binding proteins (G3BP) is the central node of condensate assembly with specificity for unfolded RNA [491] to inhibit RNA-RNA interactions. This

supports G3BP to act as an RNA chaperone [492].

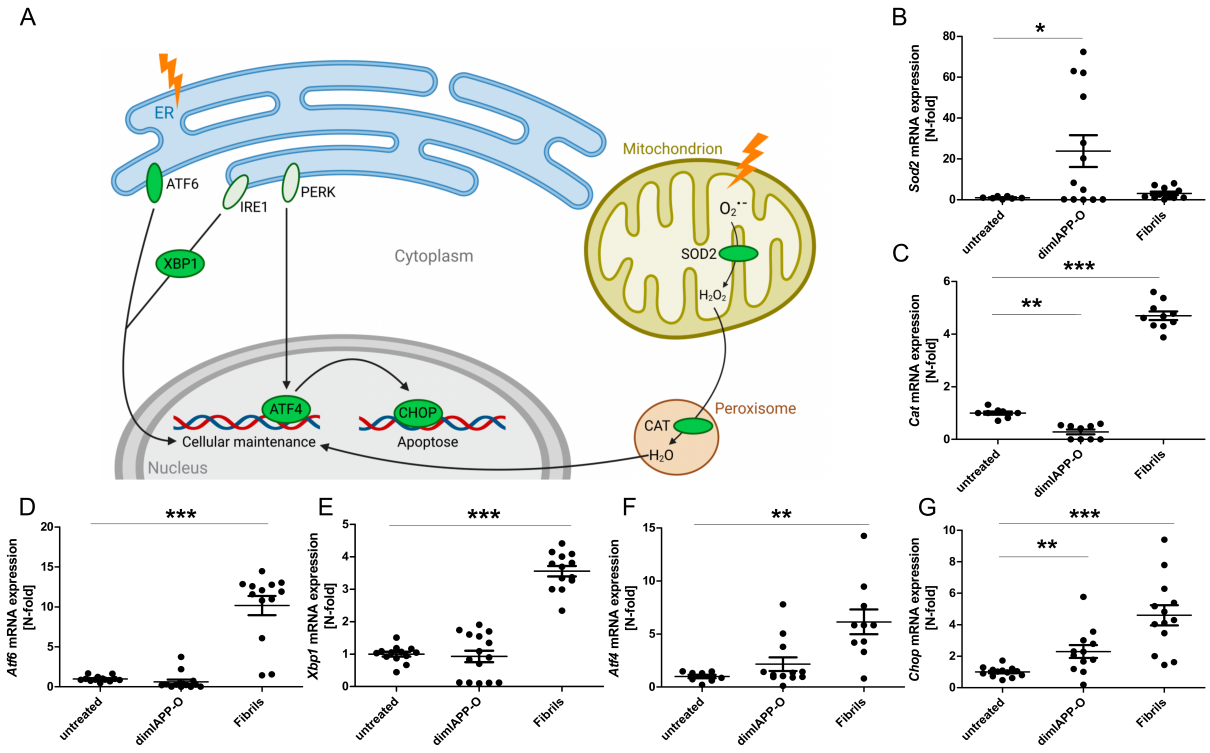

Figure 6.5: Influence of dimIAPP-O and IAPP fibrils on transcription of different ER stress and oxidative stress markers. (A) Once the cell is stressed, different stress markers get activated and the transcrition level upregulated. Activating transcription factor 6 (Atf6) and X-box binding protein 1 (Xbp1) activate mechanism of cell maintenance. Atf4 as a master manipulator controls on the one side adaptive genes of the unfolded protein response (UPR) and on the other hand CCAAT-enhancer-binding protein homologous protein (CHOP) which controls apoptotic UPR genes. Stress also influences transcription of genes involved in oxidative stress response like superoxide dismutase 2 (Sod2) and catalase (Cat). Sod2 reduces superoxide anions to hydrogen peroxide which is then further decomposed into water and gaseous oxygen. Figure is inspired by Inagi *et al.* [484]. (B-G) The transcription rates of RIN-m5f cells were investigated, when treated with 1 µM dimIAPP-O or IAPP fibrils. qPCR analysis was performed in 5 technical replicates and 3 biological replicates. Statistical analysis was applied using an unpaired student's t-test and a Grubb's outlier analysis. * = $p < 0.05$, ** = $p < 0.01$. *Sod2* transcription (B) is significantly increased in cells which were treated with dimIAPP-O while transcription of *cat* (C) is significantly decreased. Cells which were treated with IAPP fibrils exhibit an upregulated transcription of *cat*. Treatment of the cells with IAPP fibrils results in a significant upregulation of ER-stress markers *atf6* (D), *xbp1* (E), *atf4* (F) and *chop* (G). *Chop* expression is also upregulated in cells which were treated with dimIAPP-O.

We studied LLPS-induced build-up of SG by using G3BP1 as a marker protein (Figure 6.6A). We could observe a clustering of G3BP1 in the dimIAPP-O and IAPP fibril-treated cells while this clustering could not be monitored in the untreated cells (Figure 6.6B, SI Figure 6.10). Both, dimIAPP-O and IAPP fibrils trigger SG formation.

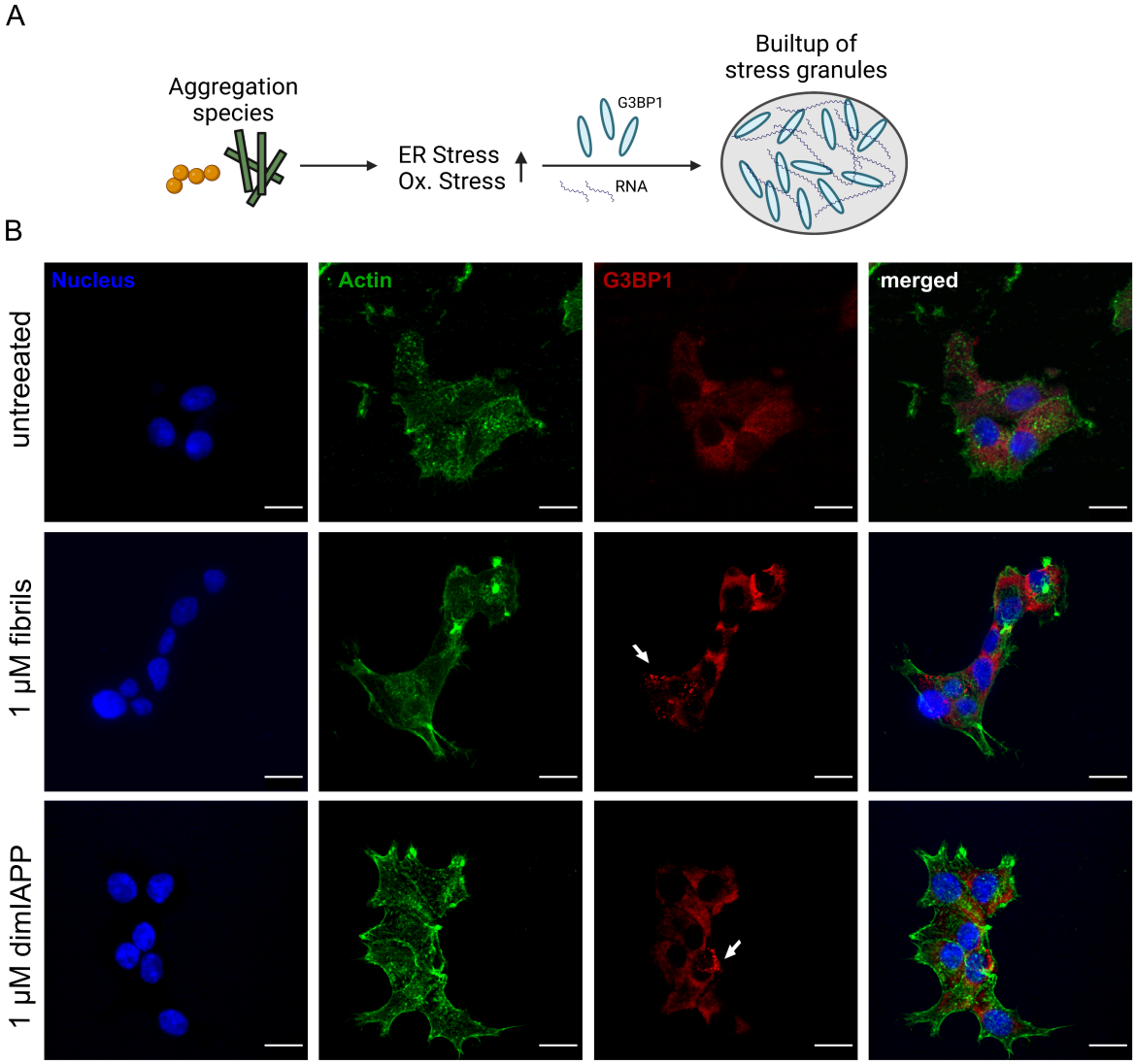

Figure 6.6: Influence of dimIAPP-O and IAPP fibrils on granular stress. (A) Using different aggregation species, ER stress and oxidative stress markers get activated and induce the formation of RNA-protein clusters known as stress granules (SG). G3BP1 is one of the proteins involved in this mechanism and is the schematic representation of all proteins involved. (B) Representative images of RIN-m5f cells treated with 1 µM IAPP fibrils or 1 µM dimIAPP-O (scale bar = 12 µm). G3BP1 (red) is distributed equally in the untreated cells, while it localizes in clusters in the treated cells (white arrows).

6.5. Discussion

Here, we introduced dimIAPP-O as a stable oligomer model, which structurally differs from fibrils as it forms curvilinear oligomers. In this work, we performed initial experiments on the effect of dimIAPP-O on the aggregation of IAPP as well as their influence on cell stress mechanisms in comparison to IAPP fibrils. In terms of aggregation, dimIAPP-O act differently than IAPP monomers by slowing down aggregation of IAPP in substoichiometric ratios. The data suggests dimIAPP-O to interfere with the aggregation mechanism of IAPP by inhibition of nucleation and/or fibrillar growth. Off-pathway oligomeric species are already known to inhibit fibril formation [326, 327, 493, 494, 495, 496, 497]. This finding is not only known for IAPP, but several other peptides and is explainable by their competition for

monomers and the consequence that the number of free monomers available for nucleation processes decreases [167].

Furthermore, this model opens the possibility to study off-pathway oligomers in more complex systems as no additional agent or condition is required to stabilize the off-pathway oligomer state once it is formed. In our experimental setup, we investigated the effect of IAPP fibrils and dimIAPP-O detached from the possibility of internal IAPP to aggregate as we chose rodent pancreatic cells. This difference to most other studies as well as the difficult determination of stable oligomers in experimental setups might be the reason for the observation that fibrils induced stronger activation of stress responses in cells than oligomers. Though Saravanan *et al.* [498] described the existence of non-toxic oligomers, however, we state that our dimIAPP model is of great relevance as it still has upregulating effects on *chop* expression. Huang *et al.* [499, 500] have already shown that the addition of human IAPP (no characterization of the IAPP species) to INS-1 rat insulinoma cells also induces the upregulation of ER stress markers on protein level. Similarly, our results indicate IAPP fibrils and dimIAPP-O to be stressful for RIN-m5f cells on transcription level which is in line with Gurlo *et al.* [501]. Our study demonstrated that the addition of external dimIAPP-O and IAPP fibrils induces ER stress, oxidative stress responses and LLPS-induced SG, which may trigger increased toxicity in a system where self-amplification leads to disease. However, the physiological relevance of curvilinear oligomers is still elusive [502].

The difference and absolute advantage of our system is the guarantee of the oligomeric species' appearance as no upregulated IAPP is used to trigger stress responses but defined aggregated species. The applicability of an artificial dimeric model in *in vitro* aggregation and cell culture experiments has also been shown by our group before [163]. Curvilinear oligomers of dimAβ inhibit Aβ aggregation and do not show effects of cytotoxicity but altered expression of Alzheimer's related Tau. In agreement with our results, it has been shown that the IAPP aggregate elicits a stress response in cells similar to the cellular responses observed in *diabetes* mouse experiments [503] confirming the relevance of added IAPP species to cells to gain complete understanding of T2DM-associated mechanisms.

To sum up, we would like to make clear once again that it is not easy to guarantee the real appearance of the "oligomers" used human IAPP [472] and oligomer models are urgently needed. Understanding the mechanisms behind IAPP oligomer toxicity is crucial for developing targeted therapeutic strategies to prevent or halt the progression of T2DM.

6.6. Material and Methods

6.6.1 Protein preparation

DimIAPP expression cassette was purchased by Genscript in the expression vector pET11-a. The expression cassette consists of a 6x his-tag, the IAPP β-wrapin HI18, a flexible $(G_4S)_3$-linker, another β-wrapin HI18, a $(G_4S)_3$-linker, a TEV cleavage site, the IAPP sequence, a $(G_4S)_4$-linker and again the IAPP sequence. This design is inspired by Mirecka *et al.* [504]. *Escherichia (E. coli)* BL21(DE3) was transformed by thawing 200 µl of the cells for 10 min on ice, adding 10 ng of the plasmid, letting them rest for 10 min on ice, heat shock at 42 °C for 1 min, letting them rest for 2 min on ice, adding 450 µl of pre-warmed (37 °C) 2YT medium and letting the cells incubate for 1 h at 37 °C under constant agitation of 800 rpm. Afterwards, the cells were plated on LB-agar plates containing ampicillin and incubated at 37 °C overnight.

A pre-culture was prepared in a volume of 50 ml. The next day, 2 l of main culture were inoculated with a OD_{600} of 0.1. They were incubated at 37 °C at constant agitation of 120 rpm until OD_{600} of 0.6 was reached. Expression was performed for 3 h at 37 °C and 120 rpm. The harvesting was performed for 10 min at 5,000 xg at 4 °C. The bacteria pellet was frozen at -20 °C.

The pellet was dissolved in 10 ml NaPi (pH 8.0), 500 mM NaCl, 6 M Urea and 0.4 mM PMSF. The cells were disrupted with a cell disruptor and spun down for 30 min at 40,000 xg at 4 °C. An immobilized metal ion affinity chromatography (IMAC) purification was performed in 20 mM NaPi (pH 8.0), 500 mM NaCl, 6 M Urea, washed with 20 mM NaPi (pH 8.0), 500 mM NaCl, 6 M Urea plus 20 mM imidazole. The elution was performed with 20 mM NaPi (pH 8.0), 500 mM NaCl, 6 M Urea plus 450 mM imidazole. The sample was concentrated to 500 µl using a concentrator with 3 MWCO.

Size exclusion chromatographie (SEC) was performed with a Superdex200 10/300 Increase column by Cytiva using 20 mM Tris (pH 8.0), 50 mM NaCl in an NGC liquid chromatography system (Bio-Rad). TEV cleavage was performed overnight. Afterwards, a HPLC run was performed using a gradient over 40 min from 20-64% acetonitrile (AcN), 0.1% TFA. A Zorbax C8 SB300 9.4x250 mm semipreparative column was used.

Human IAPP was purchased from Pepscan (purity 93.2%) and monomerized by resolving 1 mg which was aliquoted using HFIP in 500 µl 6 M guanidine hydrochloride solution. Subsequently, a SEC was performed using a Supedex75 10/300 Increase column in 10 mM MES/NaOH buffer, pH 6.0 using NGC liquid chromatography system (Bio-Rad) collected in Eppendorf Protein LoBind Tubes.

6.6.2 DimIAPP-O preparation

Lyophilized dimIAPP was resolved in HFIP and aliquoted in 1 µg, before lyophilized again. Then, dimIAPP was dissolved in 4 µl 50 mM NaOH. Then, 92 µl 50 mM MES (pH 6.5), 50 mM NaCl were added. Afterwards, 4 µl 50 mM HCl were added. The dissolved protein was incubated at 37 °C for 16 h quiescently.

DimIAPP-O were spun down at 11,000 xg for 10 min at 20 °C and the buffer was discarded. The oligomers were dissolved in buffer at a concentration of 20 µM. For all applications, oligomers were diluted to the desired concentration. The centrifugation process did not alter the appearance of the

oligomers (SI Figure 6.9E).

For cell culture experiments, the oligomers were dissolved in RPMI-1640 medium (Thermo Fischer ATCC modification, Germany). IAPP fibrils cannot be spun down, therefore they were added to the medium in the buffer in which they were prepared before (dilution factors of 1:1,000).

6.6.3 IAPP fibril preparation

IAPP was dissolved in 50 mM MES (pH 6.5), 50 mM NaCl in a concentration of 100 µM in 50 mM MES (pH 6.5), 50 mM NaCl and incubated under constant agitation at 800 rpm for 5 days.

6.6.4 Thioflavin T (ThT) fluorescence assay

Aggregation kinetics were monitored by ThT fluorescence. Freshly SEC prepared monomerized IAPP was taken. The *de novo* assays were run in 50 mM MES (pH 6.5), 25 mM $MgCl_2$ supplemented with 0.04% NaN_3 and 20 µM ThT in 96-well Half Area Black/Clear Flat Bottom Polystyrene Microplate (3881, Corning). Respective concentrations of dimIAPP-O were added to the samples. ThT measurements were recorded in a BMG FLUOstar Omega microplate reader with Reader Control software from BMG at 37 °C using excitation wavelengths of 448-10 nm and emission wavelengths of 482-10 nm. Each data point reflects to the average of orbitally measured value over 3 mm with 20 flashes per well. The plate was shaken at 300 rpm before each cycle. The observed effects are not caused by the addition of buffer in which dimIAPP-O was dissolved (SI Figure 6.9D). Each data point was normalized to the highest value of the control sample (3 µM IAPP only) run in the same measurement to equalize differences due to different gain settings.

6.6.5 Atomic Force Microscopy (AFM)

For the AFM imaging of different species after preparation, 10 µl were put onto a freshly cleaved muscovite mica surface and dried by incubating for 2 min. Subsequently, the mica was washed 3 times with MQ H_2O and blown dry with a steam of N_2. The imaging mode was intermittent contact mode (AC mode) using a JPK NanoWizard 3 AFM run with NanoWizard Control Software v.5 version 5.0.84 by JPK. The cantilever had a silicon tip (OMCL-AC160TS-R3, Olympus) with a tip radius of 9 ± 2 nm, a force constant of 26 N/m and a resonance frequency of 300 kHz. For each sample, an area of 25 μm^2 was scanned to get an overview. For the AFM imaging after ThT kinetics, the plates (96-well Half Area Black/Clear Flat Bottom Polystyrene NBS Microplate, 3881, Corning) were put into a sonication bath for 10 s. Subsequently, 10 µl of the samples were taken out of the plate and prepared like described above.

6.6.6 Reverse-Phase High-Performance Liquid Chromatography (RP-HPLC)

HPLC analysis was performed on an Agilent 1260 Infinity system using an Agilent Zorbax SB300 C8, 5 µm, 4.6x250 mm column at 80 °C column temperature. A flow rate of 1.0 ml/min was applied. After the gradient, the column was washed for 2 min with 80% AcN with 0.1% TFA. Re-equilibration was performed for 4 min using MQ water.

6.6.7 Cultivation of RIN-m5f cells

RIN-m5f cells (ATCC, CRL-11605, Manassas, VA, USA) were cultured in RPMI-1640 medium (Thermo Fisher ATCC modification, Germany) supplemented with 10% fetal calf serum (Sigma, F9665) and 1% penicillin/streptomycin (ThermoFisher, 15140122) in T75 tissue culture flasks (Sarstedt, 83.3911.002) in a humidified incubator with 5% CO_2 at 37 °C. Depending on their confluence, cells were passaged every three to five days.

For the experiments, cells were seeded in well plates (Sarstedt, Cell+ treated). When 80-90% confluence was achieved, cells were treated with 1 µM IAPP (the same amount of buffer) or 1 µM dimIAPP for 24 h at 37 °C. Buffer control were performed to confirm that the observed effect is contributed to the treatment (Figure 6.11A). For RNA isolation, cells were incubated with trypsin for 10 min at 37 °C and then harvested by centrifugation at 5,000 rpm for 5 min. After counting the cells using Neubauer chamber, the cells were dissolved in TRIzol^{TM} normalized to the same number of cells.

6.6.8 Cell viability assay

Cell viability was verified using Cell Titer Blue® assay (Promega, G8080) in a 48 well plate (Sarstedt, 83.3923.300) (SI Figure 6.11B). Cells were treated with 1 µM IAPP fibrils or 1 µM dimIAPP-O. Different puromycin concentration served as negative controls. After an additional incubation time of 24 h at 37 °C, the supernatant was decarded and 100 µl OptiMEM (Gibco^{TM}) was added. Then, 25 µl of the CellTiter-Blue® reagent was added to each well, followed by a 4 h incubation at 37 °C. Afterwards, 50 µl supernatant was transferred in a half area 96 well plate (Corning, 3881). The fluorescence was measured at 535/590 nm using a plate reader (Clariostar, BMG LABTECH, Ortenberg, Germany). Results are represented as the percentage of CTB reduction, assuming that the absorbance of positive control was 100%.

6.6.9 RNA isolation and cDNA synthesis

RNA was isolated using TRIzol™ reagent from Thermo Fisher. Subsequently, RNA was adjusted in all groups and reverse transcriped to cDNA by using SuperScript™ III Reverse Transcriptase Kit by Thermo Fisher.

6.6.10 Quantitative Polymerase Chain Reaction (qPCR)

qPCR was performed using Luna Universal qPCR Master Mix from New England Biolabs. The 2x master mix was mixed with 0.25 µM forward and reverse primer (primer sequences are shown in table 6.1) and measured at qTOWER3 by Analytik Jena.

Table 6.1: Primers used for qPCR. Shown are the name of the primers with the addition forward (fwd) and reverse (rev) as well as the primer sequence for the 5' to 3' direction.

Name of primer	Sequence of primer (5'>3')
Actb fwd	ACCGAGCATGGCTACAGCGTCACC
Actb rev	GTGGCCATCTCTTGCTCGGAGTCT
Atf4 fwd	AAGGCAGATTCTCTCGCCAA
Atf4 rev	TTCTTCCCCCTTGCCTTACG
Atf6 fwd	CGAGGGAGAGGTGTCTGTTTC
Atf6 rev	GTCTTCACCTGGTCCATGAGG
Cat fwd	CAGGGATGCCATGTTG
Cat rev	GGCTATGGATAAAGGATGGAAA
Cbp fwd	GGTGGCAGTGTCCTG
Cbp rev	CTTCTGAGTCCACGTACTG
Chop fwd	AGGAGAGAAACCGGTCCAA
Chop rev	GGACACTGTCTCAAAGGCGA
Gapdh fwd	CACTGAGCATCTCCCTCACAA
Gapdh rev	TGGTATTCGAGAAGGGAGG
Sod2 fwd	AGGGCCTGTCCCATGATGTC
Sod2 rev	AGAAACCCGTTTGCCTCTACTGAA
Xbp1 fwd	CCACTTGGTACAGACCACTCC
Xbp1 rev	AGACACTAATCAGCTGGGGG

For this study we decided to present the results as N-fold expression changes and not by using ΔΔCt-method as it was not possible to us to find suitable, expression-stable house keepers (SI Figure 6.11C).

6.6.11 Immunocytochemistry

For confocal imaging, the cells were seeded on coverslips. Four coverslips were transferred into one well of a 6-well plate (Sarstedt, 83.3920.300). The plates with the coverslips were left under the UV-lamp for 30 min. Each well containing the coverslips was washed five times with 500 µl of PBS. 500 µl of Gibco^{TM} Poly-D-lysin was added and the coverslips were incubated for 1 h at 37 °C. After the incubation, Poly-D-lysin was discarded and the coverslips were washed five times with 500 µl PBS. Then the cells were seeded on the coverslips.

After the treatment, the medium was discarded and the wells were washed 6 times with 1 ml of PBS. 350 µl of 4% PFA was added, followed by an incubation of 20 min at room temperature (RT). 4% PFA was discarded and the wells were washed eight times with 1 ml of PBS. Subsequently, the wells were then filled with 1.5 ml of PBS and the plates were stored at 4 °C until immunocytochemistry was performed.

Table 6.2: Solutions for the preparation of immunocytochemically stained RIN-m5f cells. Shown are the name of solutions with each chemical compounds.

Solutions	Chemicals
Solution 1	40 ml PBS + 100 µl TritonX-100
Solution 2	20 ml solution 1 + 20 ml PBS
Solution 3	10 ml solution 2 + 0.25 g BSA
Solution 4	5 ml solution 3 + 5 ml PBS

The coverslips containing the cells were removed from the wells. They were incubated with solution 1 (table 6.2) for 2 min at RT. The cells were blocked at RT for 1 h by pipetting 100 µl solution 3 (table 6.2) on the coverslips. This was followed by a further incubation step with the primary antibody Rabbit-anti-G3BP1 (ThermoFisher, PA5-29455) for 1 h at RT. The primary antibody was diluted 1:200 in solution 4 (table 6.2). Afterwards, the coverslips were washed three times with solution 2 (table 6.2). At RT, the secondary antibodies 647-Goat-anti-Rabbit conjugated with Alexa Fluor^{TM} 647 (ThermoFischer, A-21245) and Alexa Fluor^{TM} Plus 555 Phalloidin (ThermoFisher, A30106), diluted 1:500 in solution 4 (table 6.2) were incubated for 1 h in the dark. Afterwards, the cells were washed six times with solution 2 (table 6.2) and the cells were incubated with 300 µM DAPI for 5 minutes at RT. The cells were washed four times with solution 2 (table 6.2) and then twice with PBS. The coverslips were then shortly dipped in ddH_2O and glued onto microscopic slides using Immu-Mount (from Epredia). Confocal microscopy was performed on a Leica AF6000LX inverted microscope equipped with a Hamamatsu C9100-02-LNK00 EM CCD camera. Afterwards, the images were processed with the software Fiji to add a scale bar. A false-positive result caused by unspecific binding of the secondary antibody was excluded (SI Figure 6.10).

6.7. Acknowledgments

This project has received funding from the European Research Council under the European Union's Horizon 2020 research and innovation program, grant agreement No. 726368. AP thanks the Jürgen Manchot Foundation for funding. Figures were partially created with BioRender.com.

6.8. Supplementary Information

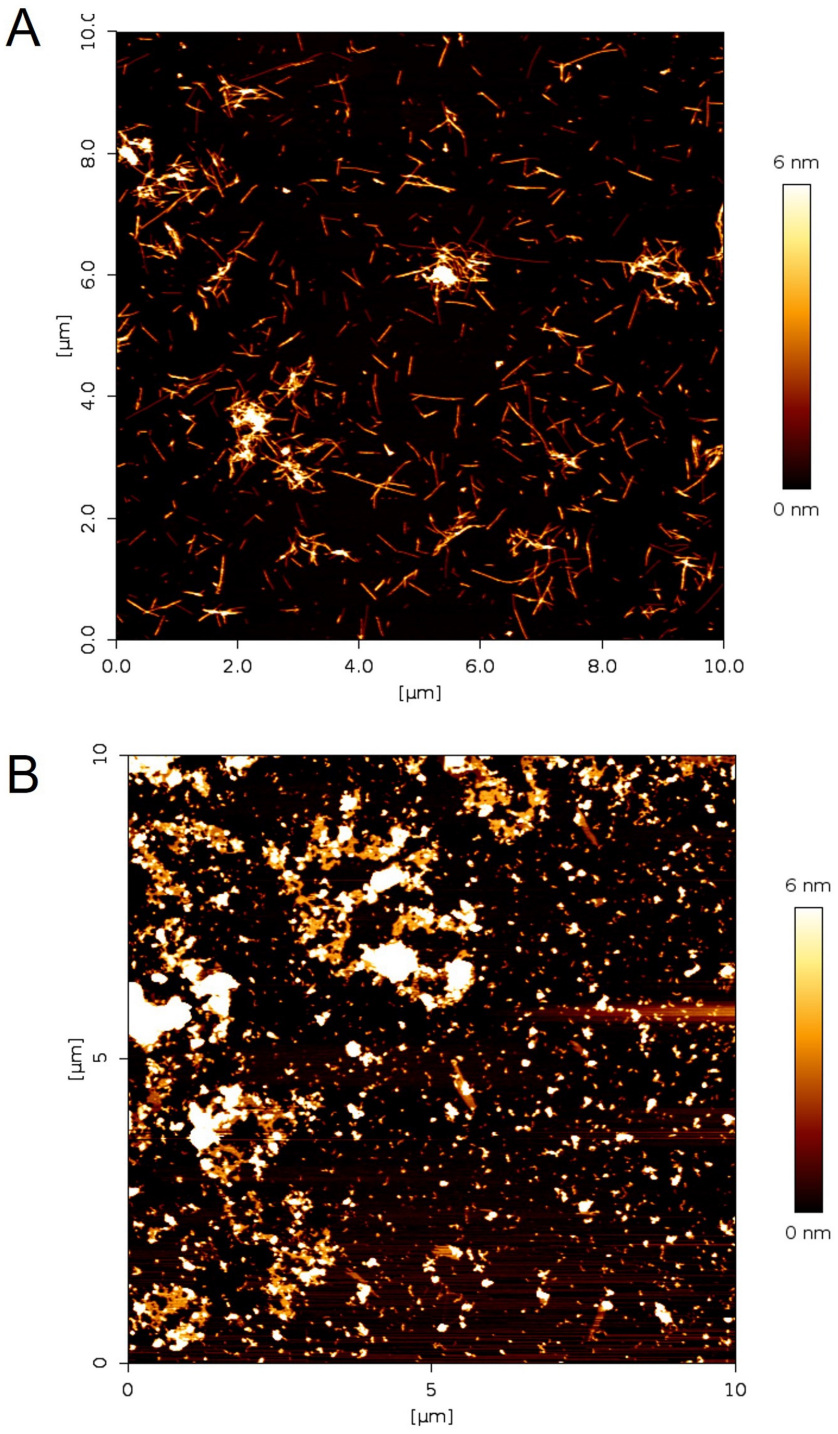

Figure 6.7: Comparing of IAPP fibrils and dimIAPP-O. AFM images of IAPP fibrils (A) and dimIAPP-O (B) after 16 h of quiescent incubation at 37 °C. Color scale: height in nm, size of images: 10x10 µm.

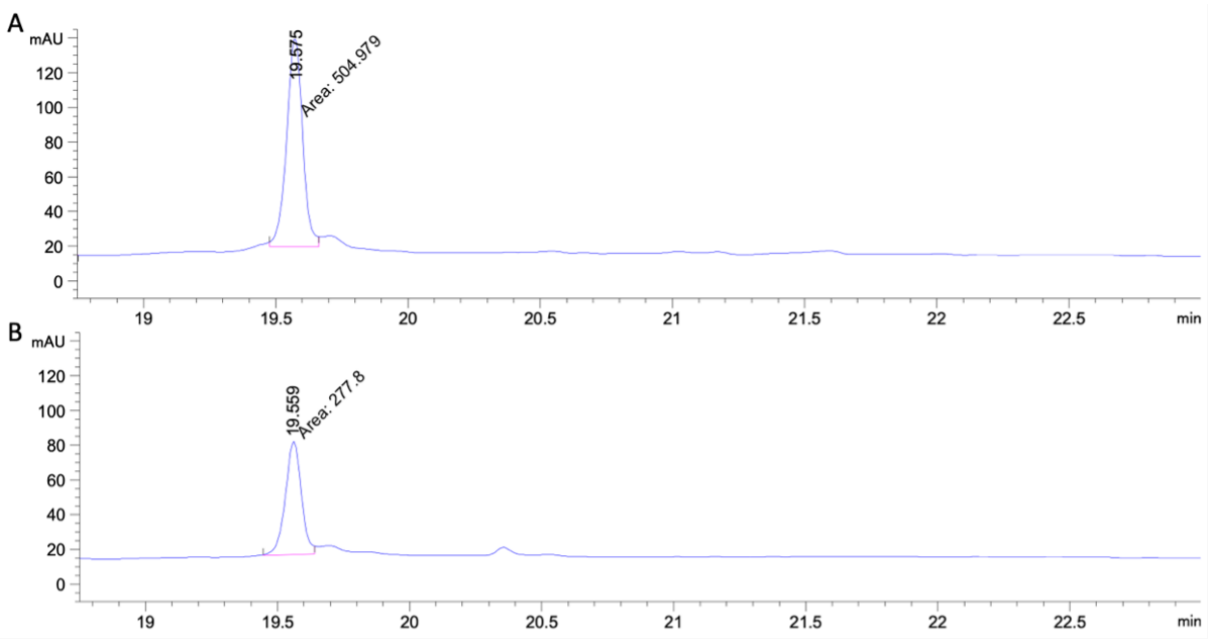

Figure 6.8: Analysis of soluble (A) and insoluble (B) fractions of dimIAPP solution. Monomeric dimIAPP at 0 h incubation time were analyzed via reversed-phase HPLC. Before applying on HPLC, the sample was centrifuged at 11,000 rpm for 5 min. (A) HPLC run of the dimIAPP in the supernatant, the soluble fraction at 0 h incubation. (B) HPLC run of the dimIAPP in the pellet, the insoluble fraction at 0 h incubation.

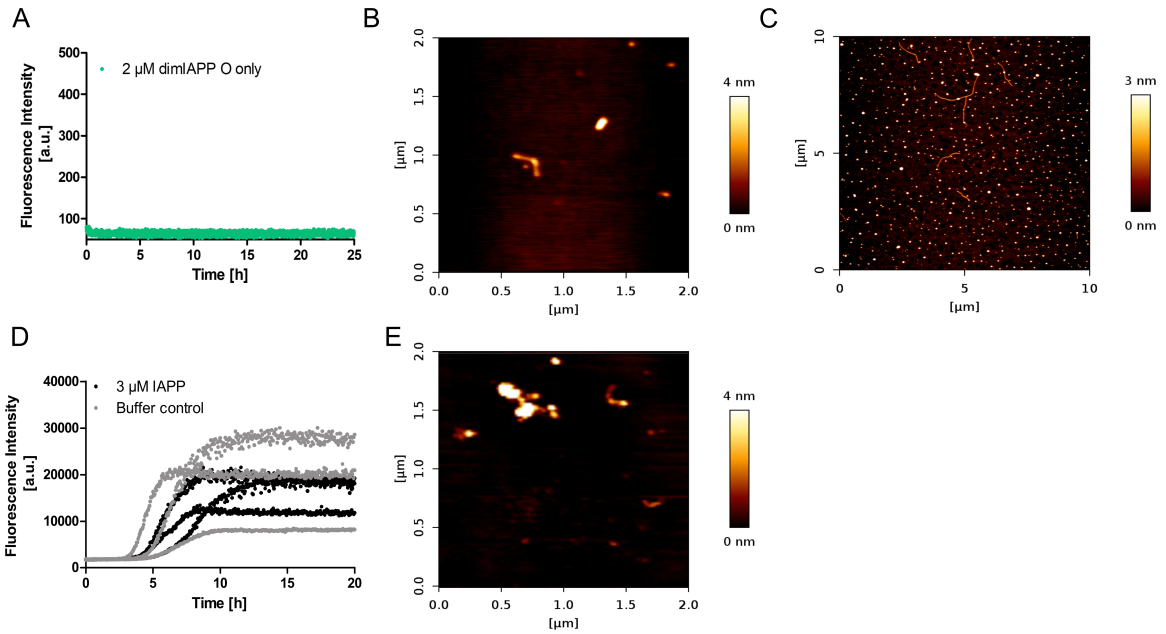

Figure 6.9: Experimental controls of dimIAPP-O preparation. (A) 2 µM of dimIAPP-O were incubated for 25 h at 37 °C and shaking. No increase of ThT fluorescence is observed. (B) AFM image of a completely inhibited aggregation of 3 µM IAPP. No fibrils, but oligomeric species are observed. Color scale: height in nm. Size of image: 2x2 µm. (C) DimIAPP-O prepared at a concentration of 10 µM in 50 mM MES pH 6.5, 50 mM NaCl. Under this condition, fibril formation was detected. (D) Aggregation kinetics of 3 µM IAPP (black) during 20 h and buffer control. The same volume of dimIAPP-O preparation buffer (50 mM MES pH 6.5, 50 mM NaCl) was added as in the condition of 2 µM dimIAPP-O (grey). The buffer has no influence on the aggregation behaviour of IAPP. (E) DimIAPP-O were formed at a concentration of 1 µM under quiescent conditions for 16 h at 37 °C. After formation, they were centrifuged for 10 min at 11,000 xg and the buffer except for 5 µl were removed. Then, each 5 µl were pooled and sonicated in an ultrasonic water bath for 5 s. AFM imaging confirmed the prescence of dimIAPP-O after the centrifugation step. The appearance of the oligomers has not changed. Color scale: height in nm. Size of image: 2x2 µm.

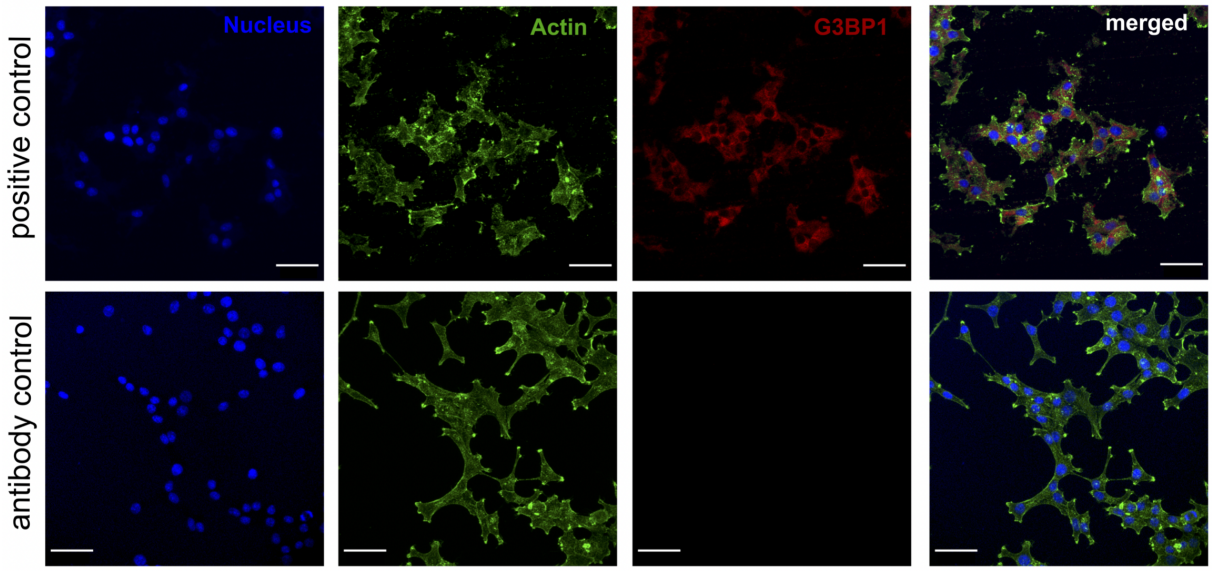

Figure 6.10: Controls for Immunocytochemistry. Representative images of untreated RIN-m5f cells (scale bar = 38 µm). Cells were treated using DAPI to stain the nucleus (blue) and Phylloidin-555 to stain actin (green). Upper row: For staining G3BP1 the first antibody rabbit-anti-G3BP1 was used to detect G3BP1 and afterwards the second antibody 647-goat-anti-rabbit (red) to stain the first antibody. Lower row: As an antibody control, cells were only treated using the secondary antibody. In this sample no signal was observed for G3BP1, so false positive signals can be excluded.

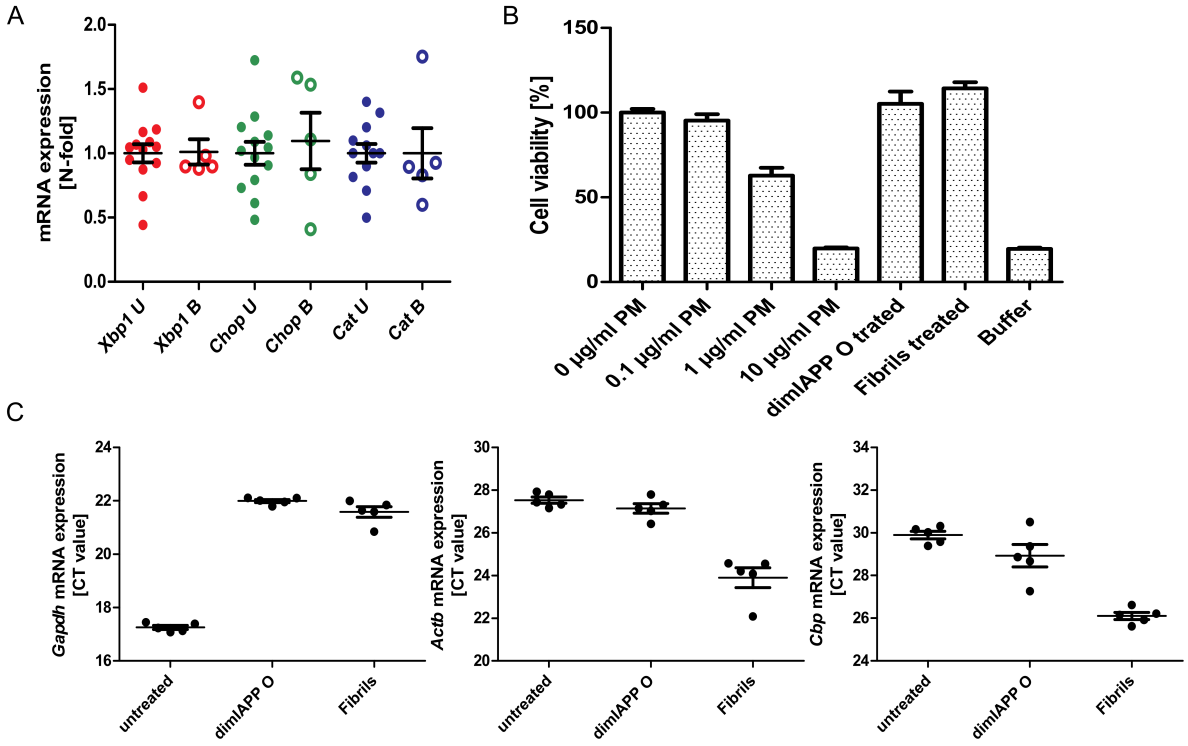

Figure 6.11: Controls of cell culture experiments. (A) RIN-m5f cells do not show an altered transcription (example: Xbp1, Chop, Cat) when the same volume of buffer was added to the cells as for 1 µM of IAPP fibrils. U = untreated, B = buffer treated. (B) CellTiter-Blue® assay of RIN-m5f cells. Cell viability decreases to 62% when 1 µg/ml puromycin was added and decreases further to 19% when 10 µg/ml puromycin was added. The cell viability of dimIAPP-O and IAPP fibril treated cells did not decrease. (C) No reliable housekeeper genes could be identified. This is the reason for not choosing the ΔΔCt-method for evaluation.

7

GENERAL DISCUSSION

The aim of this thesis was to enhance our comprehension of the progression of amyloid diseases and to explore strategies for their prevention. In the first part, two inhibitors, AS69 and CC48, were employed to investigate the mechanistic role of IDR interactions in assisting inhibitors to prevent the formation of amyloid fibrils. These aggregation inhibitors were developed by our research group prior to my dissertation. AS69, an engineered αS monomer-binder, is a dimer of two identical subunits covalently linked by a disulfide bond between the Cys-28 residues of both subunits. *In vitro* and *in vivo*, AS69 shows an inhibitory effect on elongation as well as primary and secondary nucleation [350, 353]. When a construct was created in which AS69 was fused to monomeric αS forming a pre-formed complex, this complex showed a similar inhibitory effect on secondary nucleation as the addition of AS69 alone [353]. Surprisingly, the revelation that the complex itself serves as the inhibitory species regarding secondary nucleation suggests that the IDRs exposed to the complex may play a role in the inhibition. Based on the knowledge of the structure that αS adopts when bound to AS69, a double-cysteine mutant of αS, CC48, was created to mimic the formation of the β-hairpin conformation, while leaving the other regions intrinsically unstructured analogous to WT αS [368]. CC48 was identified as a potent inhibitor of elongation, and fusion of monomeric αS to CC48 (WT-CC48) enhanced the inhibitory effect [354].

For both inhibitors, the fusion of a WT αS monomer unit had been shown to affect their activity by increasing the inhibitory potential or stabilizing the inhibitory species in the form of a stable pre-formed complex. This proves to be surprising, as the WT monomers are actively participating in the inhibition, contrary to their typical role as substrates for the aggregation reaction. This novel perspective, suggesting that WT monomers can contribute to inhibition by supporting the inhibitors, opens up new strategies for inhibitor design. However, realizing this potential requires a detailed understanding of the inhibitors' mode of action and the role of the WT monomer moiety.

In the second chapter, we offered a model that describes the mode of action of CC48. During elongation, the inhibitor CC48 is bound to the fibril end of one protofilament, while the second protofilament binds another WT αS molecule. Due to the incorporation of CC48, the subsequent monomers cannot incorporate into the fibrils in the highly ordered manner, but cluster at the ends, potentially forming a less ordered oligomer-like cap. This elongation-incompetent state results in the inhibition of fibril elongation. By directly linking CC48 to WT αS in the fusion constructs, their cooperative effect is utilized to achieve fibril end blockage at an inhibitory concentration two orders of magnitude lower than CC48 alone.

Agerschou *et al.* [354] have already demonstrated the remarkable inhibitory potential of WT-CC48 with an IC50 of 11 nM, which is currently considered as one of the most effective inhibitor in this category [356]. However, until now it was not clear which IDRs of the dimeric construct are responsible for the

strong inhibition. To elucidate this, various truncated versions of the dimeric inhibitor WT-CC48 were tested. The presence of the HP and NAC regions in both parts of the WT-CC48 dimeric construct was identified as crucial for maximal inhibitory activity. These two regions are located within the fibril core in different polymorphs. This suggests that the self-interaction of the monomers with the fibril ends is harnessed by the inhibitor, which is a modified version of the monomer, to facilitate their incorporation. It is clearly shown that the terminal regions are not required for the strong inhibition of WT-CC48. Since αS fibrils typically consist of two protofilaments, the dimeric construct WT-CC48 provides the critical regions sufficient to cover the entire β-sheet core interface exposed at the fibril ends, which may explain its high inhibitory activity.

The minimal inhibitory construct (WTΔNΔC-CC48ΔNΔC) has not been individually tested but holds significant promise for future *in vitro* and *in vivo* projects. Given that elongation is presumed to be a pivotal process to generate fibril mass in cells, investigating its potential as an effective therapeutic agent *in vivo* would be interesting. Introducing the construct into the cell may present challenges, which would require further optimizations such as the fusion of different cell-penetrating tags or the identification of the best transfection techniques. Another question that still needs to be investigated is how to stabilize the disulfide bridge in a reducing environment such as within different cell components. Peptide mimetics could address this question, but the chemical environment surrounding the residues involved in the disulfide bridge is crucial. It was shown that a CC49 construct, in which the cysteines were inserted at positions 41 and 49 instead of 41 and 48, exhibits remarkably lower inhibitory potential [354], suggesting that the use of peptide mimetics may not be expedient. Therefore, further optimization proposals would need to be explored and tested.

The aggregation species targeted by the inhibitors used in this work were summarized in a matrix in Figure 7.1. In addition to target the fibril ends, as shown for CC48, the inhibition of elongation can also occur on another target site, such as the sequestration of monomers, e.g., by AS69 (Figure 7.1). The mode of action of AS69 to inhibit elongation is well understood (Chapter 3). AS69 inhibits fibril elongation by sequestering αS monomers which lose their competence to elongate fibrils when incorporated into the AS69 complex. This was confirmed by the loss of inhibition of elongation when AS69 was already saturated with an fused αS monomer in a pre-formed complex (AS69-αS).

In contrast, the mode of action by which the inhibitor prevents nucleation processes is much more complex and less understood. While AS69 can bind free monomers, this alone does not explain the inhibitory effect observed in the substoichiometric range. The AS69:αS complex formed during this binding reaction demonstrated effective inhibition of both primary and secondary nucleation (Figure 7.1). Nucleation processes give rise to the formation of oligomeric precursors on the pathway towards amyloid fibrils with which the complex may interact (Figure 7.1). This substoichiometric activity required not only the globular part of the complex but also the αS IDRs: the presence of the intrinsically disordered NAC region (aa 60-95) was crucial for the inhibition of lipid-induced primary nucleation, whereas either the NAC or the N-terminal (amino acids 1-30) IDRs were required for the inhibition of secondary nucleation.

Somewhat surprisingly, it was possible to clearly differentiate between an inhibitor against primary and secondary nucleation, depending on the presence of the N-terminal region. Previous studies have suggested that the N-terminal interaction of αS with lipids plays a significant role in initiating primary nucleation [244, 260]. However, a recent study has challenged this notion by indicating that lipids do not initiate primary nucleation but instead facilitate the elongation of lipidic fibrils [264]. Since AS69-αS(N-B) lacks inhibitory effects on primary nucleation through self-interaction, it implies that the N-terminus may not be as intricately involved in primary nucleation as it is in preventing secondary nucleation. The question of whether primary nucleation genuinely occurs on lipids is an aspect that will

hopefully be further explored in future discussions.

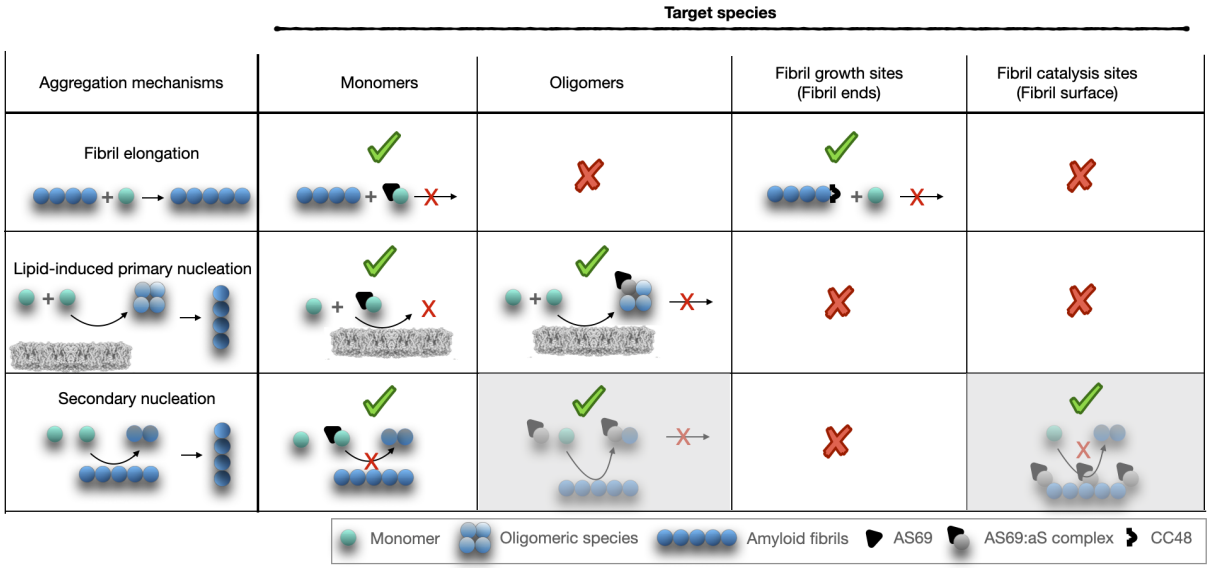

Figure 7.1: Target sides of CC48 and AS69 to selectively interfere within different mechanisms. Matrix to identified with aggregation species correspond as target point for each aggregation mechanisms. During the aggregation mechanisms, namely elongation, primary nucleation and secondary nucleation, different aggregation species are involved: monomers (green), oligomers (light blue), fibrils (dark blue). They represent different target sides for inhibitors. AS69, AS69-αS or CC48 can selectivley target each mechanisms by interfereing with certain aggregation species. For primary nucleation an experimental set up was chosen in which monomers were presented to lipids which are shown here in grey. An overview of all possible inhibitory's mode of action are shown for each mechanisms. If the interaction with this species does not result in an inhibition, it is crossed out in red. For secondary nucleation, it was not possible to identify the exact mode of action, marked by the fields which are grayed out.

In secondary nucleation, another target site for inhibitors may be the fibril surface (Figure 7.1). Our data suggests that the two IDR regions, N-terminus and NAC region are crucial for inhibiting secondary nucleation, but can substitute each other. Based on our data, it is not possible to definitively determine the exact mechanism by which the AS69-αS complex intervenes, leading to these aspects being shaded in gray (Figure 7.1). However, it must be clearly stated once again that these are only schematic representations of how the aggregation mechanisms are envisioned, and the specific intermediate steps have not been precisely elucidated. Recently, NMR studies have revealed a possible interaction of the N-terminus of the monomer with the C-termini exposed to the fibril surface, which may trigger secondary nucleation [279, 266]. This suggests that our AS69 complex, containing the N-terminus, could have the ability to bind to the surface of the fibrils. While this study did not provide a definitive indication of whether the AS69-αS(N-B) construct actually inhibits secondary nucleation by interacting with the fibril surface, the strong involvement of the N-terminal and NAC region in secondary nucleation could be shown.

Crucially, the fusion of AS69 and αS resulted in the development of a nucleation-specific inhibitor that has no effect on elongation. When applied to biosensor cells, we gained insights into the aggregation processes within the cells. The precise mechanism of aggregate proliferation in biosensor cells has not been determined before. Since the cells had to be seeded to form aggregates, the contribution of primary nucleation in the cells can be excluded. Interestingly, the results from the cellular seeding

experiment exactly reproduced the *in vitro* results. All identified inhibitors for secondary nucleation also exhibited inhibition in the biosensor cell assay. This underlines the assumption that our inhibitor design, in which different IDRs were fused, is also inhibitory in cells due to the strong involvement of the N-terminus and the NAC region. Furthermore, our data indicate that secondary nucleation is an important driver of aggregation in cells. It has often been assumed that inhibition of elongation is considered a promising target for inhibitors to reduce fibril mass in cells. However, here we want to suggest that nucleation-specific inhibitors should also be considered since our data show that a nucleation inhibitor exhibits substantial inhibition over a three-day period.

The two inhibitors under investigation, AS69-αS and WT-CC48, are notably large protein inhibitors. Even if only the essential IDRs are fused to the inhibitor, potentially reducing the constructs by almost half, they pose challenges in terms of therapeutic application. This is contingent upon three crucial factors: *i.)* It is highly improbable to deliver such large proteins into cells without utilizing transfection methods. Exploring different uptake pathways, for instance through penetration tags, could be attempted, but this would likely necessitate numerous optimizations. *ii.)* Inhibitors against synucleinopathies must cross the blood-brain barrier, as the aggregates are usually found as plaques in the brain. Due to the size of our inhibitors, crossing the blood-brain barrier is rather unlikely and poses a further problem for the use of the inhibitors as therapeutic agents. *iii.)* Moreover, the occurrence of site effects and the possibility of rapid degradation in cells are very likely with such large proteins. To circumvent undesired degradation processes, contemplating the synthesis of the inhibitors as D-peptides could be an option [505]. Nevertheless, even in this scenario, producing such a large protein with correct folding as a D-peptide would pose challenges. Due to the challenges outlined, these inhibitors are unlikely to be deemed suitable for therapeutic use, despite their excellent inhibitory potential. However, delving into their mechanism of action has yielded crucial insights into amyloid aggregation and inhibition, as well as shedded light on the significance of secondary nucleation in cellular aggregation. The fusion of the IDR of WT αS moieties emerges as a valuable strategy to enhance the effectiveness of aggregation inhibitors and holds promise for developing inhibitors that selectively target specific mechanisms.

Furthermore, these inhibitors, selectively targeting specific mechanisms, provide the opportunity to serve as artificial tools in *in vitro* experiments for identifying the underlying aggregation process (Chapter 4). This is particularly important in the diagnostically applicable SAA. Our research results indicate that under SAA conditions, secondary nucleation drives proliferation initiated by CSF from patients with PD. Remarkably, these interactions are highly protein-specific and lead to efficient amplification of homotypic seeds from the CSF. Looking ahead, this represents a particularly important discovery to gain insights in the otherwise very complex aggregation process and thereby promote the further refinement of these diagnostic tools.

Form this first part, it can be shown that different IDRs have the ability to act as assistants to inhibitors. We conclude that monomer units within therapeutics can potently inhibit amyloid formation when the capacity of IDRs to interfere with amyloid formation can be exploited. In addition, the use of certain monomer subunits leads to a specific redirection of the inhibitors towards a certain aggregation mechanism. This artificial tool also provides new evidence that secondary nucleation is a crucial process in driving aggregation under different conditions, such as in cellular seeding, as well as in diagnostic tools and therefore, should not be neglected.

In the second section of this thesis, we explored the pathophysiological consequences of various aggregation species on cells. To gain a more comprehensive understanding of cellular responses to fibril infiltration, NGS was obtained (Chapter 5). Through the establishment of a fluorescence assay, it was demonstrated that all cells uptake fibrils. This implies that fibrils enter cells through pathways that are

consistently accessible. In this project, 11 upregulated genes were identified, and 7 of them were validated by qPCR. The proteins are involved in different cell cascades, reflecting the complexity of the cellular response to fibrils. Our focus was specifically on these upregulated genes, as we aimed to initially identify potential interaction partners that might influence fibril uptake. However, the preliminary data presented in this work suggests that none of these proteins encoded by the genes of interest are directly involved in the uptake of fibrils. This is not necessarily surprising, considering that these proteins often initiate cascades to activate the immune system. This aspect needs to be further investigated in the future.

In addition to identify upregulated genes, there is also interest in downregulated genes and their associations with disease-related functions. Through a more in-depth NGS analysis of our data, these processes can be elucidated for subsequent experiments. However, it is crucial to note that we are working within artificial systems: both the artificially produced fibrils *in vitro* and the cells derived from a tumor cell line merely simulate neurons. Therefore, it is also crucial to investigate whether these upregulated genes have disease-related relevance. This can be accomplished by examining CSF from patients and a healthy control group using enzyme-linked immunosorbent assay (ELISA), thereby comparing the protein concentrations between these groups. An outlook to the further course of this project may involve the identification of potential biomarkers through these studies, which could prove significant for diagnosing and monitoring the disease's progression.

Another question that may be of interest is whether the uptake of smaller oligomeric structures by membrane penetration is more efficient than that of fibrils. However, oligomers are difficult to study, due to their transient nature, low population under standard conditions, and structural heterogeneity. Hence, an oligomer model for IAPP was developed (Chapter 6). The decision to employ IAPP as an aggregation-prone protein was influenced by the well-characterized oligomer model for Aβ (dimAβ) [163, 169, 185]. Leveraging the substantial structural similarity between Aβ and IAPP, we designed the model analogously to dimAβ, connecting a dimer of two monomeric IAPP cysteine mutants through a flexible glycine-serine linker. The substitution of cysteines with serines in the monomeric subunits of IAPP aimed to prevent the undesired, chaotic formation of disulfide bridges intra- and intermolecularly.

The strategy of utilizing a dimer to generate higher local concentrations, leading to the formation of curvilinear oligomers rather than fibrils, was successfully replicated for dimIAPP. As observed through AFM, the distinctive appearance of the aggregated species in the form of curvilinear oligomers stood in clear contrast to the rapid fibrillation exhibited by IAPP. A time-course analysis revealed that dimIAPP required 16 h of incubation at 37°C to develop these curvilinear oligomeric form. This parallels dimAβ, which also necessitates a 4 h incubation at 37°C to adopt the curvilinear species [169]. However, notable differences between these two models exist. DimIAPP is ThT-negative in contrast to dimAβ and can be spun down at 11,000 rpm for 5 min, implying that despite the high structural similarity, the aggregation pathways and generation of aggregated intermediates may differ between the two proteins.

We present preliminary data from the utilization of dimIAPP-O in both *in vitro* and *in vivo* studies to gain insights into its properties. *In vitro* ThT assays revealed that dimIAPP-O exert a retarding effect on the aggregation behavior of IAPP. It does not incorporate into fibrils in the same manner as IAPP monomers do. Applying substoichiometric concentration, dimIAPP-O can strongly to completely inhibit aggregation. The mechanism behind this inhibition at substoichiometric ratios is not yet fully understood. Similar inhibitory effects on Aβ aggregation were demonstrated with dimAβ, indicating the mode of action of curvilinear oligomers with a presumably off-pathway character [169, 185]. However, whether dimIAPP-O inhibits in the same manner as dimAβ oligomers needs to be further investigated.

Using oligomers in cell culture is inherently challenging, as the stabilization of oligomers typically requires additional substances [321, 327, 466, 469]. In our model, it was demonstrated that once dimIAPP-O was formed, it maintained its curvilinear structure stably. With this stable model, we eliminate the need for additional chemical supplementation and can examine its mode of action in complex systems. Initially, we tested the model in cells where the endogenous protein was incapable of seeding. Our aim was to investigate whether exogenous oligomers and fibrils already exert cytotoxic effects. This hypothesis was confirmed, but the treatment with fibrils led to the upregulation of several marker genes associated with ER, mitochondrial stress and stress induced by LLPS. Additionally, the oligomer-treated cells exhibited only upregulation of genes contributing to apoptosis, along with stress induced by LLPS. From these preliminary data, it is not yet possible to determine which of the two species, the fibril or our oligomer model, has a higher cytotoxicity. Further experiments are required for this, ideally to compare their seeding potential, using cell lines expressing aggregation-capable monomers. However, it is important to remember that T2DM and serveral other amyloid diseases like AD or PD do not progress aggressively, but slowly and continuously over years. The effects observed here are acute in nature and not chronic, so it is generally difficult to infer disease-related relevance from these cell culture results. Further characterization in a disease-related model would be required for a more accurate assessment. However, with the help of these initial data, we can offer an oligomer model that can be used for such experiments.

To sum up, the data obtained in this thesis, all contribute to the better understanding of amyloid formation and inhibition as well as the role of oligomers and the identification of cellular effects and response systems induced by amyloid fibrils. With this work I wanted to make a small contribution to the understanding of these widespread amyloid diseases. It is a very complex system and despite intensive research in this field, many questions remain unanswered. In order to develop suitable therapeutics, the underlying mechanisms need to be better understood in the future.

8

AUTHOR CONTRIBUTIONS

The following manuscripts reflect the content of this dissertation.

Chapter 2:
Fibril core regions in engineered α-synuclein dimer are crucial for blocking of fibril elongation
Celina M. Schulz*, Anne Pfitzer* and Wolfgang Hoyer
*: These authors contributed equally.

Contributions: Design of constructs, transformation, expression, purification, elongation assays, DGC experiments, SDS-PAGE, AFM imaging, evaluation of the ThT kinetics, preparation of figures, writing and reviewing of the manuscript.

Chapter 3:
Disordered regions of inhibitor-bound α-synuclein support the suppression of seed-induced fibril nucleation in cells
Celina M. Schulz, Emil D. Agerschou, Luis Gardon, Miriam Alexander, Matthias Stoldt, Henrike Heise, Gültekin Tamgüney and Wolfgang Hoyer

Contributions: Design of constructs, transformation, expression, purification, SDS-PAGE, CD experiments, elongation assay, lipid-induced primary nucleation assay, secondary nucleation assay, AFM imaging, evaluation of the ThT kinetics, CD data and NMR data, preparation of figures, writing and reviewing of the manuscript

Chapter 4:
Nucleation processes drive α-synuclein fibril proliferation in shaking-induced seed amplification assay
Celina M. Schulz*, Stefan Breuer*, Björn Falkenburger and Wolfgang Hoyer
*: These authors contributed equally.

Contributions: Transformation, expression, purification, elongation assay, fragmentation-elongation assay, secondary nucleation, SAA using WT αS as substrate, AFM imaging, evaluation of the ThT kinetics, preparation of figures, writing and reviewing of the manuscript

Chapter 5:

Deciphering upregulated mechanisms through expression profiling in SH-SY5Y cells when exposed to α-synuclein fibrils

Celina M. Schulz, Hamed Shayhalishahia, Nima Abedpour and Wolfgang Hoyer

Contributions: Transformation, expression, purification, labeling of aS-C140, preparation of fibrils and pHrodo-labeled fibrils, AFM imaging, SDS-PAGE and western blot, cultivating and differentiating of SH-SY5Y cells, flow cytometery, siRNA and qPCR experiments, immunocytochemistry and microscopy, analysis of the flow cytometery data and qPCR, preparation of figures, writing of this manuscript based on the preliminary data

Chapter 6:

An islet amyloid polypeptide oligomer model for the study of amyloid aggregation and oligomer induced pathophysiology

Anne Pfitzer*, Celina M. Schulz*, Robin Backer, Filip Haseck and Wolfgang Hoyer

*: These authors contributed equally.

Contributions: Preparation of dimIAPP-O and IAPP fibrils, cultivating and treatment of RIN-m5f cells, cell viability assay, qPCR experiments, immunocytochemistry and microscopy, evaluation of qPCR, preparation of figures, writing and reviewing of the manuscript

9

LITERATURE

[1] Zaida L Almeida and Rui MM Brito. Structure and aggregation mechanisms in amyloids. *Molecules*, 25(5):1195, 2020.

[2] Jean D Sipe and Alan S Cohen. History of the amyloid fibril. *Journal of structural biology*, 130(2-3):88–98, 2000.

[3] Rud Virchow. Ueber eine im gehirn und rückenmark des menschen aufgefundene substanz mit der chemischen reaction der cellulose. *Archiv für pathologische Anatomie und Physiologie und für klinische Medicin*, 6(1):135–138, 1854.

[4] Rud Virchow. Neue beobachtungen über amyloide degeneration. *Virchows Archiv*, 11(2):188–189, 1857.

[5] Nikolaus Friedreich and August Kekulé. Zur amyloidfrage. *Archiv für pathologische Anatomie und Physiologie und für klinische Medicin*, 16(1-2):50–65, 1859.

[6] Holde Puchtler, Faye Sweat, and M Levine. On the binding of congo red by amyloid. *Journal of Histochemistry Cytochemistry*, 10(3):355–364, 1962.

[7] Earl P. Benditt, Nils Eriksen, Mark A Hermodson, and Lowell H Ericsson. The major proteins of human and monkey amyloid substance: common properties including unusual n-terminal amino acid sequences. *FEBS letters*, 19(2):169–173, 1971.

[8] GG Glenner, D Ein, ED Eanes, HA Bladen, W Terry, and DL Page. Creation of "amyloid" fibrils from bence jones proteins in vitro. *Science*, 174(4010):712–714, 1971.

[9] Pedro P Costa, Arlinda S Figueira, and Fernanda R Bravo. Amyloid fibril protein related to prealbumin in familial amyloidotic polyneuropathy. *Proceedings of the National Academy of Sciences*, 75(9):4499–4503, 1978.

[10] AJ Geddes, KD Parker, Edward D T Atkins, and E Beighton. "cross-β" conformation in proteins. *Journal of molecular biology*, 32(2):343–358, 1968.

[11] Matthew G Iadanza, Matthew P Jackson, Eric W Hewitt, Neil A Ranson, and Sheena E Radford. A new era for understanding amyloid structures and disease. *Nature Reviews Molecular Cell Biology*, 19(12):755–773, 2018.

[12] Ming Tang, Gemma Comellas, and Chad M Rienstra. Advanced solid-state nmr approaches for structure determination of membrane proteins and amyloid fibrils. *Accounts of chemical research*, 46(9):2080–2088, 2013.

[13] Werner Kühlbrandt. The resolution revolution. *Science*, 343(6178):1443–1444, 2014.

[14] Dan Li and Cong Liu. Structural diversity of amyloid fibrils and advances in their structure determination. *Biochemistry*, 59(5):639–646, 2020.

[15] Christopher M Dobson. Protein folding and misfolding. *Nature*, 426(6968):884–90, 2003.

[16] Melanie R Nilsson. Techniques to study amyloid fibril formation in vitro. *Methods*, 34(1):151–160, 2004.

[17] Robyn Eisert, Liseda Felau, and Lesley R Brown. Methods for enhancing the accuracy and reproducibility of congo red and thioflavin t assays. *Analytical biochemistry*, 353(1):144–146, 2006.

[18] Robert Vassar, Brian D Bennett, Safura Babu-Khan, Steve Kahn, Elizabeth A Mendiaz, Paul Denis, David B Teplow, Sandra Ross, Patricia Amarante, and Richard Loeloff. β-secretase cleavage of alzheimer's amyloid precursor protein by the transmembrane aspartic protease bace. *Science*, 286(5440):735–741, 1999.

[19] Marie-Christine Chartier-Harlin, Jennifer Kachergus, Christophe Roumier, Vincent Mouroux, Xavier Douay, Sarah Lincoln, Clotilde Levecque, Lydie Larvor, Joris Andrieux, and Mary Hulihan. α-synuclein locus duplication as a cause of familial parkinson's disease. *The Lancet*, 364(9440):1167–1169, 2004.

[20] Per Westermark, Arne Andersson, and Gunilla T Westermark. Islet amyloid polypeptide, islet amyloid, and diabetes mellitus. *Physiological reviews*, 91(3):795–826, 2011.

[21] Daniel Otzen and Roland Riek. Functional amyloids. *Cold Spring Harbor perspectives in biology*, 11(12):a033860, 2019.

[22] Jean D Sipe. Amyloid fibril protein nomenclature: 2010 recommendations from the nomenclature committee of the international society of amyloidosis. *Amyloid*, 17:101–104, 2010.

[23] Merrill D Benson, Joel N Buxbaum, David S Eisenberg, Giampaolo Merlini, Maria JM Saraiva, Yoshiki Sekijima, Jean D Sipe, and Per Westermark. Amyloid nomenclature 2018: recommendations by the international society of amyloidosis (isa) nomenclature committee. *Amyloid*, 25(4):215–219, 2018.

[24] Joel N Buxbaum, Angela Dispenzieri, David S Eisenberg, Marcus Fändrich, Giampaolo Merlini, Maria JM Saraiva, Yoshiki Sekijima, and Per Westermark. Amyloid nomenclature 2022: update, novel proteins, and recommendations by the international society of amyloidosis (isa) nomenclature committee. *Amyloid*, 29(4):213–219, 2022.

[25] Stanley B Prusiner, Michael P McKinley, Karen A Bowman, David C Bolton, Paul E Bendheim, Darlene F Groth, and George G Glenner. Scrapie prions aggregate to form amyloid-like birefringent rods. *Cell*, 35(2):349–358, 1983.

[26] David C Bolton, Michael P McKinley, and Stanley B Prusiner. Identification of a protein that purifies with the scrapie prion. *Science*, 218(4579):1309–1311, 1982.

[27] Bruno Oesch, David Westaway, Monika Wälchli, Michael P McKinley, Stephen BH Kent, Ruedi Aebersold, Ronald A Barry, Paul Tempst, David B Teplow, and Leroy E Hood. A cellular gene encodes scrapie prp 27-30 protein. *Cell*, 40(4):735–746, 1985.

[28] Stanley B Prusiner. Molecular biology of prion diseases. *Science*, 252(5012):1515–1522, 1991.

[29] Dieter Willbold, Birgit Strodel, Gunnar F Schröder, Wolfgang Hoyer, and Henrike Heise. Amyloid-type protein aggregation and prion-like properties of amyloids. *Chemical reviews*, 121(13):8285–8307, 2021.

[30] Stanley B Prusiner. Prions. *Proceedings of the National Academy of Sciences*, 95(23):13363–13383, 1998.

[31] Fabrizio Chiti and Christopher M Dobson. Protein misfolding, functional amyloid, and human disease. *Annu. Rev. Biochem.*, 75:333–366, 2006.

[32] David Eisenberg and Mathias Jucker. The amyloid state of proteins in human diseases. *Cell*, 148(6):1188–1203, 2012.

[33] Per Westermark, Merrill D Benson, Joel N Buxbaum, Alan S Cohen, Blas Frangione, Shu-Ichi Ikeda, Colin L Masters, Giampaolo Merlini, Maria J Saraiva, and Jean D Sipe. Amyloid: Toward terminology clarification report from the nomenclature committee of the international society of amyloidosis. *Amyloid*, 12(1):1–4, 2005.

[34] M Goedert, CM Wischik, RA Crowther, JE Walker, and A Klug. Cloning and sequencing of the cdna encoding a core protein of the paired helical filament of alzheimer disease: identification as the microtubule-associated protein tau. *Proceedings of the National Academy of Sciences*, 85(11):4051–4055, 1988.

[35] Joan Selverstone Valentine, Peter A Doucette, and Soshanna Zittin Potter. Copper-zinc superoxide dismutase and amyotrophic lateral sclerosis. *Annu. Rev. Biochem.*, 74:563–593, 2005.

[36] Vaishali Sanchorawala. Light-chain (al) amyloidosis: diagnosis and treatment. *Clinical Journal of the American Society of Nephrology*, 1(6):1331–1341, 2006.

[37] Karl M Koch. Dialysis-related amyloidosis. *Kidney international*, 41(5):1416–1429, 1992.

[38] Jeffery W Kelly. The alternative conformations of amyloidogenic proteins and their multi-step assembly pathways. *Current opinion in structural biology*, 8(1):101–106, 1998.

[39] Christopher M Dobson. The structural basis of protein folding and its links with human disease. *Philosophical Transactions of the Royal Society of London. Series B: Biological Sciences*, 356(1406):133–145, 2001.

[40] Sarah Vascellari, Christina D Orrù, and Byron Caughey. Real-time quaking-induced conversion assays for prion diseases, synucleinopathies, and tauopathies. *Frontiers in Aging Neuroscience*, 14:853050, 2022.

[41] Urmi Sengupta and Rakez Kayed. Amyloid β, tau, and α-synuclein aggregates in the pathogenesis, prognosis, and therapeutics for neurodegenerative diseases. *Progress in Neurobiology*, 214:102270, 2022.

[42] Rodrigo Morales, Lisbell D Estrada, Rodrigo Diaz-Espinoza, Diego Morales-Scheihing, Maria C Jara, Joaquin Castilla, and Claudio Soto. Molecular cross talk between misfolded proteins in animal models of alzheimer's and prion diseases. *J Neurosci*, 30(13):4528–35, 2010.

[43] Janett Koppen, Anja Schulze, Lisa Machner, Michael Wermann, Rico Eichentopf, Max Guthardt, Angelika Hahnel, Jessica Klehm, Marie-Christin Kriegeskorte, Maike Hartlage-Rubsamen, Markus Morawski, Stephan von Horsten, Hans-Ulrich Demuth, Steffen Rossner, and Stephan Schilling. Amyloid-beta peptides trigger aggregation of alpha-synuclein in vitro. *Molecules*, 25(3), 2020.

[44] J. Gotz, F. Chen, J. van Dorpe, and R. M. Nitsch. Formation of neurofibrillary tangles in p301l tau transgenic mice induced by abeta 42 fibrils. *Science*, 293(5534):1491–5, 2001.

[45] Cristian A Lasagna-Reeves, Diana L Castillo-Carranza, Marcos J Guerrero-Muoz, George R Jackson, and Rakez Kayed. Preparation and characterization of neurotoxic tau oligomers. *Biochemistry*, 49(47):10039–41, 2010.

[46] I. Moreno-Gonzalez, G. Edwards Iii, N. Salvadores, M. Shahnawaz, R. Diaz-Espinoza, and C. Soto. Molecular interaction between type 2 diabetes and alzheimer's disease through cross-seeding of protein misfolding. *Mol Psychiatry*, 22(9):1327–1334, 2017.

[47] Brian O'Nuallain, Angela D Williams, Per Westermark, and Ronald Wetzel. Seeding specificity in amyloid growth induced by heterologous fibrils. *J Biol Chem*, 279(17):17490–9, 2004.

[48] Xiaohua Li, Dalin Song, and Sean X Leng. Link between type 2 diabetes and alzheimer's disease: from epidemiology to mechanism and treatment. *Clinical interventions in aging*, pages 549–560, 2015.

[49] Marie E Oskarsson, Johan F Paulsson, Sebastian W Schultz, Martin Ingelsson, Per Westermark, and Gunilla T Westermark. In vivo seeding and cross-seeding of localized amyloidosis: a molecular link between type 2 diabetes and alzheimer disease. *Am J Pathol*, 185(3):834–46, 2015.

[50] Rakez Kayed, Elizabeth Head, Jennifer L Thompson, Theresa M McIntire, Saskia C Milton, Carl W Cotman, and Charles G Glabe. Common structure of soluble amyloid oligomers implies common mechanism of pathogenesis. *Science*, 300(5618):486–9, 2003.

[51] Christian Haass and Dennis J. Selkoe. Soluble protein oligomers in neurodegeneration: lessons from the alzheimer's amyloid beta-peptide. *Nat Rev Mol Cell Biol*, 8(2):101–12, 2007.

[52] Karin Sorgjerd, Therese Klingstedt, Mikael Lindgren, Katarina Kagedal, and Per Hammarstrom. Prefibrillar transthyretin oligomers and cold stored native tetrameric transthyretin are cytotoxic in cell culture. *Biochem Biophys Res Commun*, 377(4):1072–8, 2008.

[53] Erika N Cline, Maira Assuncao Bicca, Kirsten L Viola, and William L Klein. The amyloid-beta oligomer hypothesis: Beginning of the third decade. *J Alzheimers Dis*, 64(s1):S567–S610, 2018.

[54] Karie N Dahlgren, Arlene M Manelli, W Blaine Stine, Lorinda K Baker, Grant A Krafft, and Mary Jo LaDu. Oligomeric and fibrillar species of amyloid-beta peptides differentially affect neuronal viability. *J Biol Chem*, 277(35):32046–53, 2002.

[55] Derya Emin, Yu P Zhang, Evgeniia Lobanova, Alyssa Miller, Xuecong Li, Zengjie Xia, Helen Dakin, Dimitrios I Sideris, Jeff Y L Lam, Rohan T Ranasinghe, Antonina Kouli, Yanyan Zhao, Suman De, Tuomas P J Knowles, Michele Vendruscolo, Francesco S Ruggeri, Franklin I Aigbirhio, Caroline H Williams-Gray, and David Klenerman. Small soluble alpha-synuclein aggregates are the toxic species in parkinson's disease. *Nat Commun*, 13(1):5512, 2022.

[56] Diana C Rodriguez Camargo, Divita Garg, Katalin Buday, Andras Franko, Andres Rodriguez Camargo, Fabian Schmidt, Sarah J Cox, Saba Suladze, Martin Haslbeck, and Yonatan G Mideksa. hiapp forms toxic oligomers in plasma. *Chemical Communications*, 54(43):5426–5429, 2018.

[57] Heiko Braak and Eva Braak. Neuropathological stageing of alzheimer-related changes. *Acta Neuropathol*, 82(4):239–59, 1991.

[58] Changiz Guela, Chuang-Kuo Wu, Daniel Saroff, Alfredo Lorenzo, Menglan Yuan, and Bruce A Yankner. Aging renders the brain vulnerable to amyloid β-protein neurotoxicity. *Nature medicine*, 4(7):827–831, 1998.

[59] ER Dorsey, R Constantinescu, JP Thompson, KM Biglan, RG Holloway, K Kieburtz, FJ Marshall, BM Ravina, G Schifitto, and A Siderowf. Projected number of people with parkinson disease in the most populous nations, 2005 through 2030. *Neurology*, 68(5):384–386, 2007.

[60] Petra Maresova, Blanka Klimova, Michal Novotny, and Kamil Kuca. Alzheimer's and parkinson's diseases: Expected economic impact on europe-a call for a uniform european strategy. *J Alzheimers Dis*, 54(3):1123–1133, 2016.

[61] Grace E Vitek, Boris Decourt, and Marwan N Sabbagh. Lecanemab (ban2401): an anti-beta-amyloid monoclonal antibody for the treatment of alzheimer disease. *Expert Opin Investig Drugs*, 32(2):89–94, 2023.

[62] Morteza Abyadeh, Vivek Gupta, Veer Gupta, Nitin Chitranshi, Yunqi Wu, Ardeshir Amirkhani, Anna Meyfour, Samran Sheriff, Ting Shen, Kunal Dhiman, Ghasem H. Salekdeh, Paul A. Haynes, Stuart L. Graham, and Mehdi Mirzaei. Comparative analysis of aducanumab, zagotenemab and pioglitazone as targeted treatment strategies for alzheimer's disease. *Aging and disease*, 12(8):1964, 2021.

[63] Janine Kutzsche, Sarah Schemmert, Tuyen Bujnicki, Christian Zafiu, Steffen Halbgebauer, Victoria Kraemer-Schulien, Marlene Pils, Lara Blömeke, Julia Post, and Andreas Kulawik. Oral treatment with the all-d-peptide rd2 enhances cognition in aged beagle dogs–a model of sporadic alzheimer's disease. *Heliyon*, 9(8), 2023.

[64] Germán Plascencia-Villa and George Perry. Status and future directions of clinical trials in alzheimer's disease. In *Metabolic and Bioenergetic Drivers of Neurodegenerative Disease: Neurodegenerative Disease Research and Commonalities with Metabolic Diseases*, page 3–50. Elsevier, 2020.

[65] Pedro Magalhães and Hilal A Lashuel. Opportunities and challenges of alpha-synuclein as a potential biomarker for parkinson's disease and other synucleinopathies. *npj Parkinson's Disease*, 8(1):93, 2022.

[66] Douglas M Fowler, Atanas V Koulov, Christelle Alory-Jost, Michael S Marks, William E Balch, and Jeffery W Kelly. Functional amyloid formation within mammalian tissue. *PLoS Biol*, 4(1):e6, 2006.

[67] Matthew R Chapman, Lloyd S Robinson, Jerome S Pinkner, Robyn Roth, John Heuser, Marten Hammar, Staffan Normark, and Scott J Hultgren. Role of *Escherichia coli* curli operons in directing amyloid fiber formation. *Science*, 295(5556):851–5, 2002.

[68] Xuan Wang and Matthew R Chapman. Sequence determinants of bacterial amyloid formation. *J Mol Biol*, 380(3):570–80, 2008.

[69] V Coustou, C Deleu, S Saupe, and J Begueret. The protein product of the het-s heterokaryon incompatibility gene of the fungus podospora anserina behaves as a prion analog. *Proc Natl Acad Sci USA*, 94(18):9773–8, 1997.

[70] Fabrice Barral Caudron and Yves Barral. A super-assembly of whi3 encodes memory of deceptive encounters by single cells during yeast courtship. *Cell*, 155(6):1244–57, 2013.

[71] Shady Saad, Gea Cereghetti, Yuehan Feng, Paola Picotti, Matthias Peter, and Reinhard Dechant. Reversible protein aggregation is a protective mechanism to ensure cell cycle restart after stress. *Nat Cell Biol*, 19(10):1202–1213, 2017.

[72] Asen Daskalov, Mathieu Paoletti, Frederique Ness, and Sven J Saupe. Genomic clustering and homology between het-s and the nwd2 stand protein in various fungal genomes. *PLoS One*, 7(4):e34854, 2012.

[73] Brenda Watt, Guillaume van Niel, Graca Raposo, and Michael S Marks. Pmel: a pigment cell-specific model for functional amyloid formation. *Pigment Cell Melanoma Res*, 26(3):300–15, 2013.

[74] Carolin Seuring, Jason Greenwald, Christian Wasmer, Roger Wepf, Sven J Saupe, Beat H Meier, and Roland Riek. The mechanism of toxicity in het-s/het-s prion incompatibility. *PLoS Biol*, 10(12):e1001451, 2012.

[75] Ruben Hervas, Liying Li, Amitabha Majumdar, Maria Del Carmen Fernandez-Ramirez, Jay R Unruh, Brian D Slaughter, Albert Galera-Prat, Elena Santana, Mari Suzuki, Yoshitaka Nagai, Marta Bruix, Sergio Casas-Tinto, Margarita Menendez, Douglas V Laurents, Kausik Si, and Mariano Carrion-Vazquez. Molecular basis of orb2 amyloidogenesis and blockade of memory consolidation. *PLoS Biol*, 14(1):e1002361, 2016.

[76] Maria Andreasen, Georg Meisl, Jonathan D Taylor, Thomas C T Michaels, Aviad Levin, Daniel E Otzen, Matthew R Chapman, Christopher M Dobson, Steve J Matthews, and Tuomas P J Knowles. Physical determinants of amyloid assembly in biofilm formation. *mBio*, 10(1):10–1128, 2019.

[77] Morten S Dueholm, Soren B Nielsen, Kim L Hein, Poul Nissen, Matthew Chapman, Gunna Christiansen, Per Halkjaer Nielsen, and Daniel E Otzen. Fibrillation of the major curli subunit csga under a wide range of conditions implies a robust design of aggregation. *Biochemistry*, 50(39):8281–90, 2011.

[78] Tuomas PJ Knowles and Raffaele Mezzenga. Amyloid fibrils as building blocks for natural and artificial functional materials. *Advanced materials*, 28(31):6546–6561, 2016.

[79] Samir K Maji, David Schubert, Catherine Rivier, Soon Lee, Jean E Rivier, and Roland Riek. Amyloid as a depot for the formulation of long-acting drugs. *PLoS biology*, 6(2):e17, 2008.

[80] Chaoxu Li, Jozef Adamcik, and Raffaele Mezzenga. Biodegradable nanocomposites of amyloid fibrils and graphene with shape-memory and enzyme-sensing properties. *Nature nanotechnology*, 7(7):421–427, 2012.

[81] L Sasso, S Suei, L Domigan, J Healy, V Nock, M A Williams, and J A Gerrard. Versatile multifunctionalization of protein nanofibrils for biosensor applications. *Nanoscale*, 6(3):1629–34, 2014.

[82] Sally L Gras, Anna K Tickler, Adam M Squires, Glyn L Devlin, Michael A Horton, Christopher M Dobson, and Cait E MacPhee. Functionalised amyloid fibrils for roles in cell adhesion. *Biomaterials*, 29(11):1553–62, 2008.

[83] Chaoxu Li, Anne-Kathrin Born, Thomas Schweizer, Marcy Zenobi-Wong, Marta Cerruti, and Raffaele Mezzenga. Amyloid-hydroxyapatite bone biomimetic composites. *Adv Mater*, 26(20):3207–12, 2014.

[84] Reeba S Jacob, Dhiman Ghosh, Pradeep K Singh, Santanu K Basu, Narendra Nath Jha, Subhadeep Das, Pradip K Sukul, Sachin Patil, Sadhana Sathaye, Ashutosh Kumar, Arindam Chowdhury, Sudip Malik, Shamik Sen, and Samir K Maji. Self healing hydrogels composed of amyloid nano fibrils for cell culture and stem cell differentiation. *Biomaterials*, 54:97–105, 2015.

[85] Michel W Jaworek, Vitor Schuabb, and Roland Winter. Pressure and cosolvent modulation of the catalytic activity of amyloid fibrils. *Chem Commun (Camb)*, 54(45):5696–5699, 2018.

[86] Z S Al-Garawi, B A McIntosh, D Neill-Hall, A A Hatimy, S M Sweet, M C Bagley, and L C Serpell. The amyloid architecture provides a scaffold for enzyme-like catalysts. *Nanoscale*, 9(30):10773–10783, 2017.

[87] Konstantin K Turoverov, Irina M Kuznetsova, and Vladimir N Uversky. The protein kingdom extended: ordered and intrinsically disordered proteins, their folding, supramolecular complex formation, and aggregation. *Prog Biophys Mol Biol*, 102(2-3):73–84, 2010.

[88] Thomas R Jahn and Sheena E Radford. Folding versus aggregation: polypeptide conformations on competing pathways. *Arch Biochem Biophys*, 469(1):100–17, 2008.

[89] Christian B Anfinsen. Principles that govern the folding of protein chains. *Science*, 181(4096):223–30, 1973.

[90] Andrew J Baldwin, Tuomas P J Knowles, Gian Gaetano Tartaglia, Anthony W Fitzpatrick, Glyn L Devlin, Sarah Lucy Shammas, Christopher A Waudby, Maria F Mossuto, Sarah Meehan, Sally L Gras, John Christodoulou, Spencer J Anthony-Cahill, Paul D Barker, Michele Vendruscolo, and Christopher M Dobson. Metastability of native proteins and the phenomenon of amyloid formation. *J Am Chem Soc*, 133(36):14160–3, 2011.

[91] Wei Wang, Sandeep Nema, and Dirk Teagarden. Protein aggregation–pathways and influencing factors. *Int J Pharm*, 390(2):89–99, 2010.

[92] Binsen Li, Peng Ge, Kevin A Murray, Phorum Sheth, Meng Zhang, Gayatri Nair, Michael R Sawaya, Woo Shik Shin, David R Boyer, Shulin Ye, David S Eisenberg, Z Hong Zhou, and Lin Jiang. Cryo-em of full-length alpha-synuclein reveals fibril polymorphs with a common structural kernel. *Nat Commun*, 9(1):3609, 2018.

[93] Katy E Routledge, Gian Gaetano Tartaglia, Geoffrey W Platt, Michele Vendruscolo, and Sheena E Radford. Competition between intramolecular and intermolecular interactions in an amyloid-forming protein. *Journal of molecular biology*, 389(4):776–786, 2009.

[94] D. Thirumalai and G. Reddy. Protein thermodynamics: Are native proteins metastable? *Nat Chem*, 3(12):910–1, 2011.

[95] Fabrizio Chiti, Niccolò Taddei, Fabiana Baroni, Cristina Capanni, Massimo Stefani, Giampietro Ramponi, and Christopher M Dobson. Kinetic partitioning of protein folding and aggregation. *Nature structural biology*, 9(2):137–143, 2002.

[96] Timo Eichner and Sheena E Radford. A diversity of assembly mechanisms of a generic amyloid fold. *Mol Cell*, 43(1):8–18, 2011.

[97] O Sumner Makin and Louise C Serpell. Structures for amyloid fibrils. *FEBS J*, 272(23):5950–61, 2005.

[98] Margaret Sunde and Colin Blake. The structure of amyloid fibrils by electron microscopy and x-ray diffraction. *Adv Protein Chem*, 50:123–59, 1997.

[99] Ravindra Kodali and Ronald Wetzel. Polymorphism in the intermediates and products of amyloid assembly. *Curr Opin Struct Biol*, 17(1):48–57, 2007.

[100] Margaret Sunde, Louise C Serpell, Mark Bartlam, Paul E Fraser, Mark B Pepys, and Colin C F Blake. Common core structure of amyloid fibrils by synchrotron x-ray diffraction. *J Mol Biol*, 273(3):729–39, 1997.

[101] Rebecca Nelson and David Eisenberg. Recent atomic models of amyloid fibril structure. *Curr Opin Struct Biol*, 16(2):260–5, 2006.

[102] Magdalena I Ivanova, Michael J Thompson, and David Eisenberg. A systematic screen of beta(2)-microglobulin and insulin for amyloid-like segments. *Proc Natl Acad Sci USA*, 103(11):4079–82, 2006.

[103] David S Eisenberg and Michael R Sawaya. Structural studies of amyloid proteins at the molecular level. *Annu Rev Biochem*, 86:69–95, 2017.

[104] Antonio Trovato, Fabrizio Chiti, Amos Maritan, and Flavio Seno. Insight into the structure of amyloid fibrils from the analysis of globular proteins. *PLoS computational biology*, 2(12):e170, 2006.

[105] Shilpa Sambashivan, Yanshun Liu, Michael R Sawaya, Mari Gingery, and David Eisenberg. Amyloid-like fibrils of ribonuclease a with three-dimensional domain-swapped and native-like structure. *Nature*, 437(7056):266–9, 2005.

[106] Tsuranobu Shirahama and Alan S Cohen. High-resolution electron microscopic analysis of the amyloid fibril. *J Cell Biol*, 33(3):679–708, 1967.

[107] Julia Gath, Luc Bousset, Birgit Habenstein, Ronald Melki, Anja Böckmann, and Beat H Meier. Unlike twins: an nmr comparison of two α-synuclein polymorphs featuring different toxicity. *PLoS One*, 9(3):e90659, 2014.

[108] Tuomas PJ Knowles, Alfonso De Simone, Anthony W Fitzpatrick, Andrew Baldwin, Sarah Meehan, Luke Rajah, Michele Vendruscolo, Mark E Welland, Christopher M Dobson, and Eugene M Terentjev. Twisting transition between crystalline and fibrillar phases of aggregated peptides. *Physical Review Letters*, 109(15):158101, 2012.

[109] William Close, Matthias Neumann, Andreas Schmidt, Manuel Hora, Karthikeyan Annamalai, Matthias Schmidt, Bernd Reif, Volker Schmidt, Nikolaus Grigorieff, and Marcus Fändrich. Physical basis of amyloid fibril polymorphism. *Nat Commun*, 9(1):699, 2018.

[110] Marcus Fändrich, Jessica Meinhardt, and Nikolaus Grigorieff. Structural polymorphism of alzheimer abeta and other amyloid fibrils. *Prion*, 3(2):89–93, 2009.

[111] Jessica Meinhardt, Carsten Sachse, Peter Hortschansky, Nikolaus Grigorieff, and Marcus Fändrich. Abeta(1-40) fibril polymorphism implies diverse interaction patterns in amyloid fibrils. *J Mol Biol*, 386(3):869–77, 2009.

[112] Carsten Sachse, Marcus Fändrich, and Nikolaus Grigorieff. Paired beta-sheet structure of an abeta(1-40) amyloid fibril revealed by electron microscopy. *Proc Natl Acad Sci USA*, 105(21):7462–6, 2008.

[113] Carsten Sachse, Chen Xu, Karin Wieligmann, Stephan Diekmann, Nikolaus Grigorieff, and Marcus Fändrich. Quaternary structure of a mature amyloid fibril from alzheimer's abeta(1-40) peptide. *J Mol Biol*, 362(2):347–54, 2006.

[114] Marcal Vilar, Hui-Ting Chou, Thorsten Luhrs, Samir K Maji, Dominique Riek-Loher, Rene Verel, Gerard Manning, Henning Stahlberg, and Roland Riek. The fold of alpha-synuclein fibrils. *Proc Natl Acad Sci USA*, 105(25):8637–42, 2008.

[115] Altaira D Dearborn, Joseph S Wall, Naiqian Cheng, J Bernard Heymann, Andrey V Kajava, Jobin Varkey, Ralf Langen, and Alasdair C Steven. alpha-synuclein amyloid fibrils with two entwined, asymmetrically associated protofibrils. *J Biol Chem*, 291(5):2310–8, 2016.

[116] Luc Bousset, Laura Pieri, Gemma Ruiz-Arlandis, Julia Gath, Poul Henning Jensen, Birgit Habenstein, Karine Madiona, Vincent Olieric, Anja Bockmann, Beat H Meier, and Ronald Melki. Structural and functional characterization of two alpha-synuclein strains. *Nat Commun*, 4:2575, 2013.

[117] Joeri Verasdonck, Luc Bousset, Julia Gath, Ronald Melki, Anja Bockmann, and Beat H Meier. Further exploration of the conformational space of alpha-synuclein fibrils: solid-state nmr assignment of a high-ph polymorph. *Biomol NMR Assign*, 10(1):5–12, 2016.

[118] Ali Makky, Luc Bousset, Jerome Polesel-Maris, and Ronald Melki. Nanomechanical properties of distinct fibrillar polymorphs of the protein alpha-synuclein. *Sci Rep*, 6:37970, 2016.

[119] Jozef Adamcik, Jin-Mi Jung, Jerome Flakowski, Paolo De Los Rios, Giovanni Dietler, and Raffaele Mezzenga. Understanding amyloid aggregation by statistical analysis of atomic force microscopy images. *Nat Nanotechnol*, 5(6):423–8, 2010.

[120] Karolina L Zapadka, Frederik J Becher, A L Gomes Dos Santos, and Sophie E Jackson. Factors affecting the physical stability (aggregation) of peptide therapeutics. *Interface Focus*, 7(6):20170030, 2017.

[121] Martin Wilkinson, Yong Xu, Dev Thacker, Alexander I P Taylor, Declan G Fisher, Rodrigo U Gallardo, Sheena E Radford, and Neil A Ranson. Structural evolution of fibril polymorphs during amyloid assembly. *Cell*, 186(26):5798–5811 e26, 2023.

[122] Murielle A Watzky, Aimee M Morris, Eric D Ross, and Richard G Finke. Fitting yeast and mammalian prion aggregation kinetic data with the finke-watzky two-step model of nucleation and autocatalytic growth. *Biochemistry*, 47(40):10790–800, 2008.

[123] Aimee M Morris, Murielle A Watzky, Jeffrey N Agar, and Richard G Finke. Fitting neurological protein aggregation kinetic data via a 2-step, minimal/"ockham's razor" model: the finke-watzky mechanism of nucleation followed by autocatalytic surface growth. *Biochemistry*, 47(8):2413–27, 2008.

[124] Tuomas P J Knowles, Michele Vendruscolo, and Christopher M Dobson. The amyloid state and its association with protein misfolding diseases. *Nat Rev Mol Cell Biol*, 15(6):384–96, 2014.

[125] Georg Meisl, Julius B Kirkegaard, Paolo Arosio, Thomas C T Michaels, Michele Vendruscolo, Christopher M Dobson, Sara Linse, and Tuomas P J Knowles. Molecular mechanisms of protein aggregation from global fitting of kinetic models. *Nat Protoc*, 11(2):252–72, 2016.

[126] Paolo Arosio, Tuomas P J Knowles, and Sara Linse. On the lag phase in amyloid fibril formation. *Phys Chem Chem Phys*, 17(12):7606–18, 2015.

[127] James D Harper and Peter T Lansbury Jr. Models of amyloid seeding in alzheimer's disease and scrapie: mechanistic truths and physiological consequences of the time-dependent solubility of amyloid proteins. *Annu Rev Biochem*, 66:385–407, 1997.

[128] Sarah Perrett, Alexander K Buell, Christopher M Dobson, and Tuomas PJ Knowles. The physical chemistry of the amyloid phenomenon: thermodynamics and kinetics of filamentous protein aggregation. *Essays in biochemistry*, 56:11–39, 2014.

[129] Tuomas PJ Knowles, Christopher A Waudby, Glyn L Devlin, Samuel IA Cohen, Adriano Aguzzi, Michele Vendruscolo, Eugene M Terentjev, Mark E Welland, and Christopher M Dobson. An analytical solution to the kinetics of breakable filament assembly. *Science*, 326(5959):1533–1537, 2009.

[130] Wei-Feng Xue and Sheena E Radford. An imaging and systems modeling approach to fibril breakage enables prediction of amyloid behavior. *Biophysical journal*, 105(12):2811–2819, 2013.

[131] Sara Linse. Monomer-dependent secondary nucleation in amyloid formation. *Biophys Rev*, 9(4):329–338, 2017.

[132] Samuel IA Cohen, Michele Vendruscolo, Mark E Welland, Christopher M Dobson, Eugene M Terentjev, and Tuomas PJ Knowles. Nucleated polymerization with secondary pathways. i. time evolution of the principal moments. *The Journal of chemical physics*, 135(6), 2011.

[133] Maksim I Sulatsky, Anna I Sulatskaya, Olga V Stepanenko, Olga I Povarova, I. M. Kuznetsova, and K. K. Turoverov. Denaturant effect on amyloid fibrils: Declasterization, depolymerization, denaturation and reassembly. *Int J Biol Macromol*, 150:681–694, 2020.

[134] Alessandro Sicorello, Silvia Torrassa, Gemma Soldi, Stefano Gianni, Carlo Travaglini-Allocatelli, Niccolo Taddei, Annalisa Relini, and Fabrizio Chiti. Agitation and high ionic strength induce amyloidogenesis of a folded pdz domain in native conditions. *Biophys J*, 96(6):2289–98, 2009.

[135] Alexander K Buell, Celine Galvagnion, Ricardo Gaspar, Emma Sparr, Michele Vendruscolo, Tuomas P J Knowles, Sara Linse, and Christopher M Dobson. Solution conditions determine the relative importance of nucleation and growth processes in alpha-synuclein aggregation. *Proc Natl Acad Sci USA*, 111(21):7671–6, 2014.

[136] Aimee M Morris, Murielle A Watzky, and Richard G Finke. Protein aggregation kinetics, mechanism, and curve-fitting: a review of the literature. *Biochim Biophys Acta*, 1794(3):375–97, 2009.

[137] Eri Chatani and Naoki Yamamoto. Recent progress on understanding the mechanisms of amyloid nucleation. *Biophys Rev*, 10(2):527–534, 2018.

[138] Wei-Feng Xue, Steve W Homans, and Sheena E Radford. Systematic analysis of nucleation-dependent polymerization reveals new insights into the mechanism of amyloid self-assembly. *Proc Natl Acad Sci U S A*, 105(26):8926–31, 2008.

[139] Thomas CT Michaels, Daoyuan Qian, Anđela Šarić, Michele Vendruscolo, Sara Linse, and Tuomas PJ Knowles. Amyloid formation as a protein phase transition. *Nature Reviews Physics*, 5(7):379–397, 2023.

[140] Soumik Ray, Nitu Singh, Rakesh Kumar, Komal Patel, Satyaprakash Pandey, Debalina Datta, Jaladhar Mahato, Rajlaxmi Panigrahi, Ambuja Navalkar, Surabhi Mehra, Laxmikant Gadhe, Debdeep Chatterjee, Ajay Singh Sawner, Siddhartha Maiti, Sandhya Bhatia, Juan Atilio Gerez, Arindam Chowdhury, Ashutosh Kumar, Ranjith Padinhateeri, Roland Riek, G Krishnamoorthy, and Samir K Maji. alpha-synuclein aggregation nucleates through liquid-liquid phase separation. *Nat Chem*, 12(8):705–716, 2020.

[141] Alexander J Dear, Georg Meisl, Andela Saric, Thomas C T Michaels, Magnus Kjaergaard, Sara Linse, and Tuomas P J Knowles. Identification of on- and off-pathway oligomers in amyloid fibril formation. *Chem Sci*, 11(24):6236–6247, 2020.

[142] Andela Saric, Yassmine C Chebaro, Tuomas P J Knowles, and Daan Frenkel. Crucial role of nonspecific interactions in amyloid nucleation. *Proc Natl Acad Sci USA*, 111(50):17869–74, 2014.

[143] Tam T M Phan and Jeremy D Schmit. Thermodynamics of huntingtin aggregation. *Biophys J*, 118(12):2989–2996, 2020.

[144] Andreas M Küffner, Miriam Linsenmeier, Fulvio Grigolato, Marc Prodan, Remo Zuccarini, Umberto Capasso Palmiero, Lenka Faltova, and Paolo Arosio. Sequestration within biomolecular condensates inhibits aβ-42 amyloid formation. *Chemical Science*, 12(12):4373–4382, 2021.

[145] Avinash Patel, Hyun O Lee, Louise Jawerth, Shovamayee Maharana, Marcus Jahnel, Marco Y Hein, Stoyno Stoynov, Julia Mahamid, Shambaditya Saha, Titus M Franzmann, Andrej Pozniakovski, Ina Poser, Nicola Maghelli, Loic A Royer, Martin Weigert, Eugene W Myers, Stephan Grill, David Drechsel, Anthony A Hyman, and Simon Alberti. A liquid-to-solid phase transition of the als protein fus accelerated by disease mutation. *Cell*, 162(5):1066–77, 2015.

[146] Yongdae Shin and Clifford P Brangwynne. Liquid phase condensation in cell physiology and disease. *Science*, 357(6357), 2017.

[147] Simon Alberti and Anthony A Hyman. Biomolecular condensates at the nexus of cellular stress, protein aggregation disease and ageing. *Nat Rev Mol Cell Biol*, 22(3):196–213, 2021.

[148] Sean R Collins, Adam Douglass, Ronald D Vale, and Jonathan S Weissman. Mechanism of prion propagation: amyloid growth occurs by monomer addition. *PLoS biology*, 2(10):e321, 2004.

[149] Alexander K Buell. The growth of amyloid fibrils: rates and mechanisms. *Biochem J*, 476(19):2677–2703, 2019.

[150] Zhiguang Jia, Jeremy D Schmit, and Jianhan Chen. Amyloid assembly is dominated by misregistered kinetic traps on an unbiased energy landscape. *Proceedings of the National Academy of Sciences*, 117(19):10322–10328, 2020.

[151] Munehito Arai, Kenji Sugase, H Jane Dyson, and Peter E Wright. Conformational propensities of intrinsically disordered proteins influence the mechanism of binding and folding. *Proceedings of the National Academy of sciences*, 112(31):9614–9619, 2015.

[152] Jesper Ferkinghoff-Borg, Jesper Fonslet, Christian Beyschau Andersen, Sandeep Krishna, Simone Pigolotti, Hisashi Yagi, Yuji Goto, Daniel Otzen, and Mogens H Jensen. Stop-and-go kinetics in amyloid fibrillation. *Physical Review E*, 82(1):010901, 2010.

[153] Volodymyr V Shvadchak, Kseniia Afitska, and Dmytro A Yushchenko. Inhibition of alpha-synuclein amyloid fibril elongation by blocking fibril ends. *Angew Chem Int Ed Engl*, 57(20):5690–5694, 2018.

[154] Christine Röder, Nicola Vettore, Lena N Mangels, Lothar Gremer, Raimond B G Ravelli, Dieter Willbold, Wolfgang Hoyer, Alexander K Buell, and Gunnar F Schröder. Atomic structure of pi3-kinase sh3 amyloid fibrils by cryo-electron microscopy. *Nat Commun*, 10(1):3754, 2019.

[155] Wei-Feng Xue, Andrew L Hellewell, Walraj S Gosal, Steve W Homans, Eric W Hewitt, and Sheena E Radford. Fibril fragmentation enhances amyloid cytotoxicity. *J Biol Chem*, 284(49):34272–82, 2009.

[156] Sarina Sanami, Tracey J Purton, David P Smith, Mick F Tuite, and Wei-Feng Xue. Comparative analysis of the relative fragmentation stabilities of polymorphic alpha-synuclein amyloid fibrils. *Biomolecules*, 12(5), 2022.

[157] Ricardo Gaspar, Georg Meisl, Alexander K Buell, Laurence Young, Clemens F Kaminski, Tuomas PJ Knowles, Emma Sparr, and Sara Linse. Secondary nucleation of monomers on fibril surface dominates α-synuclein aggregation and provides autocatalytic amyloid amplification. *Quarterly reviews of biophysics*, 50:e6, 2017.

[158] Mattias Törnquist, Thomas C T Michaels, Kalyani Sanagavarapu, Xiaoting Yang, Georg Meisl, Samuel I A Cohen, Tuomas P J Knowles, and Sara Linse. Secondary nucleation in amyloid formation. *Chem Commun (Camb)*, 54(63):8667–8684, 2018.

[159] Pei Huang, Fulin Lian, Yi Wen, Chenyun Guo, and Donghai Lin. Prion protein oligomer and its neurotoxicity. *Acta Biochim Biophys Sin (Shanghai)*, 45(6):442–51, 2013.

[160] Lorraine V Kalia, Suneil K Kalia, Pamela J McLean, Andres M Lozano, and Anthony E Lang. alpha-synuclein oligomers and clinical implications for parkinson disease. *Ann Neurol*, 73(2):155–69, 2013.

[161] Andisheh Abedini, Annette Plesner, Ping Cao, Zachary Ridgway, Jinghua Zhang, Ling-Hsien Tu, Chris T Middleton, Brian Chao, Daniel J Sartori, Fanling Meng, Hui Wang, Amy G Wong, Martin T Zanni, C Bruce Verchere, Daniel P Raleigh, and Ann Marie Schmidt. Time-resolved studies define the nature of toxic iapp intermediates, providing insight for anti-amyloidosis therapeutics. *Elife*, 5, 2016.

[162] Ruth E Uhlmann, Christine Rother, Jay Rasmussen, Juliane Schelle, Carina Bergmann, Emily M Ullrich Gavilanes, Sarah K Fritschi, Anika Buehler, Frank Baumann, Angelos Skodras, Rawaa Al-Shaana, Natalie Beschorner, Lan Ye, Stephan A Kaeser, Ulrike Obermuller, Soren Christensen, Fredrik Kartberg, Jeffrey B Stavenhagen, Jens-Ulrich Rahfeld, Holger Cynis, Fang Qian, Paul H Weinreb, Thierry Bussiere, Lary C Walker, Matthias Staufenbiel, and Mathias Jucker. Acute targeting of pre-amyloid seeds in transgenic mice reduces alzheimer-like pathology later in life. *Nat Neurosci*, 23(12):1580–1588, 2020.

[163] Marie P Schützmann, Filip Hasecke, Sarah Bachmann, Mara Zielinski, Sebastian Hansch, Gunnar F Schröder, Hans Zempel, and Wolfgang Hoyer. Endo-lysosomal abeta concentration and ph trigger formation of abeta oligomers that potently induce tau missorting. *Nat Commun*, 12(1):4634, 2021.

[164] Michelle A Poirier, Huilin Li, Jed Macosko, Shuowei Cai, Mario Amzel, and Christopher A Ross. Huntingtin spheroids and protofibrils as precursors in polyglutamine fibrilization. *J Biol Chem*, 277(43):41032–7, 2002.

[165] Corentin Berardet, Julia Kaffy, Frederic Halgand, Guillaume Van der Rest, Sandrine Ongeri, and Myriam Taverna. Evidence for different in vitro oligomerization behaviors of synthetic hiapp obtained from different sources. *Anal Bioanal Chem*, 412(13):3103–3111, 2020.

[166] Evan T Powers and David L Powers. Mechanisms of protein fibril formation: nucleated polymerization with competing off-pathway aggregation. *Biophys J*, 94(2):379–91, 2008.

[167] Martin Muschol and Wolfgang Hoyer. Amyloid oligomers as on-pathway precursors or off-pathway competitors of fibrils. *Front Mol Biosci*, 10:1120416, 2023.

[168] Shannon E Hill, Joshua Robinson, Garrett Matthews, and Martin Muschol. Amyloid protofibrils of lysozyme nucleate and grow via oligomer fusion. *Biophys J*, 96(9):3781–90, 2009.

[169] Filip Hasecke, Tatiana Miti, Carlos Perez, Jeremy Barton, Daniel Schölzel, Lothar Gremer, Clara S R Grüning, Garrett Matthews, Georg Meisl, Tuomas P J Knowles, Dieter Willbold, Philipp Neudecker, Henrike Heise, Ghanim Ullah, Wolfgang Hoyer, and Martin Muschol. Origin of metastable oligomers and their effects on amyloid fibril self-assembly. *Chem Sci*, 9(27):5937–5948, 2018.

[170] Arthur Laganowsky, Cong Liu, Michael R Sawaya, Julian P Whitelegge, Jiyong Park, Minglei Zhao, Anna Pensalfini, Angela B Soriaga, Meytal Landau, Poh K Teng, Duilio Cascio, Charles Glabe, and David Eisenberg. Atomic view of a toxic amyloid small oligomer. *Science*, 335(6073):1228–31, 2012.

[171] James C Stroud, Cong Liu, Poh K Teng, and David Eisenberg. Toxic fibrillar oligomers of amyloid-beta have cross-beta structure. *Proc Natl Acad Sci U S A*, 109(20):7717–22, 2012.

[172] Marcin I Apostol, Kay Perry, and Witold K Surewicz. Crystal structure of a human prion protein fragment reveals a motif for oligomer formation. *J Am Chem Soc*, 135(28):10202–5, 2013.

[173] Samuel A Kotler, Jeffrey R Brender, Subramanian Vivekanandan, Yuta Suzuki, Kazutoshi Yamamoto, Martine Monette, Janarthanan Krishnamoorthy, Patrick Walsh, Meagan Cauble, Mark M Banaszak Holl, E Neil G Marsh, and Ayyalusamy Ramamoorthy. High-resolution nmr characterization of low abundance oligomers of amyloid-beta without purification. *Sci Rep*, 5:11811, 2015.

[174] Emilie Cerf, Rabia Sarroukh, Shiori Tamamizu-Kato, Leonid Breydo, Sylvie Derclaye, Yves F Dufrene, Vasanthy Narayanaswami, Erik Goormaghtigh, Jean-Marie Ruysschaert, and Vincent Raussens. Antiparallel beta-sheet: a signature structure of the oligomeric amyloid beta-peptide. *Biochem J*, 421(3):415–23, 2009.

[175] Bappaditya Chandra, Debanjan Bhowmik, Barun Kumar Maity, Kaustubh R Mote, Debabrata Dhara, Ravindra Venkatramani, Sudipta Maiti, and Perunthiruthy K Madhu. Major reaction coordinates linking transient amyloid-beta oligomers to fibrils measured at atomic level. *Biophys J*, 113(4):805–816, 2017.

[176] Marina D Kirkitadze, Margaret M Condron, and David B Teplow. Identification and characterization of key kinetic intermediates in amyloid beta-protein fibrillogenesis. *J Mol Biol*, 312(5):1103–19, 2001.

[177] Montserrat Serra-Batiste, Marti Ninot-Pedrosa, Mariam Bayoumi, Margarida Gairi, Giovanni Maglia, and Natalia Carulla. Abeta42 assembles into specific beta-barrel pore-forming oligomers in membrane-mimicking environments. *Proc Natl Acad Sci U S A*, 113(39):10866–71, 2016.

[178] Winnie Yong, Aleksey Lomakin, Marina D Kirkitadze, David B Teplow, Sow-Hsin Chen, and George B Benedek. Structure determination of micelle-like intermediates in amyloid beta -protein fibril assembly by using small angle neutron scattering. *Proc Natl Acad Sci U S A*, 99(1):150–4, 2002.

[179] Bertrand Morel, Maria Paz Carrasco, Samuel Jurado, Carmen Marco, and Francisco Conejero-Lara. Dynamic micellar oligomers of amyloid beta peptides play a crucial role in their aggregation mechanisms. *Phys Chem Chem Phys*, 20(31):20597–20614, 2018.

[180] Walraj S Gosal, Isobel J Morten, Eric W Hewitt, D Alastair Smith, Neil H Thomson, and Sheena E Radford. Competing pathways determine fibril morphology in the self-assembly of beta2-microglobulin into amyloid. *J Mol Biol*, 351(4):850–64, 2005.

[181] Pierre O Souillac, Vladimir N Uversky, Ian S Millett, Ritu Khurana, Sebastian Doniach, and Anthony L Fink. Elucidation of the molecular mechanism during the early events in immunoglobulin light chain amyloid fibrillation. evidence for an off-pathway oligomer at acidic ph. *J Biol Chem*, 277(15):12666–79, 2002.

[182] Shannon E Hill, Tatiana Miti, Tyson Richmond, and Martin Muschol. Spatial extent of charge repulsion regulates assembly pathways for lysozyme amyloid fibrils. *PLoS One*, 6(4):e18171, 2011.

[183] Joseph Foley, Shannon E Hill, Tatiana Miti, Mentor Mulaj, Marissa Ciesla, Rhonda Robeel, Christopher Persichilli, Rachel Raynes, Sandy Westerheide, and Martin Muschol. Structural fingerprints and their evolution during oligomeric vs. oligomer-free amyloid fibril growth. *J Chem Phys*, 139(12):121901, 2013.

[184] Tatiana Miti, Mentor Mulaj, Jeremy D Schmit, and Martin Muschol. Stable, metastable, and kinetically trapped amyloid aggregate phases. *Biomacromolecules*, 16(1):326–35, 2015.

[185] Filip Hasecke, Chamani Niyangoda, Gustavo Borjas, Jianjun Pan, Garrett Matthews, Martin Muschol, and Wolfgang Hoyer. Protofibril-fibril interactions inhibit amyloid fibril assembly by obstructing secondary nucleation. *Angew Chem Int Ed Engl*, 60(6):3016–3021, 2021.

[186] Chad J. Swanson, Yong Zhang, Shobha Dhadda, Jinping Wang, June Kaplow, Robert Y. K. Lai, Lars Lannfelt, Heather Bradley, Martin Rabe, Akihiko Koyama, Larisa Reyderman, Donald A. Berry, Scott Berry, Robert Gordon, Lynn D. Kramer, and Jeffrey L. Cummings. A randomized, double-blind, phase 2b proof-of-concept clinical trial in early alzheimer's disease with lecanemab, an anti-aβ protofibril antibody. *Alzheimer's Research amp; Therapy*, 13(1), 2021.

[187] Linda Söderberg, Malin Johannesson, Patrik Nygren, Hanna Laudon, Fredrik Eriksson, Gunilla Osswald, Christer Möller, and Lars Lannfelt. Lecanemab, aducanumab, and gantenerumab — binding profiles to different forms of amyloid-beta might explain efficacy and side effects in clinical trials for alzheimer's disease. *Neurotherapeutics*, 20(1):195–206, 2023.

[188] Iryna Benilova, Eric Karran, and Bart De Strooper. The toxic abeta oligomer and alzheimer's disease: an emperor in need of clothes. *Nat Neurosci*, 15(3):349–57, 2012.

[189] Simon Makin. The amyloid hypothesis on trial. *Nature*, 559(7715):S4–S7, 2018.

[190] Monica Bucciantini, Elisa Giannoni, Fabrizio Chiti, Fabiana Baroni, Lucia Formigli, Jesus Zurdo, Niccolo Taddei, Giampietro Ramponi, Christopher M Dobson, and Massimo Stefani. Inherent toxicity of aggregates implies a common mechanism for protein misfolding diseases. *Nature*, 416(6880):507–11, 2002.

[191] Serena Baglioni, Fiorella Casamenti, Monica Bucciantini, Leila M Luheshi, Niccolo Taddei, Fabrizio Chiti, Christopher M Dobson, and Massimo Stefani. Prefibrillar amyloid aggregates could be generic toxins in higher organisms. *J Neurosci*, 26(31):8160–7, 2006.

[192] Juliette Janson, Richard H Ashley, David Harrison, Susan McIntyre, and Peter C Butler. The mechanism of islet amyloid polypeptide toxicity is membrane disruption by intermediate-sized toxic amyloid particles. *Diabetes*, 48(3):491–8, 1999.

[193] Masahiro Kawahara, Yoichiro Kuroda, Nelson Arispe, and Eduardo Rojas. Alzheimer's beta-amyloid, human islet amylin, and prion protein fragment evoke intracellular free calcium elevations by a common mechanism in a hypothalamic gnrh neuronal cell line. *J Biol Chem*, 275(19):14077–83, 2000.

[194] Cameron Wells, Samuel Brennan, Matt Keon, and Lezanne Ooi. The role of amyloid oligomers in neurodegenerative pathologies. *Int J Biol Macromol*, 181:582–604, 2021.

[195] Kenjiro Ono, Margaret M Condron, and David B Teplow. Structure-neurotoxicity relationships of amyloid beta-protein oligomers. *Proc Natl Acad Sci USA*, 106(35):14745–50, 2009.

[196] Huilai Tian, Eliot Davidowitz, Patricia Lopez, Sharareh Emadi, James Moe, and Michael Sierks. Trimeric tau is toxic to human neuronal cells at low nanomolar concentrations. *Int J Cell Biol*, 2013:260787, 2013.

[197] Metta K Jana, Roberto Cappai, Chi L L Pham, and Giuseppe D Ciccotosto. Membrane-bound tetramer and trimer abeta oligomeric species correlate with toxicity towards cultured neurons. *J Neurochem*, 136(3):594–608, 2016.

[198] Francesco Bemporad and Fabrizio Chiti. Protein misfolded oligomers: experimental approaches, mechanism of formation, and structure-toxicity relationships. *Chem Biol*, 19(3):315–27, 2012.

[199] Elizabeth A. Coon and Wolfgang Singer. Synucleinopathies. *CONTINUUM: Lifelong Learning in Neurology*, 26(1):72–92, 2020.

[200] Maria Grazia Spillantini and Michel Goedert. The β-synucleinopathies: Parkinson's disease, dementia with lewy bodies, and multiple system atrophy. *Annals of the New York Academy of Sciences*, 920(1):16–27, 2000.

[201] Bruce CV Campbell, Catriona A McLean, Janetta G Culvenor, Wei Ping Gai, Peter C Blumbergs, Pekka JaÈkaÈlaÈ, Konrad Beyreuther, Colin L Masters, and Qiao-Xin Li. The solubility of β-synuclein in multiple system atrophy differs from that of dementia with lewy bodies and parkinson's disease. *Journal of neurochemistry*, 76(1):87–96, 2001.

[202] Stanley B Prusiner, Amanda L Woerman, Daniel A Mordes, Joel C Watts, Ryan Rampersaud, David B Berry, Smita Patel, Abby Oehler, Jennifer K Lowe, and Stephanie N Kravitz. Evidence for α-synuclein prions causing multiple system atrophy in humans with parkinsonism. *Proceedings of the National Academy of Sciences*, 112(38):E5308–E5317, 2015.

[203] Carlos H Schenck, Allan L Callies, and Mark W Mahowald. Increased percentage of slow-wave sleep in rem sleep behavior disorder (rbd): a reanalysis of previously published data from a controlled study of rbd reported in sleep. *Sleep*, 26(8):1066, 2003.

[204] BF Boeve, MH Silber, JE Parisi, DW Dickson, TJ Ferman, EE Benarroch, AM Schmeichel, GE Smith, RC Petersen, and JE Ahlskog. Synucleinopathy pathology and rem sleep behavior disorder plus dementia or parkinsonism. *Neurology*, 61(1):40–45, 2003.

[205] MI Papp and PL Lantos. The distribution of oligodendroglial inclusions in multiple system atrophy and its relevance to clinical symptomatology. *Brain*, 117(2):235–243, 1994.

[206] Masayuki Inoue, Saburo Yagishita, Masafuchi Ryo, Kazuko Hasegawa, Naoji Amano, and Masaaki Matsushita. The distribution and dynamic density of oligodendroglial cytoplasmic inclusions (gcis) in multiple system atrophy: a correlation between the density of gcis and the degree of involvement of striatonigral and olivopontocerebellar systems. *Acta neuropathologica*, 93:585–591, 1997.

[207] Maria Grazia Spillantini, Marie Luise Schmidt, Virginia M-Y Lee, John Q Trojanowski, Ross Jakes, and Michel Goedert. α-synuclein in lewy bodies. *Nature*, 388(6645):839–840, 1997.

[208] Sarah H Shahmoradian, Amanda J Lewis, Christel Genoud, Jürgen Hench, Tim E Moors, Paula P Navarro, Daniel Castaño-Díez, Gabriel Schweighauser, Alexandra Graff-Meyer, Kenneth N Goldie, Rosmarie Sütterlin, Evelien Huisman, Angela Ingrassia, Yvonne de Gier, Annemieke J M Rozemuller, Jing Wang, Anne De Paepe, Johannes Erny, Andreas Staempfli, Joerg Hoernschemeyer, Frederik Großerüschkamp, Daniel Niedieker, Samir F El-Mashtoly, Marialuisa Quadri, Wilfred F J Van IJcken, Vincenzo Bonifati, Klaus Gerwert, Bernd Bohrmann, Stephan Frank, Markus Britschgi, Henning Stahlberg, Wilma D J Van de Berg, and Matthias E Lauer. Lewy pathology in parkinson's disease consists of crowded organelles and lipid membranes. *Nature Neuroscience*, 22(7):1099–1109, 2019.

[209] Chao Peng, Ronald J Gathagan, Dustin J Covell, Coraima Medellin, Anna Stieber, John L Robinson, Bin Zhang, Rose M Pitkin, Modupe F Olufemi, and Kelvin C Luk. Cellular milieu imparts distinct pathological α-synuclein strains in α-synucleinopathies. *Nature*, 557(7706):558–563, 2018.

[210] Ole-Bjorn Tysnes and Anette Storstein. Epidemiology of parkinson's disease. *J Neural Transm (Vienna)*, 124(8):901–905, 2017.

[211] James Parkinson. An essay on the shaking palsy. *Archives of Neurology*, 20(4):441–445, 1969.

[212] F Marxreiter and J Winkler. Idiopathisches parkinson-syndrom. *Nervenheilkunde*, 33(10):710–718, 2014.

[213] Michel Goedert. Alpha-synuclein and neurodegenerative diseases. *Nature reviews neuroscience*, 2(7):492–501, 2001.

[214] Lawrence I Golbe, Giuseppe Di Iorio, Vincenzo Bonavita, Douglas C Miller, and Roger C Duvoisin. A large kindred with autosomal dominant parkinson's disease. *Annals of Neurology: Official Journal of the American Neurological Association and the Child Neurology Society*, 27(3):276–282, 1990.

[215] Rejko Krüger, Wilfried Kuhn, Thomas Müller, Dirk Woitalla, Manuel Graeber, Sigfried Kösel, Horst Przuntek, Jörg T Epplen, Ludger Schols, and Olaf Riess. Alasopro mutation in the gene encoding α-synuclein in parkinson's disease. *Nature genetics*, 18(2):106–108, 1998.

[216] Juan J Zarranz, Javier Alegre, Juan C Gómez-Esteban, Elena Lezcano, Raquel Ros, Israel Ampuero, Lídice Vidal, Janet Hoenicka, Olga Rodriguez, and Begoña Atarés. The new mutation, e46k, of β-synuclein causes parkinson and lewy body dementia. *Annals of Neurology: Official Journal of the American Neurological Association and the Child Neurology Society*, 55(2):164–173, 2004.

[217] Suzanne Lesage, Mathieu Anheim, Franck Letournel, Luc Bousset, Aurélie Honoré, Nelly Rozas, Laura Pieri, Karine Madiona, Alexandra Dürr, and Ronald Melki. G51d β-synuclein mutation causes a novel parkinsonian–pyramidal syndrome. *Annals of neurology*, 73(4):459–471, 2013.

[218] Petra Pasanen, Liisa Myllykangas, Maija Siitonen, Anna Raunio, Seppo Kaakkola, Jukka Lyytinen, Pentti J Tienari, Minna Pöyhönen, and Anders Paetau. A novel α-synuclein mutation

a53e associated with atypical multiple system atrophy and parkinson's disease-type pathology. *Neurobiology of aging*, 35(9):2180. e1–2180. e5, 2014.

[219] Dorota Hoffman-Zacharska, Dariusz Koziorowski, Owen A Ross, Michał Milewski, Jarosław Poznański, Marta Jurek, Zbigniew K Wszolek, Alexandra Soto-Ortolaza, Jarosław Sławek, and Piotr Janik. Novel a18t and pa29s substitutions in α-synuclein may be associated with sporadic parkinson's disease. *Parkinsonism related disorders*, 19(11):1057–1060, 2013.

[220] Silke Appel-Cresswell, Carles Vilarino-Guell, Mary Encarnacion, Holly Sherman, Irene Yu, Brinda Shah, David Weir, Christina Thompson, Chelsea Szu-Tu, and Joanne Trinh. Alpha-synuclein p. h50q, a novel pathogenic mutation for parkinson's disease. *Movement disorders*, 28(6):811–813, 2013.

[221] AB Singleton, M Farrer, J Johnson, A Singleton, S Hague, J Kachergus, M Hulihan, T Peuralinna, A Dutra, and R Nussbaum. α-synuclein locus triplication causes parkinson's disease. *science*, 302(5646):841–841, 2003.

[222] Igor F Tsigelny, Leslie Crews, Paula Desplats, Gideon M Shaked, Yuriy Sharikov, Hideya Mizuno, Brian Spencer, Edward Rockenstein, Margarita Trejo, and Oleksandr Platoshyn. Mechanisms of hybrid oligomer formation in the pathogenesis of combined alzheimer's and parkinson's diseases. *PloS one*, 3(9):e3135, 2008.

[223] Philipp J Kahle, Manuela Neumann, Laurence Ozmen, Veronika Müller, Sabine Odoy, Noriko Okamoto, Helmut Jacobsen, Takeshi Iwatsubo, John Q Trojanowski, and Hitoshi Takahashi. Selective insolubility of α-synuclein in human lewy body diseases is recapitulated in a transgenic mouse model. *The American journal of pathology*, 159(6):2215–2225, 2001.

[224] Vladimir L Buchman, Hamish JA Hunter, Luzia GP Pinõn, Jane Thompson, Eugenia M Privalova, Natalia N Ninkina, and Alun M Davies. Persyn, a member of the synuclein family, has a distinct pattern of expression in the developing nervous system. *Journal of Neuroscience*, 18(22):9335–9341, 1998.

[225] Maria Grazia Spillantini, M Goedert, and A Divane. Assignment of human alpha-synuclein (snca) and beta-synuclein (sncb) genes to chromosomes 4q21 and 5q35. *Genomics*, 27(2), 1995.

[226] Christian Lavedan, Elisabeth Leroy, Anindya Dehejia, Stephanie Buchholtz, Amalia Dutra, Robert L Nussbaum, and Mihael H Polymeropoulos. Identification, localization and characterization of the human γ-synuclein gene. *Human genetics*, 103:106–112, 1998.

[227] David F Clayton and Julia M George. Synucleins in synaptic plasticity and neurodegenerative disorders. *Journal of neuroscience research*, 58(1):120–129, 1999.

[228] Luc Maroteaux, James T Campanelli, and Richard H Scheller. Synuclein: a neuron-specific protein localized to the nucleus and presynaptic nerve terminal. *Journal of Neuroscience*, 8(8):2804–2815, 1988.

[229] Amberley D Stephens, Maria Zacharopoulou, and Gabriele S Kaminski Schierle. The cellular environment affects monomeric α-synuclein structure. *Trends in biochemical sciences*, 44(5):453–466, 2019.

[230] Hirotomo Miake, Hidehiro Mizusawa, Takeshi Iwatsubo, and Masato Hasegawa. Biochemical characterization of the core structure of α-synuclein filaments. *Journal of Biological Chemistry*, 277(21):19213–19219, 2002.

[231] Francois-Xavier Theillet, Andres Binolfi, Beata Bekei, Andrea Martorana, Honor May Rose, Marchel Stuiver, Silvia Verzini, Dorothea Lorenz, Marleen Van Rossum, and Daniella Goldfarb. Structural disorder of monomeric α-synuclein persists in mammalian cells. *Nature*, 530(7588):45–50, 2016.

[232] Annika Öhrfelt, Henrik Zetterberg, Kerstin Andersson, Rita Persson, Dzemila Secic, Gunnar Brinkmalm, Anders Wallin, Ezra Mulugeta, Paul T Francis, and Eugeen Vanmechelen. Identification of novel α-synuclein isoforms in human brain tissue by using an online nanolc-esi-fticr-ms method. *Neurochemical research*, 36:2029–2042, 2011.

[233] Sreeganga Chandra, Xiaocheng Chen, Josep Rizo, Reinhard Jahn, and Thomas C Sudhof. A broken β-helix in folded α-synuclein. *Journal of Biological Chemistry*, 278(17):15313–15318, 2003.

[234] Benoit I Giasson, Ian VJ Murray, John Q Trojanowski, and Virginia M-Y Lee. A hydrophobic stretch of 12 amino acid residues in the middle of α-synuclein is essential for filament assembly. *Journal of Biological Chemistry*, 276(4):2380–2386, 2001.

[235] Andrés Binolfi, Rodolfo M Rasia, Carlos W Bertoncini, Marcelo Ceolin, Markus Zweckstetter, Christian Griesinger, Thomas M Jovin, and Claudio O Fernández. Interaction of α-synuclein with divalent metal ions reveals key differences: A link between structure, binding specificity and fibrillation enhancement. *Journal of the American Chemical Society*, 128(30):9893–9901, 2006.

[236] Masami Masuda, Nobuyuki Suzuki, Sayuri Taniguchi, Takayuki Oikawa, Takashi Nonaka, Takeshi Iwatsubo, Shin-ichi Hisanaga, Michel Goedert, and Masato Hasegawa. Small molecule inhibitors of α-synuclein filament assembly. *Biochemistry*, 45(19):6085–6094, 2006.

[237] Wei Wang, Iva Perovic, Johnathan Chittuluru, Alice Kaganovich, Linh TT Nguyen, Jingling Liao, Jared R Auclair, Derrick Johnson, Anuradha Landeru, and Alana K Simorellis. A soluble α-synuclein construct forms a dynamic tetramer. *Proceedings of the National Academy of Sciences*, 108(43):17797–17802, 2011.

[238] Tim Bartels, Joanna G Choi, and Dennis J Selkoe. alpha-synuclein occurs physiologically as a helically folded tetramer that resists aggregation. *Nature*, 477(7362):107–10, 2011.

[239] Jacqueline Burré, Sandro Vivona, Jiajie Diao, Manu Sharma, Axel T Brunger, and Thomas C Südhof. Properties of native brain α-synuclein. *Nature*, 498(7453):E4–E6, 2013.

[240] Michael M Wördehoff, Hamed Shaykhalishahi, Luca Groß, Lothar Gremer, Matthias Stoldt, Alexander K Buell, Dieter Willbold, and Wolfgang Hoyer. Opposed effects of dityrosine formation in soluble and aggregated α-synuclein on fibril growth. *Journal of molecular biology*, 429(20):3018–3030, 2017.

[241] José M Souza, Benoit I Giasson, Qiping Chen, Virginia M-Y Lee, and Harry Ischiropoulos. Dityrosine cross-linking promotes formation of stable α-synuclein polymers: implication of nitrative and oxidative stress in the pathogenesis of neurodegenerative synucleinopathies. *Journal of Biological Chemistry*, 275(24):18344–18349, 2000.

[242] Bruno Fauvet, Martial K Mbefo, Mohamed-Bilal Fares, Carole Desobry, Sarah Michael, Mustafa T Ardah, Elpida Tsika, Philippe Coune, Michel Prudent, and Niels Lion. α-synuclein in central nervous system and from erythrocytes, mammalian cells, and escherichia coli exists predominantly as disordered monomer. *Journal of Biological Chemistry*, 287(19):15345–15364, 2012.

[243] Hilal A Lashuel, Cassia R Overk, Abid Oueslati, and Eliezer Masliah. The many faces of α-synuclein: from structure and toxicity to therapeutic target. *Nature Reviews Neuroscience*, 14(1):38–48, 2013.

[244] Céline Galvagnion, Alexander K Buell, Georg Meisl, Thomas CT Michaels, Michele Vendruscolo, Tuomas PJ Knowles, and Christopher M Dobson. Lipid vesicles trigger α-synuclein aggregation by stimulating primary nucleation. *Nature chemical biology*, 11(3):229–234, 2015.

[245] Elizabeth R Middleton and Elizabeth Rhoades. Effects of curvature and composition on α-synuclein binding to lipid vesicles. *Biophysical journal*, 99(7):2279–2288, 2010.

[246] Jacqueline Burré, Manu Sharma, Theodoros Tsetsenis, Vladimir Buchman, Mark R Etherton, and Thomas C Südhof. α-synuclein promotes snare-complex assembly in vivo and in vitro. *Science*, 329(5999):1663–1667, 2010.

[247] Virginia Gao, Juan A Briano, Lauren E Komer, and Jacqueline Burré. Functional and pathological effects of α-synuclein on synaptic snare complexes. *Journal of molecular biology*, 435(1):167714, 2023.

[248] David Snead and David Eliezer. Alpha-synuclein function and dysfunction on cellular membranes. *Experimental neurobiology*, 23(4):292, 2014.

[249] Deborah E Cabin, Kazuhiro Shimazu, Diane Murphy, Nelson B Cole, Wolfram Gottschalk, Kellie L McIlwain, Bonnie Orrison, Amy Chen, Christopher E Ellis, and Richard Paylor. Synaptic vesicle depletion correlates with attenuated synaptic responses to prolonged repetitive stimulation in mice lacking α-synuclein. *Journal of Neuroscience*, 22(20):8797–8807, 2002.

[250] Asa Abeliovich, Yvonne Schmitz, Isabel Farinas, Derek Choi-Lundberg, Wei-Hsien Ho, Pablo E Castillo, Natasha Shinsky, Jose Manuel Garcia Verdugo, Mark Armanini, and Anne Ryan. Mice lacking α-synuclein display functional deficits in the nigrostriatal dopamine system. *Neuron*, 25(1):239–252, 2000.

[251] Diane D Murphy, Susan M Rueter, John Q Trojanowski, and Virginia M-Y Lee. Synucleins are developmentally expressed, and α-synuclein regulates the size of the presynaptic vesicular pool in primary hippocampal neurons. *Journal of Neuroscience*, 20(9):3214–3220, 2000.

[252] Sreeganga Chandra, Francesco Fornai, Hyung-Bae Kwon, Umar Yazdani, Deniz Atasoy, Xinran Liu, Robert E Hammer, Giuseppe Battaglia, Dwight C German, and Pablo E Castillo. Double-knockout mice for β-and α-synucleins: effect on synaptic functions. *Proceedings of the National Academy of Sciences*, 101(41):14966–14971, 2004.

[253] Julia M George, Hui Jin, Wendy S Woods, and David F Clayton. Characterization of a novel protein regulated during the critical period for song learning in the zebra finch. *Neuron*, 15(2):361–372, 1995.

[254] Nikolai G Kholodilov, Michael Neystat, F Oo Tinmarla, E Lo Steven, Kristin E Larsen, David Sulzer, and Robert E Burke. Increased expression of rat synuclein in the substantia nigra pars compacta identified by mrna differential display in a model of developmental target injury. *Journal of neurochemistry*, 73(6):2586–2599, 1999.

[255] Ginger S Withers, Julia M George, Gary A Banker, and David F Clayton. Delayed localization of synelfin (synuclein, nacp) to presynaptic terminals in cultured rat hippocampal neurons. *Developmental brain research*, 99(1):87–94, 1997.

[256] Ruth G Perez, Jack C Waymire, Eva Lin, Jen J Liu, Fengli Guo, and Michael J Zigmond. A role for α-synuclein in the regulation of dopamine biosynthesis. *Journal of Neuroscience*, 22(8):3090–3099, 2002.

[257] Min Zhu, Sudha Rajamani, Joanna Kaylor, Shubo Han, Feimeng Zhou, and Anthony L Fink. The flavonoid baicalein inhibits fibrillation of α-synuclein and disaggregates existing fibrils. *Journal of Biological Chemistry*, 279(26):26846–26857, 2004.

[258] Lise Giehm and Daniel E Otzen. Strategies to increase the reproducibility of protein fibrillization in plate reader assays. *Analytical biochemistry*, 400(2):270–281, 2010.

[259] Jeremy Pronchik, Xianglan He, Jason T Giurleo, and David S Talaga. In vitro formation of amyloid from α-synuclein is dominated by reactions at hydrophobic interfaces. *Journal of the American Chemical Society*, 132(28):9797–9803, 2010.

[260] Thibault Viennet, Michael M Wördehoff, Boran Uluca, Chetan Poojari, Hamed Shaykhalishahi, Dieter Willbold, Birgit Strodel, Henrike Heise, Alexander K Buell, and Wolfgang Hoyer. Structural insights from lipid-bilayer nanodiscs link α-synuclein membrane-binding modes to amyloid fibril formation. *Communications biology*, 1(1):44, 2018.

[261] Marcel Falke, Julian Victor, Michael M Wördehoff, Alessia Peduzzo, Tao Zhang, Gunnar F Schröder, Alexander K Buell, Wolfgang Hoyer, and Manuel Etzkorn. α-synuclein-derived lipoparticles in the study of α-synuclein amyloid fibril formation. *Chemistry and physics of lipids*, 220:57–65, 2019.

[262] Vladimir N Uversky, Jie Li, and Anthony L Fink. Evidence for a partially folded intermediate in α-synuclein fibril formation. *Journal of Biological Chemistry*, 276(14):10737–10744, 2001.

[263] Wolfgang Hoyer, Thomas Antony, Dmitry Cherny, Gudrun Heim, Thomas M Jovin, and Vinod Subramaniam. Dependence of α-synuclein aggregate morphology on solution conditions. *Journal of molecular biology*, 322(2):383–393, 2002.

[264] Alexander J Dear, Xiangyu Teng, Sarah R Ball, Joshua Lewin, Robert I Horne, Daniel Clow, Natasha Harper, Kim Yahya, Thomas CT Michaels, and Sara Linse. Molecular mechanism of α-synuclein aggregation on lipid membranes revealed. *bioRxiv*, 2023.

[265] Benedikt Frieg, Leif Antonschmidt, Christian Dienemann, James A. Geraets, Eszter E. Najbauer, Dirk Matthes, Bert L. de Groot, Loren B. Andreas, Stefan Becker, Christian Griesinger, and Gunnar F. Schröder. The 3d structure of lipidic fibrils of α-synuclein. *Nature Communications*, 13(1):6810, 2022.

[266] Pratibha Kumari, Dhiman Ghosh, Agathe Vanas, Yanick Fleischmann, Thomas Wiegand, Gunnar Jeschke, Roland Riek, and Cédric Eichmann. Structural insights into α-synuclein monomer–fibril interactions. *Proceedings of the National Academy of Sciences*, 118(10):e2012171118, 2021.

[267] Ian VJ Murray, Benoit I Giasson, Shawn M Quinn, Vishwanath Koppaka, Paul H Axelsen, Harry Ischiropoulos, John Q Trojanowski, and Virginia M-Y Lee. Role of α-synuclein carboxy-terminus on fibril formation in vitro. *Biochemistry*, 42(28):8530–8540, 2003.

[268] Wolfgang Hoyer, Dmitry Cherny, Vinod Subramaniam, and Thomas M Jovin. Impact of the acidic c-terminal region comprising amino acids 109 140 on α-synuclein aggregation in vitro. *Biochemistry*, 43(51):16233–16242, 2004.

[269] Ciaran PA Doherty, Sabine M Ulamec, Roberto Maya-Martinez, Sarah C Good, Jemma Makepeace, G Nasir Khan, Patricija van Oosten-Hawle, Sheena E Radford, and David J Brockwell. A short motif in the n-terminal region of α-synuclein is critical for both aggregation and function. *Nature structural molecular biology*, 27(3):249–259, 2020.

[270] Zhaohui Liang, Ho Yin Edwin Chan, Marianne M Lee, and Michael K Chan. A sumo1-derived peptide targeting sumo-interacting motif inhibits α-synuclein aggregation. *Cell Chemical Biology*, 28(2):180–190. e6, 2021.

[271] Jemil Ahmed, Tessa C Fitch, Courtney M Donnelly, Johnson A Joseph, Tyler D Ball, Mikaela M Bassil, Ahyun Son, Chen Zhang, Aurélie Ledreux, and Scott Horowitz. Foldamers reveal and validate therapeutic targets associated with toxic α-synuclein self-assembly. *Nature Communications*, 13(1):2273, 2022.

[272] Björn M Burmann, Juan A Gerez, Irena Matečko-Burmann, Silvia Campioni, Pratibha Kumari, Dhiman Ghosh, Adam Mazur, Emelie E Aspholm, Darius Šulskis, and Magdalena Wawrzyniuk. Regulation of α-synuclein by chaperones in mammalian cells. *Nature*, 577(7788):127–132, 2020.

[273] Mihael H Polymeropoulos, Christian Lavedan, Elisabeth Leroy, Susan E Ide, Anindya Dehejia, Amalia Dutra, Brian Pike, Holly Root, Jeffrey Rubenstein, and Rebecca Boyer. Mutation in the α-synuclein gene identified in families with parkinson's disease. *Science*, 276(5321):2045–2047, 1997.

[274] Gemma Comellas, Luisel R Lemkau, Andrew J Nieuwkoop, Kathryn D Kloepper, Daniel T Ladror, Reika Ebisu, Wendy S Woods, Andrew S Lipton, Julia M George, and Chad M Rienstra. Structured regions of α-synuclein fibrils include the early-onset parkinson's disease mutation sites. *Journal of molecular biology*, 411(4):881–895, 2011.

[275] Henrike Heise, Wolfgang Hoyer, Stefan Becker, Ovidiu C Andronesi, Dietmar Riedel, and Marc Baldus. Molecular-level secondary structure, polymorphism, and dynamics of full-length α-synuclein fibrils studied by solid-state nmr. *Proceedings of the National Academy of Sciences*, 102(44):15871–15876, 2005.

[276] Yaowang Li, Chunyu Zhao, Feng Luo, Zhenying Liu, Xinrui Gui, Zhipu Luo, Xiang Zhang, Dan Li, Cong Liu, and Xueming Li. Amyloid fibril structure of α-synuclein determined by cryo-electron microscopy. *Cell research*, 28(9):897–903, 2018.

[277] Guohua Lv, Ashutosh Kumar, Karin Giller, Maria L Orcellet, Dietmar Riedel, Claudio O Fernández, Stefan Becker, and Adam Lange. Structural comparison of mouse and human α-synuclein amyloid fibrils by solid-state nmr. *Journal of molecular biology*, 420(1-2):99–111, 2012.

[278] Ricardo Guerrero-Ferreira, Nicholas MI Taylor, Ana-Andreea Arteni, Pratibha Kumari, Daniel Mona, Philippe Ringler, Markus Britschgi, Matthias E Lauer, Ali Makky, and Joeri Verasdonck. Two new polymorphic structures of human full-length alpha-synuclein fibrils solved by cryo-electron microscopy. *Elife*, 8:e48907, 2019.

[279] Xue Yang, Baifan Wang, Cody L Hoop, Jonathan K Williams, and Jean Baum. Nmr unveils an n-terminal interaction interface on acetylated-α-synuclein monomers for recruitment to fibrils. *Proceedings of the National Academy of Sciences*, 118(18):e2017452118, 2021.

[280] Heiko Braak, Daniele Sandmann-Keil, WeiPing Gai, and Eva Braak. Extensive axonal lewy neurites in parkinson's disease: a novel pathological feature revealed by α-synuclein immunocytochemistry. *Neuroscience letters*, 265(1):67–69, 1999.

[281] Michel Brahic, Luc Bousset, Gregor Bieri, Ronald Melki, and Aaron D Gitler. Axonal transport and secretion of fibrillar forms of α-synuclein, aβ42 peptide and httexon 1. *Acta neuropathologica*, 131:539–548, 2016.

[282] Karin M Danzer, Wolfgang P Ruf, Preeti Putcha, Daniel Joyner, Tadafumi Hashimoto, Charles Glabe, Bradley T Hyman, and Pamela J McLean. Heat-shock protein 70 modulates toxic extracellular α-synuclein oligomers and rescues trans-synaptic toxicity. *The FASEB journal*, 25(1):326, 2011.

[283] Eric C Freundt, Nate Maynard, Eileen K Clancy, Shyamali Roy, Luc Bousset, Yannick Sourigues, Markus Covert, Ronald Melki, Karla Kirkegaard, and Michel Brahic. Neuron-to-neuron transmission of β-synuclein fibrils through axonal transport. *Annals of neurology*, 72(4):517–524, 2012.

[284] Amanda N Sacino, Mieu Brooks, Michael A Thomas, Alex B McKinney, Sooyeon Lee, Robert W Regenhardt, Nicholas H McGarvey, Jacob I Ayers, Lucia Notterpek, and David R

Borchelt. Intramuscular injection of α-synuclein induces cns α-synuclein pathology and a rapid-onset motor phenotype in transgenic mice. *Proceedings of the National Academy of Sciences*, 111(29):10732–10737, 2014.

[285] Heiko Braak and Kelly Del Tredici. *Neuroanatomy and pathology of sporadic Parkinson's disease*. Springer, 2008.

[286] He-Jin Lee, Ji-Eun Suk, Eun-Jin Bae, Jung-Ho Lee, Seung R Paik, and Seung-Jae Lee. Assembly-dependent endocytosis and clearance of extracellular a-synuclein. *The international journal of biochemistry cell biology*, 40(9):1835–1849, 2008.

[287] Brandon B Holmes, Sarah L DeVos, Najla Kfoury, Mei Li, Rachel Jacks, Kiran Yanamandra, Mohand O Ouidja, Frances M Brodsky, Jayne Marasa, and Devika P Bagchi. Heparan sulfate proteoglycans mediate internalization and propagation of specific proteopathic seeds. *Proceedings of the National Academy of Sciences*, 110(33):E3138–E3147, 2013.

[288] Oshrat Schonberger, Lior Horonchik, Ruth Gabizon, Dulce Papy-Garcia, Denis Barritault, and Albert Taraboulos. Novel heparan mimetics potently inhibit the scrapie prion protein and its endocytosis. *Biochemical and biophysical research communications*, 312(2):473–479, 2003.

[289] Xiaobo Mao, Michael Tianhao Ou, Senthilkumar S Karuppagounder, Tae-In Kam, Xiling Yin, Yulan Xiong, Preston Ge, George Essien Umanah, Saurav Brahmachari, and Joo-Ho Shin. Pathological α-synuclein transmission initiated by binding lymphocyte-activation gene 3. *Science*, 353(6307):aah3374, 2016.

[290] Amulya Nidhi Shrivastava, Virginie Redeker, Nicolas Fritz, Laura Pieri, Leandro G Almeida, Maria Spolidoro, Thomas Liebmann, Luc Bousset, Marianne Renner, and Clément Léna. β-synuclein assemblies sequester neuronal β3-na+/k+-atp ase and impair na+ gradient. *The EMBO journal*, 34(19):2408–2423, 2015.

[291] Nadine S Rösener, Lothar Gremer, Michael M Wördehoff, Tatsiana Kupreichyk, Manuel Etzkorn, Philipp Neudecker, and Wolfgang Hoyer. Clustering of human prion protein and α-synuclein oligomers requires the prion protein n-terminus. *Communications biology*, 3(1):365, 2020.

[292] Keyoumu Nazere, Tetsuya Takahashi, Naoyuki Hara, Kazuki Muguruma, Masahiro Nakamori, Yu Yamazaki, Hiroyuki Morino, and Hirofumi Maruyama. Amyloid beta is internalized via macropinocytosis, an hspg-and lipid raft-dependent and rac1-mediated process. *Frontiers in Molecular Neuroscience*, 15:804702, 2022.

[293] Karine Gousset, Edwin Schiff, Christelle Langevin, Zrinka Marijanovic, Anna Caputo, Duncan T Browman, Nicolas Chenouard, Fabrice De Chaumont, Angelo Martino, and Jost Enninga. Prions hijack tunnelling nanotubes for intercellular spread. *Nature cell biology*, 11(3):328–336, 2009.

[294] Ronald B Postuma, Daniela Berg, Matthew Stern, Werner Poewe, C Warren Olanow, Wolfgang Oertel, José Obeso, Kenneth Marek, Irene Litvan, and Anthony E Lang. Mds clinical diagnostic criteria for parkinson's disease. *Movement disorders*, 30(12):1591–1601, 2015.

[295] Thomas G Beach and Charles H Adler. Importance of low diagnostic accuracy for early parkinson's disease. *Movement Disorders*, 33(10):1551–1554, 2018.

[296] Alberto J Espay, Michael A Schwarzschild, Caroline M Tanner, Hubert H Fernandez, David K Simon, James B Leverenz, Aristide Merola, Alice Chen-Plotkin, Patrik Brundin, and Marcelo A Kauffman. Biomarker-driven phenotyping in parkinson's disease: a translational missing link in disease-modifying clinical trials. *Movement Disorders*, 32(3):319–324, 2017.

[297] Zhen Hong, Min Shi, Kathryn A Chung, Joseph F Quinn, Elaine R Peskind, Douglas Galasko, Joseph Jankovic, Cyrus P Zabetian, James B Leverenz, and Geoffrey Baird. Dj-1 and α-synuclein in human cerebrospinal fluid as biomarkers of parkinson's disease. *Brain*, 133(3):713–726, 2010.

[298] Brit Mollenhauer, Joseph J Locascio, Walter Schulz-Schaeffer, Friederike Sixel-Döring, Claudia Trenkwalder, and Michael G Schlossmacher. α-synuclein and tau concentrations in cerebrospinal fluid of patients presenting with parkinsonism: a cohort study. *The Lancet Neurology*, 10(3):230–240, 2011.

[299] Brit Mollenhauer, Ellen Trautmann, Peggy Taylor, Paul Manninger, Friederike Sixel-Döring, Jens Ebentheuer, Claudia Trenkwalder, and Michael G Schlossmacher. Total csf α-synuclein is lower in de novo parkinson patients than in healthy subjects. *Neuroscience letters*, 532:44–48, 2013.

[300] Penelope G Foulds, Osamu Yokota, A Thurston, Yvonne S Davidson, Zeshan Ahmed, Janice L Holton, Jennifer C Thompson, Haruhiko Akiyama, Tetsuaki Arai, Masato Hasegawa, Alexander Gerhard, David Allsop, and David M A Mann. Post mortem cerebrospinal fluid α-synuclein levels are raised in multiple system atrophy and distinguish this from the other α-synucleinopathies, parkinson's disease and dementia with lewy bodies. *Neurobiology of disease*, 45(1):188–195, 2012.

[301] Cristina Cariulo, Paola Martufi, Margherita Verani, Lucia Azzollini, Giordana Bruni, Andreas Weiss, Sean M Deguire, Hilal A Lashuel, Eugenia Scaricamazza, and Giulia Maria Sancesario. Phospho-s129 alpha-synuclein is present in human plasma but not in cerebrospinal fluid as determined by an ultrasensitive immunoassay. *Frontiers in neuroscience*, 13:889, 2019.

[302] Tessandra Stewart, Vesna Sossi, Jan O Aasly, Zbigniew K Wszolek, Ryan J Uitti, Kazuko Hasegawa, Teruo Yokoyama, Cyrus P Zabetian, James B Leverenz, and Alexander Jon Stoessl. Phosphorylated α-synuclein in parkinson's disease: correlation depends on disease severity. *Acta neuropathologica communications*, 3(1):1–11, 2015.

[303] Nour K Majbour, Nishant N Vaikath, Paolo Eusebi, Davide Chiasserini, Mustafa Ardah, Shiji Varghese, M Emdadul Haque, Takahiko Tokuda, Peggy Auinger, and Paolo Calabresi. Longitudinal changes in csf alpha-synuclein species reflect parkinson's disease progression. *Movement Disorders*, 31(10):1535–1542, 2016.

[304] Nour K Majbour, Nishant N Vaikath, Karin D Van Dijk, Mustafa T Ardah, Shiji Varghese, Louise B Vesterager, Liliana P Montezinho, Stephen Poole, Bared Safieh-Garabedian, and Takahiko Tokuda. Oligomeric and phosphorylated alpha-synuclein as potential csf biomarkers for parkinson's disease. *Molecular neurodegeneration*, 11:1–15, 2016.

[305] Xuemei Wang, Shun Yu, Fangfei Li, and Tao Feng. Detection of α-synuclein oligomers in red blood cells as a potential biomarker of parkinson's disease. *Neuroscience letters*, 599:115–119, 2015.

[306] Kiran Yanamandra, Marina A Gruden, Vida Casaite, Rolandas Meskys, Lars Forsgren, and Ludmilla A Morozova-Roche. α-synuclein reactive antibodies as diagnostic biomarkers in blood sera of parkinson's disease patients. *PloS one*, 6(4):e18513, 2011.

[307] Paolo Eusebi, David Giannandrea, Leonardo Biscetti, Iosief Abraha, Davide Chiasserini, Massimiliano Orso, Paolo Calabresi, and Lucilla Parnetti. Diagnostic utility of cerebrospinal fluid β-synuclein in parkinson's disease: a systematic review and meta-analysis. *Movement disorders*, 32(10):1389–1400, 2017.

[308] Un Jung Kang, Amelia K Boehme, Graham Fairfoul, Mohammad Shahnawaz, Thong Chi Ma, Samantha J Hutten, Alison Green, and Claudio Soto. Comparative study of cerebrospinal fluid

β-synuclein seeding aggregation assays for diagnosis of parkinson's disease. *Movement Disorders*, 34(4):536–544, 2019.

[309] Graham Fairfoul, Lynne I McGuire, Suvankar Pal, James W Ironside, Juliane Neumann, Sharon Christie, Catherine Joachim, Margaret Esiri, Samuel G Evetts, and Michal Rolinski. Alpha-synuclein rt-qu ic in the csf of patients with alpha-synucleinopathies. *Annals of clinical and translational neurology*, 3(10):812–818, 2016.

[310] Marco J Russo, Christina D Orru, Luis Concha-Marambio, Simone Giaisi, Bradley R Groveman, Carly M Farris, Bret Holguin, Andrew G Hughson, David-Erick LaFontant, and Chelsea Caspell-Garcia. High diagnostic performance of independent alpha-synuclein seed amplification assays for detection of early parkinson's disease. *Acta neuropathologica communications*, 9:1–13, 2021.

[311] Mohammad Shahnawaz, Abhisek Mukherjee, Sandra Pritzkow, Nicolas Mendez, Prakruti Rabadia, Xiangan Liu, Bo Hu, Ann Schmeichel, Wolfgang Singer, and Gang Wu. Discriminating α-synuclein strains in parkinson's disease and multiple system atrophy. *Nature*, 578(7794):273–277, 2020.

[312] Alexis Fenyi, Laurène Leclair-Visonneau, Thomas Clairembault, Emmanuel Coron, Michel Neunlist, Ronald Melki, Pascal Derkinderen, and Luc Bousset. Detection of alpha-synuclein aggregates in gastrointestinal biopsies by protein misfolding cyclic amplification. *Neurobiology of disease*, 129:38–43, 2019.

[313] Sireesha Manne, Naveen Kondru, Huajun Jin, Geidy E Serrano, Vellareddy Anantharam, Arthi Kanthasamy, Charles H Adler, Thomas G Beach, and Anumantha G Kanthasamy. Blinded rt-quic analysis of β-synuclein biomarker in skin tissue from parkinson's disease patients. *Movement Disorders*, 35(12):2230–2239, 2020.

[314] Shunsuke Koga, Hiroaki Sekiya, Naveen Kondru, Owen A Ross, and Dennis W Dickson. Neuropathology and molecular diagnosis of synucleinopathies. *Molecular neurodegeneration*, 16(1):83, 2021.

[315] Ilaria Poggiolini, Vandana Gupta, Michael Lawton, Seoyun Lee, Aadil El-Turabi, Agustin Querejeta-Coma, Claudia Trenkwalder, Friederike Sixel-Döring, Alexandra Foubert-Samier, and Anne Pavy-Le Traon. Diagnostic value of cerebrospinal fluid alpha-synuclein seed quantification in synucleinopathies. *Brain*, 145(2):584–595, 2022.

[316] Félix Javier Jiménez-Jiménez, Hortensia Alonso-Navarro, Elena García-Martín, Diego Santos-García, Iván Martínez-Valbuena, and José AG Agúndez. Alpha-synuclein in peripheral tissues as a possible marker for neurological diseases and other medical conditions. *Biomolecules*, 13(8):1263, 2023.

[317] Anja Schaffrath, Sophia Schleyken, Aline Seger, Hannah Jergas, Pelin özdüzenciler, Marlene Pils, Lara Blömeke, Anneliese Cousin, Johannes Willbold, and Tuyen Bujnicki. Patients with isolated rem-sleep behavior disorder have elevated levels of alpha-synuclein aggregates in stool. *npj Parkinson's Disease*, 9(1):14, 2023.

[318] Brit Mollenhauer, Johannes Zimmermann, Friederike Sixel-Döring, Niels K Focke, Tamara Wicke, Jens Ebentheuer, Martina Schaumburg, Elisabeth Lang, Ellen Trautmann, and Henrik Zetterberg. Monitoring of 30 marker candidates in early parkinson disease as progression markers. *Neurology*, 87(2):168–177, 2016.

[319] Alba Cervantes González and Olivia Belbin. Fluid markers of synapse degeneration in synucleinopathies. *Journal of Neural Transmission*, 129(2):187–206, 2022.

[320] Isabel Schulz, Niels Kruse, Roland G Gera, Thomas Kremer, Jesse Cedarbaum, Robin Barbour, Wagner Zago, Sebastian Schade, Birgit Otte, and Michael Bartl. Systematic assessment

of 10 biomarker candidates focusing on β-synuclein-related disorders. *Movement disorders*, 36(12):2874–2887, 2021.

[321] Kimberly L Sciarretta, David J Gordon, and Stephen C Meredith. Peptide-based inhibitors of amyloid assembly. *Methods Enzymol*, 413:273–312, 2006.

[322] Stuart A Sievers, John Karanicolas, Howard W Chang, Anni Zhao, Lin Jiang, Onofrio Zirafi, Jason T Stevens, Jan Munch, David Baker, and David Eisenberg. Structure-based design of non-natural amino-acid inhibitors of amyloid fibril formation. *Nature*, 475(7354):96–100, 2011.

[323] Fred E Cohen and Jeffery W Kelly. Therapeutic approaches to protein-misfolding diseases. *Nature*, 426(6968):905–909, 2003.

[324] Hong Zhang, Li-Qiong Xu, and Sarah Perrett. Studying the effects of chaperones on amyloid fibril formation. *Methods*, 53(3):285–94, 2011.

[325] Refik Pul, Richard Dodel, and Martin Stangel. Antibody-based therapy in alzheimer's disease. *Expert Opin Biol Ther*, 11(3):343–57, 2011.

[326] Yair Porat, Adel Abramowitz, and Ehud Gazit. Inhibition of amyloid fibril formation by polyphenols: structural similarity and aromatic interactions as a common inhibition mechanism. *Chem Biol Drug Des*, 67(1):27–37, 2006.

[327] Dagmar E Ehrnhoefer, Jan Bieschke, Annett Boeddrich, Martin Herbst, Laura Masino, Rudi Lurz, Sabine Engemann, Annalisa Pastore, and Erich E Wanker. Egcg redirects amyloidogenic polypeptides into unstructured, off-pathway oligomers. *Nat Struct Mol Biol*, 15(6):558–66, 2008.

[328] Axel Abelein, Lisa Lang, Christofer Lendel, Astrid Graslund, and Jens Danielsson. Transient small molecule interactions kinetically modulate amyloid beta peptide self-assembly. *FEBS Lett*, 586(22):3991–5, 2012.

[329] Sascha Weggen, Mark Rogers, and Jason Eriksen. Nsaids: small molecules for prevention of alzheimer's disease or precursors for future drug development? *Trends Pharmacol Sci*, 28(10):536–43, 2007.

[330] Anuj K Sharma, Stephanie T Pavlova, Jaekwang Kim, Darren Finkelstein, Nicholas J Hawco, Nigam P Rath, Jungsu Kim, and Liviu M Mirica. Bifunctional compounds for controlling metal-mediated aggregation of the abeta42 peptide. *J Am Chem Soc*, 134(15):6625–36, 2012.

[331] Gianluigi Forloni, Laura Colombo, Laura Girola, Fabrizio Tagliavini, and Mario Salmona. Anti-amyloidogenic activity of tetracyclines: studies in vitro. *FEBS Lett*, 487(3):404–7, 2001.

[332] Seong Il Yoo, Ming Yang, Jeffrey R Brender, Vivekanandan Subramanian, Kai Sun, Nam Eok Joo, Soo-Hwan Jeong, Ayyalusamy Ramamoorthy, and Nicholas A Kotov. Inhibition of amyloid peptide fibrillation by inorganic nanoparticles: functional similarities with proteins. *Angew Chem Int Ed Engl*, 50(22):5110–5, 2011.

[333] Celia Cabaleiro-Lago, Fiona Quinlan-Pluck, Iseult Lynch, Stina Lindman, Aedin M Minogue, Eva Thulin, Dominic M Walsh, Kenneth A Dawson, and Sara Linse. Inhibition of amyloid beta protein fibrillation by polymeric nanoparticles. *J Am Chem Soc*, 130(46):15437–43, 2008.

[334] Maksym Galkin, Anastasiia Priss, Yevhenii Kyriukha, and Volodymyr Shvadchak. Navigating alpha-synuclein aggregation inhibition: Methods, mechanisms, and molecular targets. *Chem Rec*, 24(2):e202300282, 2023.

[335] Paolo Arosio, Michele Vendruscolo, Christopher M Dobson, and Tuomas PJ Knowles. Chemical kinetics for drug discovery to combat protein aggregation diseases. *Trends in pharmacological sciences*, 35(3):127–135, 2014.

[336] Caroline Grönwall, Andreas Jonsson, Sara Lindström, Elin Gunneriusson, Stefan Ståhl, and Nina Herne. Selection and characterization of affibody ligands binding to alzheimer amyloid beta peptides. *J Biotechnol*, 128(1):162–83, 2007.

[337] Wolfgang Hoyer, Caroline Grönwall, Andreas Jonsson, Stefan Ståhl, and Torleif Härd. Stabilization of a beta-hairpin in monomeric alzheimer's amyloid-beta peptide inhibits amyloid formation. *Proc Natl Acad Sci U S A*, 105(13):5099–104, 2008.

[338] Valentina Oliveri. Toward the discovery and development of effective modulators of α-synuclein amyloid aggregation. *European Journal of Medicinal Chemistry*, 167:10–36, 2019.

[339] Hamed Shaykhalishahi, Ewa A Mirecka, Aziz Gauhar, Clara S R Grüning, Dieter Willbold, Torleif Härd, Matthias Stoldt, and Wolfgang Hoyer. A beta-hairpin-binding protein for three different disease-related amyloidogenic proteins. *Chembiochem*, 16(3):411–4, 2015.

[340] Benjamin G Wilhelm, Sunit Mandad, Sven Truckenbrodt, Katharina Kröhnert, Christina Schäfer, Burkhard Rammner, Seong Joo Koo, Gala A Classen, Michael Krauss, Volker Haucke, Henning Urlaub, and Silvio O Rizzoli. Composition of isolated synaptic boutons reveals the amounts of vesicle trafficking proteins. *Science*, 344(6187):1023–8, 2014.

[341] Robin Barbour, Kristin Kling, John P Anderson, Kelly Banducci, Tracy Cole, Linnea Diep, Michael Fox, Jason M Goldstein, Ferdie Soriano, and Peter Seubert. Red blood cells are the major source of alpha-synuclein in blood. *Neurodegenerative diseases*, 5(2):55–59, 2008.

[342] Greta Musteikyte, Akhila K Jayaram, Catherine K Xu, Michele Vendruscolo, Georg Krainer, and Tuomas P J Knowles. Interactions of alpha-synuclein oligomers with lipid membranes. *Biochim Biophys Acta Biomembr*, 1863(4):183536, 2021.

[343] Jinjian Hu, Yufen Zhao, and Yanmei Li. Rationally designed amyloid inhibitors based on amyloid-related structural studies. *Chinese Chemical Letters*, 34(2):107623, 2023.

[344] Yevhenii A Kyriukha, Kseniia Afitska, Andrii S Kurochka, Shubhra Sachan, Maksym Galkin, Dmytro A Yushchenko, and Volodymyr V Shvadchak. α-synuclein dimers as potent inhibitors of fibrillization. *Journal of Medicinal Chemistry*, 62(22):10342–10351, 2019.

[345] Kseniia Afitska, Anastasiia Priss, Dmytro A Yushchenko, and Volodymyr V Shvadchak. Structural optimization of inhibitors of α-synuclein fibril growth: affinity to the fibril end as a crucial factor. *Journal of molecular biology*, 432(4):967–977, 2020.

[346] Sean Chia, Z Faidon Brotzakis, Robert I Horne, Andrea Possenti, Benedetta Mannini, Rodrigo Cataldi, Magdalena Nowinska, Roxine Staats, Sara Linse, and Tuomas PJ Knowles. Structure-based discovery of small-molecule inhibitors of the autocatalytic proliferation of α-synuclein aggregates. *Molecular Pharmaceutics*, 20(1):183–193, 2022.

[347] Huy T Lam, Michael C Graber, Katherine A Gentry, and Jan Bieschke. Stabilization of α-synuclein fibril clusters prevents fragmentation and reduces seeding activity and toxicity. *Biochemistry*, 55(4):675–685, 2016.

[348] Diana L Price, Maya A Koike, Asma Khan, Wolfgang Wrasidlo, Edward Rockenstein, Eliezer Masliah, and Douglas Bonhaus. The small molecule alpha-synuclein misfolding inhibitor, npt200-11, produces multiple benefits in an animal model of parkinson's disease. *Scientific reports*, 8(1):16165, 2018.

[349] Diana L Price, Asma Khan, Rachel Angers, Alvaro Cardenas, Maria Key Prato, Massimo Bani, Douglas W Bonhaus, Martin Citron, and Anja-Leona Biere. In vivo effects of the alpha-synuclein misfolding inhibitor minzasolmin supports clinical development in parkinson's disease. *npj Parkinson's Disease*, 9(1):114, 2023.

[350] Ewa A Mirecka, Hamed Shaykhalishahi, Aziz Gauhar, Şerife Akgül, Justin Lecher, Dieter Willbold, Matthias Stoldt, and Wolfgang Hoyer. Sequestration of a β-hairpin for control of β-synuclein aggregation. *Angewandte Chemie International Edition*, 53(16):4227–4230, 2014.

[351] Clara SR Grüning, Ewa A Mirecka, Antonia N Klein, Eckhard Mandelkow, Dieter Willbold, Stephen F Marino, Matthias Stoldt, and Wolfgang Hoyer. Alternative conformations of the tau repeat domain in complex with an engineered binding protein. *Journal of Biological Chemistry*, 289(33):23209–23218, 2014.

[352] Ewa A Mirecka, Sophie Feuerstein, Lothar Gremer, Gunnar F Schröder, Matthias Stoldt, Dieter Willbold, and Wolfgang Hoyer. β-hairpin of islet amyloid polypeptide bound to an aggregation inhibitor. *Scientific reports*, 6(1):33474, 2016.

[353] Emil Dandanell Agerschou, Patrick Flagmeier, Theodora Saridaki, Céline Galvagnion, Daniel Komnig, Laetitia Heid, Vibha Prasad, Hamed Shaykhalishahi, Dieter Willbold, and Christopher M Dobson. An engineered monomer binding-protein for α-synuclein efficiently inhibits the proliferation of amyloid fibrils. *Elife*, 8:e46112, 2019.

[354] Emil Dandanell Agerschou, Vera Borgmann, Michael M Wördehoff, and Wolfgang Hoyer. Inhibitor and substrate cooperate to inhibit amyloid fibril elongation of α-synuclein. *Chemical science*, 11(41):11331–11337, 2020.

[355] Kevin A Murray, Carolyn J Hu, Sarah L Griner, Hope Pan, Jeannette T Bowler, Romany Abskharon, Gregory M Rosenberg, Xinyi Cheng, Paul M Seidler, and David S Eisenberg. De novo designed protein inhibitors of amyloid aggregation and seeding. *Proceedings of the National Academy of Sciences*, 119(34):e2206240119, 2022.

[356] Anastasiia Priss, Kseniia Afitska, Maksym Galkin, Dmytro A Yushchenko, and Volodymyr V Shvadchak. Rationally designed protein-based inhibitor of α-synuclein fibrillization in cells. *Journal of Medicinal Chemistry*, 64(10):6827–6837, 2021.

[357] Fabrizio Chiti and Christopher M Dobson. Protein misfolding, amyloid formation, and human disease: a summary of progress over the last decade. *Annu. Rev. Biochem*, 86(1):27–68, 2017.

[358] Heidi Olzscha, Sonya M Schermann, Andreas C Woerner, Stefan Pinkert, Michael H Hecht, Gian G Tartaglia, Michele Vendruscolo, Manajit Hayer-Hartl, F Ulrich Hartl, and R Martin Vabulas. Amyloid-like aggregates sequester numerous metastable proteins with essential cellular functions. *Cell*, 144(1):67–78, 2011.

[359] R Martin Vabulas and F Ulrich Hartl. Aberrant protein interactions in amyloid disease. 10(10):1512–1513, 2011.

[360] Christopher M Dobson. Protein misfolding, evolution and disease. *Trends in biochemical sciences*, 24(9):329–332, 1999.

[361] Edward Chuang, Acacia M Hori, Christina D Hesketh, and James Shorter. Amyloid assembly and disassembly. *Journal of Cell Science*, 131(8):jcs189928, 2018.

[362] Allison B Reiss, Hirra A Arain, Mark M Stecker, Nicolle M Siegart, and Lora J Kasselman. Amyloid toxicity in alzheimer's disease. *Reviews in the Neurosciences*, 29(6):613–627, 2018.

[363] Maria Grazia Spillantini, R Anthony Crowther, Ross Jakes, Masato Hasegawa, and Michel Goedert. α-synuclein in filamentous inclusions of lewy bodies from parkinson's disease and dementia with lewy bodies. *Proceedings of the National Academy of Sciences*, 95(11):6469–6473, 1998.

[364] José D Camino, Pablo Gracia, and Nunilo Cremades. The role of water in the primary nucleation of protein amyloid aggregation. *Biophysical Chemistry*, 269:106520, 2021.

[365] Sara Linse. Mechanism of amyloid protein aggregation and the role of inhibitors. *Pure and Applied Chemistry*, 91(2):211–229, 2019.

[366] Pietro Sormanni, Francesco A Aprile, and Michele Vendruscolo. Rational design of antibodies targeting specific epitopes within intrinsically disordered proteins. *Proceedings of the National Academy of Sciences*, 112(32):9902–9907, 2015.

[367] Smriti Sangwan, Shruti Sahay, Kevin A Murray, Sophie Morgan, Elizabeth L Guenther, Lin Jiang, Christopher K Williams, Harry V Vinters, Michel Goedert, and David S Eisenberg. Inhibition of synucleinopathic seeding by rationally designed inhibitors. *Elife*, 9:e46775, 2020.

[368] Hamed Shaykhalishahi, Aziz Gauhar, Michael M Wördehoff, Clara SR Grüning, Antonia N Klein, Oliver Bannach, Matthias Stoldt, Dieter Willbold, Torleif Härd, and Wolfgang Hoyer. Contact between the β1 and β2 segments of β-synuclein that inhibits amyloid formation. *Angewandte Chemie International Edition*, 54(30):8837–8840, 2015.

[369] Thomas van Groen, Sarah Schemmert, Oleksandr Brener, Lothar Gremer, Tamar Ziehm, Markus Tusche, Luitgard Nagel-Steger, Inga Kadish, Elena Schartmann, and Anne Elfgen. The aβ oligomer eliminating d-enantiomeric peptide rd2 improves cognition without changing plaque pathology. *Scientific reports*, 7(1):16275, 2017.

[370] Manuel Schweighauser, Yang Shi, Airi Tarutani, Fuyuki Kametani, Alexey G Murzin, Bernardino Ghetti, Tomoyasu Matsubara, Taisuke Tomita, Takashi Ando, and Kazuko Hasegawa. Structures of α-synuclein filaments from multiple system atrophy. *Nature*, 585(7825):464–469, 2020.

[371] Yunpeng Sun, Shouqiao Hou, Kun Zhao, Houfang Long, Zhenying Liu, Jing Gao, Yaoyang Zhang, Xiao-Dong Su, Dan Li, and Cong Liu. Cryo-em structure of full-length α-synuclein amyloid fibril with parkinson's disease familial a53t mutation. *Cell research*, 30(4):360–362, 2020.

[372] Kun Zhao, Yaowang Li, Zhenying Liu, Houfang Long, Chunyu Zhao, Feng Luo, Yunpeng Sun, Youqi Tao, Xiao-dong Su, and Dan Li. Parkinson's disease associated mutation e46k of α-synuclein triggers the formation of a distinct fibril structure. *Nature communications*, 11(1):2643, 2020.

[373] David R Boyer, Binsen Li, Chuanqi Sun, Weijia Fan, Kang Zhou, Michael P Hughes, Michael R Sawaya, Lin Jiang, and David S Eisenberg. The α-synuclein hereditary mutation e46k unlocks a more stable, pathogenic fibril structure. *Proceedings of the National Academy of Sciences*, 117(7):3592–3602, 2020.

[374] Kun Zhao, Yeh-Jun Lim, Zhenying Liu, Houfang Long, Yunpeng Sun, Jin-Jian Hu, Chunyu Zhao, Youqi Tao, Xing Zhang, and Dan Li. Parkinson's disease-related phosphorylation at tyr39 rearranges α-synuclein amyloid fibril structure revealed by cryo-em. *Proceedings of the National Academy of Sciences*, 117(33):20305–20315, 2020.

[375] Nadine S Rösener, Lothar Gremer, Elke Reinartz, Anna König, Oleksandr Brener, Henrike Heise, Wolfgang Hoyer, Philipp Neudecker, and Dieter Willbold. A d-enantiomeric peptide interferes with heteroassociation of amyloid-β oligomers and prion protein. *Journal of Biological Chemistry*, 293(41):15748–15764, 2018.

[376] Michel Goedert and Maria Grazia Spillantini. Synucleinopathies and tauopathies. In *Basic Neurochemistry*, pages 829–843. Elsevier, 2012.

[377] Lydia M Young, Alison E Ashcroft, and Sheena E Radford. Small molecule probes of protein aggregation. *Curr Opin Chem Biol*, 39:90–99, 2017.

[378] Aziz Gauhar, Hamed Shaykhalishahi, Lothar Gremer, Ewa A Mirecka, and Wolfgang Hoyer. Impact of subunit linkages in an engineered homodimeric binding protein to α-synuclein. *Protein Engineering, Design Selection*, 27(12):473–479, 2014.

[379] Patrick Flagmeier, Georg Meisl, Michele Vendruscolo, Tuomas P J Knowles, Christopher M Dobson, Alexander K Buell, and Celine Galvagnion. Mutations associated with familial parkinson's disease alter the initiation and amplification steps of alpha-synuclein aggregation. *Proc Natl Acad Sci U S A*, 113(37):10328–33, 2016.

[380] Silvia Campioni, Guillaume Carret, Sophia Jordens, Lucrece Nicoud, Raffaele Mezzenga, and Roland Riek. The presence of an air–water interface affects formation and elongation of α-synuclein fibrils. *Journal of the American Chemical Society*, 136(7):2866–2875, 2014.

[381] Harry LeVine. Thioflavine t interaction with amyloid β-sheet structures. *Amyloid*, 2(1):1–6, 1995.

[382] Christine Xue, Tiffany Yuwen Lin, Dennis Chang, and Zhefeng Guo. Thioflavin t as an amyloid dye: fibril quantification, optimal concentration and effect on aggregation. *R Soc Open Sci*, 4(1):160696, 2017.

[383] Yong Xu, Roberto Maya-Martinez, and Sheena E Radford. Controlling amyloid formation of intrinsically disordered proteins and peptides: slowing down or speeding up? *Essays in Biochemistry*, 66(7):959–975, 2022.

[384] Emil Dandanell Agerschou, Marie P Schützmann, Nikolas Reppert, Michael M Wördehoff, Hamed Shaykhalishahi, Alexander K Buell, and Wolfgang Hoyer. beta-turn exchanges in the alpha-synuclein segment 44-tkeg-47 reveal high sequence fidelity requirements of amyloid fibril elongation. *Biophys Chem*, 269:106519, 2021.

[385] Shahin Zibaee, Graham Fraser, Ross Jakes, David Owen, Louise C Serpell, R Anthony Crowther, and Michel Goedert. Human α-synuclein rendered fibrillogenic by designed mutations. *Journal of Biological Chemistry*, 285(49):38555–38567, 2010.

[386] Santiago Esteban-Martín, Jordi Silvestre-Ryan, Carlos W Bertoncini, and Xavier Salvatella. Identification of fibril-like tertiary contacts in soluble monomeric α-synuclein. *Biophysical journal*, 105(5):1192–1198, 2013.

[387] Carlos W Bertoncini, Young-Sang Jung, Claudio O Fernandez, Wolfgang Hoyer, Christian Griesinger, Thomas M Jovin, and Markus Zweckstetter. Release of long-range tertiary interactions potentiates aggregation of natively unstructured α-synuclein. *Proceedings of the National Academy of Sciences*, 102(5):1430–1435, 2005.

[388] Michael M Wördehoff and Wolfgang Hoyer. alpha-synuclein aggregation monitored by thioflavin t fluorescence assay. *Bio Protoc*, 8(14), 2018.

[389] Claudio O Fernandez, Wolfgang Hoyer, Markus Zweckstetter, Elizabeth A Jares-Erijman, Vinod Subramaniam, Christian Griesinger, and Thomas M Jovin. Nmr of alpha-synuclein-polyamine complexes elucidates the mechanism and kinetics of induced aggregation. *EMBO J*, 23(10):2039–46, 2004.

[390] Frank Delaglio, Stephan Grzesiek, Geerten W Vuister, Guang Zhu, John Pfeifer, and A D Bax. Nmrpipe: a multidimensional spectral processing system based on unix pipes. *J Biomol NMR*, 6(3):277–93, 1995.

[391] Wim F Vranken, Wayne Boucher, Tim J Stevens, Rasmus H Fogh, Anne Pajon, Miguel Llinas, Eldon L Ulrich, John L Markley, John Ionides, and Ernest D Laue. The ccpn data model for nmr spectroscopy: development of a software pipeline. *Proteins*, 59(4):687–96, 2005.

[392] C Nick Pace, Eric J Hebert, Kevin L Shaw, David Schell, Valentin Both, Daniela Krajcikova, Jozef Sevcik, Keith S Wilson, Zbigniew Dauter, and Robert W Hartley. Conformational stability and thermodynamics of folding of ribonucleases sa, sa2 and sa3. *Journal of molecular biology*, 279(1):271–286, 1998.

[393] Corinne Quadalti, Sebastian Palmqvist, Sara Hall, Marcello Rossi, Angela Mammana, Shorena Janelidze, Sofia Dellavalle, Niklas Mattsson-Carlgren, Simone Baiardi, and Erik Stomrud. Clinical effects of lewy body pathology in cognitively impaired individuals. *Nature Medicine*, 29(8):1964–1970, 2023.

[394] Paula Saa, Joaquin Castilla, and Claudio Soto. Ultra-efficient replication of infectious prions by automated protein misfolding cyclic amplification. *J Biol Chem*, 281(46):35245–52, 2006.

[395] Ryuichiro Atarashi, Katsuya Satoh, Kazunori Sano, Takayuki Fuse, Naohiro Yamaguchi, Daisuke Ishibashi, Takehiro Matsubara, Takehiro Nakagaki, Hitoki Yamanaka, Susumu Shirabe, Masahito Yamada, Hidehiro Mizusawa, Tetsuyuki Kitamoto, Genevieve Klug, Amelia McGlade, Steven J Collins, and Noriyuki Nishida. Ultrasensitive human prion detection in cerebrospinal fluid by real-time quaking-induced conversion. *Nat Med*, 17(2):175–8, 2011.

[396] Eri Saijo, Bradley R Groveman, Allison Kraus, Michael Metrick, Christina D Orru, Andrew G Hughson, and Byron Caughey. Ultrasensitive rt-quic seed amplification assays for disease-associated tau, alpha-synuclein, and prion aggregates. *Methods Mol Biol*, 1873:19–37, 2019.

[397] Bradley R Groveman, Christina D Orru, Andrew G Hughson, Lynne D Raymond, Gianluigi Zanusso, Bernardino Ghetti, Katrina J Campbell, Jiri Safar, Douglas Galasko, and Byron Caughey. Rapid and ultra-sensitive quantitation of disease-associated alpha-synuclein seeds in brain and cerebrospinal fluid by alphasyn rt-quic. *Acta Neuropathol Commun*, 6(1):7, 2018.

[398] Sireesha Manne, Naveen Kondru, Monica Hepker, Huajun Jin, Vellareddy Anantharam, Mechelle Lewis, Xuemei Huang, Arthi Kanthasamy, and Anumantha G Kanthasamy. Ultra-sensitive detection of aggregated alpha-synuclein in glial cells, human cerebrospinal fluid, and brain tissue using the rt-quic assay: New high-throughput neuroimmune biomarker assay for parkinsonian disorders. *J Neuroimmune Pharmacol*, 14(3):423–435, 2019.

[399] Marcello Rossi, Niccolo Candelise, Simone Baiardi, Sabina Capellari, Giulia Giannini, Christina D Orru, Elena Antelmi, Angela Mammana, Andrew G Hughson, Giovanna Calandra-Buonaura, Anna Ladogana, Giuseppe Plazzi, Pietro Cortelli, Byron Caughey, and Piero Parchi. Ultrasensitive rt-quic assay with high sensitivity and specificity for lewy body-associated synucleinopathies. *Acta Neuropathol*, 140(1):49–62, 2020.

[400] Christina D Orru, Thong C Ma, Andrew G Hughson, Bradley R Groveman, Ankit Srivastava, Douglas Galasko, Rachel Angers, Patrick Downey, Karen Crawford, Samantha J Hutten, Un Jung Kang, and Byron Caughey. A rapid alpha-synuclein seed assay of parkinson's disease csf panel shows high diagnostic accuracy. *Ann Clin Transl Neurol*, 8(2):374–384, 2021.

[401] Mitchell G Miglis, Nicholas Larsen, and Srikanth Muppidi. Rt-quic in multiple system atrophy: the biomarker of the future? and other updates on recent autonomic research. *Clin Auton Res*, 31(1):47–49, 2021.

[402] Saeid Hadi Alijanvand, Alessia Peduzzo, and Alexander K Buell. Secondary nucleation and the conservation of structural characteristics of amyloid fibril strains. *Front Mol Biosci*, 8:669994, 2021.

[403] Heidi G Standke and Allison Kraus. Seed amplification and rt-quic assays to investigate protein seed structures and strains. *Cell and Tissue Research*, 392(1):323–335, 2023.

[404] Niccolò Candelise, Simone Baiardi, Alessia Franceschini, Marcello Rossi, and Piero Parchi. Towards an improved early diagnosis of neurodegenerative diseases: the emerging role of in vitro conversion assays for protein amyloids. *Acta Neuropathologica Communications*, 8:1–16, 2020.

[405] Christina D Orru, Andrew G Hughson, Bradley R Groveman, Katrina J Campbell, Kelsie J Anson, Matteo Manca, Allison Kraus, and Byron Caughey. Factors that improve rt-quic detection of prion seeding activity. *Viruses*, 8(5):140, 2016.

[406] Michael A Metrick, Natalia do Carmo Ferreira, Eri Saijo, Allison Kraus, Kathy Newell, Gianluigi Zanusso, Michele Vendruscolo, Bernardino Ghetti, and Byron Caughey. A single ultrasensitive assay for detection and discrimination of tau aggregates of alzheimer and pick diseases. *Acta Neuropathol Commun*, 8(1):22, 2020.

[407] Stefan Bräuer, Marcello Rossi, Johann Sajapin, Thomas Henle, Thomas Gasser, Piero Parchi, Kathrin Brockmann, and Björn H Falkenburger. Kinetic parameters of alpha-synuclein seed amplification assay correlate with cognitive impairment in patients with lewy body disorders. *Acta Neuropathol Commun*, 11(1):162, 2023.

[408] Tom Scheidt, Urszula Lapinska, Janet R Kumita, Daniel R Whiten, David Klenerman, Mark R Wilson, Samuel I A Cohen, Sara Linse, Michele Vendruscolo, Christopher M Dobson, Tuomas P J Knowles, and Paolo Arosio. Secondary nucleation and elongation occur at different sites on alzheimer's amyloid-beta aggregates. *Sci Adv*, 5(4):eaau3112, 2019.

[409] Sreeganga Chandra, Gilbert Gallardo, Rafael Fernández-Chacón, Oliver M Schlüter, and Thomas C Südhof. α-synuclein cooperates with cspβ in preventing neurodegeneration. *Cell*, 123(3):383–396, 2005.

[410] Stefan Auer, Filip Meersman, Christopher M Dobson, and Michele Vendruscolo. A generic mechanism of emergence of amyloid protofilaments from disordered oligomeric aggregates. *PLoS computational biology*, 4(11):e1000222, 2008.

[411] Marcus Fändrich and Christopher M Dobson. The behaviour of polyamino acids reveals an inverse side chain effect in amyloid structure formation. *The EMBO journal*, 21(21):5682–5690, 2002.

[412] Margaret Sunde and Colin CF Blake. From the globular to the fibrous state: protein structure and structural conversion in amyloid formation. *Quarterly reviews of biophysics*, 31(1):1–39, 1998.

[413] ED Eanes and GG Glenner. X-ray diffraction studies on amyloid filaments. *Journal of Histochemistry Cytochemistry*, 16(11):673–677, 1968.

[414] Javier Simon-Sanchez, Claudia Schulte, Jose M Bras, Manu Sharma, J Raphael Gibbs, Daniela Berg, Coro Paisan-Ruiz, Peter Lichtner, Sonja W Scholz, Dena G Hernandez, Rejko Krüger, Monica Federoff, Christine Klein, Alison Goate, Joel Perlmutter, Michael Bonin, Michael A Nalls, Thomas Illig, Christian Gieger, Henry Houlden, Michael Steffens, Michael S Okun, Brad A Racette, Mark R Cookson, Kelly D Foote, Hubert H Fernandez, Bryan J Traynor, Stefan Schreiber, Sampath Arepalli, Ryan Zonozi, Katrina Gwinn, Marcel van der Brug, Grisel Lopez, Stephen J Chanock, Arthur Schatzkin, Yikyung Park, Albert Hollenbeck, Jianjun Gao, Xuemei Huang, Nick W Wood, Delia Lorenz, Günther Deuschl, Honglei Chen, Olaf Riess, John A Hardy, Andrew B Singleton, and Thomas Gasser. Genome-wide association study reveals genetic risk underlying parkinson's disease. *Nat Genet*, 41(12):1308–12, 2009.

[415] Frank Soldner, Yonatan Stelzer, Chikdu S Shivalila, Brian J Abraham, Jeanne C Latourelle, M Inmaculada Barrasa, Johanna Goldmann, Richard H Myers, Richard A Young, and Rudolf Jaenisch. Parkinson-associated risk variant in distal enhancer of alpha-synuclein modulates target gene expression. *Nature*, 533(7601):95–9, 2016.

[416] Vladimir N Uversky. Neuropathology, biochemistry, and biophysics of alpha-synuclein aggregation. *J Neurochem*, 103(1):17–37, 2007.

[417] Jing L Guo and Virginia MY Lee. Cell-to-cell transmission of pathogenic proteins in neurodegenerative diseases. *Nature medicine*, 20(2):130–138, 2014.

[418] Antony A Cooper, Aaron D Gitler, Anil Cashikar, Cole M Haynes, Kathryn J Hill, Bhupinder Bhullar, Kangning Liu, Kexiang Xu, Katherine E Strathearn, and Fang Liu. α-synuclein blocks er-golgi traffic and rab1 rescues neuron loss in parkinson's models. *Science*, 313(5785):324–328, 2006.

[419] Kelvin C Luk, Victoria Kehm, Jenna Carroll, Bin Zhang, Patrick O'Brien, John Q Trojanowski, and Virginia M-Y Lee. Pathological alpha-synuclein transmission initiates parkinson-like neurodegeneration in nontransgenic mice. *Science*, 338(6109):949–53, 2012.

[420] Laura A Volpicelli-Daley, Kelvin C Luk, Tapan P Patel, Selcuk A Tanik, Dawn M Riddle, Anna Stieber, David F Meaney, John Q Trojanowski, and Virginia M-Y Lee. Exogenous alpha-synuclein fibrils induce lewy body pathology leading to synaptic dysfunction and neuron death. *Neuron*, 72(1):57–71, 2011.

[421] Masatoshi Konno, Takafumi Hasegawa, Toru Baba, Emiko Miura, Naoto Sugeno, Akio Kikuchi, Fabienne C Fiesel, Tsutomu Sasaki, Masashi Aoki, Yasuto Itoyama, and Atsushi Takeda. Suppression of dynamin gtpase decreases alpha-synuclein uptake by neuronal and oligodendroglial cells: a potent therapeutic target for synucleinopathy. *Mol Neurodegener*, 7:38, 2012.

[422] Satyajit Mayor and Richard E Pagano. Pathways of clathrin-independent endocytosis. *Nat Rev Mol Cell Biol*, 8(8):603–12, 2007.

[423] Pravin Hivare, Joshna Gadhavi, Dhiraj Bhatia, and Sharad Gupta. β-synuclein fibrils explore actin-mediated macropinocytosis for cellular entry into model neuroblastoma neurons. *Traffic*, 23(7):391–410, 2022.

[424] He-Jin Lee, Smita Patel, and Seung-Jae Lee. Intravesicular localization and exocytosis of alpha-synuclein and its aggregates. *J Neurosci*, 25(25):6016–24, 2005.

[425] Elisabet Ihse, Hodaka Yamakado, Xander M van Wijk, Roger Lawrence, Jeffrey D Esko, and Eliezer Masliah. Cellular internalization of alpha-synuclein aggregates by cell surface heparan sulfate depends on aggregate conformation and cell type. *Scientific reports*, 7(1):9008, 2017.

[426] Thomas L Williams and Louise C Serpell. Membrane and surface interactions of alzheimer's aβ peptide–insights into the mechanism of cytotoxicity. *The FEBS journal*, 278(20):3905–3917, 2011.

[427] Sara M Butterfield and Hilal A Lashuel. Amyloidogenic protein–membrane interactions: mechanistic insight from model systems. *Angewandte Chemie International Edition*, 49(33):5628–5654, 2010.

[428] Frits Kamp and Klaus Beyer. Binding of α-synuclein affects the lipid packing in bilayers of small vesicles. *Journal of Biological Chemistry*, 281(14):9251–9259, 2006.

[429] Saïda Abounit and Chiara Zurzolo. Wiring through tunneling nanotubes–from electrical signals to organelle transfer. *Journal of cell science*, 125(5):1089–1098, 2012.

[430] Qian Yang, Hua She, Marla Gearing, Emanuela Colla, Michael Lee, John J Shacka, and Zixu Mao. Regulation of neuronal survival factor mef2d by chaperone-mediated autophagy. *Science*, 323(5910):124–127, 2009.

[431] Darius Ebrahimi-Fakhari, Laiq-Jan Saidi, and Lara Wahlster. Molecular chaperones and protein folding as therapeutic targets in parkinson's disease and other synucleinopathies. *Acta neuropathologica communications*, 1(1):1–15, 2013.

[432] Stephan N Witt. Hsp70 molecular chaperones and parkinson's disease. *Biopolymers: Original Research on Biomolecules*, 93(3):218–228, 2010.

[433] Ranjita Betarbet, Todd B Sherer, and J Timothy Greenamyre. Ubiquitin–proteasome system and parkinson's diseases. *Experimental neurology*, 191:S17–S27, 2005.

[434] Xu Hou, Jens O Watzlawik, Fabienne C Fiesel, and Wolfdieter Springer. Autophagy in parkinson's disease. *Journal of molecular biology*, 432(8):2651–2672, 2020.

[435] Melinda A Lynch-Day, Kai Mao, Ke Wang, Mantong Zhao, and Daniel J Klionsky. The role of autophagy in parkinson's disease. *Cold Spring Harbor perspectives in medicine*, 2(4), 2012.

[436] Etienne C Hirsch, Sheela Vyas, and Stéphane Hunot. Neuroinflammation in parkinson's disease. *Parkinsonism related disorders*, 18:S210–S212, 2012.

[437] Qinqin Wang, Yingjun Liu, and Jiawei Zhou. Neuroinflammation in parkinson's disease and its potential as therapeutic target. *Translational neurodegeneration*, 4:1–9, 2015.

[438] R Constantinescu, AT Constantinescu, H Reichmann, and B Janetzky. Neuronal differentiation and long-term culture of the human neuroblastoma line sh-sy5y. In *Neuropsychiatric Disorders An Integrative Approach.*, pages 17–28. Springer, 2007.

[439] Min Zhu, Jie Li, and Anthony L Fink. The association of α-synuclein with membranes affects bilayer structure, stability, and fibril formation. *Journal of Biological Chemistry*, 278(41):40186–40197, 2003.

[440] Tsui-Wen Chou, Nydia P Chang, Medha Krishnagiri, Aisha P Patel, Marissa Lindman, Juan P Angel, Po-Lun Kung, Colm Atkins, and Brian P Daniels. Fibrillar α-synuclein induces neurotoxic astrocyte activation via rip kinase signaling and nf-b. *Cell Death Disease*, 12(8):756, 2021.

[441] Gregor Bieri, Aaron D Gitler, and Michel Brahic. Internalization, axonal transport and release of fibrillar forms of alpha-synuclein. *Neurobiology of disease*, 109:219–225, 2018.

[442] Jordi Bella and Michael G Rossmann. Icam-1 receptors and cold viruses. *Pharmacochemistry Library*, 31:291–297, 2000.

[443] Jean-Francois Fortin, Rejean Cantin, Ginette Lamontagne, and Michel Tremblay. Host-derived icam-1 glycoproteins incorporated on human immunodeficiency virus type 1 are biologically active and enhance viral infectivity. *Journal of virology*, 71(5):3588–3596, 1997.

[444] Jianfeng Dai, Penghua Wang, Fengwei Bai, Terrence Town, and Erol Fikrig. Icam-1 participates in the entry of west nile virus into the central nervous system. *Journal of virology*, 82(8):4164–4168, 2008.

[445] Alexandra E Butler, Juliette Janson, Susan Bonner-Weir, Robert Ritzel, Robert A Rizza, and Peter C Butler. β-cell deficit and increased β-cell apoptosis in humans with type 2 diabetes. *Diabetes*, 52(1):102–110, 2003.

[446] Steven E Kahn, Sofianos Andrikopoulos, and C Bruce Verchere. Islet amyloid: a long-recognized but underappreciated pathological feature of type 2 diabetes. *Diabetes*, 48(2):241–253, 1999.

[447] Per Westermark. Amyloid and polypeptide hormones: what is their interrelationship? *Amyloid*, 1(1):47–60, 1994.

[448] Juliette Janson, Walter C Soeller, Patrick C Roche, Robin T Nelson, Anthony J Torchia, David K Kreutter, and Peter C Butler. Spontaneous diabetes mellitus in transgenic mice expressing human islet amyloid polypeptide. *Proceedings of the National Academy of Sciences*, 93(14):7283–7288, 1996.

[449] Myriam M Altamirano-Bustamante, Nelly F Altamirano-Bustamante, Mateo Larralde-Laborde, Reyna Lara-Martínez, Edgar Leyva-García, Eulalia Garrido-Magaña, Gerardo Rojas, Luis Felipe Jiménez-García, Cristina Revilla-Monsalve, and Perla Altamirano. Unpacking the aggregation-oligomerization-fibrillization process of naturally-occurring hiapp amyloid oligomers isolated directly from sera of children with obesity or diabetes mellitus. *Scientific Reports*, 9(1):18465, 2019.

[450] Nelly F Altamirano-Bustamante, Eulalia Garrido-Magaña, Eugenia Morán, Aurora Calderón, Karina Pasten-Hidalgo, Rosa Angélica Castillo-Rodríguez, Gerardo Rojas, Reyna Lara-Martínez, Edgar Leyva-Garcia, and Mateo Larralde-Laborde. Protein-conformational diseases in childhood: Naturally-occurring hiapp amyloid-oligomers and early β-cell damage in obesity and diabetes. *Plos one*, 15(8):e0237667, 2020.

[451] Melissa Birol, Sunil Kumar, Elizabeth Rhoades, and Andrew D Miranker. Conformational switching within dynamic oligomers underpins toxic gain-of-function by diabetes-associated amyloid. *Nature communications*, 9(1):1312, 2018.

[452] Steven E Kahn, David A D'Alessio, Michael W Schwartz, Wilfred Y Fujimoto, John W Ensinck, Gerald J Taborsky Jr, and Daniel Porte Jr. Evidence of cosecretion of islet amyloid polypeptide and insulin by β-cells. *Diabetes*, 39(5):634–638, 1990.

[453] Hans J Woerle, Max Albrecht, Rainer Linke, Silvia Zschau, Christoph Neumann, Mathias Nicolaus, John E Gerich, Burkhard Goke, and Joerg Schirra. Impaired hyperglycemia-induced delay in gastric emptying in patients with type 1 diabetes deficient for islet amyloid polypeptide. *Diabetes Care*, 31(12):2325–2331, 2008.

[454] A Kanatsuka, H Makino, H Ohsawa, Y Tokuyama, T Yamaguchi, S Yoshida, and M Adachi. Secretion of islet amyloid polypeptide in response to glucose. *FEBS letters*, 259(1):199–201, 1989.

[455] Urban Arnelo. *Islet amyloid polypeptide in the control of food intake: an experimental study in the rat*. Inst för klinisk vetenskap, intervention och teknik / Dept of Clinical Science, Intervention and Technology, 1997.

[456] Björn Åkesson, Georgios Panagiotidis, Per Westermark, and Ingmar Lundquist. Islet amyloid polypeptide inhibits glucagon release and exerts a dual action on insulin release from isolated islets. *Regulatory peptides*, 111(1-3):55–60, 2003.

[457] Lothar Gremer, Daniel Schölzel, Carla Schenk, Elke Reinartz, Jörg Labahn, Raimond BG Ravelli, Markus Tusche, Carmen Lopez-Iglesias, Wolfgang Hoyer, and Henrike Heise. Fibril structure of amyloid-β (1–42) by cryo–electron microscopy. *Science*, 358(6359):116–119, 2017.

[458] Christine Röder, Tatsiana Kupreichyk, Lothar Gremer, Luisa U Schäfer, Karunakar R Pothula, Raimond BG Ravelli, Dieter Willbold, Wolfgang Hoyer, and Gunnar F Schröder. Cryo-em structure of islet amyloid polypeptide fibrils reveals similarities with amyloid-β fibrils. *Nature structural molecular biology*, 27(7):660–667, 2020.

[459] Eugene L Opie. On the relation of chronic interstitial pancreatitis to the islands of langerhans and to diabetes melutus. *The Journal of experimental medicine*, 5(4):397, 1901.

[460] A Weichselbaum and E Stangl. Zur kenntnis der feineren veränderungen des pankreas bei diabetes mellitus. *Wiener Klinische Wochenschrift*, 14(1):968–972, 1901.

[461] Per Westermark, Christer Wernstedt, Erik Wilander, and Knut Sletten. A novel peptide in the calcitonin gene related peptide family as an amyloid fibril protein in the endocrine pancreas. *Biochemical and biophysical research communications*, 140(3):827–831, 1986.

[462] Per Westermark. Amyloid fibrils in the human insulinoma and islets of langerhans of the diabetic cats are derived from a neuropeptide-like protein also present in normal islet cells. *Proc Natl Acad Sci USA*, 84:9628–9632, 1987.

[463] Leena Haataja, Tatyana Gurlo, Chang J Huang, and Peter C Butler. Islet amyloid in type 2 diabetes, and the toxic oligomer hypothesis. *Endocrine reviews*, 29(3):303–316, 2008.

[464] Alexandra E Butler, Juliette Janson, Walter C Soeller, and Peter C Butler. Increased β-cell apoptosis prevents adaptive increase in β-cell mass in mouse model of type 2 diabetes: evidence for role of islet amyloid formation rather than direct action of amyloid. *Diabetes*, 52(9):2304–2314, 2003.

[465] Tatyana Gurlo, Sergey Ryazantsev, Chang-jiang Huang, Michael W Yeh, Howard A Reber, O Joe Hines, Timothy D O'Brien, Charles G Glabe, and Peter C Butler. Evidence for proteotoxicity in β cells in type 2 diabetes: toxic islet amyloid polypeptide oligomers form intracellularly in the secretory pathway. *The American journal of pathology*, 176(2):861–869, 2010.

[466] Chia-Yu Lin, Tatyana Gurlo, Rakez Kayed, Alexandra E Butler, Leena Haataja, Charles G Glabe, and Peter C Butler. Toxic human islet amyloid polypeptide (h-iapp) oligomers are intracellular, and vaccination to induce anti-toxic oligomer antibodies does not prevent h-iapp–induced β-cell apoptosis in h-iapp transgenic mice. *Diabetes*, 56(5):1324–1332, 2007.

[467] Seth L Masters, Aisling Dunne, Shoba L Subramanian, Rebecca L Hull, Gillian M Tannahill, Fiona A Sharp, Christine Becker, Luigi Franchi, Eiji Yoshihara, and Zhe Chen. Activation of the nlrp3 inflammasome by islet amyloid polypeptide provides a mechanism for enhanced il-1β in type 2 diabetes. *Nature immunology*, 11(10):897–904, 2010.

[468] Juris J Meier, Rakez Kayed, Chia-Yu Lin, Tatyana Gurlo, Leena Haataja, Sajith Jayasinghe, Ralf Langen, Charles G Glabe, and Peter C Butler. Inhibition of human iapp fibril formation does not prevent β-cell death: evidence for distinct actions of oligomers and fibrils of human iapp. *American Journal of Physiology-Endocrinology and Metabolism*, 291(6):E1317–E1324, 2006.

[469] Yaron Bram, Anat Frydman-Marom, Inbal Yanai, Sharon Gilead, Ronit Shaltiel-Karyo, Nadav Amdursky, and Ehud Gazit. Apoptosis induced by islet amyloid polypeptide soluble oligomers is neutralized by diabetes-associated specific antibodies. *Scientific reports*, 4(1):4267, 2014.

[470] Emma E Cawood, Theodoros K Karamanos, Andrew J Wilson, and Sheena E Radford. Visualizing and trapping transient oligomers in amyloid assembly pathways. *Biophysical chemistry*, 268:106505, 2021.

[471] Dominic M Walsh and Dennis J Selkoe. Aβ oligomers–a decade of discovery. *Journal of neurochemistry*, 101(5):1172–1184, 2007.

[472] S Zraika, RL Hull, CB Verchere, A Clark, KJ Potter, PE Fraser, DP Raleigh, and SE Kahn. Toxic oligomers and islet beta cell death: guilty by association or convicted by circumstantial evidence? *Diabetologia*, 53:1046–1056, 2010.

[473] James P Cleary, Dominic M Walsh, Jacki J Hofmeister, Ganesh M Shankar, Michael A Kuskowski, Dennis J Selkoe, and Karen H Ashe. Natural oligomers of the amyloid-β protein specifically disrupt cognitive function. *Nature neuroscience*, 8(1):79–84, 2005.

[474] Rakez Kayed, Yuri Sokolov, Brian Edmonds, Theresa M McIntire, Saskia C Milton, James E Hall, and Charles G Glabe. Permeabilization of lipid bilayers is a common conformation-

dependent activity of soluble amyloid oligomers in protein misfolding diseases. *Journal of Biological Chemistry*, 279(45):46363–46366, 2004.

[475] Marcelo NN Vieira, Letícia Forny-Germano, Leonardo M Saraiva, Adriano Sebollela, Ana M Blanco Martinez, Jean-Christophe Houzel, Fernanda G De Felice, and Sérgio T Ferreira. Soluble oligomers from a non-disease related protein mimic aβ-induced tau hyperphosphorylation and neurodegeneration. *Journal of neurochemistry*, 103(2):736–748, 2007.

[476] Miao Yuan, Xuan Tang, and Wei Han. Anatomy and formation mechanisms of early amyloid-β oligomers with lateral branching: graph network analysis on large-scale simulations. *Chemical Science*, 13(9):2649–2660, 2022.

[477] Erika Andreetto, Li-Mei Yan, Marianna Tatarek-Nossol, Aleksandra Velkova, Ronald Frank, and Aphrodite Kapurniotu. Identification of hot regions of the aβ–iapp interaction interface as high-affinity binding sites in both cross-and self-association. *Angewandte Chemie International Edition*, 49(17):3081–3085, 2010.

[478] Rodrigo Gallardo, Matthew G Iadanza, Yong Xu, George R Heath, Richard Foster, Sheena E Radford, and Neil A Ranson. Fibril structures of diabetes-related amylin variants reveal a basis for surface-templated assembly. *Nature Structural Molecular Biology*, 27(11):1048–1056, 2020.

[479] Qin Cao, David R Boyer, Michael R Sawaya, Peng Ge, and David S Eisenberg. Cryo-em structure and inhibitor design of human iapp (amylin) fibrils. *Nature structural molecular biology*, 27(7):653–659, 2020.

[480] Bon W Koo and Andrew D Miranker. Contribution of the intrinsic disulfide to the assembly mechanism of islet amyloid. *Protein Science*, 14(1):231–239, 2005.

[481] Katherine Esposito, M Ciotola, B Schisano, L Misso, G Giannetti, A Ceriello, and Dario Giugliano. Oxidative stress in the metabolic syndrome. *Journal of endocrinological investigation*, 29:791–795, 2006.

[482] Alba Fernández-Sánchez, Eduardo Madrigal-Santillán, Mirandeli Bautista, Jaime Esquivel-Soto, Ángel Morales-González, Cesar Esquivel-Chirino, Irene Durante-Montiel, Graciela Sánchez-Rivera, Carmen Valadez-Vega, and José A Morales-González. Inflammation, oxidative stress, and obesity. *International journal of molecular sciences*, 12(5):3117–3132, 2011.

[483] D Allan Butterfield, Jennifer Drake, Chava Pocernich, and Alessandra Castegna. Evidence of oxidative damage in alzheimer's disease brain: central role for amyloid β-peptide. *Trends in molecular medicine*, 7(12):548–554, 2001.

[484] Reiko Inagi, Yu Ishimoto, and Masaomi Nangaku. Proteostasis in endoplasmic reticulum—new mechanisms in kidney disease. *Nature Reviews Nephrology*, 10(7):369–378, 2014.

[485] Stewart Siyan Cao and Randal J Kaufman. Unfolded protein response. *Current biology*, 22(16):R622–R626, 2012.

[486] Yiming Li, Yunshan Guo, Juan Tang, Jianli Jiang, and Zhinan Chen. New insights into the roles of chop-induced apoptosis in er stress. *Acta Biochim Biophys Sin*, 46(8):629–640, 2014.

[487] Nancy L Kedersha, Mita Gupta, Wei Li, Ira Miller, and Paul Anderson. Rna-binding proteins tia-1 and tiar link the phosphorylation of eif-2β to the assembly of mammalian stress granules. *The Journal of cell biology*, 147(7):1431–1442, 1999.

[488] Peiguo Yang, Cécile Mathieu, Regina-Maria Kolaitis, Peipei Zhang, James Messing, Ugur Yurtsever, Zemin Yang, Jinjun Wu, Yuxin Li, and Qingfei Pan. G3bp1 is a tunable switch that triggers phase separation to assemble stress granules. *Cell*, 181(2):325–345. e28, 2020.

[489] L Nover, KD Scharf, and D Neumann. Formation of cytoplasmic heat shock granules in tomato cell cultures and leaves. *Molecular and cellular biology*, 3(9):1648–1655, 1983.

[490] David W Sanders, Nancy Kedersha, Daniel SW Lee, Amy R Strom, Victoria Drake, Joshua A Riback, Dan Bracha, Jorine M Eeftens, Allana Iwanicki, and Alicia Wang. Competing protein-rna interaction networks control multiphase intracellular organization. *Cell*, 181(2):306–324. e28, 2020.

[491] Antoine Cléry, Markus Blatter, and Frédéric HT Allain. Rna recognition motifs: boring? not quite. *Current opinion in structural biology*, 18(3):290–298, 2008.

[492] Jordina Guillén-Boixet, Andrii Kopach, Alex S Holehouse, Sina Wittmann, Marcus Jahnel, Raimund Schlüßler, Kyoohyun Kim, Irmela REA Trussina, Jie Wang, and Daniel Mateju. Rna-induced conformational switching and clustering of g3bp drive stress granule assembly by condensation. *Cell*, 181(2):346–361. e17, 2020.

[493] Praveen Nedumpully-Govindan, Aleksandr Kakinen, Emily H Pilkington, Thomas P Davis, Pu Chun Ke, and Feng Ding. Stabilizing off-pathway oligomers by polyphenol nanoassemblies for iapp aggregation inhibition. *Scientific reports*, 6(1):19463, 2016.

[494] Fernando L Palhano, Jiyong Lee, Neil P Grimster, and Jeffery W Kelly. Toward the molecular mechanism (s) by which egcg treatment remodels mature amyloid fibrils. *Journal of the American Chemical Society*, 135(20):7503–7510, 2013.

[495] Ping Cao and Daniel P Raleigh. Analysis of the inhibition and remodeling of islet amyloid polypeptide amyloid fibers by flavanols. *Biochemistry*, 51(13):2670–2683, 2012.

[496] Fanling Meng, Andisheh Abedini, Annette Plesner, C Bruce Verchere, and Daniel P Raleigh. The flavanol (-)-epigallocatechin 3-gallate inhibits amyloid formation by islet amyloid polypeptide, disaggregates amyloid fibrils, and protects cultured cells against iapp-induced toxicity. *Biochemistry*, 49(37):8127–8133, 2010.

[497] Amit Pithadia, Jeffrey R Brender, Carol A Fierke, and Ayyalusamy Ramamoorthy. Inhibition of iapp aggregation and toxicity by natural products and derivatives. *Journal of diabetes research*, 2016, 2016.

[498] Manikam S Saravanan, Sergey Ryazanov, Andrei Leonov, Janine Nicolai, Patrique Praest, Armin Giese, Roland Winter, Lucie Khemtemourian, Christian Griesinger, and J Antoinette Killian. The small molecule inhibitor anle145c thermodynamically traps human islet amyloid peptide in the form of non-cytotoxic oligomers. *Scientific Reports*, 9(1):19023, 2019.

[499] Chang-jiang Huang, Leena Haataja, Tatyana Gurlo, Alexandra E Butler, Xiuju Wu, Walter C Soeller, and Peter C Butler. Induction of endoplasmic reticulum stress-induced β-cell apoptosis and accumulation of polyubiquitinated proteins by human islet amyloid polypeptide. *American Journal of Physiology-Endocrinology and Metabolism*, 293(6):E1656–E1662, 2007.

[500] Chang-jiang Huang, Chia-yu Lin, Leena Haataja, Tatyana Gurlo, Alexandra E Butler, Robert A Rizza, and Peter C Butler. High expression rates of human islet amyloid polypeptide induce endoplasmic reticulum stress–mediated β-cell apoptosis, a characteristic of humans with type 2 but not type 1 diabetes. *Diabetes*, 56(8):2016–2027, 2007.

[501] T Gurlo, JF Rivera, AE Butler, M Cory, J Hoang, S Costes, and Peter C Butler. Chop contributes to, but is not the only mediator of, iapp induced β-cell apoptosis. *Molecular endocrinology*, 30(4):446–454, 2016.

[502] Mara Zielinski, Christine Röder, and Gunnar F Schröder. Challenges in sample preparation and structure determination of amyloids by cryo-em. *Journal of Biological Chemistry*, 297(2):100938, 2021.

[503] Ying Fan, Kyung Lee, Niansong Wang, and John Cijiang He. The role of endoplasmic reticulum stress in diabetic nephropathy. *Current diabetes reports*, 17:1–7, 2017.

[504] Ewa Agnieszka Mirecka, Lothar Gremer, Stephanie Schiefer, Filipp Oesterhelt, Matthias Stoldt, Dieter Willbold, and Wolfgang Hoyer. Engineered aggregation inhibitor fusion for production of highly amyloidogenic human islet amyloid polypeptide. *Journal of Biotechnology*, 191:221–227, December 2014.

[505] Susanne Aileen Funke and Dieter Willbold. Mirror image phage display—a method to generate d-peptide ligands for use in diagnostic or therapeutical applications. *Molecular BioSystems*, 5(8):783–786, 2009.